INCLUSIVE PHOTOPRODUCTION AT 20.5 GeV/c USING THE SLAC HYBRID FACILITY

by

Patricia Rankin

A thesis submitted for the degree
of Doctor of Philosophy of the
University of London

Dept. of Physics
Imperial College
London SW7

May 1982

ABSTRACT

Results on inclusive photoproduction at 20.5 GeV (peak beam energy) are presented. Data were taken in the SLAC 40" rapid cycling bubble chamber. The fast trigger used to selectively fire the bubble chamber flash guns will be described and the fraction of the total cross section triggered on is estimated. Current theoretical ideas about the photon structure functions are discussed as is the possible importance of photoproduction as an experimental test of the Recombination model. Inclusive distributions are considered from the viewpoint of whether or not they show evidence of point-like photon behaviour. A comparison is made to Recombination model predictions.

CONTENTS

TABLES

FIGURES

CHAPTER 1

THE EXPERIMENT

1.1 The Aims of the Experiment

The discovery of charmed mesons in late 1974 provided experimental support for the GIM hypothesis [1]. Since then the importance of charm physics as a testing ground for theoretical ideas has continued. Despite high statistics colliding beam experiments which have successfully established the spectroscopy of the charmed mesons (which can be produced by e^+e^- annihilation), the lifetimes of those mesons and the properties of the charmed baryons are still relatively unknown. The BC 72/73 experiment was intended to increase the available information both on charmed particles specifically and on photoproduction in general.

The peak energy of the photon beam was expected to give the maximum ratio of the amount of associated production of charmed baryons relative to that of the production of charmed particles by any mechanism. The theoretical estimates of the cross section for charm production at this energy ranged between 30nb and 3μb. The experiment was designed to be sensitive to charm production at the lower cross sectional limit and it was felt that if the cross section was at least 300nb that the properties of charmed particles (production mechanisms, decay modes etc) could be studied in detail.

The 4π acceptance of the bubble chamber coupled with the attachment to it of a high resolution camera make it possible to detect charm particle decays at the scanning stage of the experiment. Unlike an emulsion experiment, although the decays of very short lived particles go undetected, the chance of missing those of comparatively long lived particles (even if they are neutral) is small. The preliminary results already obtained on charm lifetimes by this experiment will not be discussed in this thesis. This reflects their importance rather than a lack of interest on the author's part. They are already the subject of a publication [2] which represents the efforts of many people. Instead I

shall concentrate on the photoproduction of charged particles without restricting myself to exclusive channels.

The decision when to trigger the bubble chamber flash tubes was made very non specific in order to make it possible to isolate essentially unbiased samples of nearly all hadronic final states. This makes the data suitable for use in investigating the properties of inclusive distributions. The possibility that the photon can interact directly as a gauge boson as well as (more conventionally) as a vector meson allows firmer predictions to be made about these inclusive distributions than can be made about those produced by a hadronic beam. This experiment contributes substantially to the available information on inclusive photoproduction at moderate energies (around 20 GeV).

1.2 The Beam

The photon beam used in this experiment has a peak energy of 20.5 GeV and is produced by backscattering 4.68 eV photons off a 29.5 GeV electron beam. The energy spectrum as measured by a pair spectrometer (situated just in front of the bubble chamber) is shown in Figure 1.2.1. It is

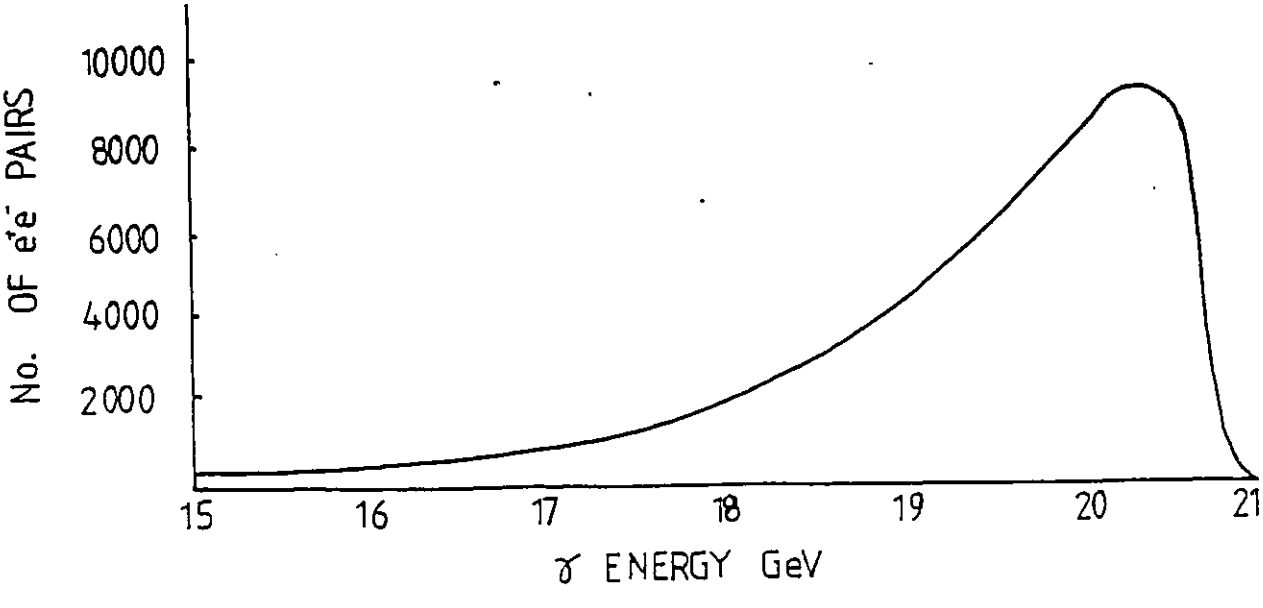

Figure 1.2.1

estimated that less than ten percent of the photons reaching the bubble chamber have energies below 15 GeV.

The source of the initial (4.68 eV) photons is a four level solid state laser which uses a Nd:YAG (Neodymium-doped Yttrium Aluminium Garnet) crystal as the lasing material. The fundamental frequency of the laser is quadrupled by putting KDP (Potassium Di-Phosphate) and KD*P (Potassium Di-Deuterium-Phosphate) crystals into the beam in series, thus generating the fourth harmonic beam finally output. In order to produce the short intense pulses of light needed, the lasing action is controlled by a Q-switch. The Q-switch contains an electro-optical crystal which polarises light passing through it, the sense of the polarisation depending on an electric-field applied to the crystal. While the upper energy level of the Nd:YAG crystal is being filled the aim is to prevent light emitted from the crystal from re-entering it (and stimulating further emission). A system of polarisers in conjunction with the Q-switch blocks the return of light during pumping. When the upper level is full however the field applied to the electro-optical crystal is suddenly switched, the polarisers now allow the light through, and lasing takes place. The laser is run at a repetition rate of 10Hz and each pulse consists of an average of 10^{17} linearly polarised photons. The main components of the laser's optical system are shown in Figure 1.2.2.

To produce an electron beam at about 30 GeV, the linac is operated in the SLED 1 [3] mode. The power radiated from a heavily overcoupled microwave cavity approaches four times the incident generator power immediately after the generator is switched off. This radiated power normally travels as a reverse wave back toward the generator. However some microwave networks can direct the radiated power into an external load. One such network consists of two identical cavities attached to a large coupler (e.g. 3-db). The sledded beam is produced by

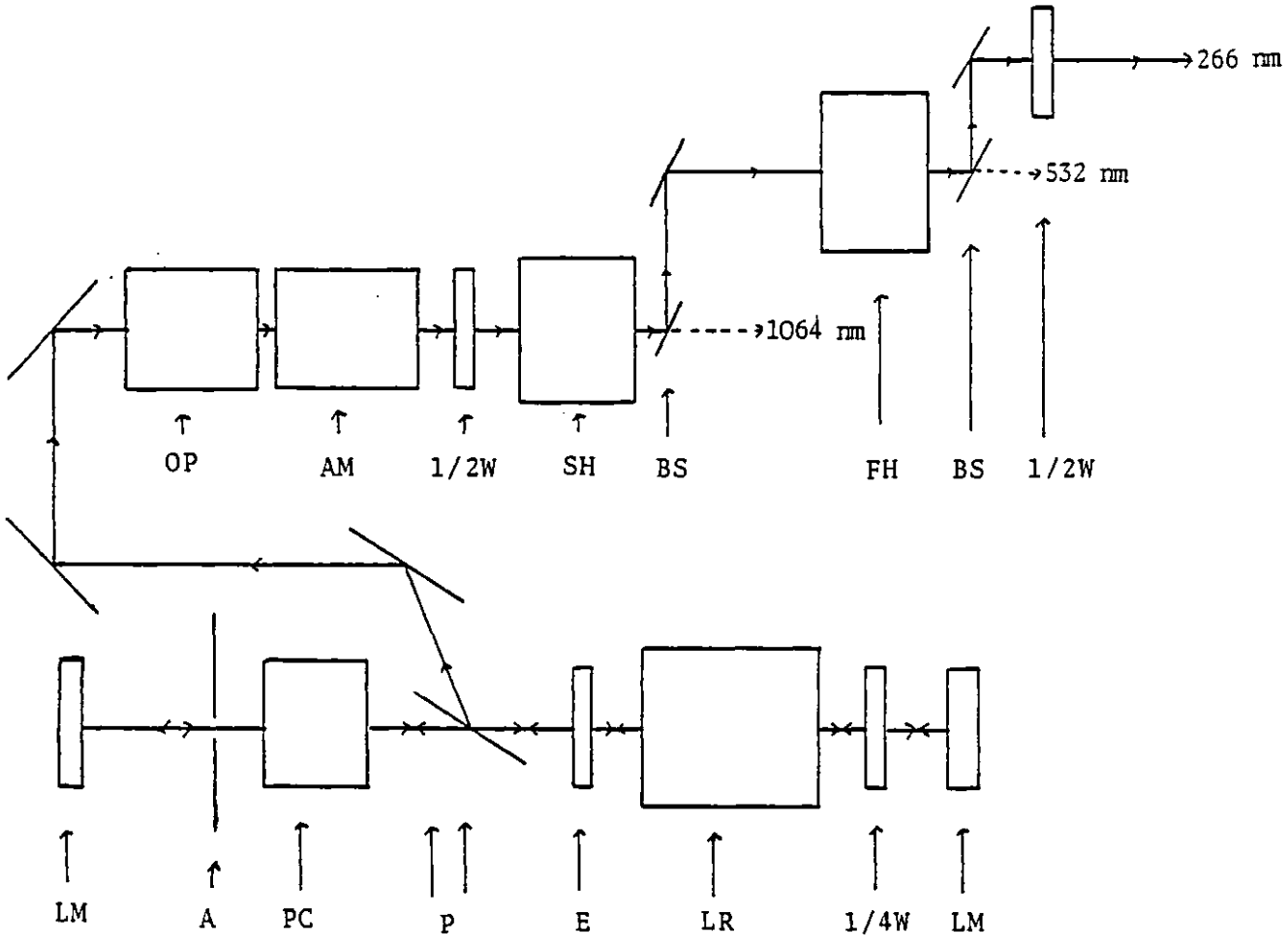

FIGURE 1.2.2

SCHEMATIC OF LASER OPTICS

Key

LR	Lasing material, Nd:YAG rod		
LM	Laser Mirrors		
A	Aperture	AM	Amplifier
PC	Pockels cell/Q-switch	SH	Second harmonic generator
P	Polarisers	BS	Dichroic beam splitter
E	Etalon	FH	Fourth harmonic generator
$\frac{1}{4}$w, $\frac{1}{2}$w	$\frac{1}{4}$ and $\frac{1}{2}$ wave plates		
OP	Optical isolator		

using a system of dual cavities spaced at intervals along the beam line to modify the RF produced by the linac. The width of the RF pulses is reduced but their peak power increases (by a factor of 1.4) increasing the boost given to the electron beam energy. The beam is run at 180 Hz, each pulse having a duration of 200 nsec and comprised on average of 10^{11} electrons.

The laser beam intersects the electron beam at 2 milliradian. The yield of photons varied during the run between 5 and 80 but in general we operated at around 25 photons/pulse at a rate of 10 Hz (determined by the laser's repetition rate). The beam has a linear polarisation of around 55 percent and the axis of polarisation was alternated during the run between parallel and perpendicular to the horizontal. The beam has a diameter of 3mm. Figure 1.2.3 shows the main elements of the beam line and detectors associated with it. A derivation of the formula for calculating the energy of a backscattered photon beam is given in Appendix A.

1.3 The SLAC Hybrid Facility

The facility can be divided into three sections; the upstream detectors, the SLAC 40" bubble chamber, and the downstream detectors.

1.3.A The Upstream System

There are two upstream detectors. The quadrant detector is used to check the steering of the beam and ensure that it is aligned correctly. The pair spectrometer (P.S.) is used to analyse the momentum of e^+e^- pairs produced by photons converting in its radiator foils and hence provides information on the beam's spectrum and intensity. The relative locations of these detectors are shown in Figure 1.2.3. Table 1.3.A.1 gives more details.

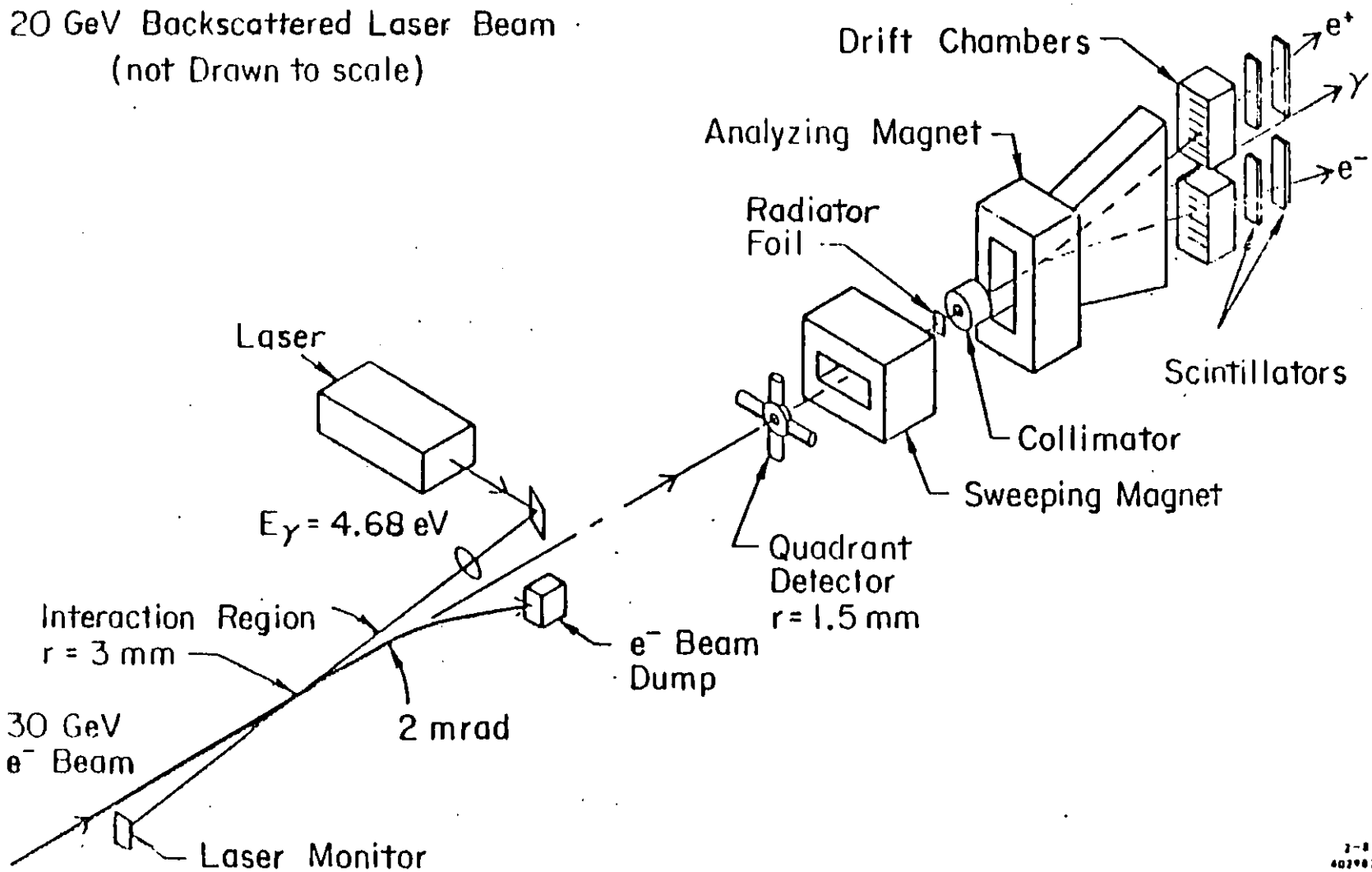

Figure 1.2.3 SHF BEAM LINE

COMPONENT	X POSITION / CM
Interaction region	16722 (± 300)
Quadrant Detector	1722
Sweeping Magnet (27D4)	1570
P.S. Collimator	1443
Analysing Magnet (27D5)	1275
Sense Wire #1 of Lower drift chamber	815
Sense Wire #1 of Upper drift chamber	817
Scintillators #1 and #3	791
Scintillators #2 and #4	781
Centre of Bubble Chamber	0.0

Table 1.3.A.1
POSITION OF MAIN COMPONENTS OF UPSTREAM SYSTEM

There are thirty wires in each of the pair spectrometer drift chambers arranged in two rows which are 5.6 cm apart. The vertical separation between wires in a particular row is 2.6 cm. The vertical separation between wires is 1.3 cm.

1.3.B The Bubble Chamber

The bubble chamber acts as both the liquid hydrogen target for the photon beam and as the first charged track detector of the downstream system. Its essential features are listed in Table 1.3.B.1

The bubble chamber was run hot at a temperature of approximately 29K in order to obtain a slow bubble growth rate and a high bubble density (about 70 bubbles/cm compared to the more usual 15 bubbles/cm).

In addition to the usual 3 cameras the chamber was also equipped with a centrally placed high resolution camera. This has a Schneider

Chamber Diameter	1 metre
Chamber Depth	43 cm
Pulsing Rate	10-15 Hz
Entrance and Exit Windows	1.5mm Stainless Steel
Magnetic Field	26 kG
Illumination	Bright Field (Piston covered with Scotchlite)
Camera Rate	2 Hz Maximum

Table 1.3.B.1 ELEMENTS OF THE SLAC 40" BUBBLE CHAMBER

COMPONON S lens of 360mm focal length which was operated at f/11. The high resolution camera views a volume of dimensions 76 x 13 x 1.2 cm^3 centred on the beam and chamber. Within this volume the optical resolution obtainable is 55 μm although the actual resolution achieved depended on the operating conditions (about 65 μm during the first two runs over about ± 33cm). Without this camera it would not be possible to search directly for charm decays at the scanning stage of the film analysis.

1.3.C The Downstream System

The downstream detectors supply information for use on-line in deciding when to trigger the bubble chamber flash tubes, and increase the available data on particles involved in interactions in the bubble chamber. All of the detectors are deadened about the X x Z plane containing the background due to beam photon pair conversions. Figure 1.3.C.1 shows the layout of the system.

There are four proportional wire counter chambers. Three of these contain vertical (y), horizontal (z), and diagonal (u) wire planes, the fourth contains only y and z planes. The wire planes within a chamber are separated by 3.8 cm and the diagonal wires (when present) form a

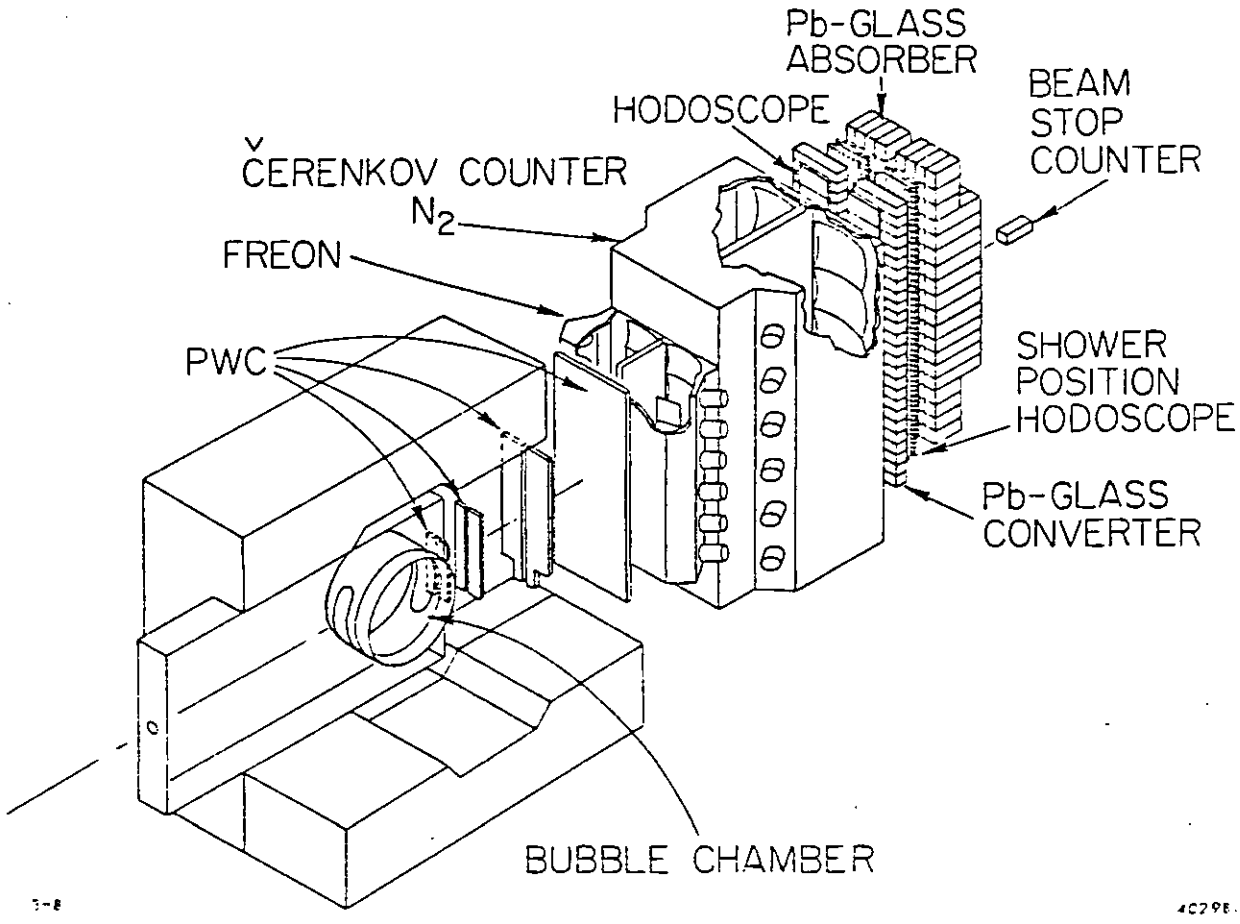

Figure 1.3.C.1 BUBBLE CHAMBER AND DOWNSTREAM SYSTEM

3:4:5 triangle with the others (39.6° to the horizontal). The hit information from z-alpha, z-beta, and z-gamma is used in making a triggering decision. The data from all the planes helps refine the determination of the momentum of (fast) charged tracks (see section 2.3 on hybridisation). The specifications of the counters are given in table 1.3.C.1.

PWC	X POSITION OF Z PLANE CM	DIMENSIONS (YxZ) CM	WIRES/INCH
α	81	72 x 22	12
β	123	104 x 33	12
γ	207	168 x 60	12
δ	269	193 x 96	1

Table 1.3.C.1 DETAILS OF PWCs

(NB The centre of the bubble chamber acts as the origin of the co-ordinate system, the x-axis lies along the beam direction).

There are two threshold atmospheric gas Cerenkovs, C1 and C2 filled with freon 12 and nitrogen respectively. These enable tracks of 3.0 GeV/c or more to be identified as pions or kaons/protons and tracks of 10.6 GeV/c or more can be further separated into kaons and protons. Table 1.3.C.2 gives more details [4].

	C1	C2
Gas, Refractive Index	Freon 12, 1.00108	Nitrogen, 1.0003
Threshold Momenta (GeV/c) (e/π/K/p)	0.01/3.0/10.6/20.2	0.02/5.7/20.2/38.3
Mean Number of Photoelectrons Detected	10	10
Position of entrance Window (cm)	310.0	381.5
Exit window (cm)	381.5	586.5
ℓ/ℓ_{rad}(%)	9.70	3.55
ℓ/ℓ_{coll}(%)	8.00	3.14

Table 1.3.C.2 DETAILS OF CERENKOV SYSTEM

The lead glass wall shower detector is comprised of a filter hodoscope, a lead shield, an active converter, two planes of finger hodoscopes (vertical and horizontal), and an array of back blocks (lead glass absorber). A gap down the centre, of variable width, divides the detector into a north and a south half. Each part of the detector is subdivided by detector modules; the important details of the various modules and their distribution are given in Table 1.3.C.3.

ELEMENT	NUMBER OF MODULES	DIMENSION OF MODULES (y x z x x) cm^3	RADIATION LENGTH (ℓ/ℓ_{rad})	DISTRIBUTION WITHIN A SECTION (y x z)
Filter Hodoscope	24	22 x 60 x .64		12 x 1
Lead Shield	2	290 x 63 x .64	1.13	1 x 1
Active Converter	52	10.9 x 90 x 10	3.3	26 x 1
Vertical Filter Hodoscope (measures horizontal positions)	46	274 x 2.5 x 1.3		1 x 23
Horizontal Filter Hodoscope	204	2.5 x 61 x 1.3		102 x 1
Back Blocks; Top	32	15.3 x 15.3 x 32.2	10.5	4 x 4
Centre	88	15.3 x 15.3 x 64.4	21.0	11 x 4
Bottom	32	15.3 x 15.3 x 32.2	10.5	4 x 4

Table 1.3.C.3 COMPONENTS OF THE LEAD GLASS WALL

A flash tube trigger is generated if energy deposited in either the north or south active converter columns or in the north or south absorber columns exceeds set thresholds in those columns (i.e. the detector is acting as a hadron calorimeter). Off-line the information from the detector is used to reconstruct pi zeros and to help identify electrons [5].

1.4 Data Taking

The data discussed in this thesis has been taken by the SLAC Hybrid Facility Photon Collaboration, a group of ninety-four physicists based at eighteen institutions in four countries (Israel, Japan, the United Kingdom, and the United States of America). The data was taken in three separate runs which are summarised in Table 1.4.1

DATE	NUMBER OF PICTURES TAKEN	NUMBER OF HADRONIC INTERACTIONS IN FIDUCIAL VOLUME	NUMBER OF HADRONIC INTERACTIONS SCANNABLE FOR CHARM
Summer 1980	92000	11000	4000
Autumn 1980	445000	75000	50000
Spring 1981	635000	140000	105000

Table 1.4.1 SUMMARY OF DATA TAKEN

An event is within the fiducial volume of the bubble chamber if it occurs within x limits of -45.0 cm and 30.0 cm. Events which are clearly visible on the high resolution view of the event (i.e. all tracks in focus, vertex not under a flare, tracks not distorted by local thermal fluctuations in bubble chamber etc.) can be examined for evidence of charm particle decays. As can be seen the proportion of usable events contained in the pictures taken has increased with time and experience.

Chapter 1 - References

[1] S.L. Glashow, J. Iliopoulos and L. Maiani; Phys. Rev. D2, 1285 (1970)

[2] SHF Photon Collaboration; SLAC-PUB-2870 (forms part of Appendix C)

[3] Z.D. Farkas, H.A. Hogg, G.A. Loew and P.B. Wilson; SLAC-PUB-1453

[4] A.V. Bevan et al; IC/HENP/82/1, submitted to NIM

[5] J.E. Brau et al; SLAC-PUB-2773

CHAPTER 2

THE EVENT PROCESSING CHAIN

2.1 Introduction

The bubble chamber technique enables a three dimensional reconstruction of the tracks of the charged particles involved in an interaction to be made. The charged particles traversing the bubble chamber leave behind a trail of ions which provide centres for bubble formation when the liquid in the bubble chamber suddenly becomes superheated. The superheating is a result of rapidly expanding the chamber, reducing the pressure on the liquid inside but holding its temperature constant. The chamber is then illuminated with flash lights and (for bright field illumination) the bubbles scatter the light so that the track's shadow is cast on the film in the bubble chamber cameras which is otherwise exposed. Photographs must be taken from at least two angles if a stereoscopic recording of the event is to be made.

The data processing chain consists of the steps needed to transform the raw data on film (and on tape from the electronic counters) into information on a data summary tape (DST) about the type and the momentum vectors of the particles produced in the reaction. The exact details of the stages of analysis differed from laboratory to laboratory (dependent on the resources available) so I will describe specifically the methods used at Imperial College.

2.2 Scanning and Measuring

Not every frame of film is useful, either because there is no interaction on it or because the interaction is not usable. The film is scanned to select those frames that will continue through the analysis chain and be measured. The use of a high resolution camera meant that two types of pictures were produced; some of the charm processing being done separately.

2.2.A Scanning and Measuring - Ordinary Events

Any hadronic interaction visible on the usual pictures (ordinary magnification, three views) was recorded. If the event was within the fiducial volume it was then measured. The exceptions to this rule were one prong interactions, and events with tracks scattering too close to the primary vertex.

The event measurement was performed by a computer controlled system, the Hough Powell device (HPD) [1] which was operated in a "road guidance" mode. This required that an initial rough digitisation of the event was done by hand; two fiducials, the vertex, and the middle and end of each track were measured on each view. These data were then converted into input for the HPD analysis program (HAZE) by another program (MIST). HAZE used the rough measurements to define a circular band, known as a road (about 0.5 to 1mm wide on the film), within which digitisings were used to calculate master points for the tracks. Events which failed HAZE were recovered if possible by using a program called RESCUE which enabled a human to intervene in defining the road for a track. The HAZE/RESCUE output was then processed by yet another program (SMOG) which combined data from all three views to produce the input for the geometry reconstruction program, HYDRA [2] geometry being used.

2.2.B Scanning and Measuring - Charm Candidates

The high resolution film was scanned twice, any hadronic interaction anywhere on the film being recorded. A third scan was then done of all the events found by either or both of the initial scans. The purpose of this scan was to select all possible candidates for being charm particle decays. Initially this scanning was done by physicists, later experienced scanners were used. All events which were charm candidates were sketched and photographed on the scan table (the photograph produced was at the same magnification as the view on the scan table).

The photographs were then examined by a group of physicists who decided if the events really could contain charm.

The necessary condition for an event to be a charm candidate was the presence of any track which could not come from the primary interaction vertex and which originated within the "charm box" (see Figure 2.2.B.1). This defined the limits on the area of space on the scan table

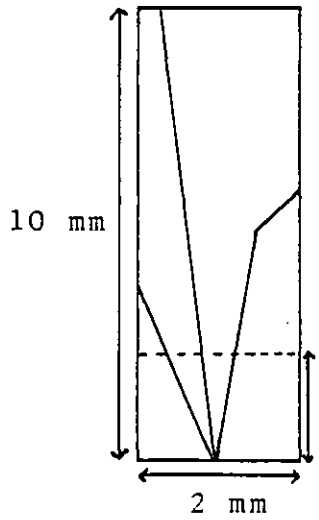

Figure 2.2.B.1

DEFINITION OF CHARM BOX

within which a charm particle was likely to occur (based on kinematic arguments and a long lifetime estimate). All tracks were carefully examined to see if they had an impact parameter, even events where this was marginal were classed as candidates at this stage (though frequently they were dropped after examination by the group of physicists). Events with several such tracks or with a decay within the inner charm box were marked as especially interesting. Any charged particle decays to more than one charged particle or neutral decays to more than two charged particles were immediately classed as "gold plated" charm.

Charm candidates were measured separately from other events and several measurements of a given event were made. These digitisings were made using a SWEEPNIK [3] machine, the nature of the events making them especially likely to fail HPD measurement. The purpose of making several measurements was to minimise to possibility of a measurement error

leading to failure to properly reconstruct the event at a later stage. Figure 2.2.B.2 is an example of a candidate which was accepted as a charm event.

2.3 Geometrical Reconstruction and Hybridisation [4]

The geometrical reconstruction program recreates the event in three-dimensional space. The principles behind the reconstruction are common to all bubble chamber experiments and are discussed in reference five. The output basically consists of the spatial co-ordinates (x, y, z) of all vertices, the momentum, dip, and azimuthal angles (p, λ, ϕ) for all tracks produced at those vertices and mass dependent residuals for all those tracks. The residuals measure how well the energy lost by a track fits the energy that the track has, assuming the particle producing it has a given mass; in some cases (low momentum tracks) the particle can be identified.

The hybrid program combines the results of the bubble chamber measurement with information from the proportional wire counters downstream in order to improve the accuracy of the final results. The three momenta and vertex position are used as starting values to swim fast tracks through the downstream pwc's. Hits close to the trajectory are searched for and the track parameters are then adjusted to minimise the displacement to both bubble chamber and PWC points. The hybridised values are accepted if the χ^2 is good. Otherwise the bubble chamber values are output unaltered. For a track to hybridise, hits in at least two wire planes are required.

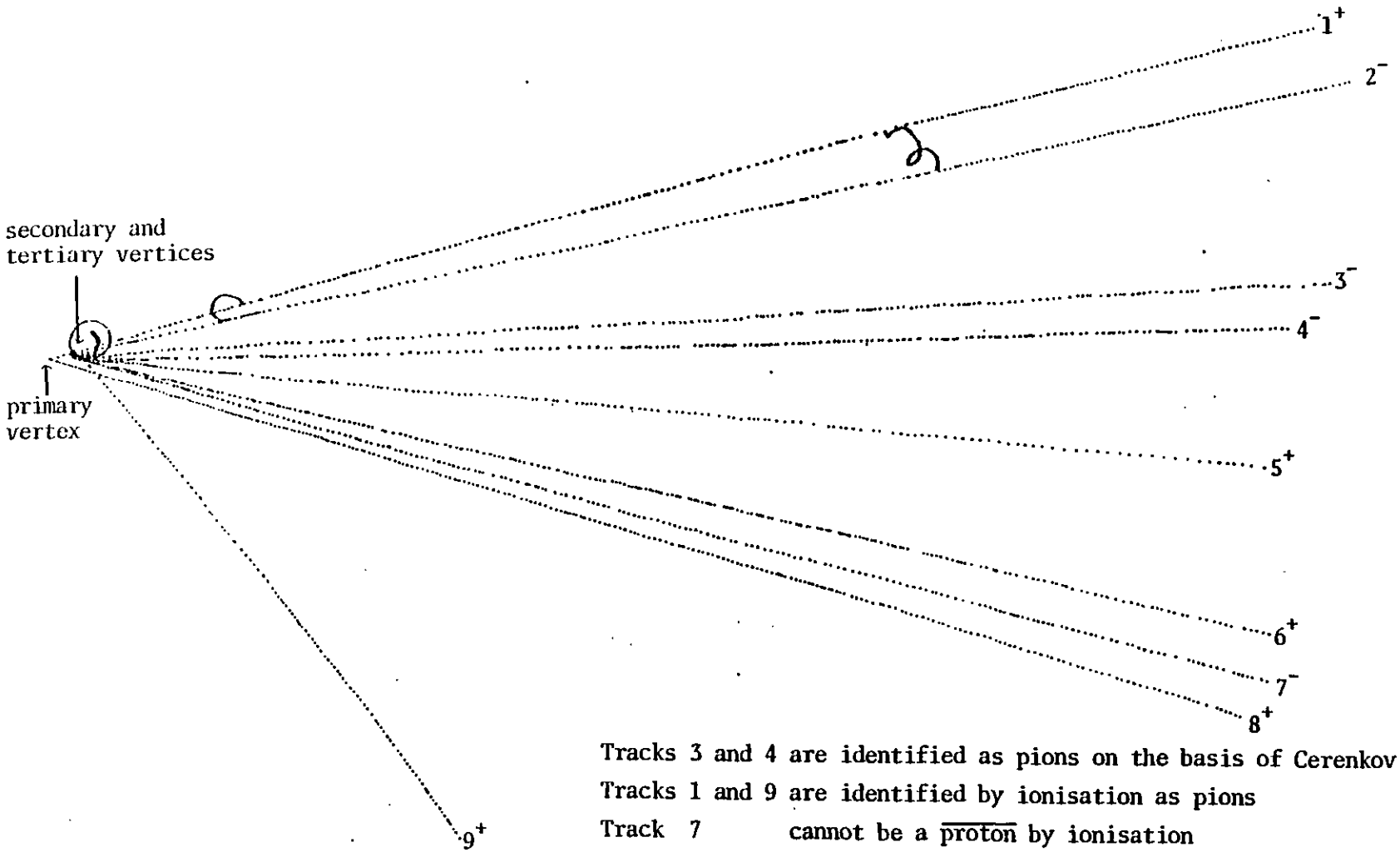

Tracks 3 and 4 are identified as pions on the basis of Cerenkov information
Tracks 1 and 9 are identified by ionisation as pions
Track 7 cannot be a $\overline{\text{proton}}$ by ionisation

Tracks 4,5,6,and 7 form a $\overline{D}^{*}$ with mass 1860±8 Mev if track 6 is a kaon
The other charmed particle is unconstrained.

Figure 2.2.B.2 A TRACING OF H.R.O. VIEW AS SEEN ON SCAN TABLE FOR FRAME 0085,ROLL 1216

2.4 Kinematical Reconstruction

The object of a kinematics program is to give a physical interpretation to the event in terms of the participating particles and their three momenta. Possible masses and quantum numbers are assigned to the particles in such a way that the relevant conservation laws are not violated. The most important constraint operating is that requiring that energy and momentum be conserved overall. For each topology a set of all the possible mass permutations of interest of the final state particles was compiled and used to setup the kinematics program GRIND [6] to process the HYDRA geometry output.

One difficulty in this experiment as opposed to charged beam experiments is that the interacting beam particle does not leave a visible, measurable track itself. Although the direction of the beam was well defined its energy could vary within wide limits (although the majority of photons have an energy above 15 GeV; see section 1.2). A dummy beam track was inserted into the event, the direction being specified but not the beam's energy. The result of this procedure was that the energy constraint was lost.

The fitting procedure involves testing the various hypotheses corresponding to the topology of the event. The track parameters are varied (within errors) to obtain fits satisfying the three momentum constraints to a preset accuracy. A chi-squared probability for the fit, reflecting the amount of variation introduced into the track parameters is then computed.

The errors on the tracks were adjusted until the stretch functions had the expected form. The stretch function is a normal distribution function with the standardised variable

$$z = \frac{X_M - X_F}{\sqrt{\Delta^2(X_M) - \Delta^2(X_F)}} \qquad 2.4.1$$

such that;

$$f(z) = \frac{1}{\sqrt{2\pi}} e^{-z^2/2} \qquad 2.4.2$$

where,

X_M and X_F are the measured and fitted track parameters respectively.

Equation 2.4.2 thus implies that for variables having Gaussianly distributed errors, z has a normal distribution centred on zero and a standard deviation of one. Since the parameters ($\frac{1}{p}$, λ, ϕ) have nearly Gaussian errors, the errors can be estimated realistically by examining the stretch distributions in three constraint fits. The stretches for the beam dip and angle to the x-axis of the system are shown in figure 2.4.1.

The type of fit obtained depends on the number of kinematic constraints and the number of unknowns. If there are no missing particles or unmeasurable tracks a three constraint fit (3C fit) may be obtained. If a single particle is missing there are three unknowns (p, λ and ϕ for the missing particle) and so only a solution for the unknown parameters is possible. In this case the fit is termed a zero constraint fit (0C). In this experiment the majority of events are unconstrained.

2.5 Event Recovery and DST Production

Events can fail to pass satisfactorily through to the end of the processing chain for several reasons. They may not be found, they may be mismeasured or they may be unmeasurable. A list of all events known about, known as the Master-List, is prepared initially from the input data to HAZE. This is updated at each step of the chain and information

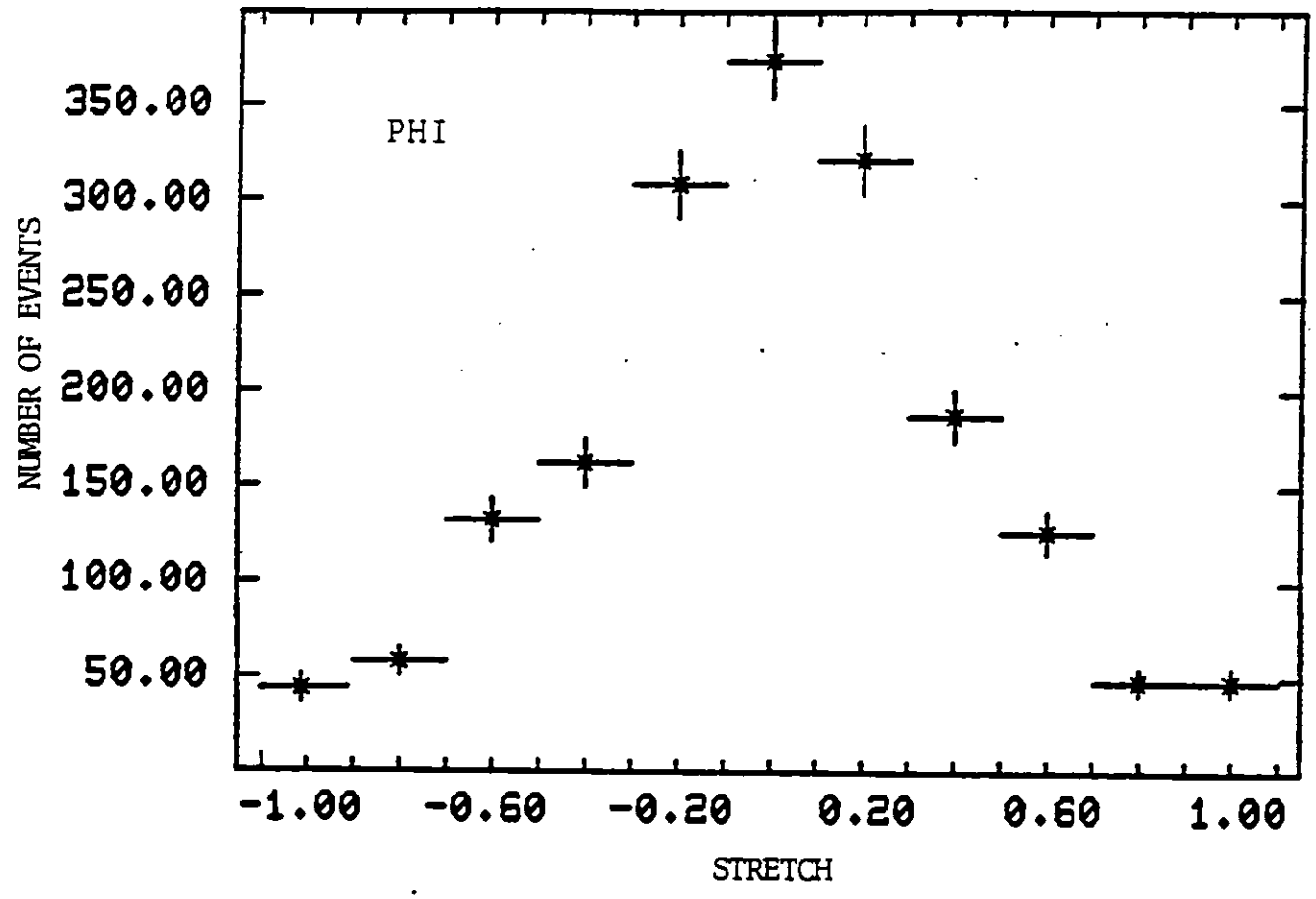

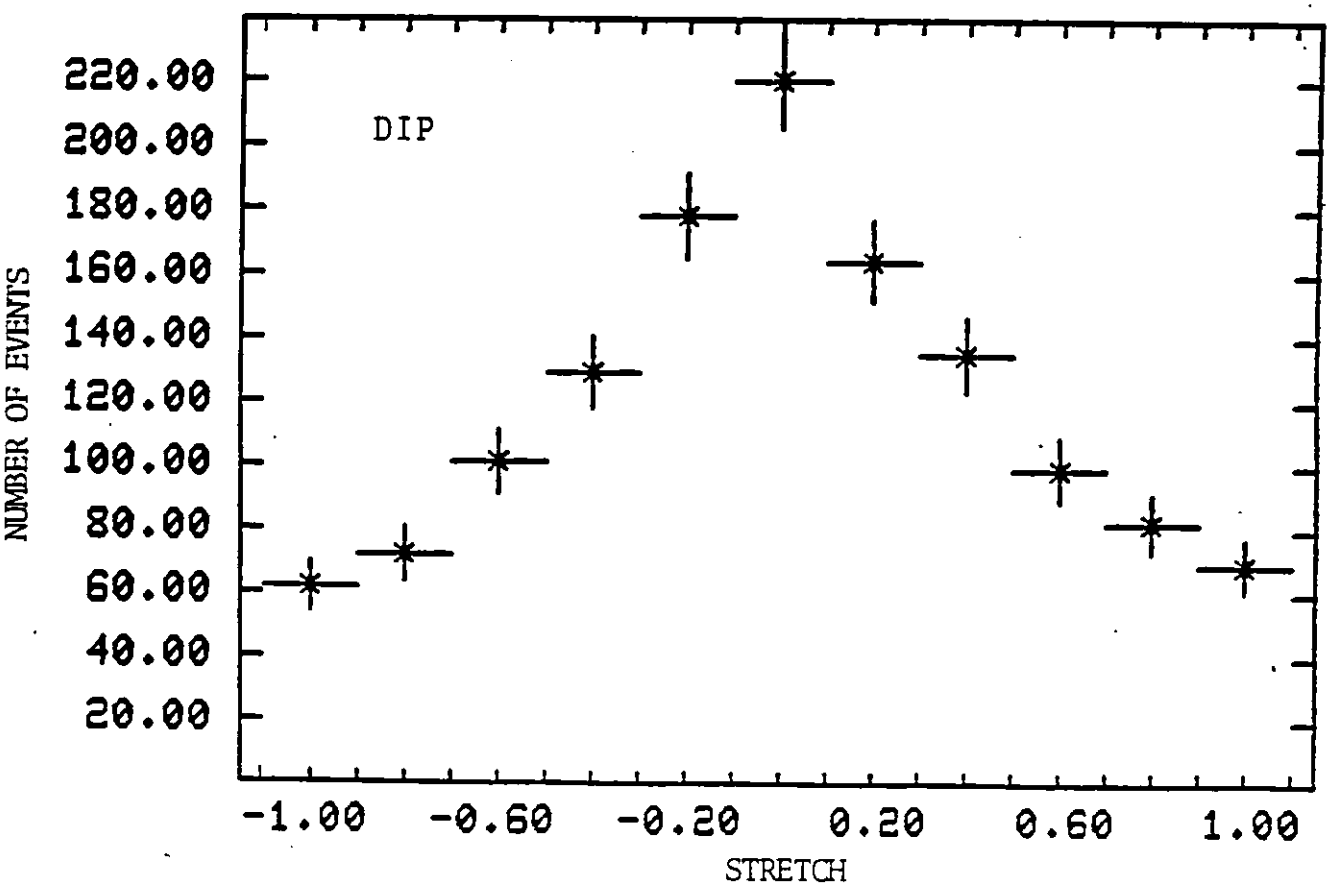

Figure 2.4.1 BEAM STRETCHES FOR DIP AND PHI,
(USING 3C EVENTS ONLY)

on the status of the event is incorporated into it.

Essentially the Master-List contains the roll/frame event numbers, the topology of the event and whether it has been successfully measured, been classified as unmeasurable or needs remeasurement. Events which failed measurement were sent for measurement on Sweepnik if they failed more than one measurement attempt on the HPD. Events found on the HRO scan but not the main frame scan were also included in the remeasurement pass (the remaining number of events not found by any scan was a small, calculable loss). In cases of conflict between the topology noted during the main views scan and the HRO topology (e.g. over the presence of close in Vee's) the event was classified by its main view topology.

Events were checked after kinematical reconstruction to identify particles by ionisation and residual. Any errors spotted in the checking - such as tracks not being measured (e.g. a five prong measured as a three prong) lead to the event being remeasured.

The Master-List was then used in conjunction with the GRIND output tape to prepare the DST for physics analysis.

Chapter 2 - References

[1] B. Penney; PhD Thesis, Imperial College (1971)

[2] Program 'HYDRA GEOMETRY'; CERN Program Library

[3] D.J.M. Davies, O.R. Frisch and G.S.B. Street; NIM 82, 54 (1970)

[4] G. Hall; Imperial College Internal Memo IC/HENP/PN/27 (1975)

[5] P. Villemoes; Lectures at the 1970 CERN School of computing and data processing, CERN Report 71-6

[6] Program 'GRIND'; CERN TC Program Library long write-up

CHAPTER 3

THE ON-LINE TRIGGER

3.1 Introduction

Bubble chamber experiments can be divided into two groups; triggered (or hybrid) and untriggered. Untriggered experiments yield an unbiased sample of the total cross section because no system of limited acceptance is used in determining whether or not to expose the film in the bubble chamber cameras. If the chance of the interaction to be studied occurring within the fiducial volume during a pulse of the chamber is small, though, such experiments waste film and scanning effort. Hybrid experiments use the information available from detectors associated with the bubble chamber to enhance the ratio of events on film per frame of film taken. Although the aim is to photograph, exclusively, the entire cross section of interest, usually a compromise is required between the sensitivity of a trigger and its selectivity.

The trigger used by a specific experiment is determined by what is to be investigated, by what detectors can provide data and, by the time available for a triggering decision. This chapter describes the evolution, operation, and further development of the BC72/73 trigger. The intention was to trigger on the total photoproduction cross section using initially the hits in the downstream proportional wire chambers as input to the triggering algorithm. The most important restriction acting on the complexity of this algorithm was a time constraint; the next section explains why.

3.2 Time Constraints

The primary aim of the BC72/73 experiment is to study the lifetimes of the weakly decaying charmed particles. These lifetimes are typically in the range of 10^{-12} to 10^{-13} seconds with corresponding decay lengths (at our energy) of a few hundred microns at most. The

high resolution camera technique (described in section 1.3.B) was developed in order to make it possible to see decays this close to the primary vertex, when scanning the film under high magnification (50 to 100 times space). It was established that to have a reasonable detection efficiency for such decays required the particles to have travelled at least two bubble diameters away from the production vertex before decaying.

The maximum allowed bubble size was chosen to be 80 microns. Since, if the running conditions of the bubble chamber are kept constant, bubble size increases with the square root of time, this decision determined the most time that could be spent judging whether or not to expose the film in the HRO camera. The 40" bubble chamber was run hot (at $29^{o}K$) to give a high bubble density (about 70 bubbles/cm). After 250 microseconds under these running conditions the average bubble size reached the allowed maximum. The minimum bubble size approximately matches the resolution of the lens although differing flash delays and flash intensities were tried out to find the combination yielding the clearest tracks. A minimum flash delay of 150 microseconds (giving 55 micron bubbles) has been used for most of the running so far.

The very short time available for a triggering decision to be made (a 250 microsecond cut off compared to the 2 milliseconds cut used by earlier experiments at the SHF) meant that only a hardware trigger or a very simple software one was worth considering. The time available for execution of a software triggering algorithm is reduced from the maximum flash delay by the time taken to readout the information from appropriate detectors and transfer it into computer memory, further restricting its complexity. The next section describes work done to establish how simple a trigger could be whilst requiring it to reject a large fraction of the background.

3.3 Background Rejection

The hadronic cross section for photoproduction at 20 GeV is approximately 115 microbarn. The probability of a hadronic interaction occurring within a fiducial length of 75 centimetres (that of the SLAC 40 inch bubble chamber) is therefore about 3×10^{-4}. Hence, running at a typical flux of around 30 photons/pulse would yield 1 interaction of interest every 100 frames if no selection was made of the pictures taken. As explained below, it was decided to aim for a signal to noise ratio of 1 event every 4 pictures, requiring the rejection of 96 out of every 100 possible triggers by the on-line triggering algorithm.

The initial work on the trigger preceded an operational photon beam by about a year. It was therefore necessary to estimate the background noise in the detectors (and thus the background trigger rate) by simulating the effect of such a beam on them. It was possible to run a 16 GeV electron beam down the SHF beam-line at this time. Monte Carlo studies had established that a 16 GeV electron was equivalent to 5 photons in terms of the electromagnetic background resulting in the detectors. However the effect of 30 photons/pulse could not be duplicated by using a flux of 6 electrons/spill because of the far greater spread of the electron beam when compared to the photon beam. Fortunately however, it was possible to get around this problem.

The SHF at this time had, in addition to the multiwire proportional chambers it has at present, two sets of pairs of proportional planes (Y and Z only) upstream of the bubble chamber. These chambers were used to define the position and direction of charged beam tracks. A very low intensity electron beam was sent down the beam-line (so low that a veto was used to reject spills that gave no hits in the upstream chambers) and the hits in the detectors recorded on to magnetic tape for offline analysis.

Single electron spills were then defined to be spills which gave one hit and only one hit (after excluding "hot" wires - i.e. those which fired every time) in the upstream wire chambers. The electron trajectory was known for these spills and the translation in space needed to map that track onto a nominal trajectory (that of the "photon" beam) could be calculated. Since there was only one track the same transformation could be applied to shift the locations of the downstream hits. The result of this was to produce a set of records corresponding to the background in the detectors caused by an electron beam with no spread. These records were then combined with each other to build up sets of data equivalent to various fluxes. Figure 3.3.1 shows the steps taken in producing such overlay data.

It was assumed that the proportional wire counters (in common with all the downstream detectors) would be deadened in the region of the beam. The dead region was intended to be large enough to exclude the majority of e^+e^- pairs formed by beam photon conversions from registering in the detectors. The bubble chamber field is aligned along the z direction so the dead region covered the xy plane containing the photon beam. The extent of the dead region in z increased with increasing detector distance from the bubble chamber (due to the effect of scattering). The PWC dead regions in z were expected to be $\pm$ 12mm in $z\alpha$ increasing to $\pm$ 20mm in $z\gamma$ and these values were used in rejecting hits in the dead regions from the overlaid records before running the trigger program on them.

The first tests run on this data established the frequency of background triggers that would be yielded by the use of a fairly elaborate trigger, simple variants of which had been used by earlier experiments at the SHF. Figure 3.3.2 shows the main elements of this trigger which was based upon the use of match or space points. These are groups of hits in the y, u and z planes of a multiwire proportional

Figure 3.3.1 OVERLAY PROGRAM STRUCTURE

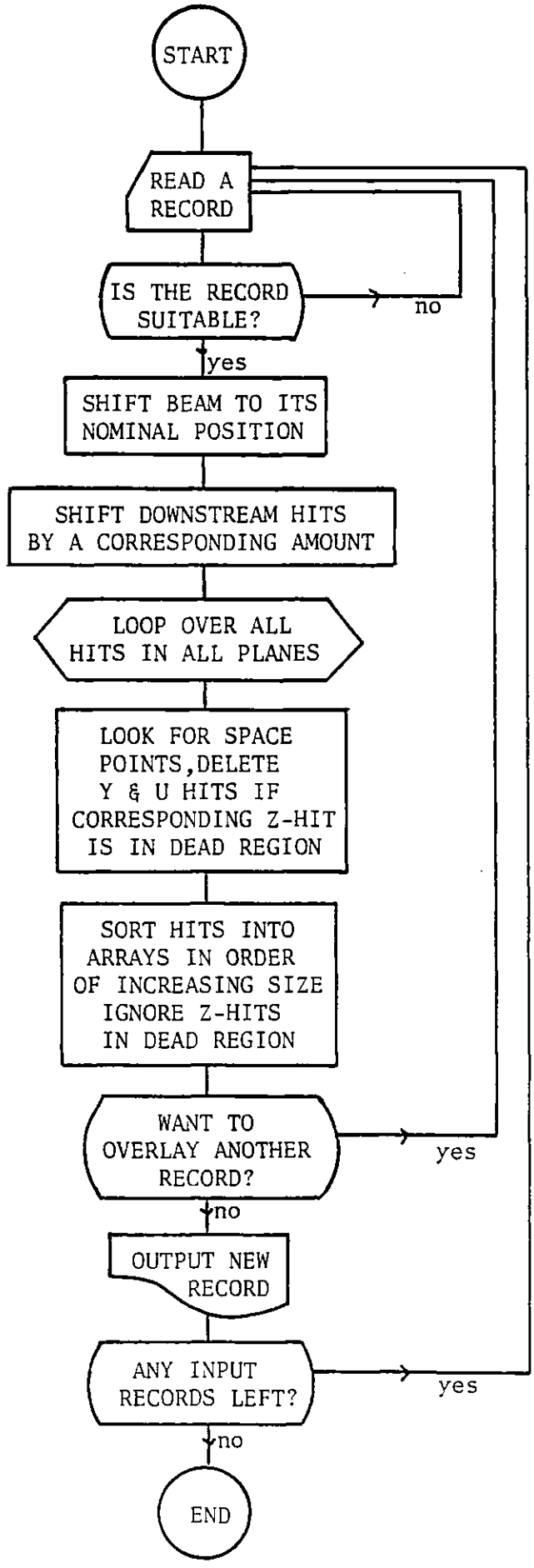

Figure 3.3.2 LOGIC OF "OLDSTYLE" ALGORITHM

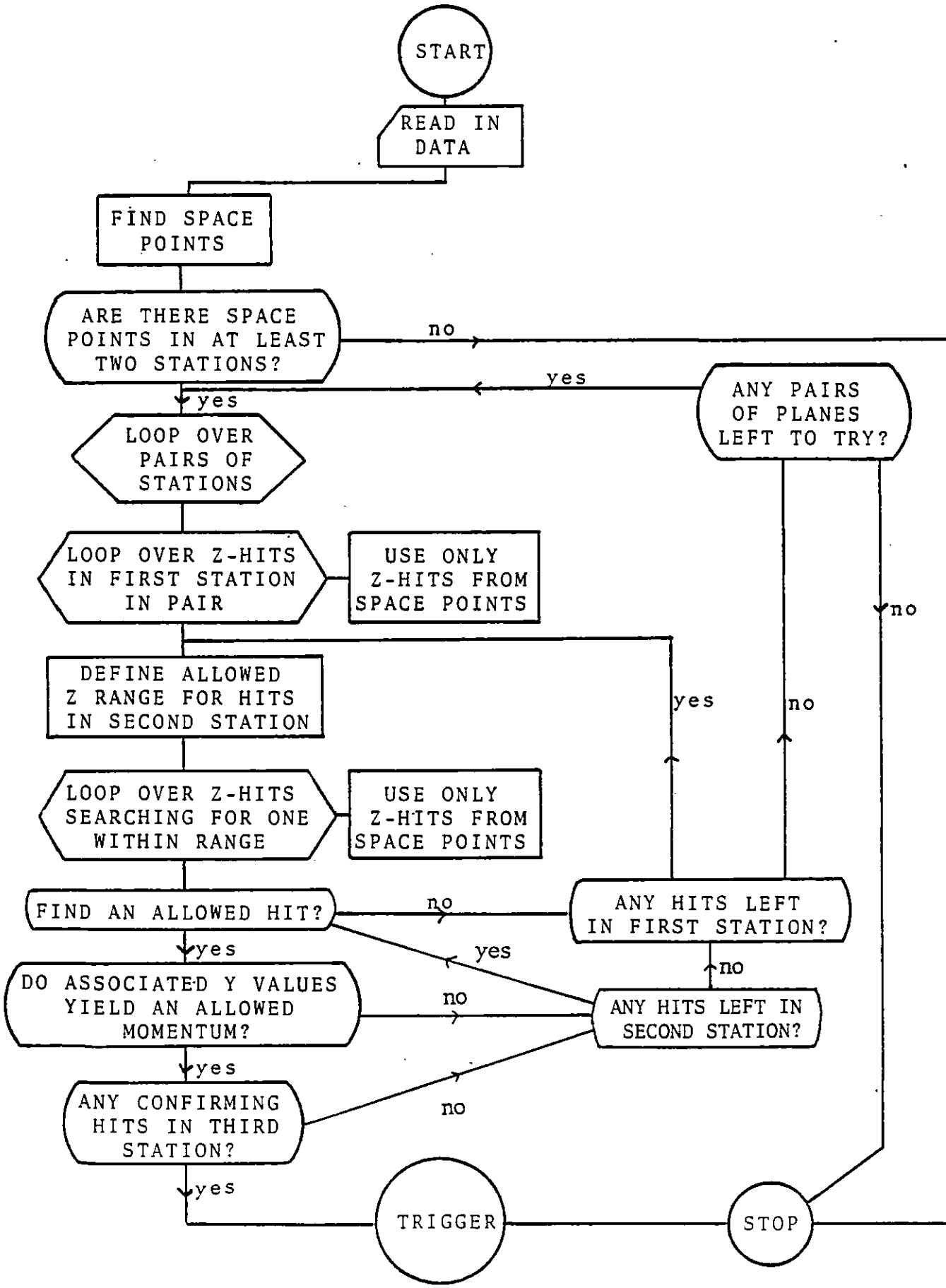

station which define a unique point in space (the third plane removing the ambiguities that exist if only two planes are used). Only z hits giving space points are used in the main section of the triggering algorithm. In this way most of the random z hits in the PWCs are filtered out (at the expense of some loss of efficiency since hits are required in three PWC planes not just one).

Finding space points however requires a lot of computer time (a few hundred microseconds of 168/E time for example), the time taken increasing with the product of the number of hits in each plane. The first simple trigger tried therefore, dispensed with finding space points. The trigger program searched for lines in z (the non bend plane) using hits from each of the first three z planes (α β and γ), allowance being made for some coulomb scattering. Table 3.3.I compares the performance of this trigger and the standard one. It was rejected as inadequate.

	Events/Frame	
Estimated Photon Flux	Standard Trigger	Simple Trigger
5	.70	.34
10	.70	.32
25	.59	.25
50	.47	.18
75	.29	.14

Table 3.3.1 COMPARISON OF STANDARD TRIGGER TO PROPOSED (SIMPLE) TRIGGER

The next step was to constrain the lines in z by demanding that they lie on a plane which intersected the photon beam within the fiducial limits of the bubble chamber. The range of allowed wire hits in zβ for a given hit in zα, under these conditions, is defined by the geometry of the

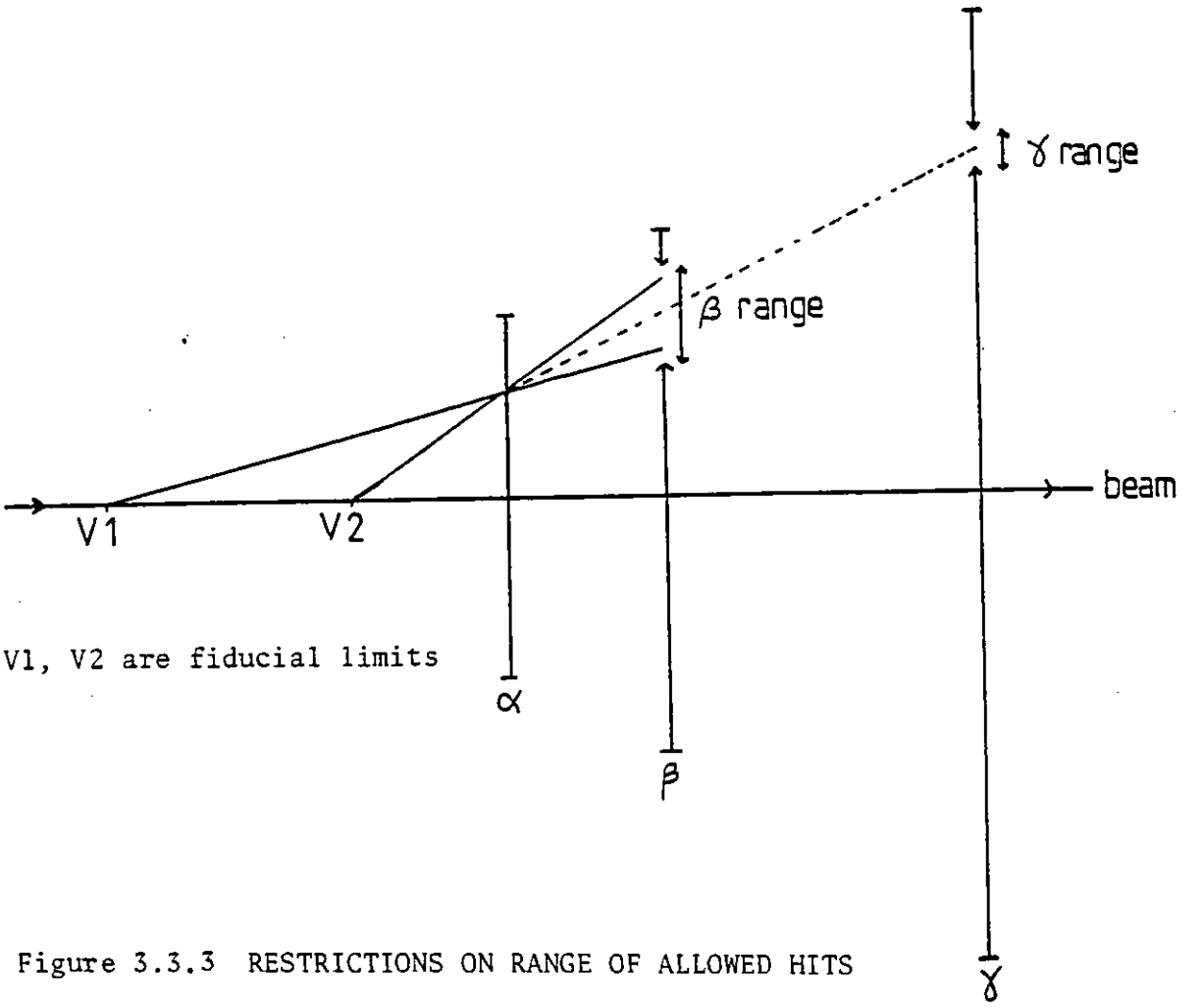

Figure 3.3.3 RESTRICTIONS ON RANGE OF ALLOWED HITS

system, as shown in figure 3.3.3, and by multiple coulomb scattering which extends the allowed range over the geometric limits. The range of possible z_γ hits is fixed by the z_α to z_β displacement and again by coulomb scattering. To try out the trigger arbitrary(but reasonable) limits were set on the increases of allowed range resulting from coulomb scattering. The background trigger rate fell to about 1 trigger/20 pulses at 75 photons/pulse (compared with a value of 1 trigger/6 pulses for the simplest trigger tried). It was decided that it was worth doing further work on this trigger improving the scattering estimate and checking that it would trigger efficiently on hadronic interactions.

3.4 Refining the Basic Trigger

A Monte Carlo program already existed for use in estimating the effect of multiple coulomb scattering on the trajectories of particles

formed by charged beam interactions in the SLAC 40" chamber. This was more complicated than was needed for the present application since it allowed for the spread in the charged beam and for the scattering of the charged beam particles themselves before they interacted. These contributions to the range of z-beta hits allowed for a given hit in z-alpha were removed by fixing the position of the interaction in y and z.

Tracks were generated randomly in x throughout the fiducial volume of the bubble chamber and swum out through the downstream proportional wire counters. The track was kinked at various points in the system. The angles of kink given to tracks at a given point obeyed a gaussian distribution centred around the mean amount of scattering expected between that point and the prior scattering centre. The estimate of this mean amount was based upon the amount of material the track had traversed and assumed a track momentum of 2.0 GeV/c. 2.0 GeV/c was used because this was the lowest track momentum we wanted to be reasonably sure of triggering on, lower momentum tracks are unlikely to hit z-gamma and thus rarely satisfy the requirements for a triggering track, higher momentum tracks would be scattered less.

To establish the tolerances needed histograms were made of the difference in wire numbers between the actual wire hit by a track and the wire that a straight-line projection of the track would have predicted to be hit. In the case of the tolerance to be allowed at z-beta the straight-line prediction used the vertex position and the position of the track at z-alpha, for the z-gamma tolerance the prediction was based upon the z-alpha to z-beta track displacement. Figure 3.4.1 shows an example of the plots obtained.

In order to keep background triggers to a minimum, the tolerances

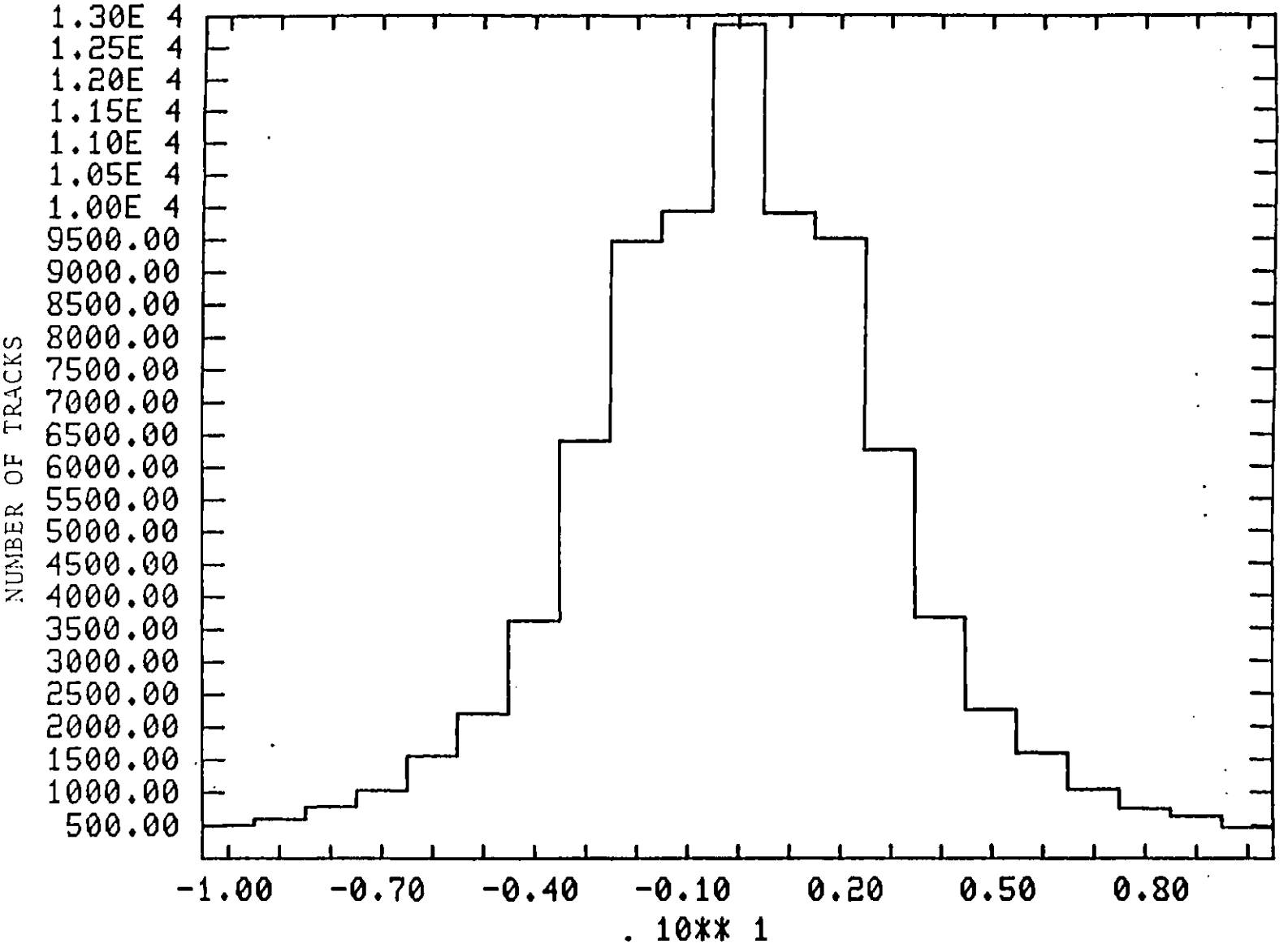

Figure 3.4.1 DIFFERENCE BETWEEN WIRE NUMBER OF PREDICTED HIT IN Z-GAMMA AND ACTUAL HIT IN Z-GAMMA

allowed could not be loose enough to allow even a maximally scattered track to trigger however, some losses had to be accepted. To adjust the tolerances we needed to use real tracks and check how frequently they satisfied our proposed trigger requirements. We decided to define real tracks as those which gave a trigger if the old style triggering algorithm described in section 3.3, figure 3.3.2 was used. This trigger was very efficient ($\sim$ 94%). We again needed to translate the downstream hits in the pwcs so as to make the tracks appear to come from the interactions of a pencil-like beam. We therefore discarded the pwc record associated with a triggering track if that record did not satisfy the overlay program condition that there were only single hits in each of the upstream pwc planes. We then ran the overlay program on each of the remaining records, singly, and obtained suitably dummied pwc records as output. These were then used as input to the proposed triggering algorithm and by adjusting the scattering tolerances we achieved an acceptable triggering efficiency on genuine tracks.

Although by this time we had a reasonable straightforward trigger, it was less efficient (by about 10%) than earlier triggers and not quite as good at rejecting the electromagnetic background. Several modifications to the basic trigger were considered to rectify these faults including searching for trajectories in the y and u planes either as alternatives to the z track (increasing efficiency) or as confirmatory tracks (removing background triggers). The most promising approach searched for tracks through the fourth z-plane, delta, if none were found using the first three stations. This increased the efficiency of finding good tracks but also raised the background trigger rate. To compensate for this an additional constraint was imposed that two of the z hits used in making a trajectory had then to be associated with space points. To save time the space points would be found using a hardware processor

(the point finder referred to in SLAC-PUB-2726 which is given as appendix C). The momentum of the triggering track could then be estimated using the y value of the vertex and the y values associated with the two space points and a cut applied if necessary.

It was unlikely however that a trigger using point processors would be ready for use at the start of the experiment. As an interim solution, effort was concentrated on getting the simple (3 hits in a line) trigger operational. The existing method of pwc readout took over a hundred microseconds to make digitised pwc hits available for use by a software triggering algorithm and so needed changing. Section 3.7 discussing the on-line trigger system describes the modifications made. Even with a fast readout however the triggering algorithm needed to be encoded so that as few computer cycles as possible were taken up in making a triggering decision. This coding (described in section 3.6) was partially determined by the use of a 168/E as an on-line processor. The following section discusses the features of the 168/E system of the SHF which make it suitable for such uses.

3.5 The 168/E Processor

A 168/E is a small processor designed specifically for use in high energy physics applications [1]. It emulates that fraction of the instruction set of the IBM 168/370 series of computers needed for execution of a typical, large data analysis program (for example that of the Large Aperture Solenoidal Spectrometer (LASS) [2] experiment). Using a 168/E is a very cost effective way of increasing the computing power available to an experiment; at less than one-thousandth the cost of an IBM 168/370 it is only about twice as slow (on average) in executing programs.

In operation the 168/E acts as slave to a host computer, which is required to control input and output processes. The SHF system (the main elements of which are shown in Figure 3.5.1) has as host computer a Data General NOVA 4/X. This is linked to each of three 168/Es currently in use at the facility via SNOOP module CAMAC interfaces[3] which are controlled by standard CAMAC commands.

One of the advantages of any 168/E system is that the user can tailor each processor to his specific needs. For instance the board which enables the emulation of floating point instructions can be removed from the processor if it is unnecessary. Similarly, memory boards (the most expensive component) need not be supplied in excess of requirements. Table 3.5.1 shows that the SHF system makes full use of this flexibility, each of the three processors,designated CPU#0, #1, and #2 respectively, have features which fit them for their particular uses. Cards common to all the processors, however, are completely interchangeable. If a problem develops on such a card in the processor controlling the PWC trigger it can be temporarily replaced by a board from one of the less essential processors. This keeps the down-time of the experiment resulting from computer faults to a minimum.

Another advantage of 168/Es over most microprocessors is that programming them requires little specialist knowledge since a user can write programs in Fortran. The program needed to translate code into 168/E microcode can be treated as a black box. This translator program will also accept as input programs written in IBM assembler (providing that only instructions emulated by the 168/E are used). Since IBM assembler is a lower level language than Fortran more control can be exercised over the microcode version of the program by writing the original in assembler (otherwise a compiler must first be used to convert the Fortran statements into assembler which may not result in

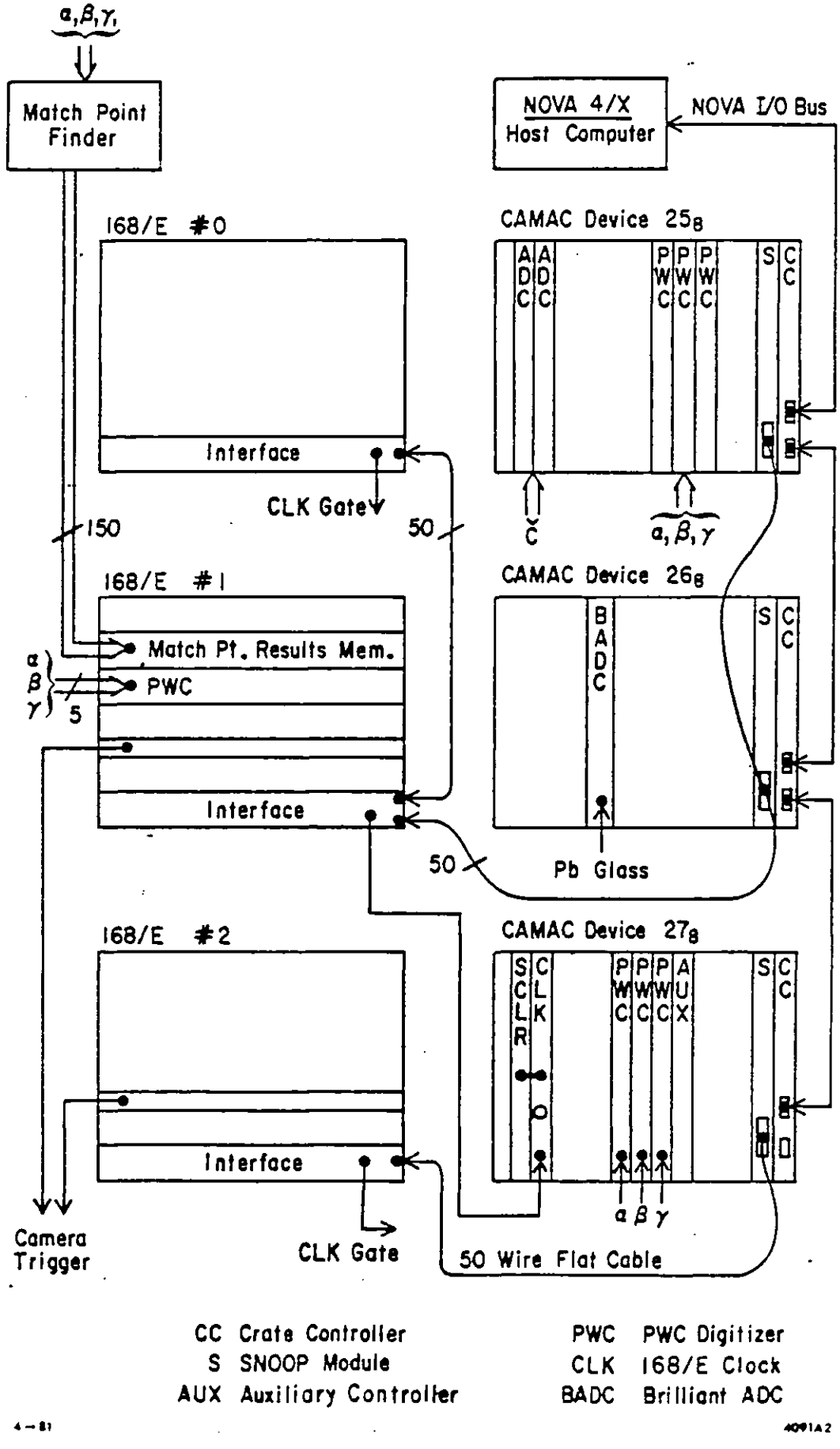

Figure 3.5.1 ORGANISATION OF THE 168/E AND CAMAC SYSTEM AT THE SLAC HYBRID FACILITY

CPU#	CONTENTS/CONNECTIONS	FUNCTIONS
0	Integer and floating point CPU Three memory boards (48K bytes) Interface to CAMAC crates 25_8 26_8	Fortran monitor program Old style algorithm
1	Interger CPU One memory board, eight channel PWC digitiser card, interface to CAMAC crates 25_8 and 26_8 Camera trigger card	Alternates with CPU#2 for on-line algorithm development. Currently fast PWC algorithm running on it (Fall 1981)
2	Integer CPU One memory board Interface to CAMAC crate 27_8 Camera trigger card	Originally the fast PWC algorithm ran on CPU#0 Now used to check performance of CPU#1

Table 3.5.1

USE OF 168/E PROCESSORS AT SHF

the fastest code for a specific application). All the trigger programs used at the SHF have been written in assembler to make them as fast as possible.

The fact that the original programs are written in standard (if restricted) programming languages means that these programs can also be run on real IBM computers. This means that program development and program debugging need not tie-up the 168/E system and may even be done off site. It also enables the performance of the 168/E system to be monitored easily. If everything is operating correctly then off-line checks using the same data as input to the original programs should give identical results to those of the on-line system. Conflicts may be caused by hardware errors (such as a faulty chip in the 168/E) or (less probably) by software faults (the translator program giving a false output).

If the program being run is new to the 168/E errors in the microcode translation are a posssibility (provided that other programs are executing as usual). It is possible to insert halt instructions into the 168/E program code at any point pausing execution of the program. An interactive editor program (DPEDIT) running on the NOVA 4/X can then be used to examine the contents of the data memory and the register of the processor. The values of these can then be compared to the expected values (given by running the original program on an IBM) and the point at which they begin to diverge established. This in turn gives the instruction which is causing the difficulties and the microcode corresponding to this instruction can be checked.

In the pre-run checkout of the BC72/73 trigger program only one problem was caused by mistranslation. A set of dummy data which contained a valid set of hits for a triggering trajectory was rejected by the trigger program. A run on the same data off-line using an IBM 168 produced different results, the trigger program working as planned,

showing that the source code was correct. The fault was traced to an instruction to shift the contents of a register one place to the left (usually done by adding a register to itself) which did not always result in the contents of that register doubling in value. Further investigation showed that everything worked correctly if an odd numbered register was involved but not if an even numbered register was the subject of the instruction. An even numbered register would in fact be added not to itself but to the next highest numbered odd register. The diagnostic program used to test the instruction had not shown up the fault because it used an odd numbered register.

Had the microcode been correct then a hardware fault would have been looked for. If a discrepancy had been found after the program had been running on the 168/E for some time then a hardware problem would have been suspected immediately. A standard check during running is to compare the results of running on the PWC data off-line with the on-line results. If an inconsistency occurred it could then be traced partly by using standard diagnostic programs and partly by checking signal levels at various points in the circuit using an oscilloscope probe.

The translator program actually produces two output files one of which contains the equivalent of program instructions, the other containing data used by the program. These files are stored on the host computers disks until needed. A fortran callable subroutine (DPDOWN) which runs on the NOVA 4/X transfers these files into program and data memory respectively. DPDOWN also reads back from the 168/E memory the stored code, compares it to the original, and sets an error flag if they disagree.

The location of variables in data memory has to match the location assumed by the program microcode. If the program is changed it will be re-translated, the translation program will make the data memory consistent with the program code, changing the location of some variables if necessary.

This has no other effects if the variable is internal to the program that has been changed. If it is external (e.g. the number of hits in z-alpha) and has to be fed into data memory by another program then this change in location would require changes to be made in all the programs involving that variable. To get round this problem variables in 168/E programs are divided into two types, those in common blocks and those not (local variables). The position a common block (and hence variables in it) occupies in data memory can be specified (by using a Locate card in the translator programs JCL). The position of local variables can change each time the program is translated.

3.6 The PWC Trigger-Algorithm Coding

The PWC trigger algorithm was coded so as little time as possible was taken in making a triggering decision. Figure 3.6.1 shows the structure of the coding. As little calculation as possible is done on-line. The allowed range of z-beta hits is defined by a look-up table indexed by the z-alpha hit. The PWC hits in a given plane are always digitised in ascending order. Thus, if when the program is looping through the z-beta hits, a z-beta value above the upper limit (on z-beta hits for that particular z-alpha hit) is reached, the z-beta loop can be terminated. Similarly the range of allowed z-gamma minus z-alpha differences is defined by a look-up indexed by the z-beta z-alpha displacement. If the z-gamma hit picked up on looping becomes too high the z-gamma loop can be ended and a new value of z-beta tried. As few as possible combinations of hits are considered in the search for a triggering sequence.

3.7 The On-line Data Acquisition System

Figure 3.5.1 shows the configuration of the on-line system. The

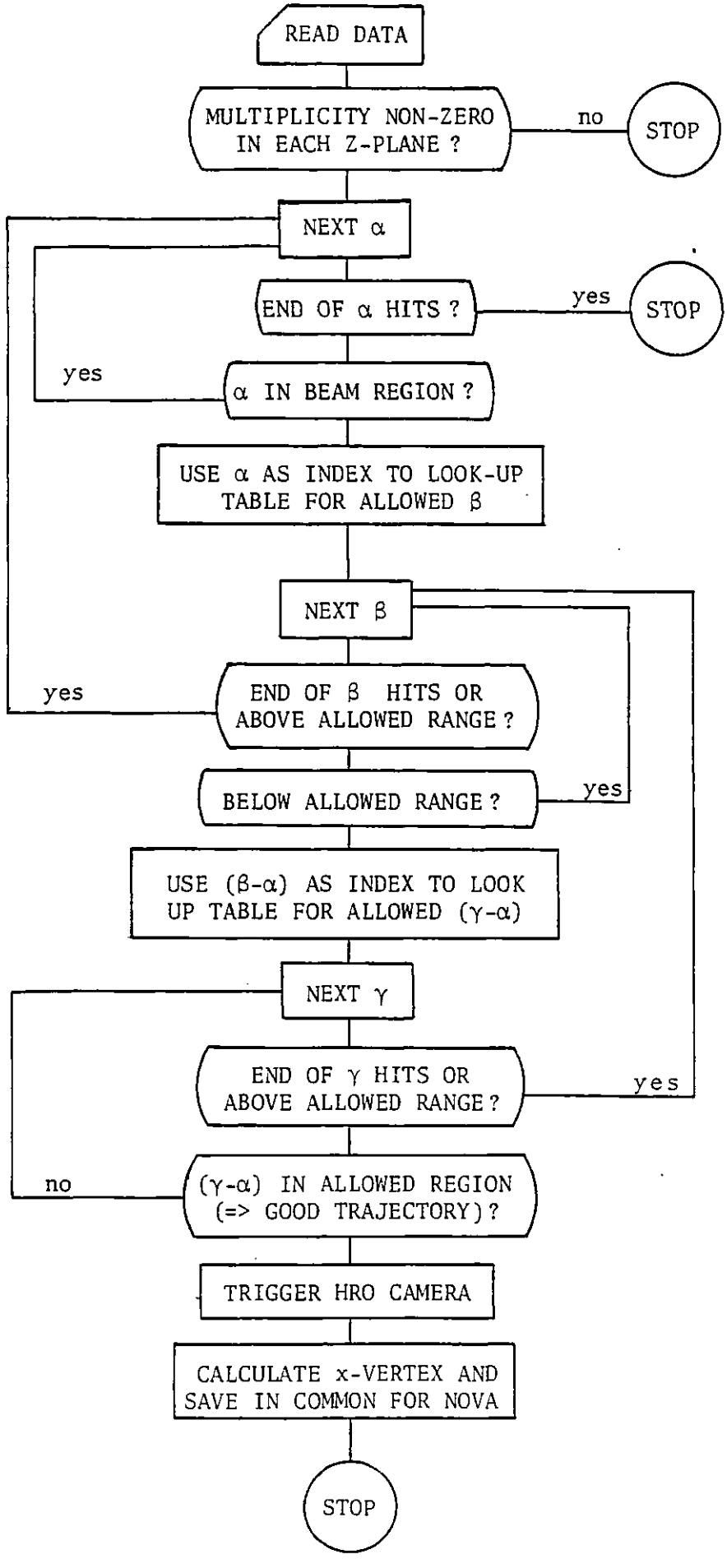

Figure 3.6.1 FLOW CHART FOR ALGORITHM TO FIND

SNOOP modules which link the 4/X to its slaves (168/Es) also allow data to be transferred directly from CAMAC dataways into 168/E memory saving some time. To save more time CAMAC crate 27_8 contains a specifically modified crate controller, an auxiliary controller. This is used to transfer just the z-plane PWC hit digitisings from the Cindies (a type of digitising board [4]) into the memory of CPU#2. Full details are given in Appendix C (SLAC-PUB-2726). Ultimately the time taken to transfer data from the PWC planes was eliminated completely by mounting a PWC digitiser inside CPU#1, the results of which were available as read only memory (see section 3.9.A).

Whilst data is being taken, the NOVA 4/X is run in a foreground background mode. Background tasks are those whichare not time critical; foreground tasks are, and are associated with the picture taking sequence itself.

The main activities controlled by the foreground which are related to the HRO trigger are summarised in table 3.7.1. If a picture is taken processing of pre-beam interrupts is paused to allow for the film in the camera to be wound on and for data from the downstream counters to be written to tape. This results in a dead time of about half a second before the system is ready to take data again.

Every fifty frames a picture is taken untriggered. These frames are examined for e^+e^- pairs which are then measured and used to estimate the beam flux (and obtain the energy spectra of the beam). The data in the downstream counters is written to tape after a fixed number of pulses (the standard is thirty) whether or not there has been a picture trigger. This information is used to check that the trigger is working correctly and to test modified triggers.

Table 3.7.1 TIMING OF DATA TAKING SEQUENCE

TIME (μs)	ACTIVITY
-2025	Pre-beam interrupt. RDOS (real-time disk operating system) suspends operation of Background tasks and initiates the execution of the foreground program.
-1550 → -1050	Start match point processor and execution of program in CPU#1. (The exact timing of this step and the one following depends on the status of the Background program when the interrupt is received). The algorithm in CPU#1 first writes to the results memory of its internal digitiser to clear it. It then makes continual checks on the status of the digitiser ready flag.
-1425 → -925	Initialize algorithm on CPU#2 and arm the auxiliary controller. The Foreground now avoids I/O to crate 27_8 until the HRO algorithm has finished execution.
0	Beam pulse arrives
+33	All z plane hits have been digitised. Once the auxiliary controller has finished reading z-gamma and transferring hits via a SNOOP module into CPU#2 it will disable Listen Mode in the SNOOP. The ready flag on the digitiser in CPU#1 has been set, this stops the algorithm in CPU#1 looping on this flag and starts execution of the algorithm proper.
+54	Auxiliary controller starts algorithm proper on CPU#2
+120 → 300	Depending on the number of hits in each plane and the number of combinations considered the algorithm reaches a triggering decision.
38000	Foreground suspends itself and RDOS restores Background execution.
97975	Next pre-beam interrupt.

3.8 Trigger Developments

The PWC triggering algorithm was developed under the assumption that the PWCs would be deadened in the beam region, but initially (Summer 1980) we ran with undeadened wire planes. The triggering algorithm was therefore modified to incorporate cuts on the values of z wires used to make a trajectory. The software dead region cuts were much smaller than the proposed hardware cuts. This was to enable the effect of widening the dead region on the trigger sensitivity and its selectivity to be investigated offline. Table 3.8.1 shows how the software dead region has increased with time.

The main disadvantage of not having the planes modified was that the electromagnetic background raised the average multiplicity of hits in the PWCs. This increased the probability of saturating the readout from a particular plane (limited to the lowest eight hits in each plane) and made it more likely that hits associated with tracks from hadronic interactions were lost. This decreased the efficiency of the PWC trigger.

One method of checking the efficiency of a trigger is to take a sample of untriggered data and run the triggering algorithm on it to see what fraction of the untriggered events survive. Another way is to take data with an independent trigger and cross check the triggers against each other.

In order to obtain a sample of 100 events over 20 rolls of film would have been needed (about 20% of the initial exposure). Fortunately a hardware trigger using the lead glass wall detector was also available for use. This trigger uses fast analogue circuitry to give a signal proportional (approximately) to the energy deposited in both the back blocks and the active converter units of the lead glass wall. A signal above threshold in either the back

RUN	ROLL NUMBER AT START OF RUNNING	LEAD GLASS WALL TRIGGER	PWC TRIGGER	PWC TRIGGER DEAD REGIONS IN WIRE NUMBER		
				Z-ALPHA	Z-BETA	Z-GAMMA
Summer 1980	110	Signal above threshold in either the active converter (AC) or back blocks (BB)	Three hits in a line intersecting photon beam within fiducial volume of bubble chamber. Less than or equal to eight hits/ Z-plane used	±4	±6	±12
Fall 1980	300	Signal above threshold in either side of AC or either side of BB	"	±7	±11	±19
	403	"	"	±9	±14	±25
Spring 1981	900	"	"	±10	±16	±28
Fall 1981	1500	"	"	±10	±16	±28
	1770	"	Up to 12 hits/Z-plane now used	±10	±16	±28

Table 3.8.1 SUMMARY OF TRIGGERS USED DURING RUNNING

blocks or the active converter segments led to a trigger. This triggering decision was available within a microsecond of the beam spill.

About 30% of the lead glass wall triggers failed to give PWC triggers; either the planes had saturated, or wires had failed to fire, or hits had been part of a sequence which had been suppressed, or no tracks had gone through an active region of the PWCs. Since the aim of the experiment was to study the entire photoproduction cross-section it was decided to use an "OR" of the lead glass and PWC triggers in all future running. Figure 3.8.1 shows the logic of the trigger finally adopted. The beam veto prevents pictures being taken when the beam flux is less than or equal to 3γ/pulse, since experience had shown that pictures taken under such conditions rarely yielded hadronic interactions on the frame.

During the summer of 1980 both components of the trigger were studied with the aim of improving the events/frame ratio (which was about 1 event per 10 frames). In doing this it was assumed that the trigger we had been running with was 100% efficient.

Various dead region cuts were tried out on a sample of a few typical rolls of data. We found that when we plotted efficiency against events/frame the points all lay in a fairly narrow band, defining a PWC trigger contour showing the limits on the efficiency attainable if a given events per frame ratio was wanted. Figure 3.8.2 shows the results and indicates the points on the curve given by the dead regions used in data taking. This contour indicates that the maximum efficiency of the PWC trigger would be less than eighty-five percent even if no dead region cuts were imposed but that the efficiency does not fall off too rapidly with increases in the dead region.

It is more difficult to adjust the lead glass wall trigger through

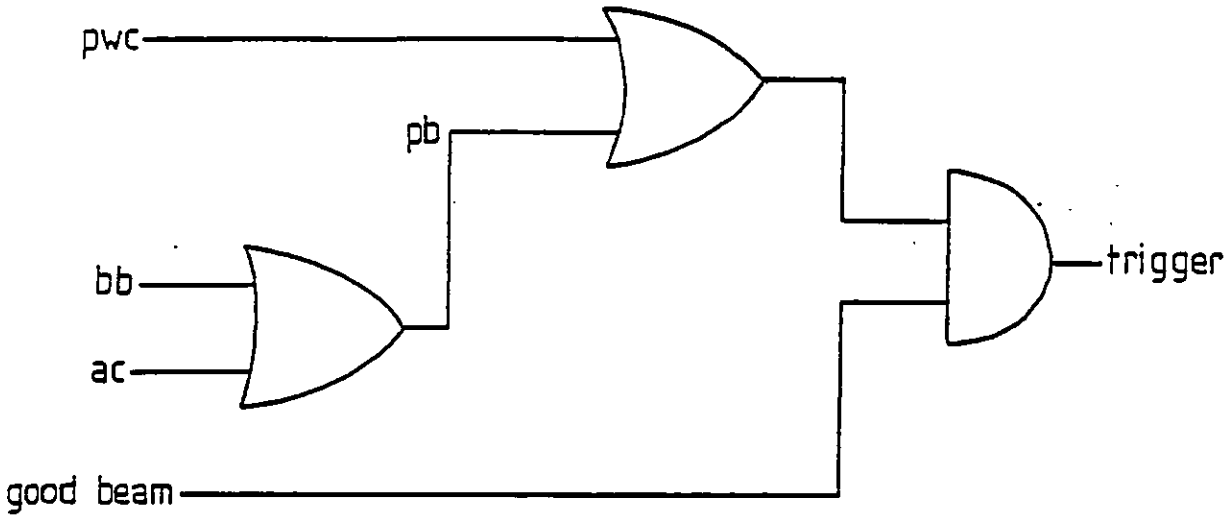

Figure 3.8.1 BC 72/73 TRIGGER LOGIC

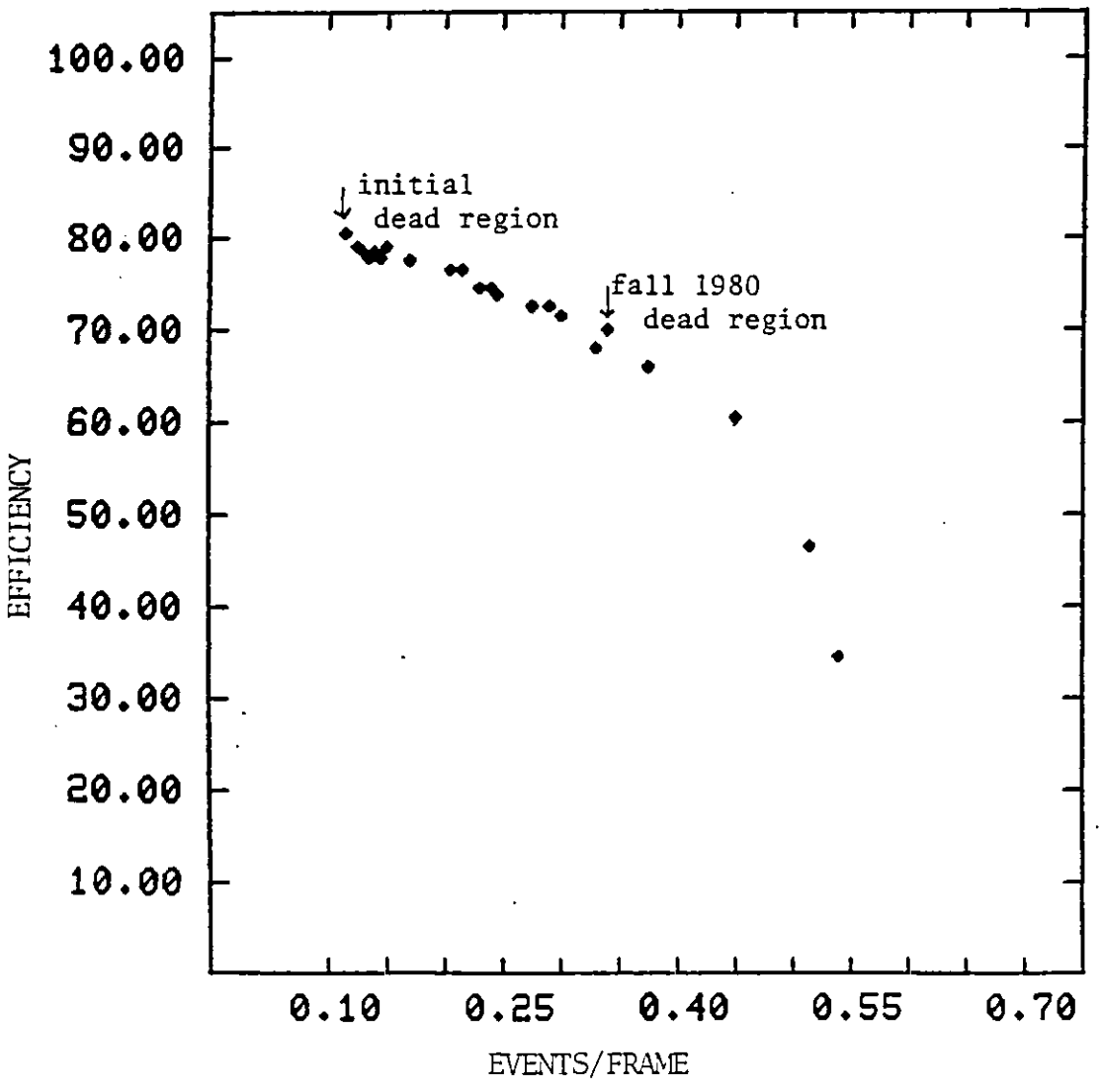

Figure 3.8.2 PWC TRIGGER CONTOUR

off-line studies. The resolution of the detector is insufficient to accurately locate the position of energy deposits resulting in a trigger, especially those in the fingers of the active converter, and in any case to adjust the dead region would require the two halves of the detector (separated by the "plane" containing the electromagnetic background) to be physically moved. Also once the trigger levels of the lead glass wall discriminators are raised above a minimum determined by the noise level in the dynodes little improvement in the signal to noise level results from further increases. One change was made in the trigger between the Summer 1980 and Fall 1980 runs however; instead of taking dynode sums for all the active converter units and for all the back blocks, the energy in each half of each component of the wall was summed separately. This meant that the overall lead glass trigger became an "OR" of four possible triggers; energy deposited above the thresholds set in the north side of the active converter, the south side of the active converter, the north side of the absorber or the south side of the absorber. The aim of this change was to prevent two tracks from a photon pair conversion contributing to a single dynode sum.

The use of this lead glass trigger in combination with the PWC algorithm trigger has yielded a combined trigger which was more efficient at a given events/frame ratio than either trigger would have been if used independently. The gain in efficiency however decreases as the signal to noise ratio is improved.

3.9 PWC Trigger Losses

A hadronic interaction in the bubble chamber will fail to give a PWC trigger if none of the tracks from the event produce digitisable hits in all three of the z planes in the downstream PWC stations. This failure may be the result of:-

i) No charged track from the interaction traversing all three PWC stations (whether or not this is the case is determined by the geometrical acceptance of the detectors).

or

ii) All of the charged tracks which do pass through z-alpha, z-beta and z-gamma, fail to yield hits in all three planes. This may be due to wires failing to register a hit (because they are not one hundred percent efficient) or because a PWC plane readout is saturated and a hit associated with the track is not output by a digitiser.

Only the probability of a wire responding or failing to respond to a track close to it is independent of the character of the interaction. Factors such as the number of charged tracks coming from the primary vertex and their momentum and orientation with respect to the beam determine how many tracks are likely to go through the PWCs. The more tracks that do so the more likely the PWCs are to saturate. This saturation only reduces the chance of a PWC trigger if z-alpha is saturated by hits associated with tracks which do not reach z-gamma

3.9.A Saturation Losses

The mean number of hits in the z-alpha plane increases from $4.29 \pm .15$ for events with three tracks coming from the primary vertex to $5.95 \pm .21$ for events with seven or more tracks at the primary vertex considered. The digitisers in use when this data was taken (pre roll 1770) read out only the first eight hits from each of the PWC planes, (in asscending order, lowest wire numbers first) so the difference in mean multiplicity appears significant. Figure 3.9.A.1 shows the z-alpha multiplicity distributions for beam spills giving rise to a camera trigger, and for beam spills not giving a trigger.

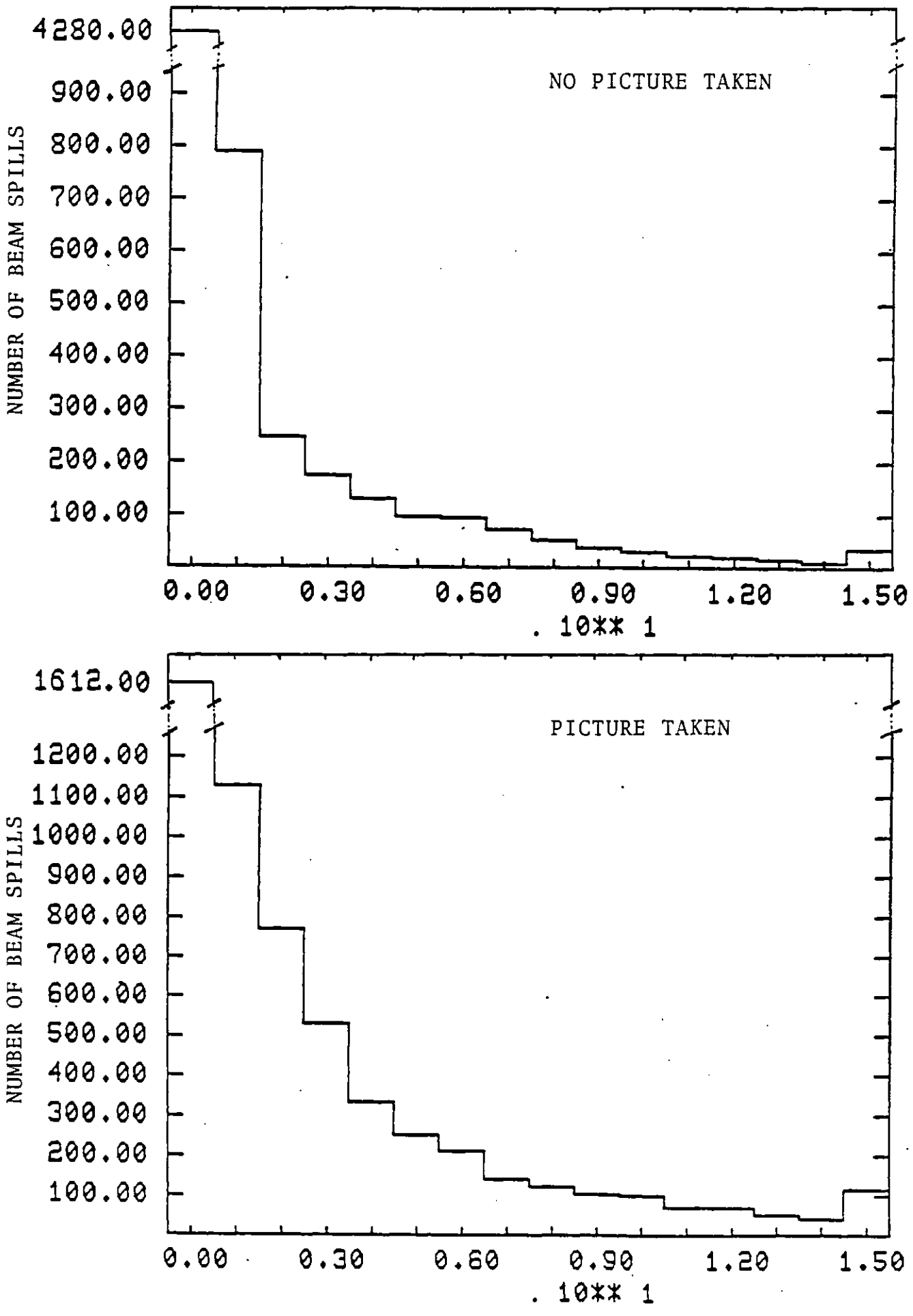

Figure 3.9.A.1 MULTIPLICITY DISTRIBUTIONS FOR HITS IN Z-ALPHA

The raw multiplicity distributions however cannot be used to predict trigger losses because of PWC saturation. Although there may be nine hits in a plane, the triggering trajectory may be associated with the first hit readout.

It is convenient in what follows to continue to consider events with three charged tracks coming from the primary vertex and those with seven or more such tracks as belonging to two distinct classes of triggering interactions. I shall refer to these classes as A and B respectively. Five prong events form an intermediate class and the triggering behaviour of these events is correspondingly intermediate. Although the distinctions between A and B would be more pronounced if type B events were restricted to those with nine or more tracks the statistical significance of any results would be much poorer.

Figure 3.9.A.2 shows how frequently a hit in a particular position in the z-alpha readout sequence (the third hit for example) is used in making up the triggering trajectory, that is a set of hits satisfying the constraints imposed by the PWC algorithm. The results for A and for B type events are shown separately. As can be seen B type events are more likely to require hits readout later in the digitising sequence (if a maximum of four hits was readout for example about 13% of the B events currently triggering would have been lost compared to around 10% of A type events). Estimates of the fraction of events lost because only eight z-alpha hits were recorded are complicated however because of the poor statistics governing the tail of the distributions shown in Figure 3.9.A.2. Table 3.9.A.1 gives a range of estimates based on three differing assumptions:-

i) The rate at which the distribution falls off is given by comparing the number of triggers using one of the first four hits readout to the number using one of the last four hits

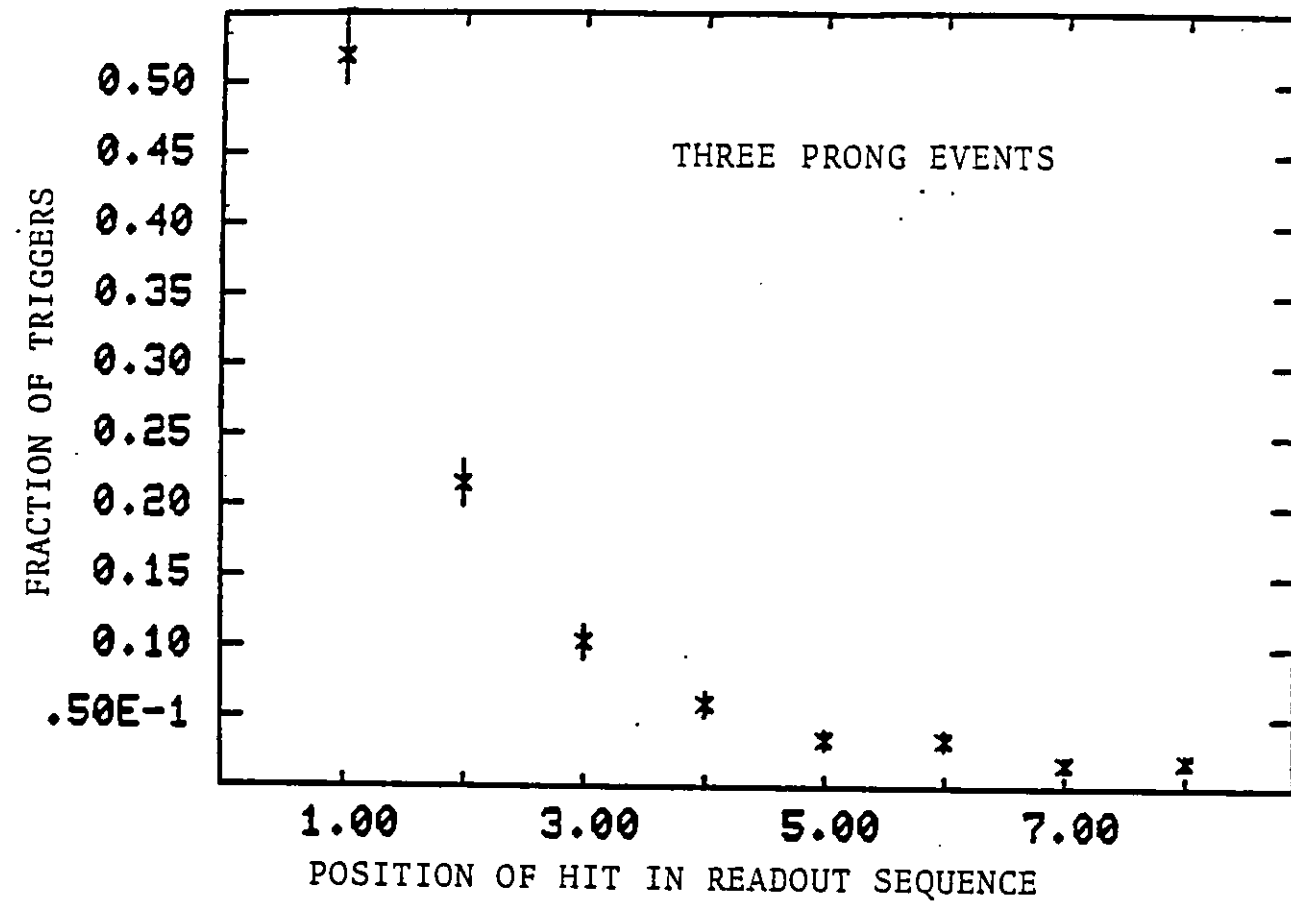

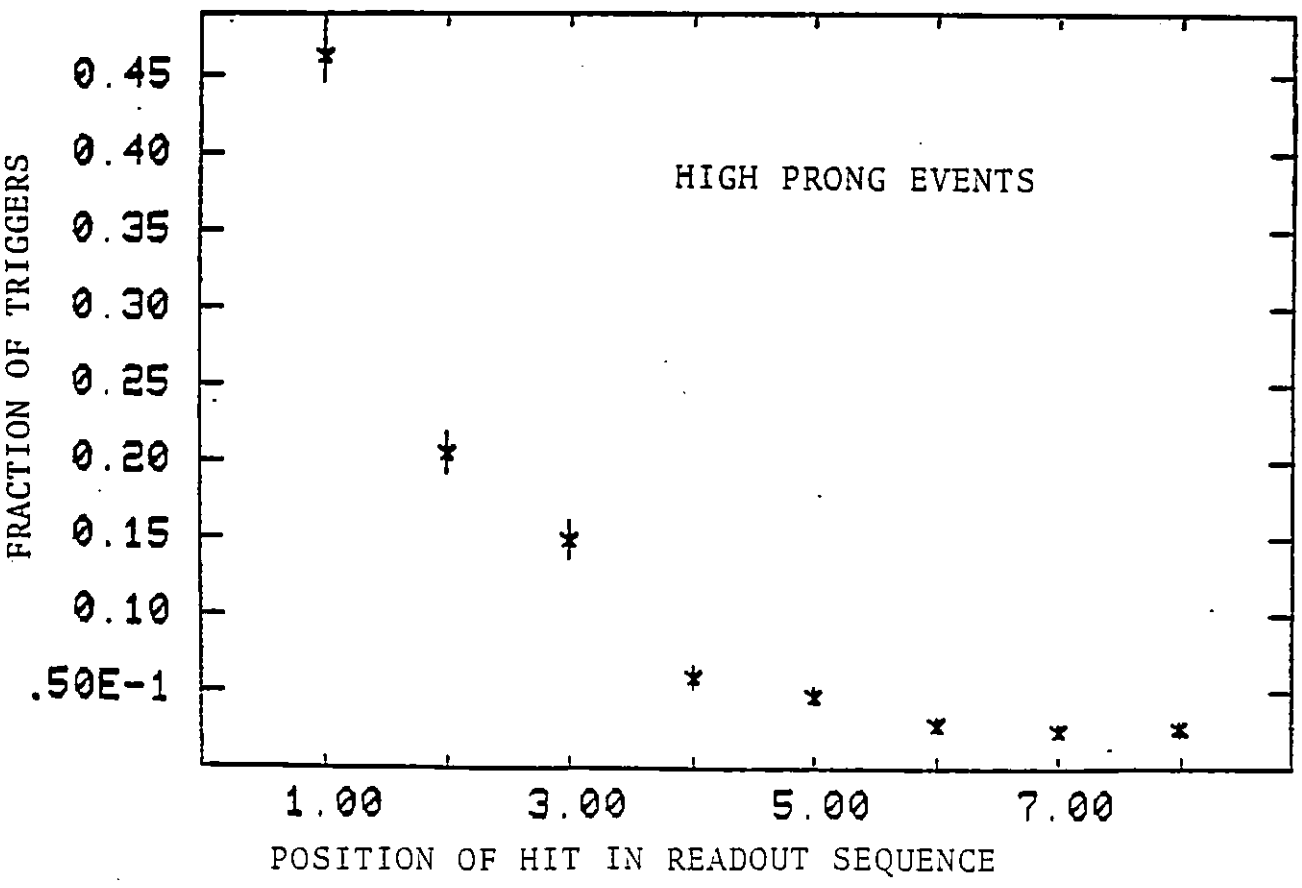

Figure 3.9.A.2 FRACTION OF TOTAL PWC TRIGGERS OF GIVEN TYPE USING A HIT IN A PARTICULAR POSITION IN READOUT SEQUENCE

readout. Since the rate of fall off is in fact flattening off this assumption leads to an underestimate of triggering losses.

ii) The rate of decrease is given by comparing the number of triggers using the fifth or sixth hit readout with the number using the seventh or eighth.

or

iii) The distribution becomes flat and continues at a level defined as the mean of the percentage of triggers using the sixth, seventh or eighth hit. Z-alpha is assumed never to contain more than twenty hits. This assumption clearly leads to an overestimate of saturation losses.

Assumption (ii) probably yields the most reasonable estimate of the triggering loss due to z-alpha saturation. The overall loss due to any of the z planes saturating is of the same order. This is partially because the z-beta and z-gamma planes have a lower mean multiplicity than the z-alpha plane and hits on the triggering trajectory tend to occur lower down in the digitising sequence (only half as many triggers use the sixth, seventh or eighth hit readout from the z-gamma plane as use hits in the corresponding readout positions from the z-alpha plane). Saturation of the z-beta and/or z-gamma planes also tends to be correlated with z-alpha being saturated (12% of three prong triggers have eight or more hits in z-alpha, 16% have eight or more hits in at least one z plane).

	TYPE A	TYPE B
i	1 ± ½%	2 ± 1%
ii	4 ± 1%	11 ± 1%
iii	28 ± 2%	32 ± 2%

Table 3.9.A.1

TRIGGERING LOSSES DUE TO SATURATION OF Z-ALPHA DIGITISER AS A PERCENTAGE OF EVENTS TRIGGERING THE PWC ALGORITHM

Charm events tend to have a large number of associated charged tracks however (especially including tracks from close in decays which, given the resolution of the downstream detectors, appear to come from the primary vertex). Therefore, although the triggering losses due to saturation are not large, charm events, which act as type B events as far as the PWC trigger is concerned, are in the worst affected class of triggers Since the experiment was set-up to study charm any change in the trigger improving the acceptance of such events would be worthwhile.

Two problems needed solving before more than eight hits per z plane could be recorded and the effective multiplicity restriction on PWC triggers removed. The first was that the digitising cards then being used by the system could not be modified to readout greater than eight hits. The second was that if more hits were recorded, the transfer time needed to make the hits available in computer memory would increase, and also the algorithm itself would take longer to make a decision because more combinations of hits would need to be tried. Both of these problems were solved by mounting special digitising boards [5] inside CPU#1.

The results memory of these digitisers forms part of the data memory of CPU#1 and as such is directly accessible. The transfer time usually needed from a digitiser into computer memory is thus completely eliminated. This makes it realistic to digitise more than the eight hits which is the maximum capability of the Cindy [4] cards and still make a triggering decision in the time available. These digitisers were fitted into CPU#1 during the Spring 1981 cycle but they were not used in production running until the Fall 1981 cycle.

The algorithm running in CPU#1 was modified to use up to twelve hits per z plane at the start of the Fall cycle. Data taken between rolls 1703 and 1769 was then checked through off-line to make sure that the digitiser and the modified algorithm were working correctly (during

this time the triggering decision was taken by the algorithm running in CPU#2). There were no conflicts between the PWC hits readout from the new digitisers and those from the Cindies in over 10^5 records and there were no occasions when the algorithm using only 8 hits/plane triggered and that using 12 did not. 12 hits/plane triggers were a few percent more frequent than 8 hits/plane ones. When they agreed the triggering decision was reached 20-40 μsec earlier by the algorithm running in CPU#1 (containing the new digitisers), shifting the algorithm timing curve shown in Appendix C so that the majority of triggers occur within 100μsec of the beam spill.

From roll 1770 onwards the triggering decision (for the PWC trigger) has been made by the algorithm running in CPU#1 using 12 hits/plane not 8. The data taken with this new trigger has, at the time of writing, still to be completely scanned and is unavailable for a detailed study. However, preliminary studies made on a small fraction of the data considering only PWC triggers using the ninth, tenth, eleventh or twelth hit readout from any of the z planes indicates that the ratio of type A events to type B events is $1.07 \pm .40$ showing that readout saturation did indeed affect type B event acceptance more significantly than type A. The PWC triggering acceptance of type B events has increased by about 6% and of type A by 2%. The triggering acceptance of the combined trigger (PWC.OR.Lead Glass Wall) has also been increased by the change since not all the "extra" PWC triggers are joint with the lead glass wall.

3.9.B Losses due to the Geometrical Acceptance of the PWC Stations

The geometrical acceptance of the PWC stations may be estimated in several ways. One method is to set-up a Monte-Carlo which generates tracks in the bubble chamber and swims them out through the downstream system to find out which detectors they go through. Tracks of a

given three-momentum can then be assigned a weight inversely proportional to the probability of their reaching a particular detector. The difficulty in extending this method to calculate the probability of triggering on a three prong interaction, for example is that the overall triggering probability depends on all three tracks. This means that a model which determines the probability of track 2 having a particular momentum given the momentum of track 1 (and so on for all the tracks in an event) must be incorporated into the Monte Carlo program. The triggering acceptance calculated thus becomes dependent on the assumptions in the model. A method which is not so dependent is to consider the events which do yield a trigger and use these to estimate the proportion failing to trigger.

The PWC triggering algorithm used demands only that a track from the event gives hits in z-alpha, z-beta and z-gamma. This puts no explicit constraint on the momentum of the triggering track. However the probability of a track hitting a particular plane depends on the z and on the y acceptance of that plane and although the z acceptance is not momentum dependent the y acceptance is. The chance of a track hitting all three PWC stations therefore depends on its momentum as well as its initial orientation.

The geometric acceptance of the PWC detectors is closely matched in the z direction to that of the bubble chamber exit window; the acceptance of any single plane governs the acceptance of all. The distributions shown in Figure 3.9.B.1 give the distance from the centre of z-alpha of hits lying on the triggering trajectory closest into the centre for type A and type B triggers. The distributions indicate that the loss of triggers due to events having no tracks at small theta is negligible (the majority of triggers use hits close to the centre). Similar distributions also imply that losses due to limited y acceptance are

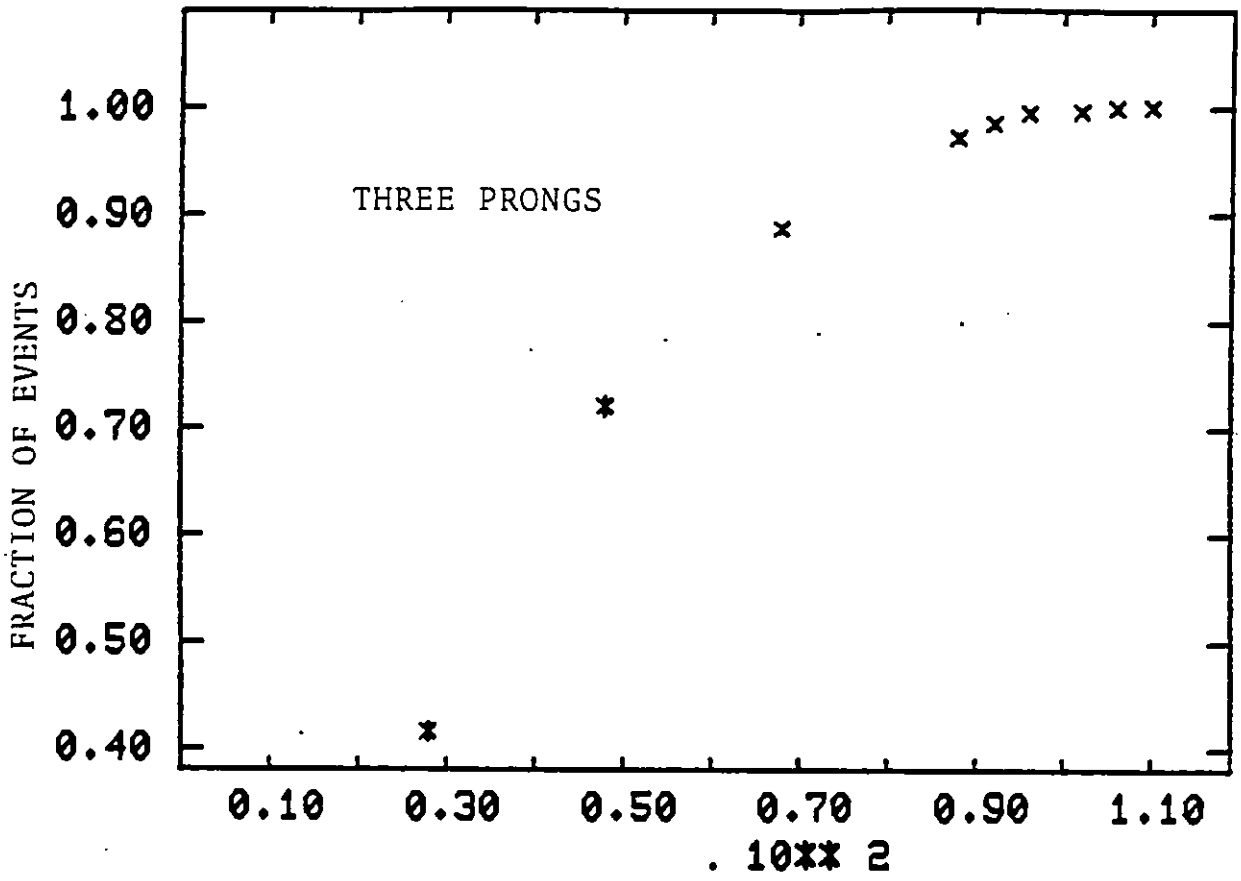

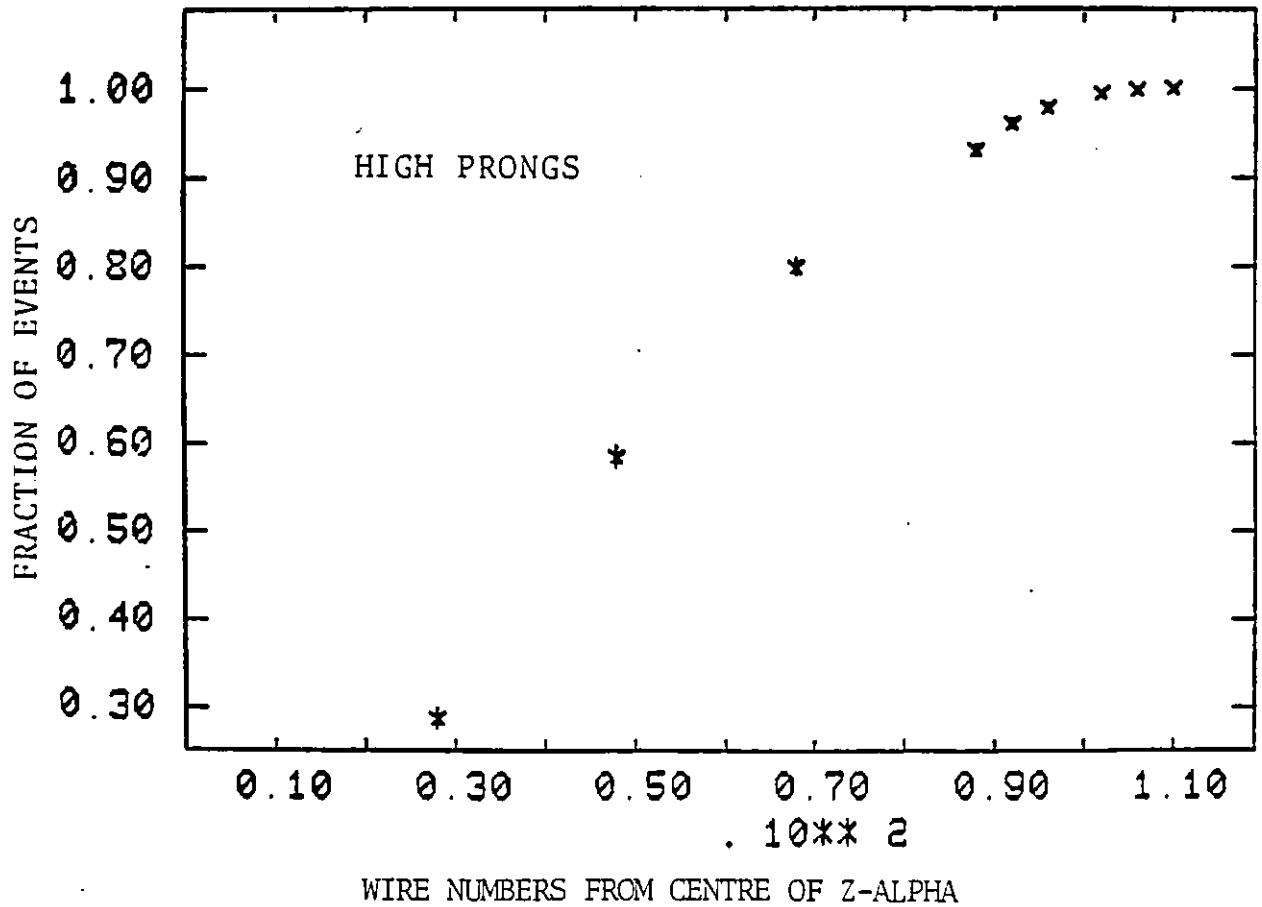

Figure 3.9.B.1 FRACTION OF EVENTS TRIGGERING PWC ALGORITHM AS A FUNCTION OF THE SIZE OF Z-ALPHA

also small, providing that the track has momentum of at least two GeV/c.

The distribution of the z positions of hits lying on the trajectory furthest from the centre of z-alpha (figure 3.9.B.2) on the other hand show that dead region losses are significant (dead region losses are dependent on the z position at which the track intercepts alpha, not the y position). The number of type A and type B events that would trigger the PWC algorithm decreases linearly for each type of trigger until the dead region is a significant fraction of the z-alpha plane. The data used was taken with a dead region of plus or minus ten wire numbers about the beam position in z-alpha so the rate of loss of events within these limits has to be estimated. Linear extrapolations (which fit the data well) indicate that 11 ± 1% of seven or more prong triggers are lost due to the ten wire dead region and that the loss of three prong triggers is substantially larger at 19 ± 1%. The extrapolations imply that the ratio of type A to type B triggers if a plus or minus four wire number cut had been used would have been around 1.7. The Summer 1980 data which was taken with this dead region yields a value of 1.8 ±0.1 for this ratio. Since there were no dead regions in the PWCs in Summer 1980 and saturation losses would have been higher (decreasing the number of type B events) the extrapolations seem reasonable.

3.9.C Single Wire Inefficiency Losses

The average efficiency of wires in a given plane can be calculated by comparing the number of hybrid tracks giving hits in all nine PWC planes in the downstream stations with the number missing a hit from the given plane.

Let the probability of a hit in z-alpha be $P_{z\alpha}$ and the probability of hits in all other planes be similarly denoted;

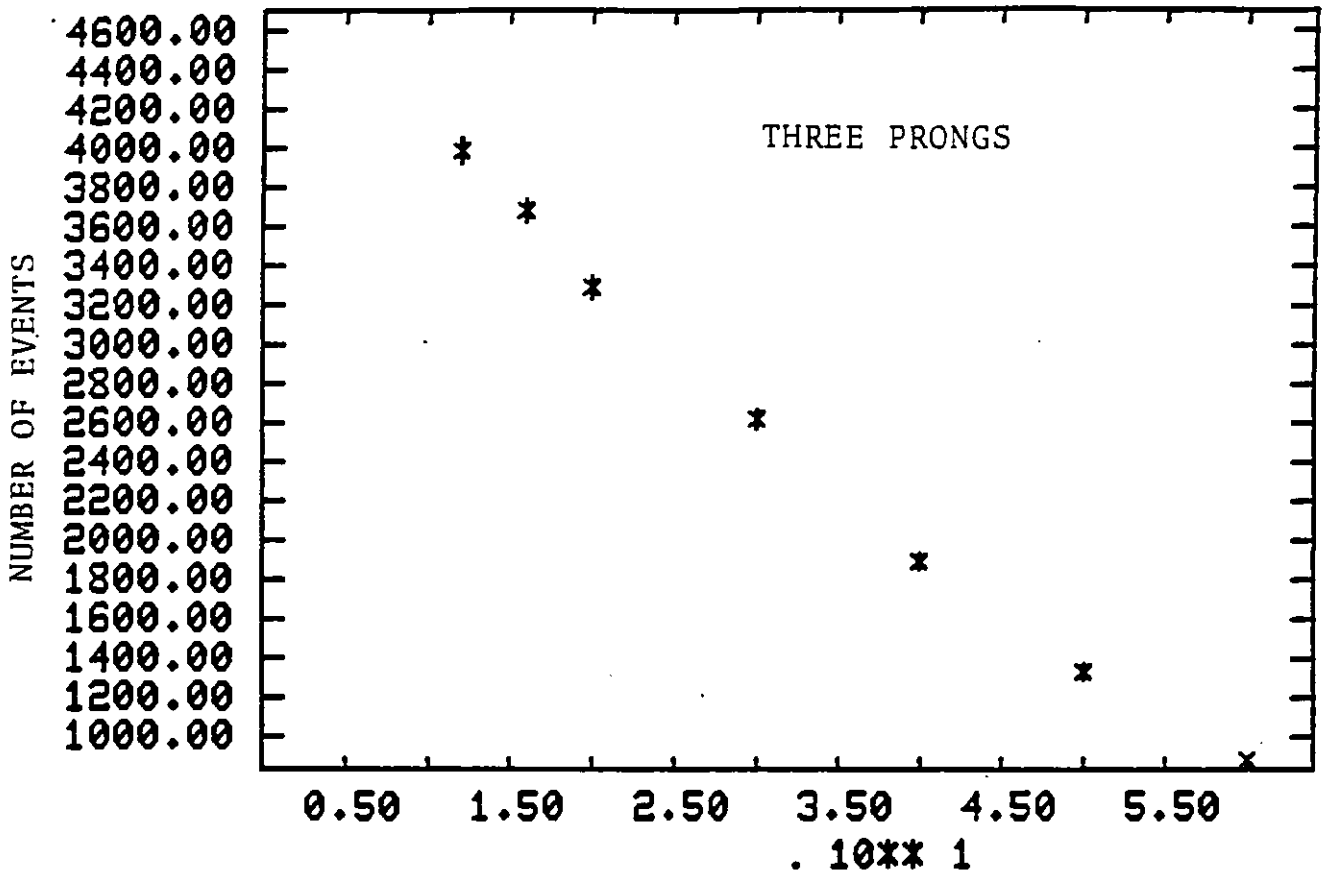

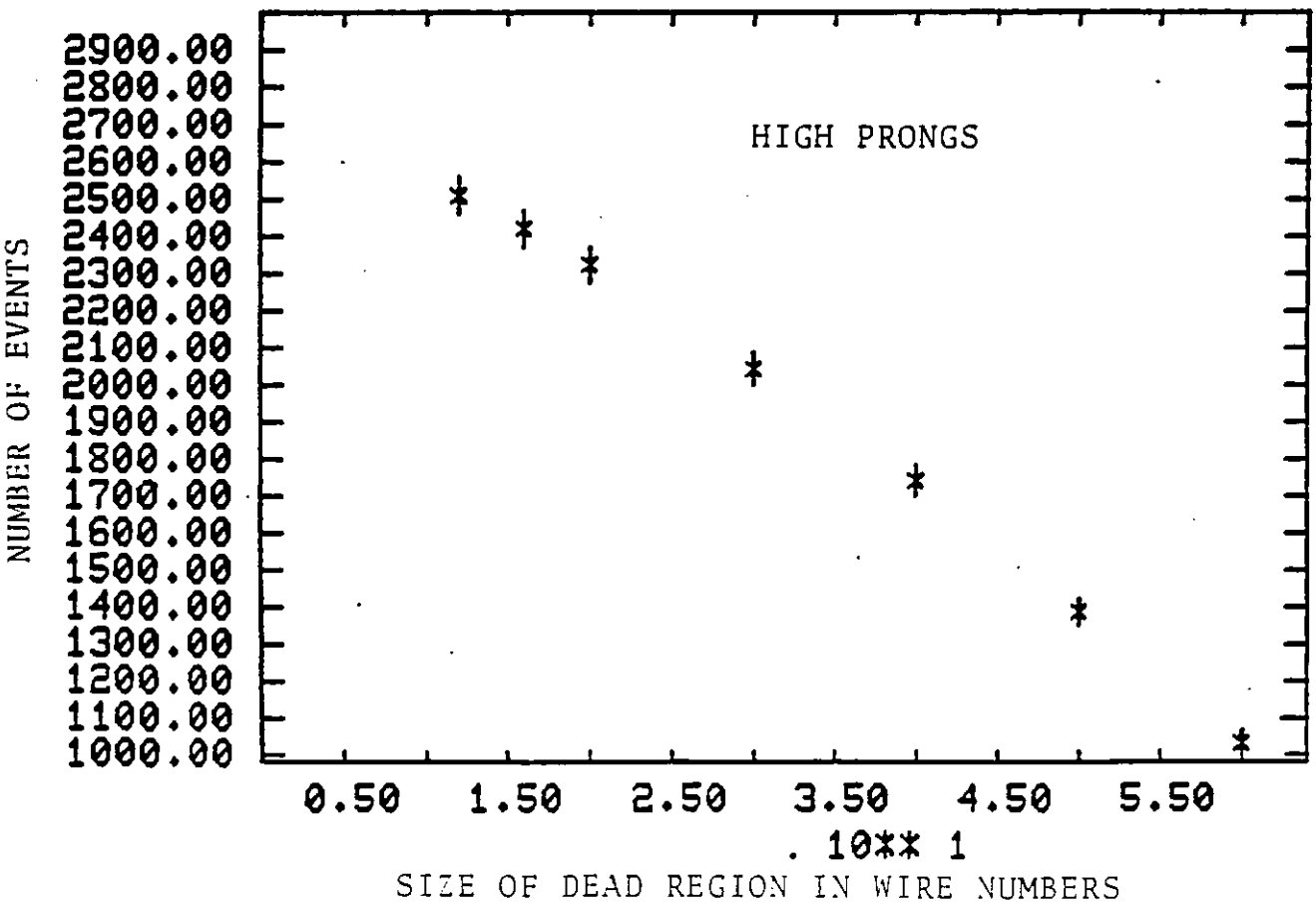

Figure 3.9.B.2 NUMBER OF EVENTS TRIGGERING PWC ALGORITHM AS A FUNCTION OF THE SIZE OF THE Z-ALPHA DEAD REGION

Then probability of a hit in all nine planes

$$P_{TOT} = P_{z\alpha}\, P_{z\beta}\, P_{z\gamma}\, P_{y\alpha}\, P_{y\beta}\, P_{y\gamma}\, P_{u\alpha}\, P_{u\beta}\, P_{u\gamma}$$

and the probability of missing a hit only in z-alpha

$$P_{\overline{z\alpha}} = P_{TOT} \times \frac{(1 - P_{z\alpha})}{P_{z\alpha}}$$

$\therefore$ Relative probability of track with nine hits compared to track with eight

$$\frac{P_{TOT}}{P_{\overline{z\alpha}}} = \left(\frac{1 - P_{z\alpha}}{P_{z\alpha}}\right)^{-1}$$

$$= \frac{\text{number of tracks with nine hits}}{\text{number missing only the z-alpha hit}}$$

$$= \frac{N_9}{N_{\overline{z\alpha}}}$$

$$\therefore \quad P_{z\alpha} = \frac{N_9}{N_9 + N_{\overline{z\alpha}}}$$

Tracks which go through saturated wire planes should be discarded from the comparison (their inclusion would lower the calculated efficiency). If the Summer 1980 data is excluded from the calculations (different PWCs were used) the average z plane efficiencies obtained are;

$$P_{z\alpha} = 92 \pm 2\%$$

$$P_{z\beta} = 88 \pm 2\%$$

and $$P_{z\gamma} = 96 \pm 2\%$$

The z plane efficiencies obtained if only type A or only type B events are used agree with these values as expected. The probability of a trigger on a single track is thus about 78% $\pm$ 3%. Table 3.9.C.1 shows how the probability of triggering on an event increases as the number

of tracks in the PWCs rises assuming probabilities of triggering on an individual track of 85, 78 and 70 percent. The formula used to calculate the probability is

$$P = \sum_{i=0}^{N-1} P_t^{N-i} (1-P_t)^i \frac{N!}{i!(N-i)!}$$

were N is the number of tracks through all three stations and P_t is the probability a track will trigger.

NUMBER OF TRACKS (N) \ PROBABILITY A TRACK WILL TRIGGER (P_t)	85%	78%	70%
1	85%	78%	70%
2	98%	95%	91%
3	∿ 100%	99%	97%
4	∿ 100%	∿ 100%	99%

Table 3.9.C.1

PROBABILITY OF AN EVENT TRIGGERING AS A FUNCTION OF THE NUMBER OF TRACKS THROUGH ALL THREE PLANES AND PROBABILITY AN INDIVIDUAL TRACK WILL TRIGGER.

The number of events of each type with one or more tracks through the PWC system is given by the number of interactions of each type with one or more hybrid tracks which give a hit in gamma (the probability of a track hitting gamma and not causing at least one hit is less than one percent). The number of interactions with a given number of tracks which there would have been if all the wires were fully efficient is calculated by multiplying the number which give a PWC trigger by the appropriate efficiency factor for triggering on such events (the reciprocals of the probabilities given in table 3.9.C.1).

For the moment I will ignore events which have no hybrid track. These events do not contribute to the cross section that the PWC trigger could trigger on (distinguishing between events where the hybrid track is lost because of the geometrical acceptance of the system and events which have no charged tracks leaving the bubble chamber). Assuming that a single track has a 78 ± 3% chance of causing a trigger the percentage of type A events lost is 17± 4% (expressed relative to the number of events triggering) and the percentage of type B events lost is 11 ± 4%.

3.9.D Summary of PWC Trigger Losses

The percentages of triggers lost due to saturation, the geometrical acceptance of the PWC stations and, single wire inefficiences are tabulated in Table 3.9.D.1. In each case the percentage is expressed relative to the number of events which do trigger. The saturation losses quoted are based on the small number of twelve hit per plane triggers analysed. Finally the percentages of the triggerable cross sections which are accepted by the PWC trigger are quoted for type A and type B events. The values obtained are similar showing that the overall triggering probability does not depend strongly on topology.

	TYPE A	TYPE B
SATURATION LOSSES	2 ± 3%	6 ± 4%
ACCEPTANCE LOSSES	19 ± 1%	11 ± 1%
WIRE INEFFICIENCY LOSSES	17 ± 4%	11 ± 4%
ACCEPTED FRACTION OF TRIGGERING CROSS SECTION	70 ± 5%	77 ± 5%

Table 3.9.D.1 PWC TRIGGER LOSSES (AUTUMN 80,SPRING 81)
(As a fraction of events triggering)

3.10 Acceptance of the Combined Trigger

To calculate the fraction of the total cross section which the PWC algorithm triggers on, the number of events which it cannot trigger on (as opposed to the number it fails to trigger on) must be known.

The fraction of the cross-section to which the PWC trigger is insensitive may be estimated by firstly assuming that any event which cannot trigger the PWC algorithm will cause a lead glass wall trigger. I then, excluded any event which gave only a lead glass trigger but had at least one hybrid track which gave a hit in gamma from the count. Since not all tracks which give a PWC trigger hybridise (because of "accidental" triggers, poor measurement and different scattering tolerances) some events give a PWC trigger but have no hybrid track. Using these events to estimate the fraction of lead glass only events which lack a hybrid track for similar reasons, I obtained the number of "lead glass only" events which I have attributed as being due to neutral triggering tracks. 10 $\pm$ 1% of the triggering cross sections for both type A and type B events independently yield only neutral triggering tracks.

The PWC algorithm therefore triggers on;

64 $\pm$ 5% of the total three prong cross section

and 70 $\pm$ 5% of the total cross section of seven or more charged track events.

The acceptance of the combined trigger (PWC or Lead Glass Wall) can now be calculated from the number of PWC triggers and the number of lead glass only triggers.

The overall triggering cross sections are:

92 $\pm$ 7% of the three prong cross sections

and 84 $\pm$ 7% of the seven or more prong cross sections

These values raise the possibility that the combined trigger acceptance decreases as the number of charged tracks increases. This has implications in calculating the charm cross section, and so is worth considering further.

The mean negative pion multiplicity at an incident photon energy of 20.0 GeV is predicted to be 1.67 $\pm$ 0.23; (extrapolating from data taken at photon energies of 2.8, 4.7 and 9.3 GeV [6]). We find a mean negative particle multiplicity of 1.71 $\pm$ 0.02. However, even if the number of seven or more prong events is increased by fifteen percent and the number of three prong events left unchanged, the mean multiplicity increases by only 0.04 to 1.75 $\pm$ 0.02. The errors on the expected value make it unreasonable to rule out a significant relative loss of high prong events.

Figure 3.10.1 shows the relative acceptances (R.A.) of the various components of the combined trigger as a function of the number of charged tracks produced at the primary vertex. The relative acceptance is defined as:-

$$\text{R.A.}(n) = \frac{\text{number of triggers of type X on events with n charged tracks}}{\text{total number of triggers on events with n charged tracks}}$$

The plots show that while the PWC acceptance is increasing the lead glass acceptance is falling off rapidly.

While the chance of a PWC trigger is improved by increasing the number of tracks through the PWCs the chance of a lead glass wall trigger only increases if more energy is deposited in the wall. The mean number of tracks hitting alpha is 1.14 $\pm$ 0.02 for three track events compared to 1.90 $\pm$ 0.04 for seven or more track events. However, the chance that a track hitting alpha reaches gamma is 0.95 $\pm$ 0.02 if the event is a three prong and only 0.82 $\pm$ 0.02 if the event has at least seven tracks. This difference is due to the fact that tracks from high prong events

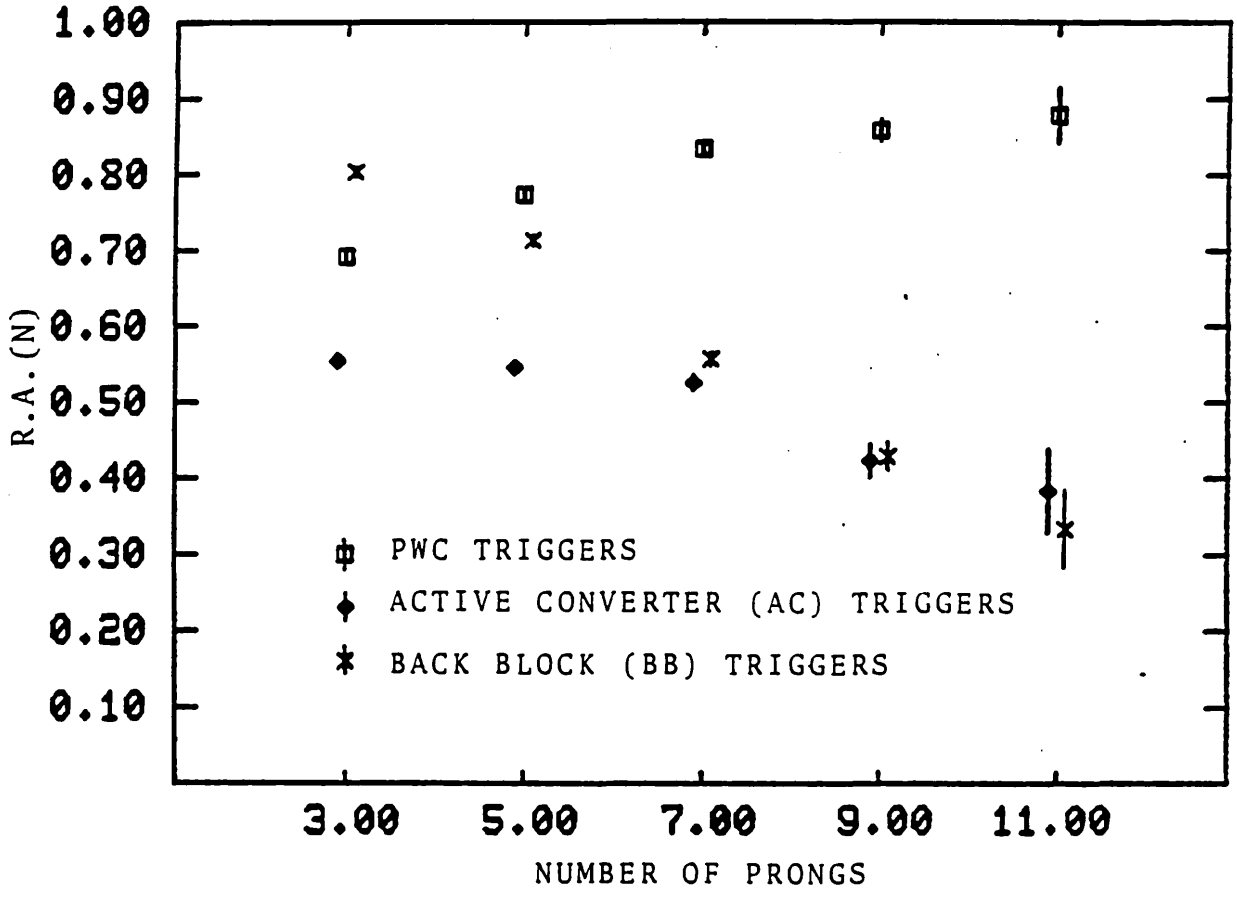

Figure 3.10.1 RELATIVE ACCEPTANCES OF PWC,AC,AND BB TRIGGERS AS A FUNCTION OF NUMBER OF TRACKS FROM PRIMARY VERTEX

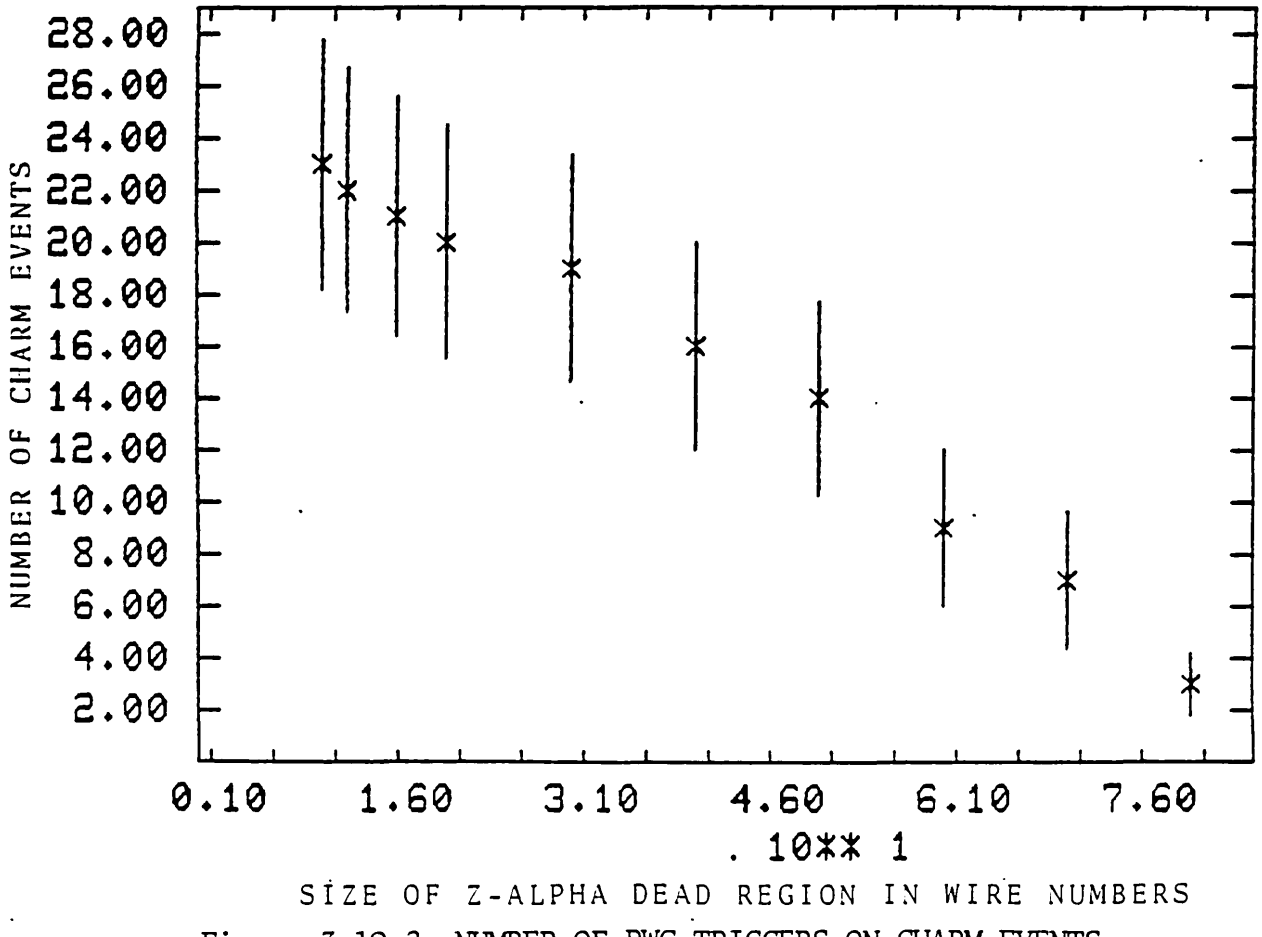

Figure 3.10.2 NUMBER OF PWC TRIGGERS ON CHARM EVENTS AS A FUNCTION OF DEAD REGION SIZE

have a lower mean momentum than tracks from three prongs and are more likely to be swept out by the magnetic field. Although the difference is not large enough to decrease the average number of tracks through the PWCs for a seven prong below the average number for a three prong it is large enough to reduce the average energy deposited in the Lead glass wall (which has worse geometrical acceptance than the PWCs). While the relative acceptance of the active converter is falling off slowly the relative acceptance of the back blocks (with a much higher threshold level) is falling off very rapidly.

TRIGGER	PREDICTED ACCEPTANCE	ACTUAL ACCEPTANCE
PWC	82 ± 1%	$85 \pm^{7}_{17}$ %
Active Converter	51 ± 1%	$56 \pm^{13}_{15}$ %
Back Blocks	60 ± 1%	$37 \pm^{13}_{11}$ %

Table 3.10.1

PREDICTED RELATIVE ACCEPTANCE OF CHARM COMPARED TO ACTUAL RELATIVE ACCEPTANCE

Table 3.10.1 gives the relative acceptances expected for charm events (given the proportions of five, seven, nine and eleven prongs in the data) and the actual values found. The relative acceptance of the back block trigger is lower than predicted implying that the charm events may form an atypical sample of the data.

Figure 3.10.2 shows the number of PWC charm triggers as a function of the z-alpha dead region. The slope of the fall off is consistent with dead region losses of 11%, i.e. similar to those expected for high prong events. Little can be said about saturation losses except that one of the four charm events that failed to cause a PWC trigger had a

saturated z plane. The charm events do however tend to have more tracks that could give a PWC trigger than do typical high prongs (2.26 $\pm$ 0.54 averaged over all the PWC charm triggers compared to an expected mean of 2.04). This changes the loss expected because of single wire inefficiencies to 7 $\pm$ 6%. Assuming that all other losses are the same as for type B events gives that

72 $\pm$ 12% of all charm events cause a PWC trigger (errors quoted are twice statistical)

The number of lead glass wall only triggers (four out of twenty seven) implies that the overall triggering acceptance is

$$85 \pm^{15}_{30} \%$$

Chapter 3 - References

[1] P.F. Kunz, R.N. Fall, and M.F. Gravina; SLAC-PUB-2418

[2] P.F. Kunz, R.N. Fall, and M.F. Gravina; SLAC-PUB-2198

[3] D. Bernstein, J.T. Caroll, V.H. Mitnick, L.Paffrath, and D.B.Parker; SLAC-PUB-2413

[4] L. Barker; SLAC-TN-75-10

[5] D.R. Price and R.W. Hatley; Internal BC72/73 memorandum

[6] J. Ballam et al; Phys Rev. D7 3150 (1973)

CHAPTER 4

PHOTOPRODUCTION - A THEORETICAL VIEW

4.1 Introduction

Photoproduction can be considered as on the boundary between electroproduction (where the electron acts as a photon source) and hadroproduction. This is a result of the properties of the photon, properties which make it unique amongst those particles which can at present be studied. It is a gauge particle and so can interact directly with the charged constituents of hadrons. In addition, it can sometimes be thought of as a vector meson and to itself behave as a hadron. The photon structure functions reflect this dual nature, part of them being exactly calculable.

The division of the photon structure functions into two parts, a hadronic component (acting as if the associated quark distributions were those of a vector meson), and a point-like (photonic or anomalous) component, was discussed ten years ago by Brodsky et al [1]. Recently, theoretical interest in studying the structure functions was renewed, following the advent of the possibility of experimentally measuring them at e^+e^- intersecting storage rings (via the two photon process). They have been calculated using the operator-product expansion technique [2], by diagrammatic methods [3], and by an approach based on the Altarelli-Parisi evolution equations [4].

All the methods used give the result that the deep inelastic structure functions derive almost entirely from the point-like component of the photon. Frazer and Gunion [5] have shown that the dominance of this component over the hadronic component is maintained down to quite low values of Q^2 for the probing photon. However the hadronic component may reassert itself and be the only significant contributor to low P_t photoproduction.

Estimates of the hadronic contribution vary. Experimental

evidence for non hadron-like behaviour of the inclusive cross section would enable limits to be put on this. If the point-like component is not negligible even at low P_t, photoproduction will then be an important testing ground for the models of low P_t inclusive physics, especially the Recombination model (see section 5.2).

In this chapter I will discuss photon interactions from the viewpoint of whether the photon is acting as a gauge particle or as a hadron. I will summarise the results of the photon structure function calculations, presenting where possible the underlying physical assumptions, and showing that predictions based on these calculations become unreliable at low q^2. I will then discuss photon interactions with a proton target and how the point-like contribution may be experimentally isolated.

4.2 The Photon Structure Functions - Point-like Component

The references given in the introduction to this chapter indicate that the range of approaches to the calculation of the photon structure functions covers all the currently available QCD renormalisation techniques. Many others have also considered the problem. The articles cited in references 6-10 were particularly useful sources of information.

Consider two photon interactions in e^+e^- in which one photon is real or nearly real, the other far off mass shell, both photons being unpolarised. Then there are two independent photon structure functions, corresponding to the absorption by the partons in the target of transverse photons (helicity $\pm$ 1), and the absorption of longitudinal scalar photons (helicity 0).

The total cross section is related by the optical theorem to the imaginary part of the forward Compton amplitude. The non perturbative

parton model formulated by Landshoff et al [11] made the hadronic cross section scale at large Q^2 by restricting diagrams contributing to the forward amplitude to those of the form shown in figure 4.2.1.

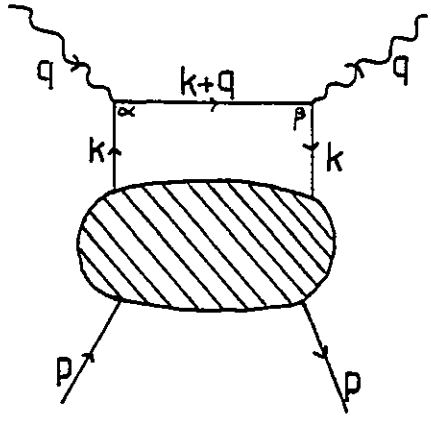

Figure 4.2.1

"BOX" OR "HANDBAG" DIAGRAM

The "blob" represented thus in  in figure 4.2.1 contains an arbitrary number of interacting partons and it comprises the parton hadron scattering part of the interaction. The parton interacting with the parton at α is knocked off its mass shell by the interaction. The postulate of the model is that the parton photon scattering amplitude tends rapidly to zero if the parton is off mass shell. This means that the parton has to remain external to the blob until it is on mass shell again (e.g. by radiating a photon at β). Any diagram that requires the struck parton to enter the blob and interact before it returns to its mass shell has zero amplitude and so does not contribute to the cross section.

If the photoproduction cross section is considered, rather than a hadronic one, the handbag diagram is still the only one which needs to be considered, provided the probing photon is heavy. However the blob now contains the possibility that the photon converts to a quark antiquark pair. In this case the coupling between the photon, quark and antiquark is pointlike, no such coupling exists between a hadron and a quark antiquark pair. Since the coupling is pointlike there is no restriction (or scale) applying to the masses involved so in this case the parton

scattering off the probe can itself be far off mass shell. The contribution to the total cross section resulting from this coupling is represented by the diagram shown in Figure 4.2.2 (and its crossed version).

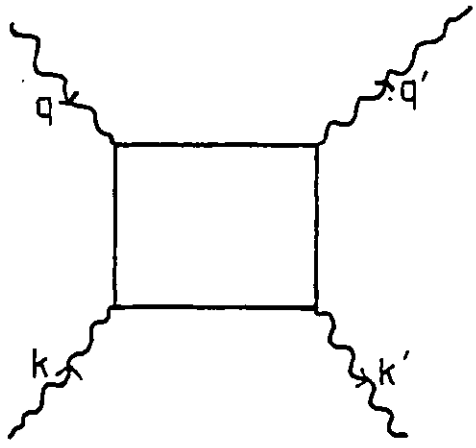

Figure 4.2.2

THE BORN TERM

The diagram shown in Figure 4.2.2 is sometimes referred to as a box diagram as before. It is also known as the Born term diagram (though strictly there are other Born terms). As might be expected the fraction of the cross section it represents can be straightforwardly calculated at least to leading order in $\ln q^2$. The related structure functions are (following normal conventions)

$$W_{L_\gamma} = \frac{\nu W}{2} W_2 - W_1$$

$$= e^4 \frac{3}{2\pi^2} \sum_{i=1}^{nf} Q_i^4 \; x \; (1 - x) \qquad (4.2.1)$$

and

$$W_{1\gamma} = e^4 \frac{3}{8\pi^2} \sum_{i=1}^{nf} Q_i^4 \; (x^2 + (1-x)^2) \; \ln \{ \frac{|q^2|}{M_i^2} \cdot \frac{(1-x)}{x} \} + O(1) \qquad (4.2.2)$$

where: the sum is over parton (quark) flavours, the colour factor having been explicitly taken out.

e is the electric charge;

Q_i is the fractional charge of the i^{th} flavour of partons;

x is the Bjorken x variable (which at high q^2 is equivalent

to the share of the photon's momentum carried by the parton).

and M_i^2 is a mass scale (the current mass squared of the interacting parton, $\sim$ (300 MeV)^2 by experiment for light (u, d) quarks).

These formulae highlight the anomalous behaviour of the point like structure functions (so called because they derive from a point like coupling). $W_{1\gamma}$ is a function of both x and q^2 and so does not scale. $W_{L\gamma}$ is non zero, therefore the pointlike structure functions violate the Callan Gross relation.

The Callan-Gross relation arises from helicity conservation at the probe parton vertex. In a frame in which they collide head on, scattering through 180^o, spin flip is ruled out by angular momentum conservation if the parton is spin $\frac{1}{2}$ and the photon has zero helicity, that is

$$\frac{\sigma_L}{\sigma_t} \to 0.0 \qquad 4.2.3$$

However in practice the transverse parton momentum k_t and its mass (m) modify this relation (4.2.3) to

$$\frac{\sigma_L}{\sigma_t} \to \frac{4(M^2 + k_t^2)}{Q^2} \qquad (Q^2 = -q^2) \qquad 4.2.4$$

In general for on mass shell partons there is little difference between 4.2.3 and 4.2.4. If the parton is formed by the $\gamma \to q\bar{q}$ subprocess however the $(M^2 + k_t^2)$ term can be significant and so the Callan-Gross relation ceases to hold for all x. As x tends to one though, the parton carries an increasing share of the photon target's helicity (cf $\gamma \to e^+e^-$). A helicity one particle cannot scatter off a helicity zero particle and so the longitudinal cross section again tends to zero.

The analogue of the box diagram in QCD is a ladder diagram (Figure 4.2.3). The strong interaction can be thought of as contributing the ladder rungs.

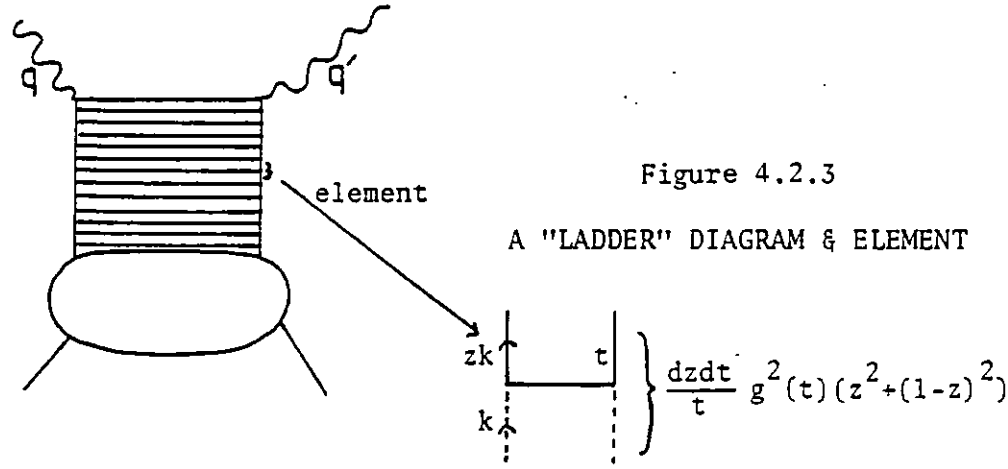

Figure 4.2.3

A "LADDER" DIAGRAM & ELEMENT

The typical elements can be calculated provided that the running coupling constant $g^2(t)$ is small enough for perturbative methods to be applicable. This means that the momenta involved have to be large in comparison to λ, the parameter scaling the coupling constant. As we go "down" the ladder towards the blob the momentum flowing around the elements decreases (so as to retain a finite parton hadron scattering amplitude) and so these elements are not calculable. Once more however the photon can couple directly to a parton and the terms in the structure function related to this can be excluded from the blob. The structure function can be written symbolically as

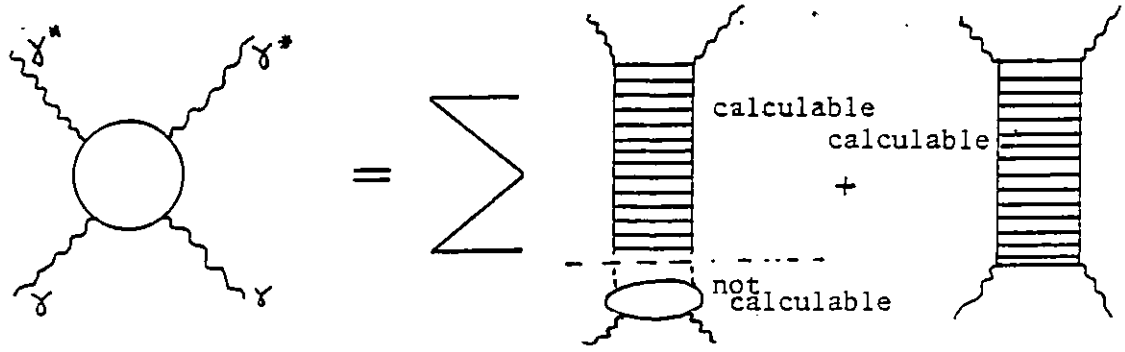

Figure 4.2.4

It is important to note that even when the photon couples directly the running coupling constant constraint applies. Since the elements of the

ladder diagram contribute terms with a $(x^2 + (1-x)^2)$ structure the form of the structure functions calculated using the box diagram is obtained.

$W_{L\gamma}$ is unchanged

$$W_{1\gamma} = e^4 \frac{3}{8\pi^2} \sum_{i=1}^{nf} Q_i^4 (x^2 + (1-x)^2) \ln\left(\frac{|q^2|}{\lambda^2}\right)$$

$$= 1.5 \times 10^{-3} e^2 \ln\left|\frac{q^2}{\lambda^2}\right| (x^2 + (1-x)^2) \qquad 4.2.5$$

We must now consider if these anomalous contributions are significant in comparison to the non-calculable hadronic terms. These are estimated in the next section.

4.3 Photon Structure Functions - Hadronic Component

The hadronic components of the photon structure functions, as their name implies, behave like hadronic structure functions, specifically, like those of a vector meson. The concept that the photon acts as if it were a superposition of vector mesons forms the core of the vector meson dominance model (VMD) which is summarised by equation 4.3.1

$$|\gamma\rangle^h = \sum_V f_V(q^2) |V\rangle \qquad 4.3.1$$

where; The superscript h denotes the fact we are considering the photon as a hadron

$f_V(q^2)$ is the vector meson-photon coupling.

and the sum is taken over all particles v for which $J^P = 1^-$, including radial excitations.

It is conventional to assume that the coupling $f_V(q^2)$ has no dependence on q^2. This allows the coupling factor measured in e^+e^- collisions at $q^2 = M_V^2$ to be identified with that appropriate to real photons($q^2 = 0$).

(Although not everyone agrees that f_v is independent of q^2[12], and sometimes the possibility of a dependence is used to explain discrepancies between the model and experiment).

The hadronic structure function is given by ($W_L \simeq 0.0$)

$$W_1^h = e^2 \sum_i Q_i^2 \cdot G_{i/h}(x, Q^2) \qquad 4.3.2$$

where; the sum is over quarks and antiquarks

and $G_{i/h}$ is the distribution function of parton i in hadron h

Equation 4.3.2 in conjunction with 4.3.1 yields

$$W_{1\gamma}^h = e^2 \sum_{vi} Q_i^2 \cdot G_{i/h}(x, Q^2)\, f_v(q^2) \qquad 4.3.3$$

where; q^2 relates to the photon target

Q^2 relates to the probe of the target's structure

In order to estimate the magnitude of $W_{1\gamma}^h$ we need to assume a form for $G_{i/h}$. If h is a vector meson counting rule arguments [13] give (neglecting Q^2 dependence)

$$G_{i/v} = \frac{1}{3} \cdot \frac{1}{2} \cdot \frac{1}{4} \frac{(1 - x)}{x} \qquad 4.3.4$$

where; the factor $\frac{1}{3}$ is due to colour

the factor $\frac{1}{2}$ comes from spin averaging

and the factor $\frac{1}{4}$ assumes that on average quarks carry 25% of the momentum of v, antiquarks 25% and the remainder is carried by gluons.

substituting for $G_{i/v}$ in 4.3.3 we obtain

$$W_{1\gamma}^h = 3\, e^2 \sum_v \sum_i Q_i^2 \frac{1}{24} \cdot \frac{(1 - x)}{x} f_v(q^2) \qquad 4.3.5$$

where the sum over colour has been done.

Gunion and Frazer [5] reduced the sum over vector mesons to include just the ρ term (the largest) in order to numerically estimate the value of 4.3.5. They used the experimental value of the ρ - γ coupling ($f_\rho = \alpha/2.2$) and obtained

$$W_{1\gamma}^{h} \sim 4.6 \times 10^{-4} . e^2 . \left(\frac{1 - x}{x}\right) \qquad 4.3.6$$

I will use 4.3.6 later in section 4 when I discuss how large $W_{1\gamma}^{h}$ is in comparison to $W_{1\gamma}^{pL}$ (using the pL superscript to denote point-like). However I feel it is worth pointing out here that the inclusive photoproduction cross section can be estimated from inclusive pion cross sections [6]. In this case the photon acts as a ρ, the ρ as a superposition of π^+ and π^-. This phenomenological estimate of the hadronic contribution can lead to predictions of hadronic contributions an order of magnitude greater than Gunion's & Frazer's. Although the pointlike contributions can be calculated (above λ^2) the hadronic contributions can only be estimated. Comparisons between the two are therefore unreliable.

4.4 The Relative Magnitude of the Hadronic and Point-like Components of the Photon Structure Functions

In section 2 the photonic structure functions were calculated from the viewpoint of deep inelastic scattering. The hadronic structure function on the other hand was estimated more directly by considering the relevant parton distribution functions. It is assumed that these approaches are equivalent i.e. that the parton distributions in a photon do not depend on the process used to study them. This allows us to directly compare 4.2.5 and 4.3.6.

If we take the ratio of $W_{1\gamma}^{h}$ and $W_{1\gamma}^{pL}$ in the limit of $x \to 1$ we

obtain relationship 4.4.1

$$\frac{W_{1\gamma}^{h}}{W_{1\gamma}^{pL}} \overset{x\to 1}{\propto} (1 - x) \qquad 4.4.1$$

This means that the dominance of the calculable part of the total structure function over the hadronic fraction can always be assured by considering a kinematic region restricted to sufficiently high x. Frequently however the contribution of the hadronic element is minimal over the entire x range.

For instance, in the case of testing the Recombination model (see section 5.4) we are interested primarily in the parton momentum distributions. This means that we are measuring the momentum moment of the structure functions. The ratio of the hadronic moment to the anomalous one is .

$$\frac{W_{1\gamma,\,m}^{h}}{W_{1\gamma,\,m}^{pL}} \approx \frac{0.5}{\ln Q^2/\lambda^2} \qquad 4.4.2$$

where; the subscript m denotes that we are taking the ratio of the momentum moments of the structure function.

As Q^2 tends to infinity the pointlike structure function is increasingly dominant. This can be understood intuitively by considering the Q^2 evolution of the hadronic structure function. The quarks in a hadron are bound together by gluons. As the distances probed inside the target become smaller, it becomes increasingly likely that any "quark" will be resolved as a quark and a gluon. Since momentum must be conserved overall the quarks "appearing" at high Q^2 will tend to have less momentum than those resolved by a low Q^2 probe. The effect of going to higher and higher Q^2 is to bunch the quarks together at low x.

The quarks produced by the photon converting to a quark-antiquark pair are bare, that is they are not accompanied by gluons. This means that the photonic structure function does not "evolve down" in the way the hadronic one does.

All the above assumes that Q^2 is larger than λ^2. Figure 4.4.1 shows how the ratio 4.4.2 changes with Q^2 for λ chosen to be 0.5 GeV. As Q^2 approaches λ^2 the ratio tends to infinity, if Q^2 is taken to be less than λ^2 the ratio has an unphysical (negative) value. This could be interpreted as meaning that the point-like component is zero if Q^2 equals λ^2. It is more likely that the calculated expression for $W_{1\gamma}^{pL}$ is no longer valid since we have entered the kinematic region in which perturbative methods can no longer be justified.

It is possible to prove $W_{1\gamma}^{pL}$ is finite in the $Q^2 = 0.0$ limit by showing that the cross section for $\gamma p \to hx$ falls off more weakly with x than would be expected if the photon behaved purely as a hadron. Counting rule arguments give

$$\frac{d\sigma}{dx}(\rho p \to hx) \propto (1 - x) \qquad 4.4.3$$

using relation 4.4.1 we can predict;

$$\frac{d\sigma}{dx}(\gamma^{pL} p \to hx) \overset{x\to 1}{\propto} (1 - x)^{\circ} \qquad 4.4.4$$

That is the point-like photon is more likely to act as a source of high x quarks than a hadron-like photon. In the next section I will consider the real photon interacting with the proton's constituents and the evidence for it not being totally vector meson dominated.

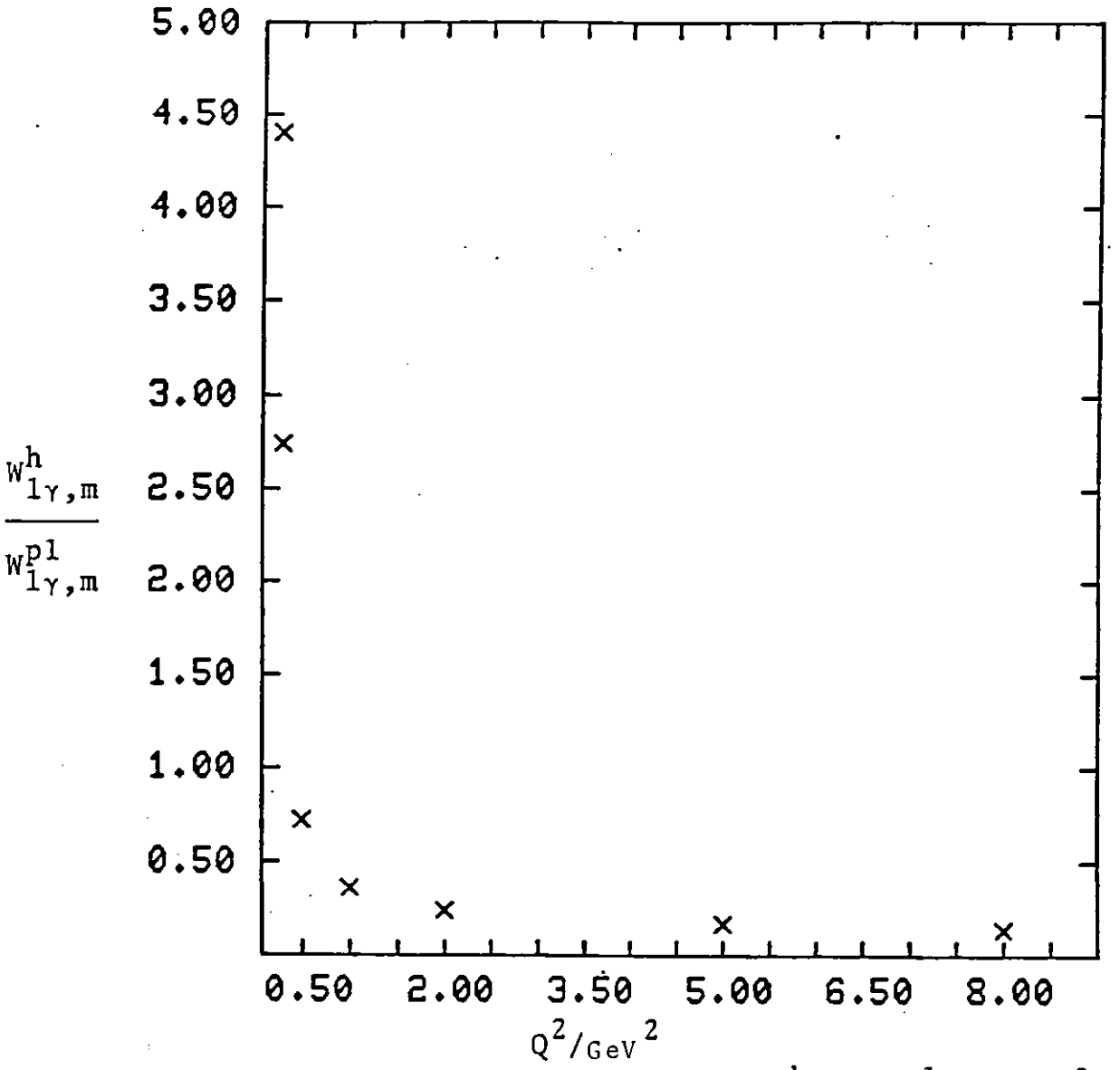

Figure 4.4.1 DEPENDENCE OF $W^{h}_{1\gamma,m}/W^{pl}_{1\gamma,m}$ ON Q^2 FOR λ=0.5 GeV

4.5 Real Photon Interactions with Protons

The total photoproduction cross-section is given by calculating the imaginary part of the forward Compton scattering amplitude. In section 4.2,it was stated that only contributions from "box" diagrams (such as Figure 4.2.1) needed to be considered when evaluating deep inelastic scattering cross-sections. This was because a high Q^2 photon would knock the parton it interacted with far off shell, and in this state it could not re-enter the "blob". This constraint does not hold when a real photon interacts with a parton, and so diagrams of the form shown in Figure 4.5.1 need to be included in the calculation.

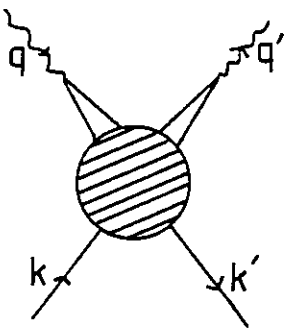

Figure 4.5.1

A "CATS EARS" DIAGRAM

The "cat's ears" diagram makes what is termed a six point contribution to the scattering amplitude; the photon interacting with the proton via a connected off shell parton-parton-proton six point function. The "box" diagram yields a four point contribution the parton propagating freely between photon interactions. This free propagation gives rise to the fact that the box diagram makes a finite contribution to the cross-section in the $q^2 \to \infty$ limit (scaling limit), whereas the six point term vanishes.

The four point diagrams cannot be vector meson dominated [10], the freely propagating parton rules out the possibility of their having poles in the photon channels. The six point diagram must contain a vector meson associated part. If we compare processes that only proceed via six point routes and involve a photon, with the equivalent six point

only vector meson incorporating process, the extent of the vector meson contribution can be estimated. One such process [10] is $\gamma p \rightarrow \rho p$ which can be compared to $\rho p \rightarrow \rho p$.

These processes can only involve six point diagrams since the partons connected to the vector meson must interact with each other if they are to be bound together. The coupling constant required experimentally if the six point diagram is to be considered 100% vector meson dominated is equal to that measured in e^+e^- experiments. The hadronic side to the photon is thus described by the "cats ears" diagram.

If we consider the reaction $\gamma p \rightarrow \gamma p$ however, both six point and four point diagrams can contribute. The six point contribution can be estimated (by applying vector meson dominance arguments) to be:-

$$\frac{d\sigma}{dt}(\gamma p \rightarrow \gamma p) = \sum_V f_V(q^2) \frac{d\sigma}{dt}(\gamma p \rightarrow Vp) \qquad 4.5.1$$

Figure 4.5.2 shows the comparison between a vector meson dominance estimate (the sum of ρ, ω and ϕ contributions) and an experimental measurement. Neither the normalisation of this estimate nor its shape fits the data well. Although the deficit in magnitude can be made up by including higher mass vector mesons in the sum, the shape is harder to change. A four point component could explain the discrepancies however because it has a different t dependence. Estimates of the size of this component make it account for about 20% of the interactions of real photons. This evidence then that the point-like photon (identified with the box diagram) contributes to the reactions of real photons with protons rules out the λ^2 cut off implied if equation 4.4.2 is taken at face value. This is reasonable since point-like couplings do not have an associated scale.

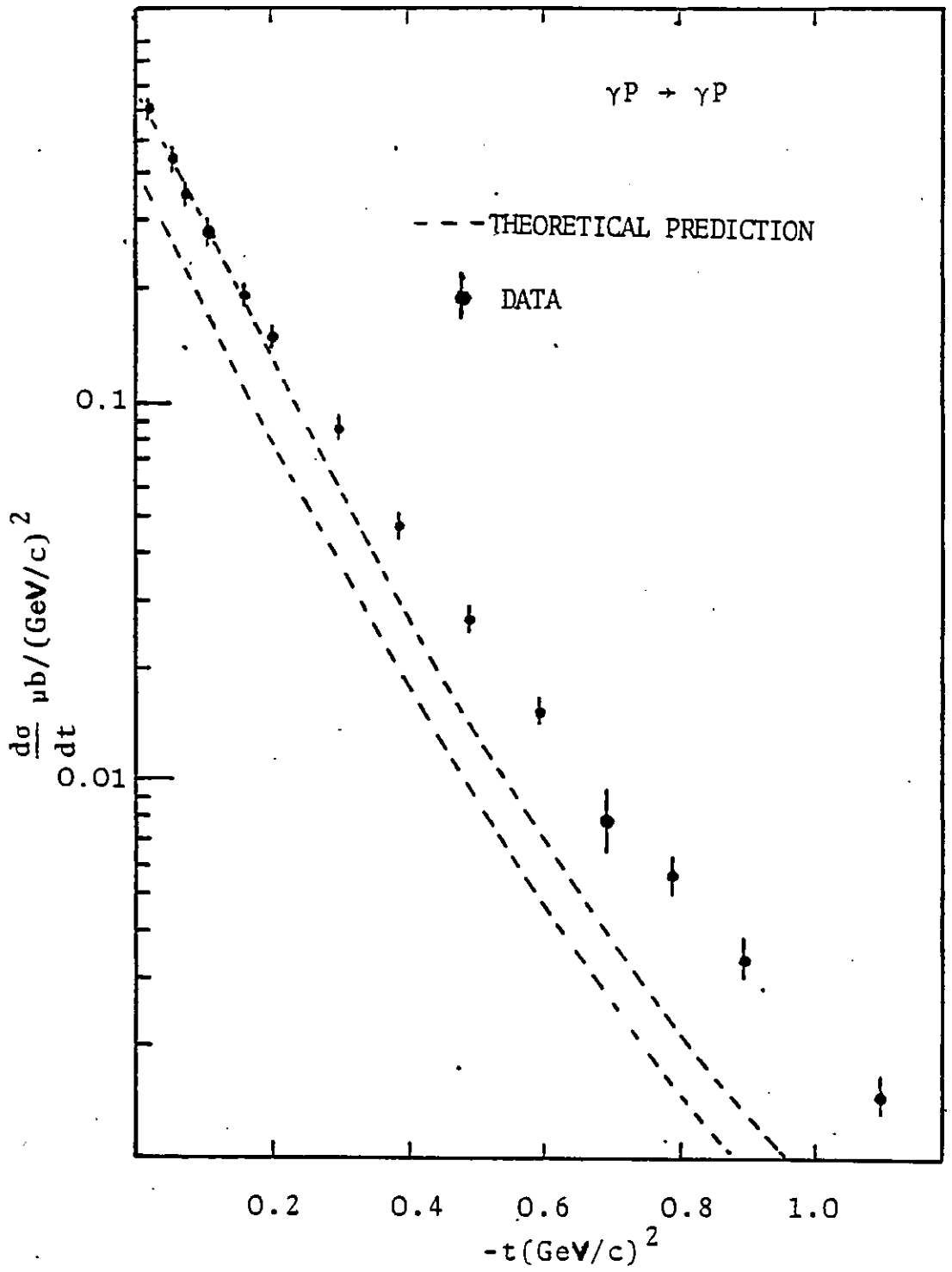

Figure 4.5.2 COMPARISON BETWEEN DATA AND VMD PREDICTION FOR COMPTON SCATTERING AT 16.6 GeV/c
(From reference 10)

The point-like interactions can be divided into those in which the photon converts into a quark antiquark pair and the bare partons interact with those of the proton, and those in which the photon directly couples to a parton in the proton (the QCD Compton effect). The QCD Compton effect can be largely separated out from the other types of interaction of the photon. In the leading logarithm approximation the contribution it makes to the inclusive cross-section can be written;

$$E\frac{d\sigma}{dt}(\gamma p \to hx) = \frac{1}{\pi}\sum_{\alpha}\int dx\, dz\, G_{\alpha/p}(x, Q^2)\, \hat{s}\frac{d\sigma}{dt}(\gamma\alpha \to \alpha X) \times \frac{D_{\alpha}^{h}}{z^2}(z)\, \delta(\hat{s} + \hat{t} + \hat{u}) \qquad 4.5.2$$

where; the sum is over the parton types found in the proton.

$\hat{s}, \hat{t}, \hat{u}$ are the Mandelstam variables for the subprocess $\gamma\alpha \to bc$

$G_{\alpha/p}$ is the function which describes the distribution of α in the proton

$D_{\alpha}^{h}(z)$ is the fragmentation function giving the likelihood of forming a hadron h with fraction z of the momentum carried by parton b

and $$\frac{d\sigma}{dt}(\gamma q_i \to q_i g) = [\tfrac{4}{3}]\, 2\pi e^2 \alpha\, \alpha_s(Q^2).\frac{Q_i^2}{\hat{s}^2}\cdot(-\frac{\hat{t}}{\hat{s}} - \frac{\hat{s}}{\hat{t}}) \qquad 4.5.3$$

where; [ ] term is a colour factor

$\alpha_s(Q^2)$ is the strong coupling constant

Q_i^2 is the fractional charge squared carried by quark type i.

The fragmentation functions are well established only for quarks, the distribution functions only for valence quarks. However, as pointed out by Fontannaz et al [6], if one defines a quantity

$$\Delta^{\pi}(p) = E\frac{d\sigma}{dp}(\gamma p \rightarrow \pi^{+}x) - E\frac{d\sigma}{dp}(\gamma p \rightarrow \pi^{-}x) \qquad 4.5.4$$

then $\Delta^{\pi}(p)$ is independent of terms involving unknown distributions.

This is because the point-like photon coupling to a quark (or anti-quark) depends only on the quark charge squared. The contributions to the pion cross-sections arising from the photon interacting with the sea cancel each other; the photon is as likely to couple to a u sea quark as to an anti-u sea quark, for example.

The photon-valence quark scattering however does not contribute equally to both the positive and the negative cross sections. Not only is the photon four times as likely to couple to a u valence quark as a d quark because of their relative charges but there are also twice as many u valence quarks as d valence quarks in the proton. This yields a factor of eight, overall, between the probabilities of the photon coupling to a u quark or to a d quark. Since the u quark is more likely to fragment or combine into a positive pion than a negative one $\Delta^{\pi}(p)$ will be non zero. The hadronic interactions of the photon have a weaker charge coupling and should not mask the symmetry.

4.6 Summary

There are three basic ways that the photon can interact.

α)

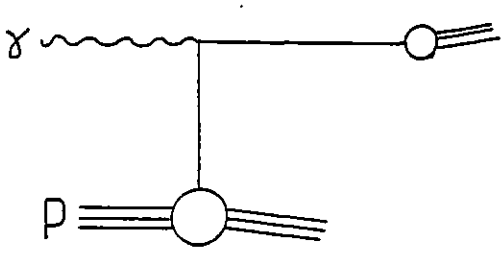

It can couple directly to a charged constituent of the proton;QCD Compton Effect (Gauge boson/point-like)

β)

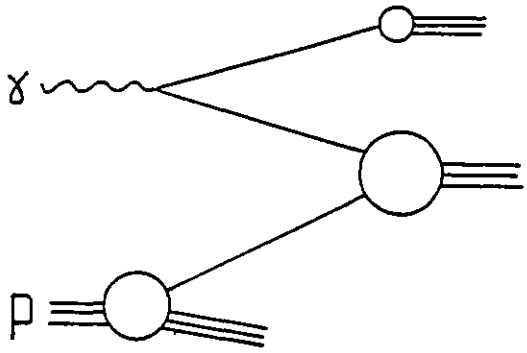

It can convert to a quark antiquark system. A bare quark (antiquark) then interacts with dressed proton constituents (point-like).

γ)

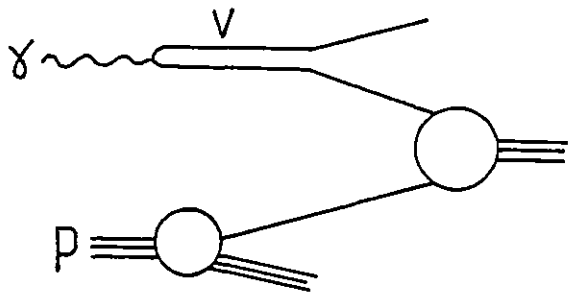

It acts as a vector meson and supplies dressed quarks to the interaction region

(hadronic)

(A dressed quark is one which is accompanied by gluons near to it in rapidity space).

Short range interactions (such as high P_t scattering) will reveal the photon as point-like more frequently than they highlight its hadronic behaviour. This is a consequence of the fact that the photonic (anomalous, pointlike) structure function dominates the hadronic one at high Q^2 (sections 4.2 - 4.4).

At low q^2 the situation is less clear because perturbative methods cannot be used to calculate the point like structure functions. However approaches based on the parton model indicate that the photon does not only interact as a vector meson (sections 4.4 - 4.5).

The QCD Compton effect can be studied by looking at the difference between positive and negative pion (or kaon etc) inclusive cross sections, because of asymmetries resulting from the charged squared nature of the coupling (section 4.5).

The point-like photon is more likely to be a source of quarks at

high x than a hadronic one. This will cause the slope predicted for the inclusive cross sections to decrease at high x (section 4.4).

CHAPTER 4 - References

[1] S.J. Brodsky, T. Kinoshita, and H. Terezawa; Phys. Rev. Lett. 27, 280 (1971)

[2] E. Witten; Nucl. Phys. B120, 189 (1977)

[3] C.H. Llewellyn Smith; Phys. Lett. 79B 83(1978)

[4] R.J. DeWitt, L.M. Jones, J.D. Sullivan, D.E. Willen, and H.W. Wyled Jr; Phys. Rev. D19, 7, 2046 (1979)
Phys. Rev. D20, 1751 (1979) (modified calcs.)

[5] W.R. Frazer and J.F. Gunion; University of California preprint, UCD-78-5, UCSD-10P10-199

[6] M. Fontannaz. A. Montrach, D. Schiff, and B. Piré; Zeit. Phys. C6, 241 (1980)

[7] J.F. Owens; Phys. Rev. D21, 54 (1980)

[8] T.F. Walsh and P. Zerwas; Phys. Lett. 4 B, 195 (1973)

[9] J.F. Gunion; SLAC-PUB-2503

[10] S.J. Brodsky, F.E. Close, and J.F. Gunion; SLAC-PUB-2012

[11] P.V. Landshoff, J.C. Polkinghorne, and R. Short; Nucl. Phys. B28, 255 (1971)

[12] A. Bradley, and F.D. Gault; Nucl. Phys. B128, 313 (1977)
D. Sivers, J. Townsend, and G. West; Phys. Rev. D13, 1234 (1976)

[13] S.J. Brodsky, T.E. de Grand, J.F. Gunion and J. Weis; Phys. Rev. Lett. 41, 672 (1978).

CHAPTER 5

INCLUSIVE PHYSICS AT LOW P_t

5.1 Introduction

Any theory of inclusive hadroproduction should be capable of explaining two experimental observations made by Ochs[1]:-

i) Particle/Antiparticle ratios show similar behaviour as a function of $x_{\parallel}$ (fraction of the maximum possible momentum a track can carry which is actually carried by the hadron along the beam axis) for both large and small scattering angle data, provided that leading particle effects are discounted. The hadronic yield at all angles reflects the quantum numbers carried by the incoming particles.

ii) The cross section $\frac{d\sigma}{dx_{\parallel}}^{(pp\to\pi^{+}x)}$ has the same dependence on $x_{\parallel}$ as $U^{p}(x)$ (i.e. as the u quark distribution function in the proton as derived from deep inelastic scattering results), the distributions both having a $(1-x)^{3}$ dependence.

In general, the low and high P_t regimes have different signatures (for example, the single particle inclusive cross section falls off much more rapidly with increasing $x_{\perp}$ than it does with increasing $x_{\parallel}$) and hence tend to be described by different types of models. The models concerned with low P_t data are often Regge based, those describing high P_t data are usually related to the Parton Model.

The fact that the particle ratio results are independent of P_t suggests however that both types of data can be used to probe hadron structure and implies the existence of a model applicable at any P_t. It may even be argued that the low P_t data relates more directly to hadron structure and to the Parton Model than high P_t data because it involves less complex processes. The effects due to the primordial P_t

of the interacting partons can be neglected and there are no hard subprocesses to give rise to uncertainties.

A particular class of simple models of particle production is immediately ruled out by Och's observations. Not all particle-antiparticle ratios are independent of angle. Leading particle effects are seen in, for example, the dependence of the proton-antiproton ratio on angle in proton proton scattering. This dependence rules out models (including bremsstrahlung models) which proceed via the decay of an excited state (e.g. a proton, in proton proton scattering).

The favoured models all involve a constituent (or constituents) of the hadron which carries some of its momentum, the remaining constituents being incorporated into the leading particle. The scattering of constituents of unequal momenta off the target leads to the slight dependence on angle seen in the data.

Any model which seeks to describe particle production in strong interactions must correctly predict the behaviour of the inclusive pion cross sections which are produced by proton-proton collisions. Models involving the decay of a single quark yield cross sections which are proportional to $D_q^{\pi}(x)$, the quark to pion fragmentation function. A quark decay into a pion must involve the quark losing energy, e.g. by radiating a gluon. The produced pion therefore has less energy than its quark parent and hence the x distribution of the pions is biased towards lower values of x than that of the parent quark. Since the parent quark for π^+ production is most likely to be a u-valence quark, decay models require the differential cross section to fall off more strongly than $U_v^p(x)$, and so do not agree with experiment.

There are models at present which do predict the correct dependence on x for $\frac{d\sigma}{dx}^{(pp\to\pi X)}$. These can be divided into three groups;

the Dual models [2] which involve Regge type postulates, the gluon exchange based models [3], and the Recombination models [4]. The Valon model [5] is closely related to those in the Recombination model group and will be considered as a development within that group. In as much as the photon acts as a hadron any successful description of hadroproduction should also succeed in describing photoproduction. However, as discussed in the preceeding chapter, the photon can also interact directly as a gauge boson. This component of the photon's behaviour can be treated more quantitatively than the hadronic component. It enables firmer forecasts to be made in kinematic regions in which the point-like behaviour is dominant than in others and Recombination model theorists have attempted to exploit this fact in making testable predictions.

5.2 Recombination Models

All Recombination models assume that meson production (at least at high X_F) results from the association of a fast valence quark (or antiquark) with a slow sea antiquark (or quark). Baryon production is more complex and may proceed via a diquark. The recombination is (explicitly or implicitly) assumed to occur between quarks and antiquark travelling in the same direction, this usually being interpreted as a requirement that they come from the same incident particle.

In fact it is probably more accurate to say that the recombination mechanism requires that the valence quark forming the hadron has an associated gluon cloud which travels along with it and which acts as a source for the antiquark (this implies that the quark is dressed and has the characteristics of a valon). This viewpoint explains why the recombination mechanism is initially inoperative in e^+e^- annihilation and in high P_t processes. The quarks produced in such processes are

far off mass-shell and bare (they lack gluons nearby in rapidity). Once these high Q^2 quarks fragment into low Q^2 quarks and gluons they can then hadronise via recombination.

More quantitatively, Recombination models assume that the single meson differential cross section can be expressed as follows;

$$\frac{x_o}{\sigma_T}\frac{d\sigma^M}{dx_F} = \int dz_1\, dz_2\, f_{q_1\bar{q}_2}(z_1, z_2)\, R_{q_1\bar{q}_2}(z_1, z_2, x_F) \qquad 5.2.1$$

where; $R^M_{q_1\bar{q}_2}(z_1,z_2,x_F)$ is the quark-antiquark recombination function
This gives the probability that a quark (fractional momentum z_1) will combine with an antiquark (fractional momentum z_2) to yield a meson, M, with fractional momentum x_F.

$f_{q_1\bar{q}_2}(z_1,z_2)$ is a two quark structure function, i.e. it gives the probability density for finding (independently) quarks and antiquarks with the specified momentum fractions.

The several versions of Recombination models which are phenomenologically successful differ from each other mainly over the choice of assumptions made in deriving a two quark structure function. The form of the recombination function is essentially the same for all models and is much more easily justified. $R^M_{q_1\bar{q}_2}$ is usually broken down into two parts;

i) $R^M_2(\xi_1, \xi_2)$

and

ii) $R^M_x(\xi_1, \xi_2)$

where $\xi_1 = \frac{z_1}{x_F}$ and $\xi_2 = \frac{z_2}{x_F}$

Scale invariance is therefore assumed. R_2^M gives the probability that only the appropriate valence quarks needed to form the meson, M, recombine. R_x^M gives the probability that in addition to the recombination of the valence quarks gluons and quark-antiquark pairs are incorporated into the system to form a sea. R_χ^M, which specifies the probability of a much more complex process than R_2^M, is therefore expected to be negligible in comparison to R_2^M, and so is usually ignored.

The general expression for the dominant component of the recombination function is;

$$R_2^M(\xi_1, \xi_2) = \alpha_M \xi_1^a \xi_2^b \delta(\xi_1 + \xi_2 - 1)\delta_{M;q_1\bar{q}_2} \qquad 5.2.2$$

where, α_M is a scale normalisation factor

and a, b may be fractional

The first delta function in equation 5.2.2 guarantees that momentum is conserved in the process, the second (frequently omitted) controls the types of quarks involved.

α_M is constrained by a sum rule to be less than or equal to six since

$$1 = \int_0^1 dz_1 \int_0^1 dz_2 \, R^M_{q_1\bar{q}_2}(z_1, z_2, x_F) \qquad 5.2.3$$

a and b are usually both chosen to have value one. Qualitatively this is the most reasonable decision that can be made since valence quark distributions in mesons depend on $(1 - x)^1$ (by dimensional counting rule arguments). R_2^M defines the interaction range (in rapidity space) of the recombination mechanism. Reducing the power to which ξ_1 and ξ_2 are raised increases the range of the interaction. Ultimately the differential cross section (equation 5.2.1) will become divergent at small x because of the effects of the wee parton sea. It is worth

noting that in deriving equation 5.2.1 it is implicitly assumed that the interaction is short range because the impulse approximation must be valid.

Although two body recombination is considered to dominate over more complex processes in initiating meson production, the final state meson cannot consist merely of valence quarks. A redistribution of momenta between gluons and sea quarks in the central region of the interaction space and the emerging final state mesons at its extremes is needed. The difficulties involved in specifying a mechanism for this redistribution are removed by assuming that the two bodies involved in the recombination are not valence quarks but are valons.

A valon consists of a valence quark core, this core being dressed by virtual QCD processes which effectively surround it by a cloud of gluons and quark-antiquark pairs. The structure of this cloud can only be resolved by a probe of Q^2 greater than Q_o^2, where Q_o^2 defines the scale of the structure. Below this value of Q^2 a probe investigating the valon cannot distinguish it from a constituent quark. Although an early attempt to replace valence quarks with valons gave an unsymmetric recombination function [6] (because only one of the two quarks was dressed, the dressed quark only having gluons in the surrounding cloud and being termed a "chameleon" quark because it could easily change colour) the present Valon model gives the same form for R [6] as the early recombination models assumed, that is;

$$R^{M}_{q_1\bar{q}_2}(\xi_1, \xi_2) = 1.\ \xi_1\ \xi_2\ \delta(\xi_1 + \xi_2 - 1)\ \delta_{M;q_1\bar{q}_2} \qquad 5.2.4$$

In order to make firm predictions however which can be tested experimentally it is necessary to be as sure of the form the two quark structure function takes as one is of that of the recombination function. The simplest assumption that can be made is that the

recombining quarks and antiquarks are uncorrelated if kinematic constraints are ignored. Das and Hwa [4] argue that this is a reasonable assumption since the motivation behind the model requires that one quark carries the majority of the momentum of the final state and that the other (usually a sea) quark carries very little. They adopt a factorizable form for $f_{q_1\bar{q}_2}$, namely,

$$f_{q_1\bar{q}_2}(z_1,z_2) = f_{q_1}(z_1)\ \rho(z_1,z_2)\ f_{\bar{q}_2}(z_2) \qquad 5.2.5$$

where, $f_{q_1}(z_1)$, $f_{\bar{q}_2}(z_2)$ are single quark/antiquark structure functions and $\rho(z_1,z_2)$ is a phase space factor.

Das and Hwa chose to make the phase space factor vary linearly with $(1-z_1-z_2)$, Van Hove [7] on the other hand assumed there was no dependence on $\rho(z_1, z_2)$.

Another approach derives the two quark structure functions within the framework of the Kuti-Weisskopf [8] model. This model postulates that;

i) Valence quarks are distinguishable;

ii) Sea quarks are indistinguishable and are distributed statistically (obeying Poisson statistics);

and iii) Total momentum is conserved.

In this model any multiquark structure function is expressed as a sum of the products of primitive quark structure functions with a correlation function, the sum extending over all combinations of valence and sea quarks, together with a combinatorial factor to account for the identical nature of the sea quarks. Correlations arise because of momentum conservation and specify the reduced momentum available to the remaining partons not incorporated into the multiquark structure function. Since the sea quarks obey Poisson statistics, only the valence

quarks determine the correlation functions. Details of the calculation can be found in reference nine. The answer obtained is similar to that of Das and Hwa but substitutes primitive structure functions for the single quark structure functions of equation 5.2.5. The assumption that the quarks are uncorrelated restricts the applicability of the model to valence-sea or sea-sea recombinations.

Which ever approach is used at some point an ansatz must be used to substitute definite expressions for the structure functions. This process by its very nature introduces arbitrary parameters into the equations which are usually justified after the event if the calculations prove successful. Some theorists accept such ad hoc methods for calculating single particle inclusive distributions, using these to fix the parameters needed to calculate two particle inclusive distributions. Chang and Hwa [10] have pointed out however that if a photon beam is used the two quark structure function is calculable (at least over some x_F range).

5.3 The Two Quark Structure Function in Photoproduction

As was discussed in chapter four the structure function associated with the point-like behaviour of the photon is exactly calculable. This structure function determines the distribution of quarks and anti-quarks within the point-like photon. By analogy with equation 4.3.2 and using the notation of chapter four;

$$W_{l\gamma}^{pL} = 2 \cdot \sum_i e^2 Q_i^2 \, G_{i/\gamma}(x, Q^2) \qquad 5.3.1$$

(the sum being taken over quark flavours)

Chang and Hwa showed that the two quark structure function could be written as;

$$F^{\gamma}_{q_1\bar{q}_2}(z_1,z_2,Q^2) = z_1 z_2\, G^{\gamma}_{q_1\bar{q}_2}(z_1,z_2,Q^2) \qquad 5.3.2$$

where $G^{\gamma}_{q_1\bar{q}_2}$ specifies the evolution of the initial quarks found in the photon into those required to form the final state meson.

Full details of the calculation of equation 5.3.2 are given in reference ten. It is worth noting however that to calculate $G^{\gamma}_{q_1\bar{q}_2}$ requires a knowledge of the quark decay functions as well as of the quark distribution functions. The quark decay functions give the probability that a quark q_i will radiate something and become q_1 with momentum fraction z_1 for example. Two cases can be distinguished; one in which one quark or antiquark produces both of the final state valence quarks, and one in which two different quarks are needed to produce the final state quarks. The first case corresponds to particle production by quark dissociation or fragmentation, the second yields final state spectra much more closely related to those of the initial quarks. The second type of mechanism was thus assumed by Chang and Hwa to be occurring before recombination took place.

The Q^2 dependence introduced into equation 5.3.2 takes the form of an explicit multiplicative factor of $\log Q^2/\Lambda^2$ and reflects the dependence of the structure function on Q^2. Figure 5.3.1 shows the values of $F^{\gamma}_{q_i\bar{q}_2}(x_1x_2)$ calculated by Chang and Hwa. Figure 5.3.2 shows their prediction for the inclusive cross section of photoproduced pions.

5.4 Testing the Recombination Model

The calculations discussed in section 5.3 apply only to the direct production of pions which have their origins in a point-like photon. No account was taken of contributions to the overall cross section from resonance decay, from the interactions of hadron-like photons or from

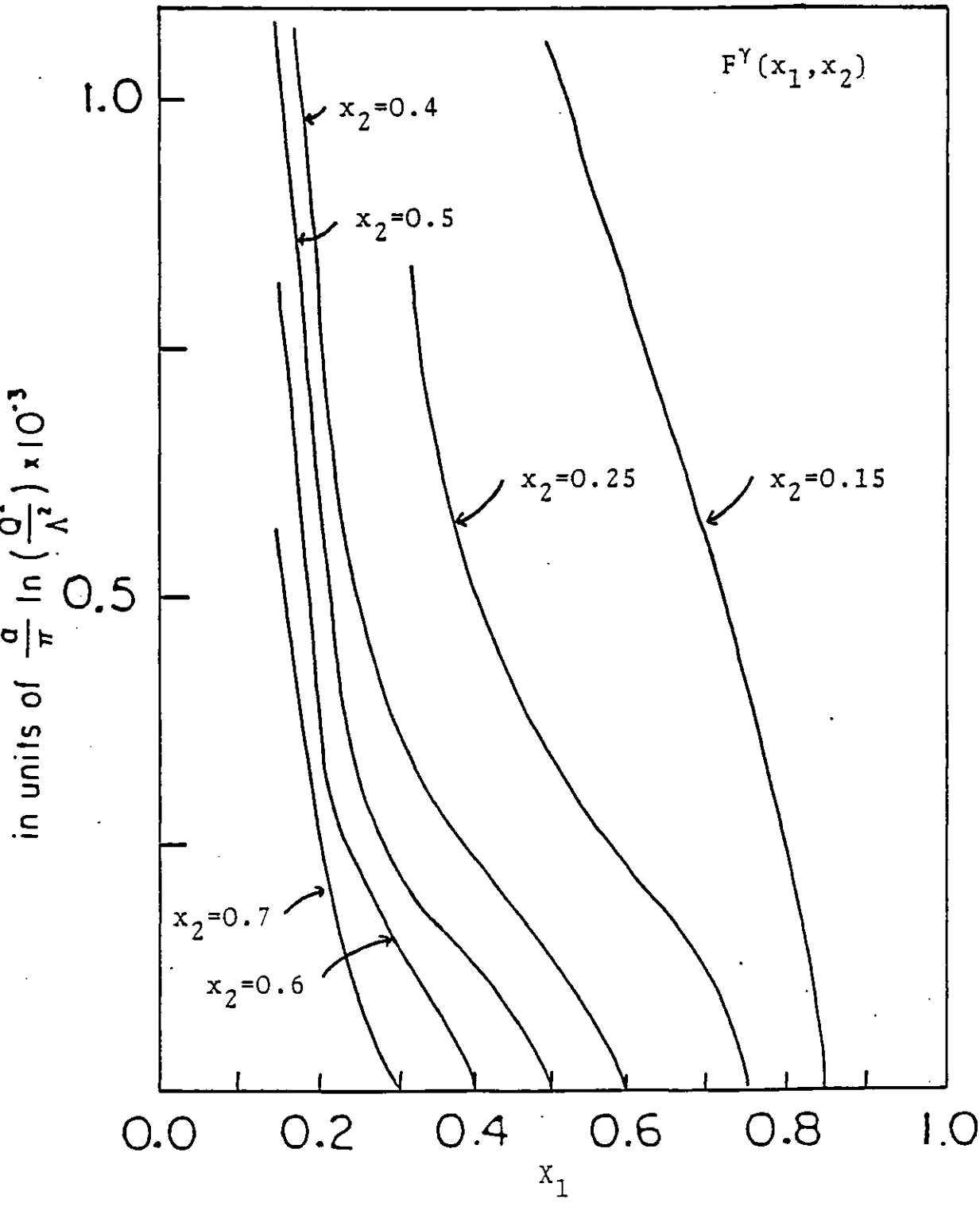

Figure 5.3.1 TWO PARTON DISTRIBUTION $F^{\gamma}(x_1,x_2)$ IN A PHOTON PLOTTED IN UNITS OF $(\alpha/\pi)\text{LOG}(Q^2/\Lambda^2)\times10^{-3}$

(From reference 10)

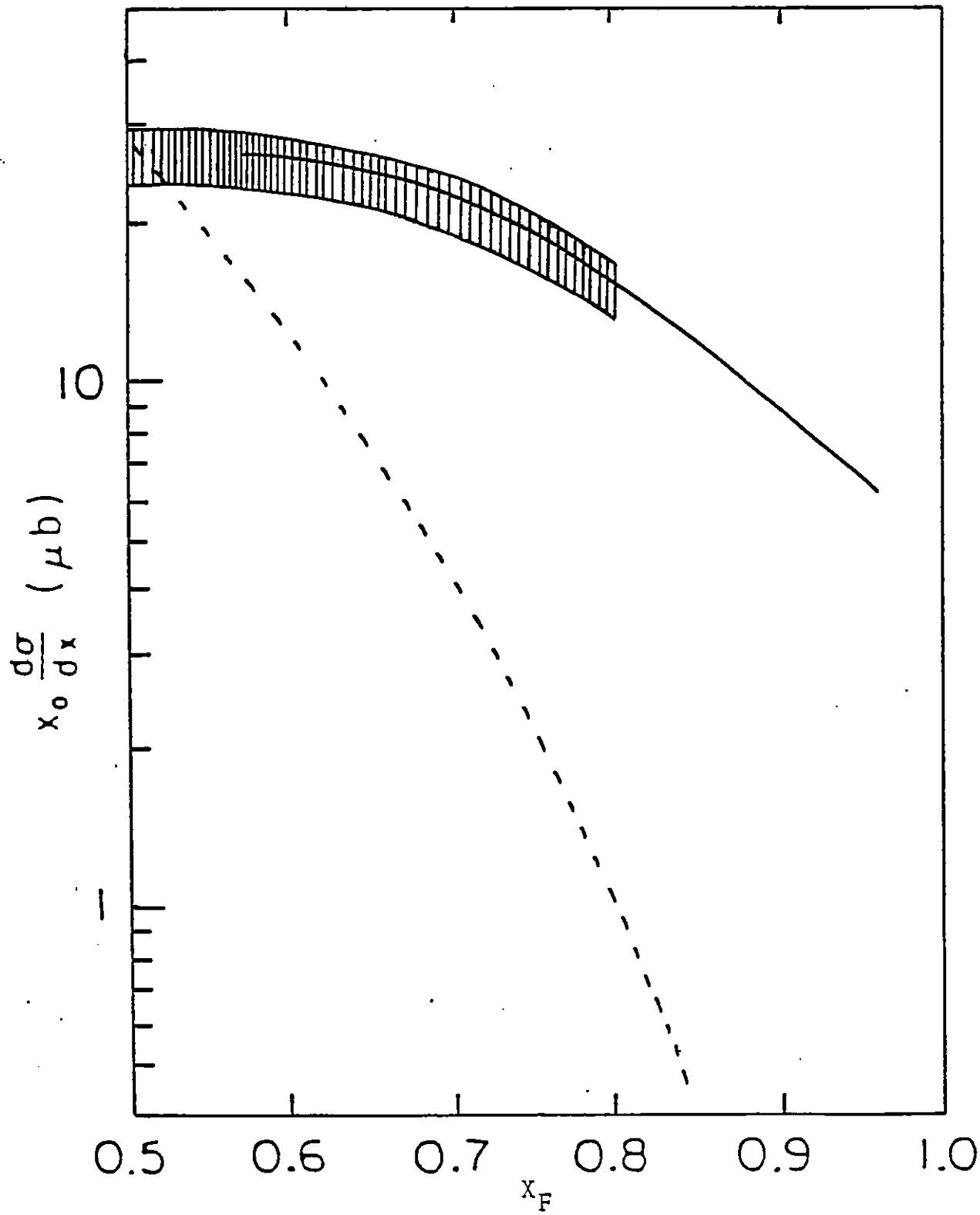

Figure 5.3.2 INCLUSIVE CROSS SECTION OF PHOTOPRODUCED PIONS.DATA (SHADED BAND) CORRESPOND TO AN EARLIER PHOTOPRODUCTION EXPERIMENT AT 18.0 Gev. SOLID LINE IS CALCULATED CROSS SECTION FOR THE RECOMBINATION PROCESS NORMALISED TO FIT THE DATA.THE DASHED LINE GIVES THE RESULT FOR THE QUARK FRAGMENTATION PROCESS.
(From reference 10)

pion production by any other mechanism. To test the predictions of the model therefore the calculable component of the cross section must be isolatable, and for this reason Chang and Hwa restricted their studies to the high X_F region.

Earlier papers on inclusive production at high P_L concluded that any mesons formed through the decay of a single quark would populate the low X_F region and so quark fragmentation could be neglected in the beam fragmentation region. An experimental justification for this is found in Ochs'observations that inclusive spectra fall off too gently at high X to be produced by a decay mechanism.

Pions produced by resonance decay tend to carry less momentum than the directly produced parent resonance. Such pions will tend therefore to populate a lower X_F region than directly produced pions. It is only valid to argue that such pions can be discounted however if the resonance itself is produced in the central region, the argument increasing in validity with increasing multiplicity of decay products. In photo-production however the resonances involved are frequently diffractively formed vector mesons which carry most of the beam's momentum. Figure 5.4.1 shows the fractional contribution to the overall X_F distribution for three prong tracks of particles consistent with being pions which are produced by rho meson decay. They do not contribute to the low X_F region. However it is still possible to subtract the effects of such decays from the overall cross section (by removing pions which are used in obtaining a rho fit or more drastically by taking out any event of the type $\gamma p \rightarrow X^+X^-p$ which could have had a rho in the intermediate state).

The main difficulty involved in believing that agreement between the model's predictions and experimental measurements is the result of

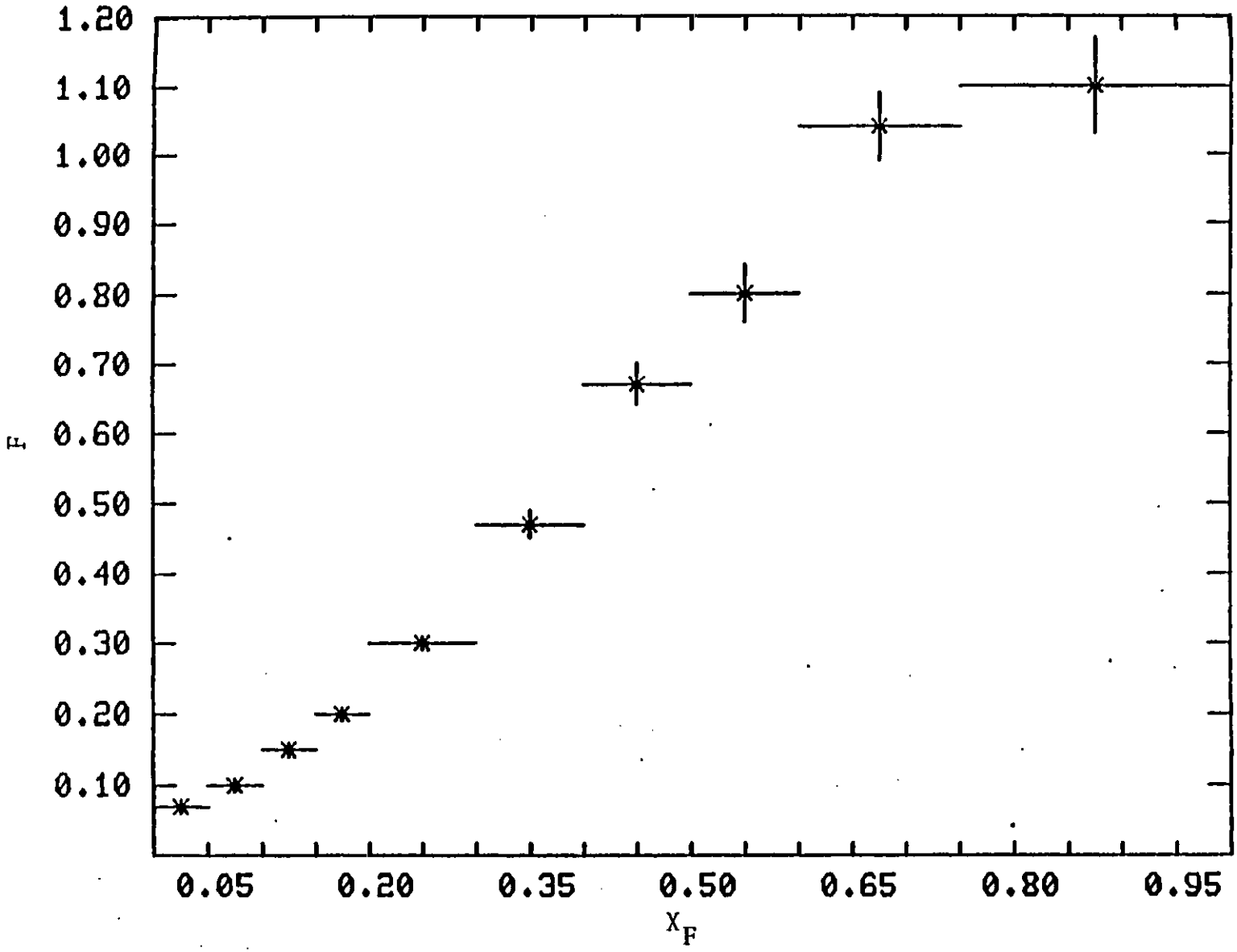

Figure 5.4.1 RATIO,F,OF NUMBER OF PION TRACKS FROM RHO DECAYS PRODUCED AT A PARTICULAR X_F COMPARED TO NUMBER OF TRACKS FROM THREE PRONG EVENTS NOT YIELDING A RHO FIT

the model being correct is that the comparison is only meaningful if the photon acts as a point-like particle. Chang and Hwa assumed that the results of Frazer and Gunion, obtained for Q^2 as low as 1.5 $(GeV/c)^2$, which showed that the point-like component was dominant by an order of magnitude above $X_F = 0.6$ could be taken as evidence that the point-like component remained dominant even in low P_t processes. However as I discussed in section 4.4 it is unreasonable to push the theoretical predictions to this limit.

There is some evidence (see section 4.5) for a point-like photon in this kinematic region however and I believe it is still useful to compare the predictions to experiment (good agreement was obtained with data from an 18 GeV/c bremstrahlung photon beam counter experiment). The importance attached to the result should depend on whether or not supporting evidence for the pointlike nature of the photon is found using the same data. Some effects of an anomalous component of the photon wave function are discussed in sections 4.4 and 4.5. Perhaps the most direct way of searching for a point-like photon, though, is to search for the inclusive symmetry frame.

5.5 The Symmetry Frame In Inclusive Physics

The ideas behind looking for a frame of reference (usually called the R-frame or Q-frame) in which inclusive particle distributions are symmetric became popular about a decade ago [11]. The expectation is that in this frame, the interacting constituents of the beam and target carry equal and opposite momenta, and that by finding this frame the ratio of the number of interacting constituents in the beam and target particles can be estimated. For this purpose it is convenient to differentiate between frames of reference in terms of the ratio, Q, of the target particle's momentum to that of the beam particle

as measured in a particular frame. Q equals one, for example, denotes the centre of mass frame, Q equals zero the laboratory frame (in fixed target physics).

In order to interpret the Q value specifying the symmetry frame in terms of the number of interacting components in the system, it is necessary to assume that all the interacting constituents in the beam particle share its momentum equally, and, likewise, so do those in the target particle. We can then calculate the ratio of the number of interacting particles as follows:-

$$Q = \left| \frac{\vec{P}_{target}}{\vec{P}_{beam}} \right| \qquad 5.1$$

$$= \left| \frac{\sum_{i=1}^{n} \vec{P}_{i,ct}}{\sum_{j=1}^{m} \vec{P}_{j,cb}} \right|$$

where; n is the number of target particle constituents of momentum $\vec{P}_{i,ct}$

and m is the number of beam particle constituents of momentum $\vec{P}_{j,cb}$

Since however the constituents share the momentum of the whole

$$Q = \left| \frac{n\vec{P}_{i,ct}}{m\vec{P}_{j,cb}} \right|$$

And since in the symmetry frame;

$$\vec{P}_{i,ct} = -\vec{P}_{j,cb}$$

we obtain finally that $Q = \frac{n}{m}$ 5.2

A Q value of one then for the symmetry frame implies that the beam and target particles both contain the same number of interacting constituents. If a value of greater than one is obtained for Q then this means that the target contains more constituents than the beam.

If the photon interacts as a hadron then one would expect Q to be 1.5 [12] (assuming that the interacting constituents are valence quarks). Alternatively if the photon interacts as a single point-like particle then values of Q nearer to three will characterise the symmetry frame. The value of Q actually found experimentally should therefore give a clue as to the presence or absence of interactions in which the photon is not acting as a vector meson.

If the concept of a symmetry frame is valid then any type of distribution studied should give the same value of Q, since only one frame can exist (for a given type of interaction) in which equation 5.2 is valid. However the difference in the kinematical regions stressed by various distributions may cause some apparent variations. For example consider the difference between studying the longitudinal momentum distributions and studying the rapidity distributions of photoproduced pions. The former emphasises data in the fragmentation zones (that is the momentum of particles which are carrying a substantial fraction of the momentum of the beam or target particles and which are interpreted as originating from either the beam or the target particles). The latter emphasises data in the central region (the rapidity of particles of low energy, not associated kinematically with either the beam or the target). Both distributions are studied in chapter seven.

Chapter 5 - References

[1] W. Ochs; Nuclear Physics B118, 397 (1977)

[2] - [4] The papers given below are typical representatives of their type rather than an exhaustive list.

J.F. Gunion; SLAC-PUB-2607 (1980) is a good review of all candidate models and contains many further references.

[2] B. Andersson, G. Gustafson & C. Peterson; Phys. Lett. 69B 221 (1977)

[3] J.F. Gunion; SLAC-PUB-2491 (1980)

[4] M.J. Teper, RAL preprint, unpublished RL-78-022/A reviews the models, K.P. Das and R.C. Hwa; Phys. Lett. 68B, 459 (1977) is probably the most important paper on the subject.

[5] R.C. Hwa; Phys. Rev. D22 759 (1980)

[6] V. Chang and R.C. Hwa; Phys. Rev. Lett. 44, 439 (1980)

[7] L. Van Hove; CERN report Th-2628 (1978)

[8] J. Kuti and V.F. Weisskopf; Phys. Rev. D4, 3418 (1971)

[9] E. Takasugi, X. Tata, C. Chiu and R. Kaul; Phys. Rev. D20, 211 (1979)

[10] V. Chang and R.C. Hwa, Phys. Lett. 85B 285 (1979)

[11] ABBCCHLVW collaboration; Nucl. Phys. B46. 371 (1972)

[12] V.V. Anisovich and V.M. Shekhter, Nucl. Phys. B55 455 (1973)

CHAPTER 6

EXPERIMENTAL BIASES

6.1 Difficulties Involved in Using the Centre of Mass Frame

Although one of the tenets of relativity theory is that there is no preferred inertial frame of reference, high energy physics results are commonly presented in the centre of mass frame of the beam and target particles. Boosting quantities measured in the laboratory frame to the centre of mass frame requires (for a fixed target experiment) a knowledge of the beam's four momentum. Although the energy spectrum of the photon beam used in this experiment is known, the energy of an individual interacting photon can only be deduced if the momenta of all the particles produced in the interaction are known. If there are no missing neutrals the beam's momentum can be calculated but otherwise only lower limits can be found. This section discusses the effect of assuming a nominal energy for all the interacting photons.

One of the more important inclusive distributions is that of the Feynman $X(X_F)$ of produced tracks. If P_L^* is the longitudinal momentum of a track in the centre of mass frame, and s is the invariant mass squared of the initial system, then the X_F of the track is defined thus

$$X_F = \frac{2P_L^*}{\sqrt{s}}$$

It can be shown (see Appendix B) that the systematic shift in the calculated value of X_F which results from assuming a nominal beam energy is not a linear function of the difference between the true and the assumed beam energies. The X_F of a track is underestimated more for events due to photons with an energy ΔE below the nominal value, than it is overestimated for events caused by photons with an energy ΔE above the nominal value. This is illustrated by Figure 6.1.1 which is a plot of the ratio of the shifts resulting when calculating X_F for a particular track, given true beam energies equidistant above and

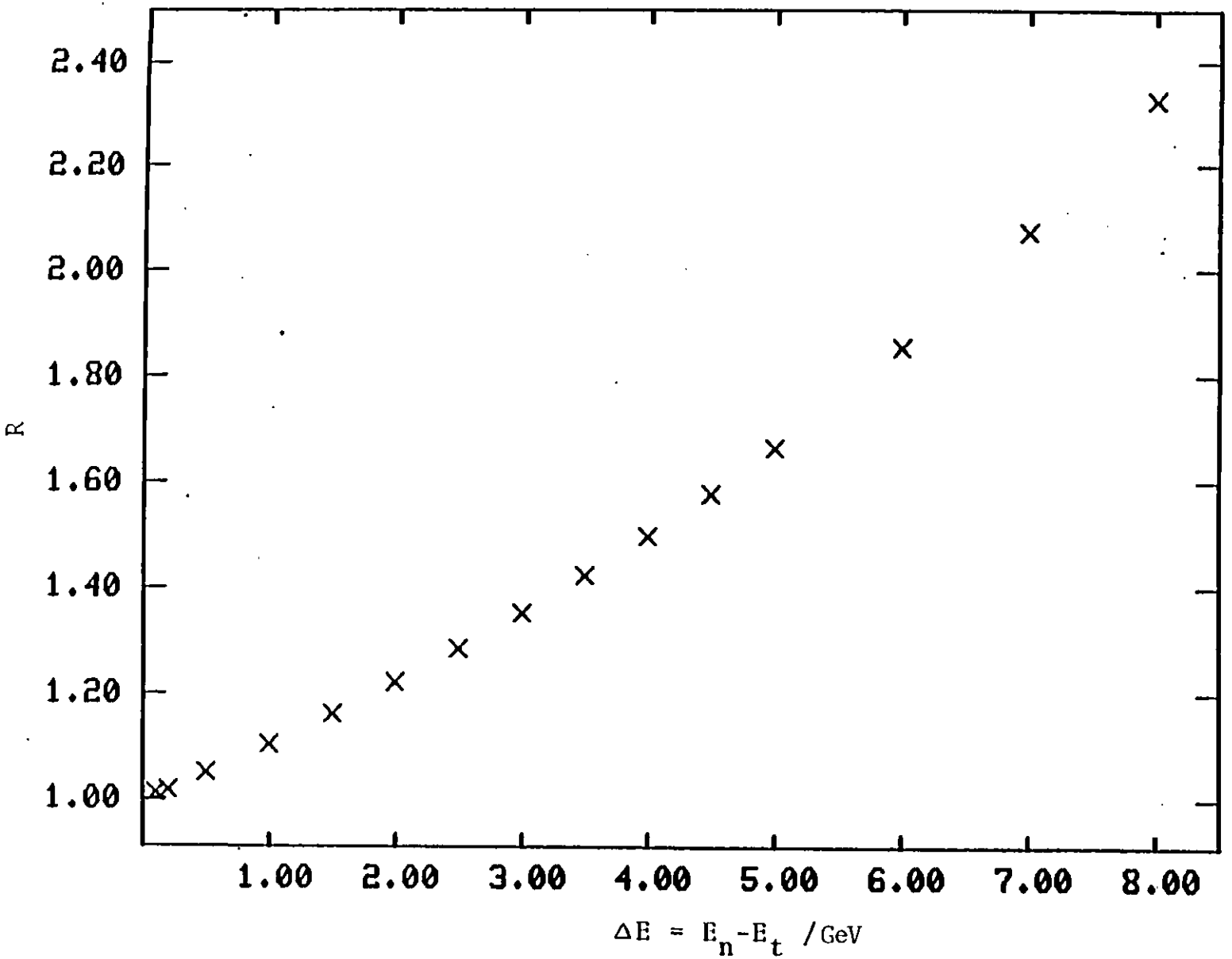

Figure 6.1.1 EFFECT OF USING A NOMINAL BEAM ENERGY.

$$R = \frac{\text{Error due to using beam value } \Delta E \text{ too high}}{\text{Error due to using beam value } \Delta E \text{ too low}}$$

E_t is taken to be 19.6 Gev

below the nominal value used. The ratio is only dependent on the energy differences involved, however the absolute value of the shifts involved increases with X_F of the track concerned.

This asymmetry in shifts caused by under or over estimating the beam energy tends to result in too low a value of the mean of the X_F distribution being obtained if all events are assumed to be caused by average energy photons. The discrepancy between the true and the apparent values is accentuated by the fact that the distribution of photon energies around the average (mean) value is not normal but is negatively skewed. However, the lower momentum of tracks from the interactions of lower energy photons will compensate for the asymmetry. The mean of the X_F distribution, obtained for pion tracks for events constrained to fit $\gamma p \rightarrow \pi\pi p$, is only 7% higher if fitted beam momenta are used rather than the average beam momentum (assumed to be 19.6 GeV/c).

Qualitative predictions of the effect on the shape of the distribution of using a nominal beam energy are more difficult to make. This is because the distributions for each particular beam energy which are shifted relative to each other are not uniformly flat. The loss of tracks from a particular X_F bin, caused by underestimating the X_F of tracks from events caused by low energy photons is compensated by a gain of tracks from high energy photon interactions. The lost tracks are displaced from a higher X_F bin to a lower, the gained tracks from a lower X_F bin to a higher. Whilst there might be no net effect over some range of X_F, it is unlikely that the shape of the entire distribution is unaltered.

To study the effects of using a nominal beam momentum more quantitatively I investigated the changes in the shape of the X_F distribution of tracks from 3C (constrained fits). The distributions obtained using various nominal beam momenta were compared to those resulting from using

the fitted beam momentum to calculate the X_F of tracks. Only tracks that had been fitted as pions were used; fits with a χ^2 probability of less than 0.01 were rejected. The π^+ and π^- data was combined to improve statistics. I checked that both sets of data behaved similarly before combining them however by looking at the behaviour of the ratio of the number of π^- tracks in a given X_F range to the number of π^+ tracks in the same range. Figure 6.1.2 is a plot of this ratio showing that it is independent of X_F, the combined distribution being therefore a reasonable representation of either the π^+ or the π^- distribution.

I decided to parameterise the distortion in shape in terms of the ratio of the number of tracks in a particular X_F bin when a nominal beam energy was used to the number in that bin when fitted energies were used. To show how strongly this ratio (D) depends on the nominal energy used Figure 6.1.3 shows the variation of D with X_F for $E_{nominal}$ = 19.2 GeV and $E_{nominal}$ = 20.0 GeV. (To make the plot clearer the points are slightly offset from the centre of the relevant bins and the horizontal bars indicating the bin width have been dropped). At low X_F there is little difference between the values of D obtained although the trend initially is for the 20.0 GeV values to be higher than the 19.2 GeV ones. This trend reverses around $X_F \sim 0.6$ and the discrepancy in the values of D becomes increasingly significant. If fits requiring the photon energy to be above 22.0 GeV are excluded from the comparison only the $X_F = .95 \pm .05$ data point is significantly altered (from $.94 \pm .17$ to $.67 \pm .14$ for $E_{nominal}$ = 20.0 GeV) suggesting that the rise at very high X_F is related to the high energy tail of the photon spectrum.

The distortion factors obtained by studying 3C distributions are not, however, generally applicable. This is because the amount of distortion depends upon the original shape of the distribution as well as on that of the beam energy spectrum. The X_F distribution of the

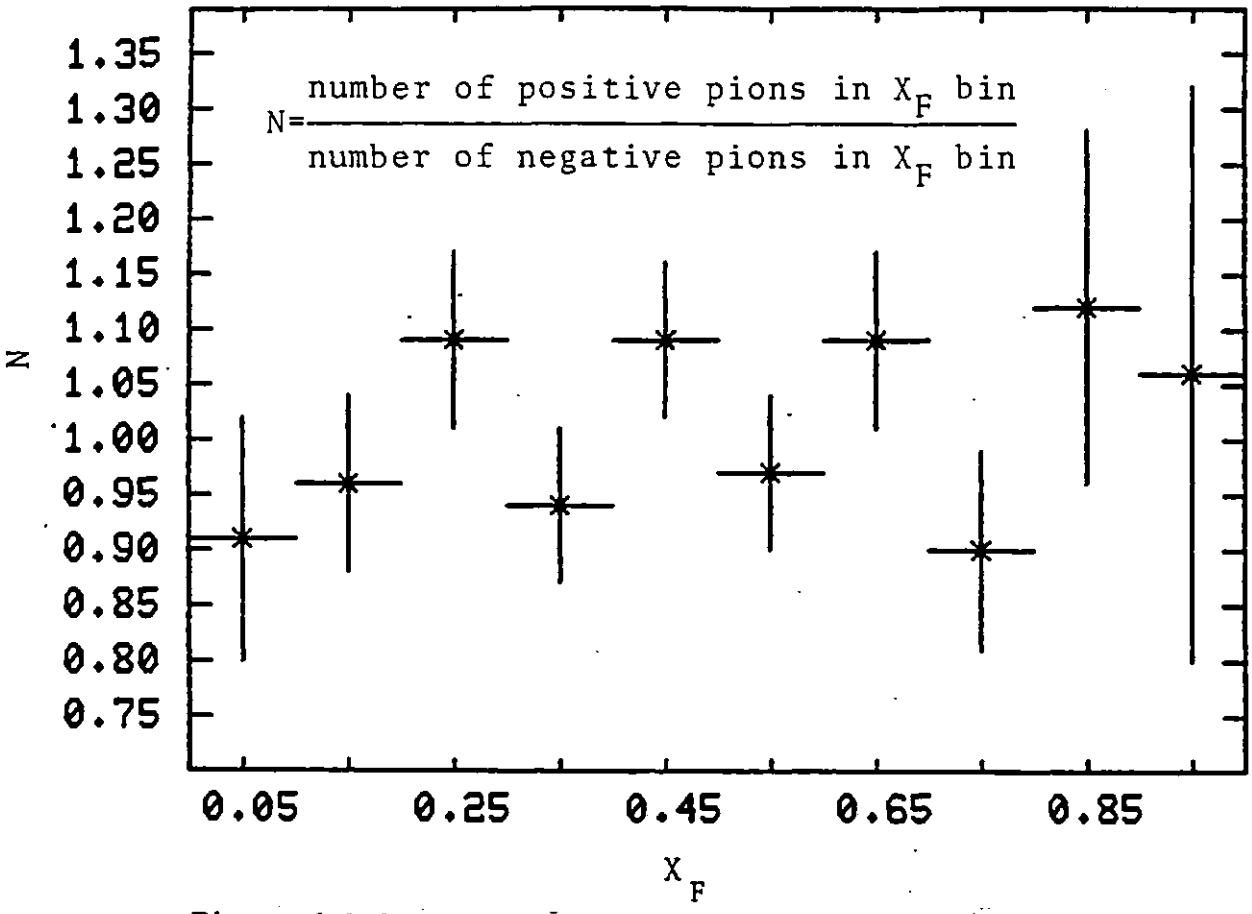

Figure 6.1.2 RATIO,N,SHOWING LACK OF POSITIVE/NEGATIVE ASYMMETRY FOR PION TRACKS FROM RHO DECAYS

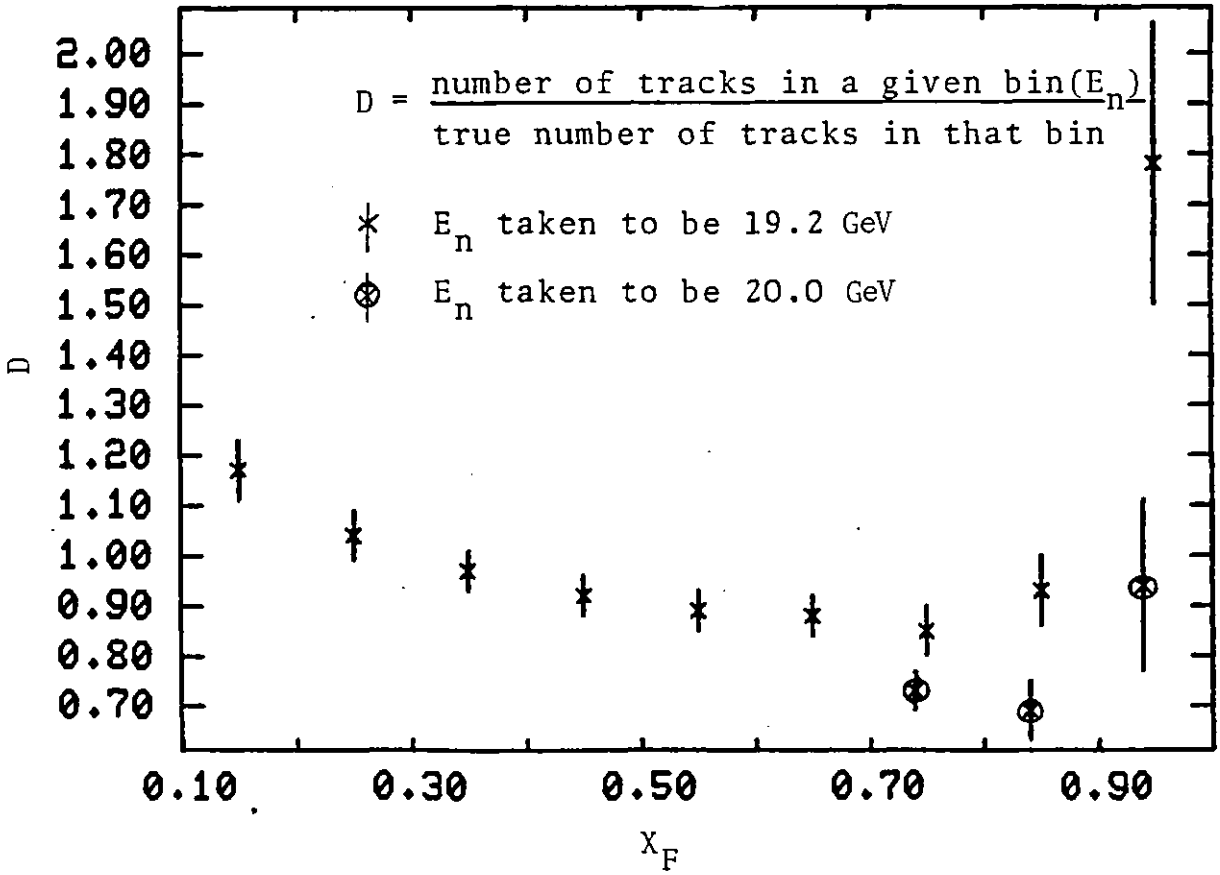

Figure 6.1.3 EFFECT OF USING NOMINAL BEAM ENERGY RATHER THAN FITTED BEAM ENERGY ON NUMBER OF TRACKS IN A GIVEN X_F BIN

pion tracks from three prong 3C fits (see Figure 6.1.4) is roughly Gaussian and is centred around a mean X_F of about 0.47. Most of the X_F distributions discussed peak at small absolute values of X_F, and fall off exponentially (with different slopes in the forward and backward directions). Since the distortions of these distributions are also of interest, a technique for calculating them was developed.

A Monte Carlo program was set up which generated a specified X_F distribution (by weighting the probability of having a track with a particular X_F appropriately). The program then calculated what the X_F distribution would appear to be like. To do this it assumed each track came from the interaction of a photon of energy E, this energy being supplied for each track by a subroutine, the probability of the photon having a particular energy being weighted so as to generate the appropriate beam spectrum. The momentum of the track was then transformed from the centre of mass frame to the laboratory frame. Then, the momentum of the track in the centre of mass frame was recalculated using the nominal beam energy to derive the Lorentz boost needed.

To check out the procedure I used it to try to find the distortion factors associated with the 3C X_F distribution. The beam energy spectrum generated by the subroutine was therefore matched to the fitted beam energy spectrum yielded by the constrained fits. The transverse momentum (P_t) distribution of the tracks has little effect on the overall shifts but it too was assumed to match the experimentally measured distribution. The P_t of a track was assumed not to correlate with its X_F.

I compared the distortion factors obtained experimentally from events due only to photons with a fitted beam energy between 5.0 and 21.0 GeV, with the theoretically calculated values (applying the same cuts). The high energy cut was to remove a region of the fitted beam

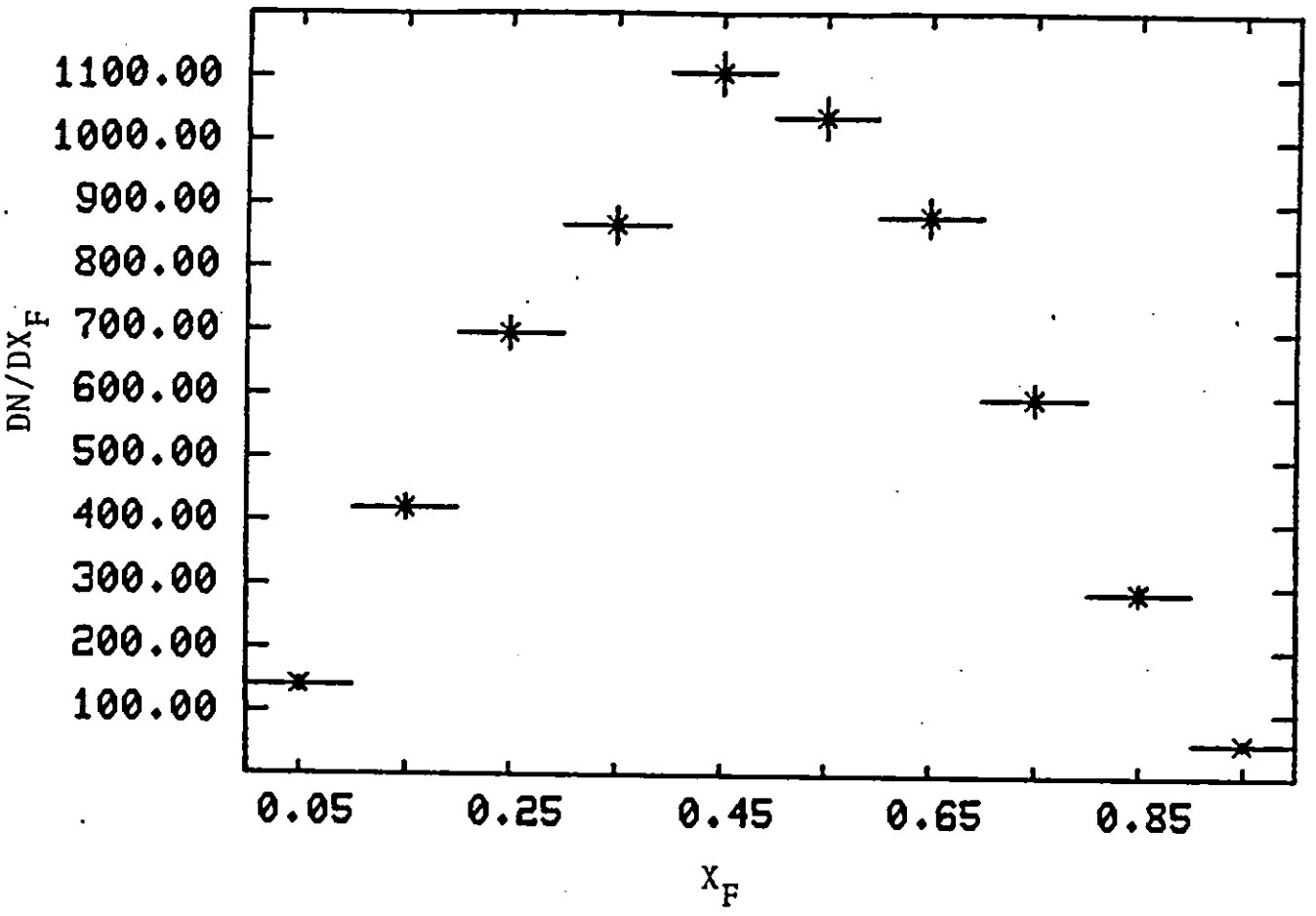

Figure 6.1.4 X_F DISTRIBUTION FOR PIONS FROM RHO DECAYS

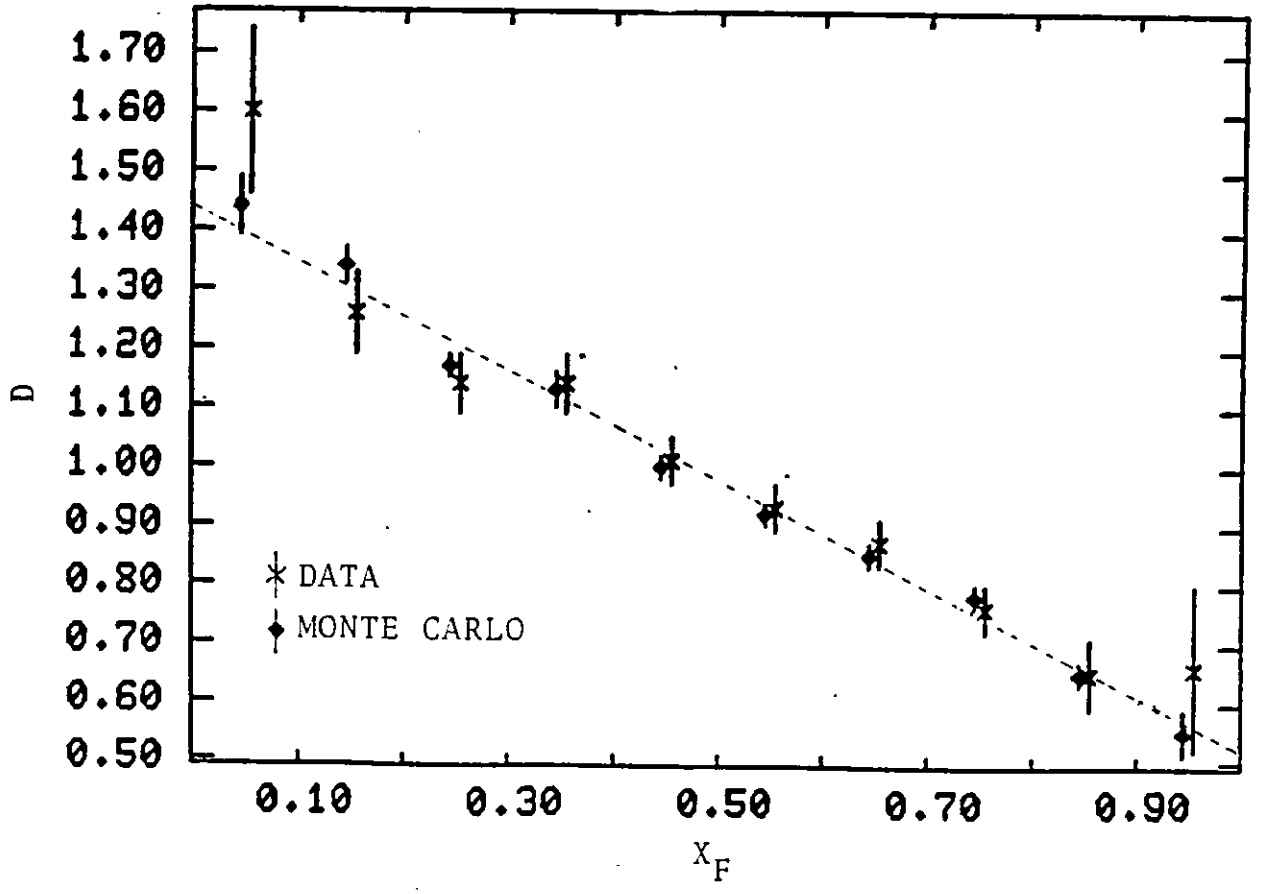

Figure 6.1.5 COMPARISON BETWEEN DATA AND RESULTS OF MONTE CARLO USED TO ESTIMATE BEAM SPREAD EFFECTS

spectrum which was poorly defined statistically. Similarly the low energy cut removed a region of the spectrum it was difficult to parameterise accurately. The two distributions are shown in Figure 6.1.5. The match is good except at the extremes, where the comparatively large statistical errors make the discrepancies insignificant. Also shown in Figure 6.1.5 is a straight line fit to the distortion factors calculated by the Monte Carlo method. The fact that a good fit is obtained is due to the fact that a nominal beam energy of 20.0 GeV was used.

Unfortunately few distributions yield distortion factors which parameterise so well. Figure 6.1.6 shows the values of D obtained for three Gaussian distributions (centred on X_F equals 0.47 and with half-widths of 0.35, 0.25 and 0.15 units of X_F respectively). As the width of the distributions decreases the deviation of the D values away from a straight line becomes increasingly significant. Nor, as Figure 6.1.7 shows does changing the nominal beam energy help. Lowering the nominal beam momentum reduces (initially) the overall range of the D values but does not improve the linearity of their distribution (the range of D values covered at high X_F values starts to increase). Raising the nominal beam momentum increases the overall distortion of the distribution.

There is no ideal nominal beam energy that causes no distortion. Whilst the average (mean) beam momentum should be used to minimise the values of the distortion factors, this does not imply that it should be used to minimise the distortion of a distribution. A different choice of nominal energy might yield a set of distortion factors slowly varying over the X_F range of interest. There is also no single average beam momentum. The energy threshold for photon interactions giving seven charged tracks is different to that for photon interactions yielding only three, for example, and so the mean energy of the interacting photons is higher for seven prong only distributions than for three prong

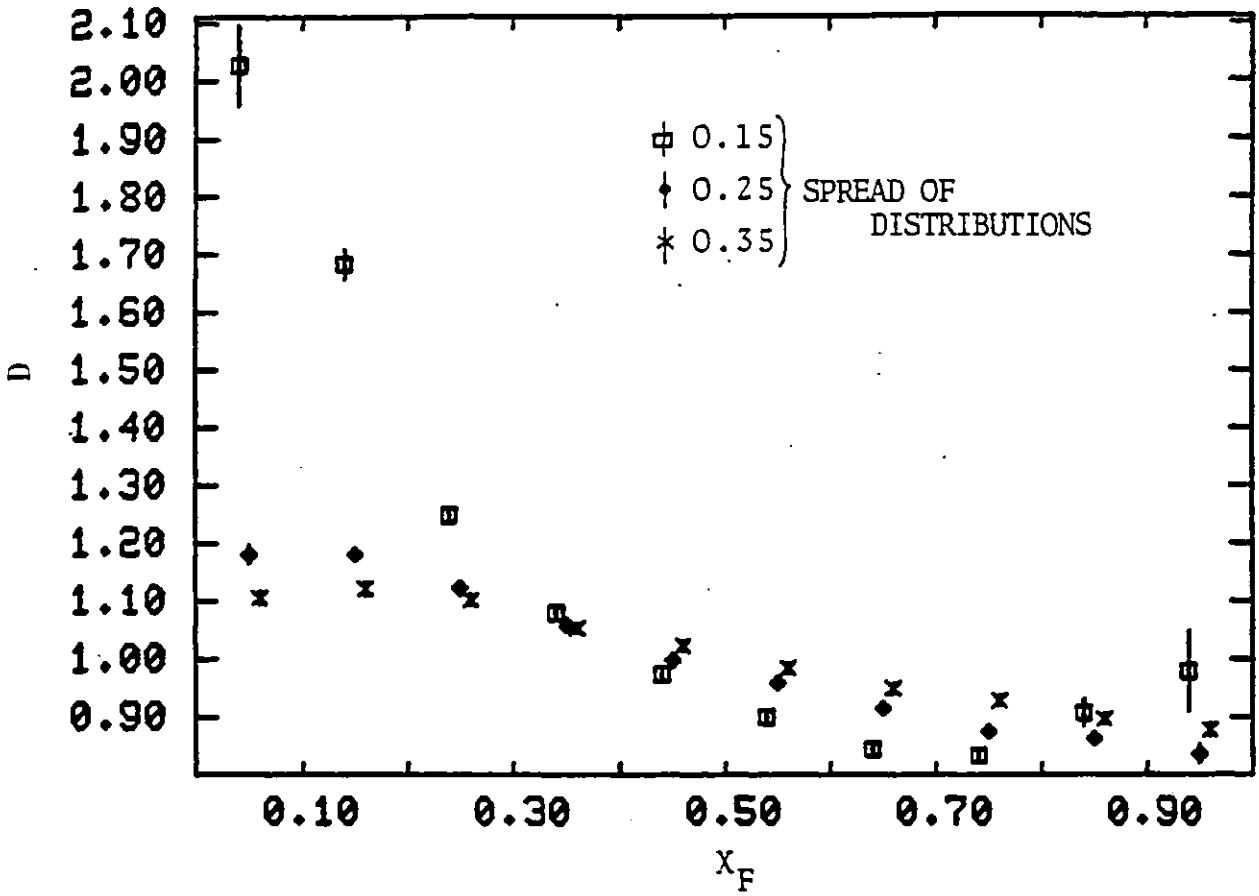

Figure 6.1.6 DEPENDENCE OF BEAM SPREAD EFFECTS ON SHAPE OF ORIGINAL DISTRIBUTION

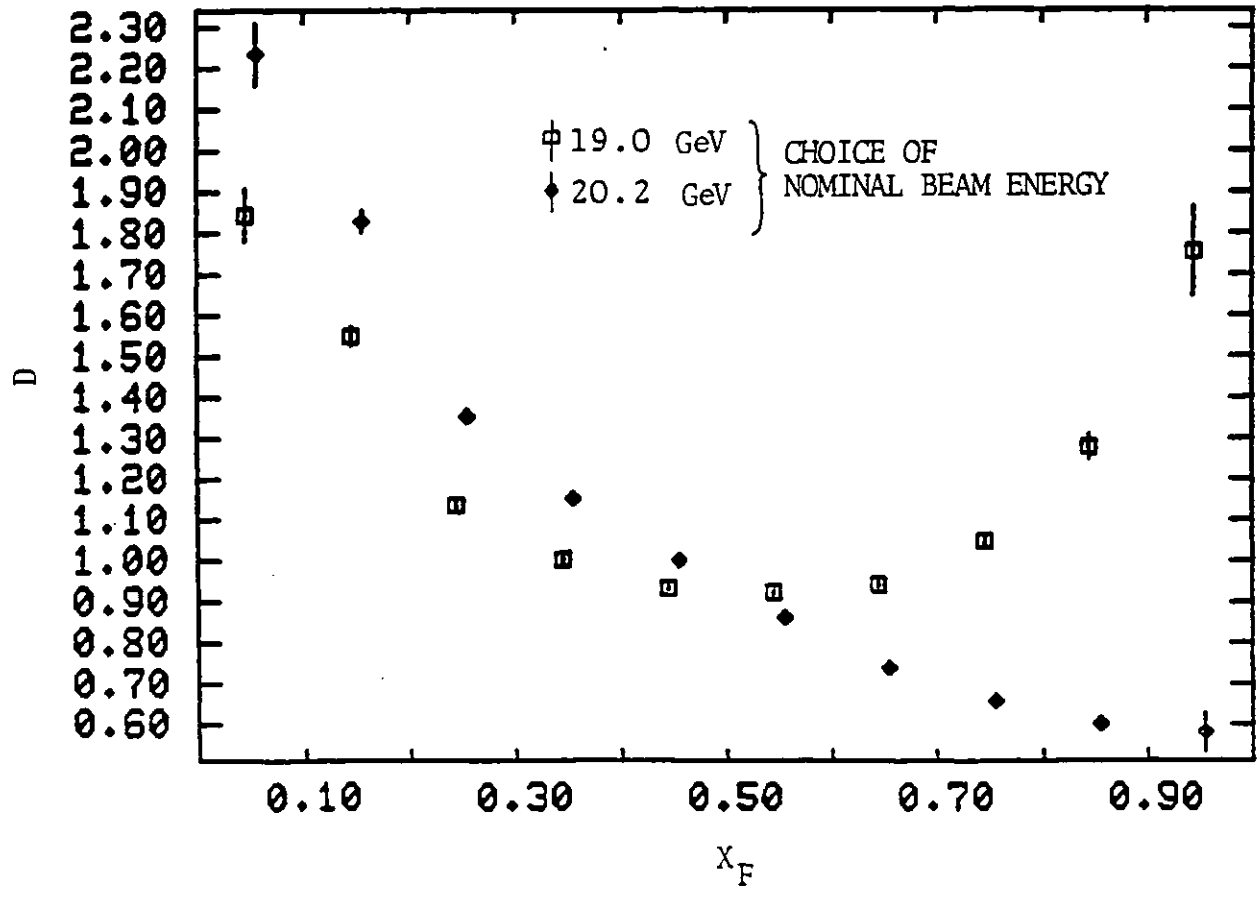

Figure 6.1.7 DEPENDENCE OF BEAM SPREAD EFFECTS ON CHOICE OF NOMINAL BEAM ENERGY

only ones. Rather than use several different nominal beam energies I have always used 19.6 GeV. This choice tends to give reasonable values of the distortion factor over the entire X_F range.

To widen the applicability of the program it was set up to generate the original distributions in any frame of interest. The beam spectrum was converted from that relevant to the $\gamma p \rightarrow p\pi\pi$ pion distribution by folding in the dependence of the ρ cross section on energy (reducing the low energy tail) to give a truer beam spectrum. The results obtained from the program will be used in later sections on the inclusive results.

Before leaving the subject however, it is worth noting that even distributions of quantities as measured in the laboratory frame are affected by the beam's energy spread. Consider for example the rapidity (y) distribution of the tracks. If the distribution is symmetric in some frame of reference, e.g. the centre of mass frame, then because rapidity is an additive variable the distribution is symmetric in all frames of reference, provided that the same boost is applied to all events to transfer between frames. However, the laboratory frame is not equidistant from a particular frame for all events. The greater the separation in rapidity of the two frames the greater the influence of the energy of the interacting photon on the boost needed to translate between them. If we examine a distribution in the laboratory frame it is distorted because some events have been shifted further along the axis than others. Figure 6.1.8 shows the translation in rapidity space needed to transform from the centre of mass frame to the laboratory frame for varying photon energies.

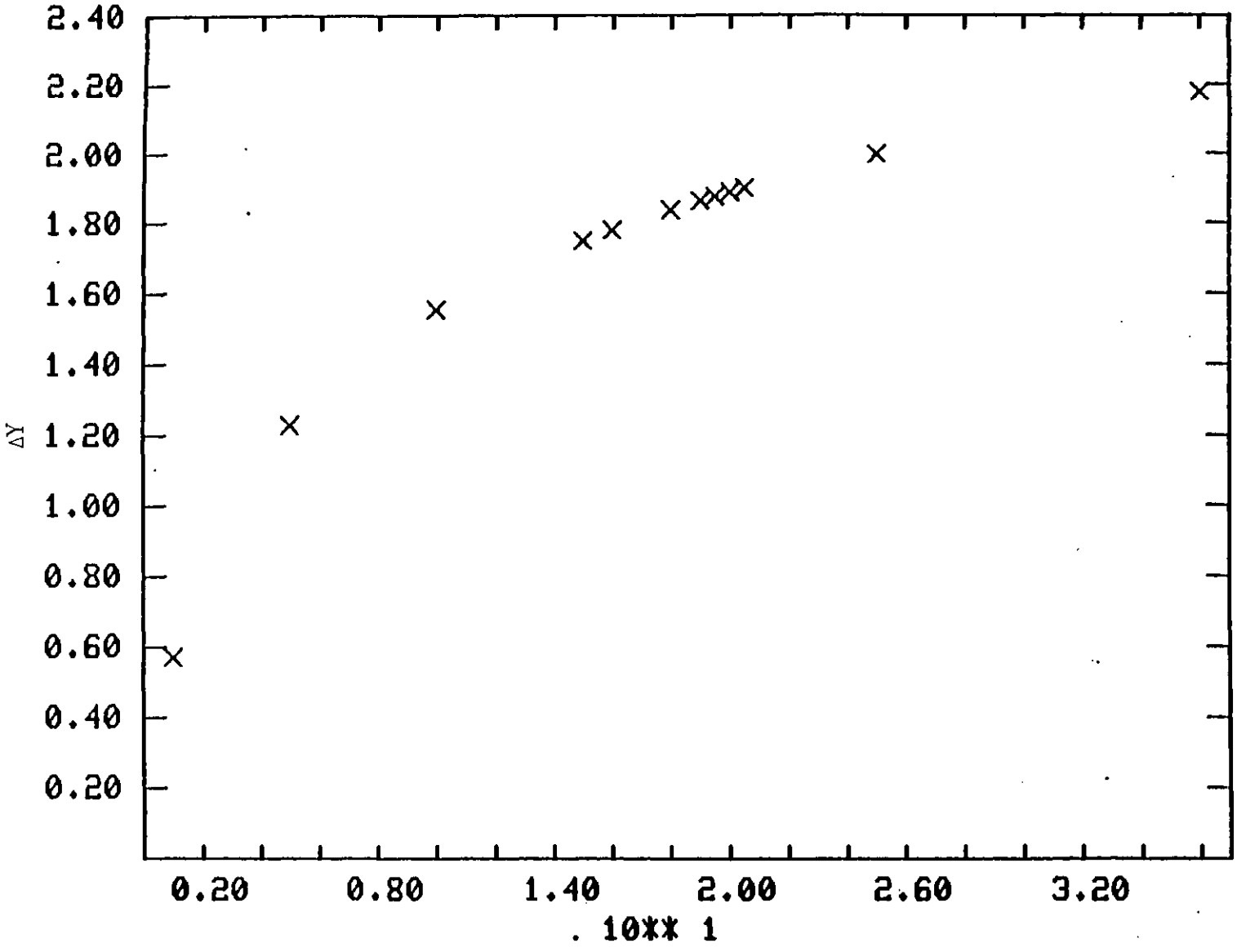

Figure 6.1.8 VARIATION WITH BEAM ENERGY OF RAPIDITY DIFFERENCE BETWEEN CENTRE OF MASS AND LABORATORY FRAMES OF REFERENCE

6.2 Limited Particle Identification and its consequence

There are three main methods by which charged particles produced in interactions at the SHF may be identified; by kinematic fit, by the bubble density along their tracks in the bubble chamber, and by the production or otherwise of light in the downstream Cerenkovs. It is also possible to identify some charged particles by the way that the electromagnetic showers they produce in the lead glass wall develop. This technique is more complex than the others however, and is useful mainly for differentiating between leptons and hadrons.

Although identification by fit can, in principle, give information about particle types over an entire kinematic range, that information is only available for particles produced via specific exclusive channels (essentially those which do not yield undetected neutral particles). This means that significant biases are introduced if, for example, kaon tracks associated with a phi resonance are removed from inclusive distributions in an attempt to study only pion photoproduction. Since the production of neutral particles decreases the energy available for the production of charged particles the kaons which are eliminated will come predominantly from amongst the high energy tails of the distributions.

Only low momentum tracks (1.5 GeV/c at most) can be typed by the ionisation they produce. The probability that such tracks will be identifiable is smaller in this experiment than in earlier SHF experiments. The conditions imposed on bubble growth in order to make charm decays detectable result in particle tracks on the ordinary resolution photographs being saturated by bubbles. This means that only the HRO view can be used in measuring bubble density. The small depth of field means that tracks quickly go out of perfect focus and the resultant blurring of the track makes it unidentifiable. Less than half the tracks which have momenta low enough to make them potentially

classifiable as pions, kaons or protons are judged clear enough when scanned for a decision to be made. If a decision is made it is frequently only partial; tracks often being pion/kaon or kaon/proton ambiguous.

The two threshold Cerenkovs become increasingly useful in identifying particles as particle momentum increases. Figure 6.2.1 shows the thresholds for light in each Cerenkov for pions and kaons in terms of the corresponding X_F values. It was assumed that the particles were produced by a photon of energy 19.6 GeV. The results are shown for tracks with zero transverse momentum (P_t) and for tracks with a P_t of 0.5 GeV/c. As expected, the greater the P_t of a track the lower its longitudinal momentum to give light.

If there were no sources of background in the Cerenkovs (such as electrons produced via pi zero decays and which give light in C2 if they are above 0.02 GeV/c in momenta), and if they had perfect geometric acceptance, particles could be unambiguously identified as pions above X_F values of around 0.15. Unfortunately, neither of the above conditions are satisfied. Since the background leads to light in Cerenkov cells where there might not otherwise be light it will result in the misidentification of particles as pions. The gain in pion tracks will be compensated for by pions which do not give light in the predicted cell(s) because they scatter or because of inefficiencies in the photon collection system (most significant close to threshold). Tracks which give light only in C2 cannot be identified since either inefficiencies or background may be the cause of the inconsistency.

The probabilities involved in correctly deducing the type of particle giving rise to a particular track have been the subject of detailed studies the results of which are quoted in reference 1. Although not the author's work I shall summarise the main points here for convenience. Well above threshold (see figure 6.2.2) over 98% of pions

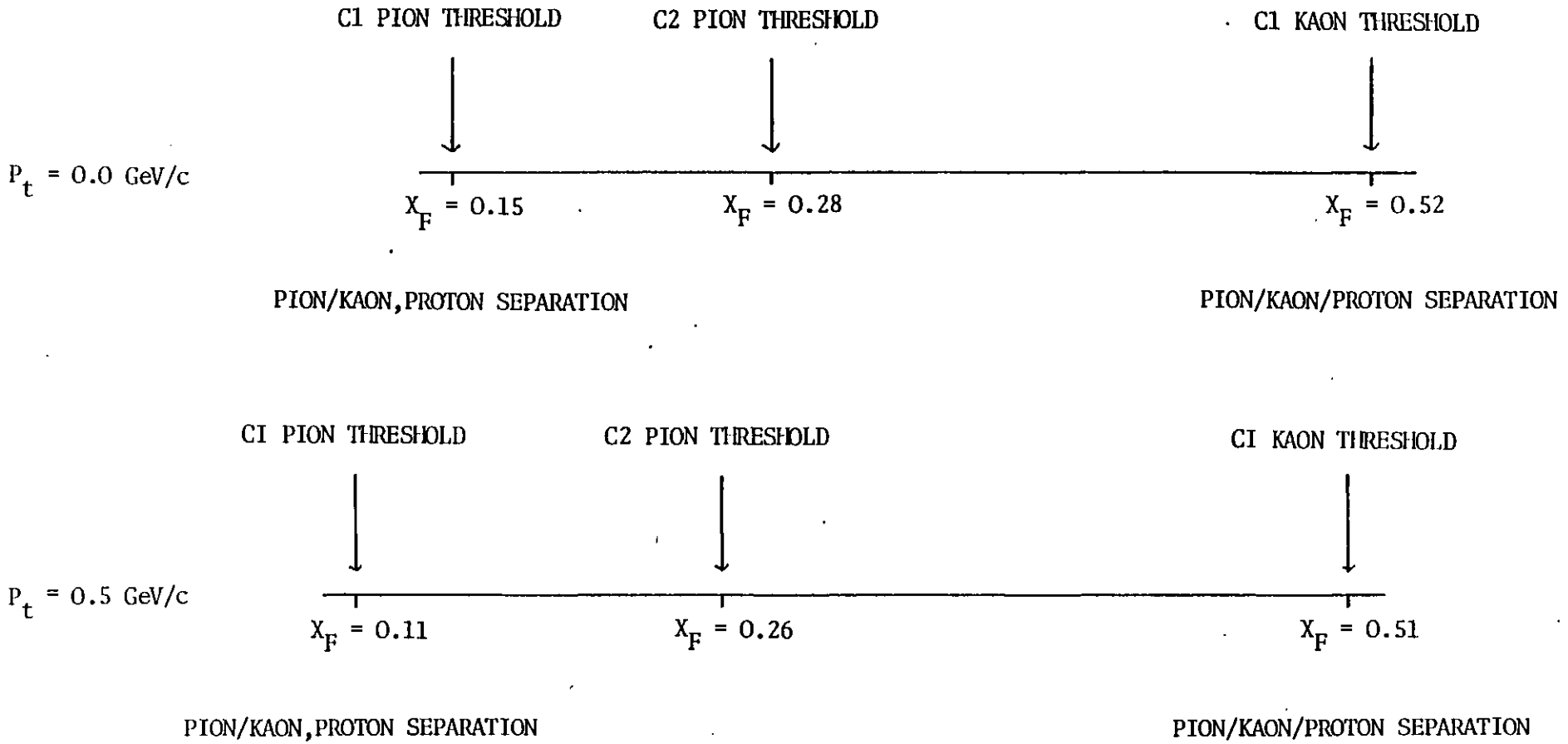

Figure 6.2.1 CERENKOV IDENTIFICATION THRESHOLDS AS A FUNCTION OF X_F

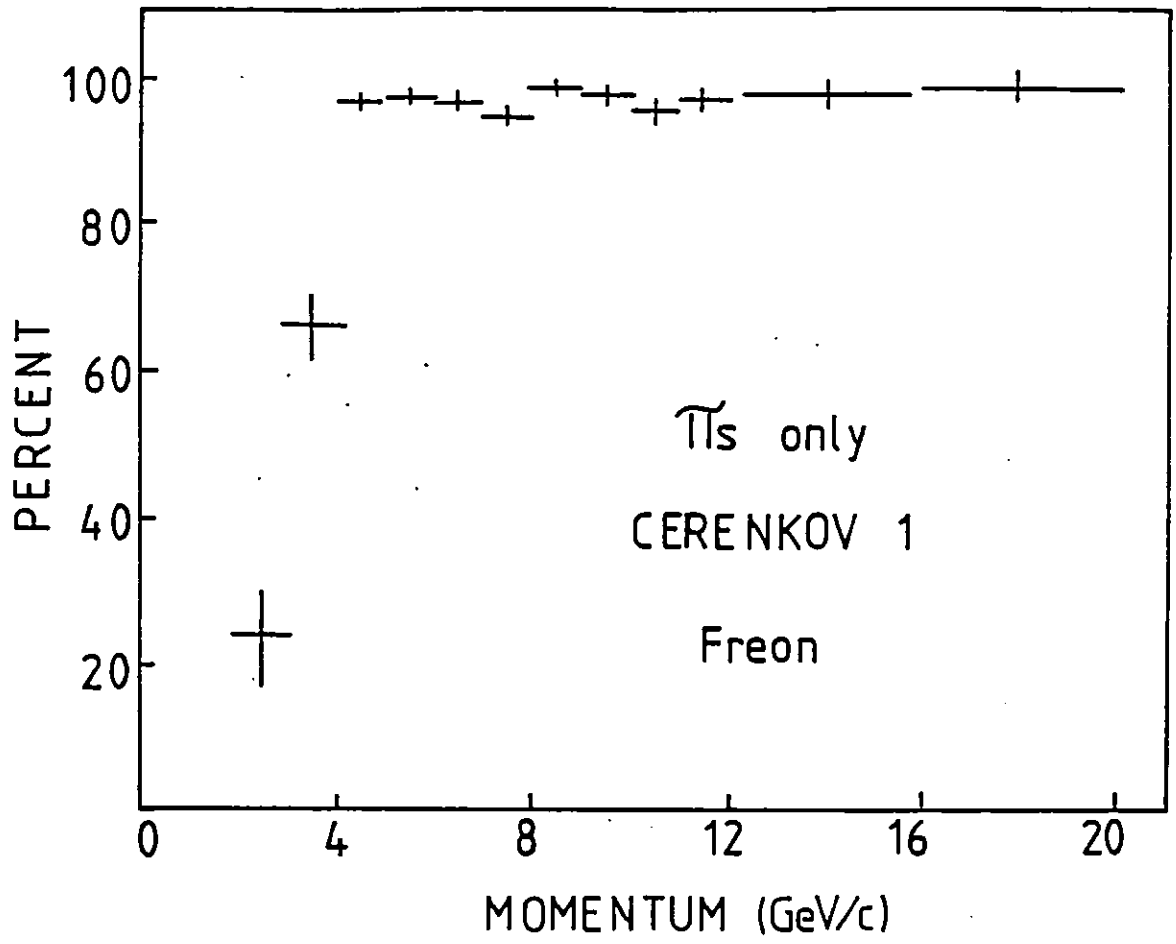

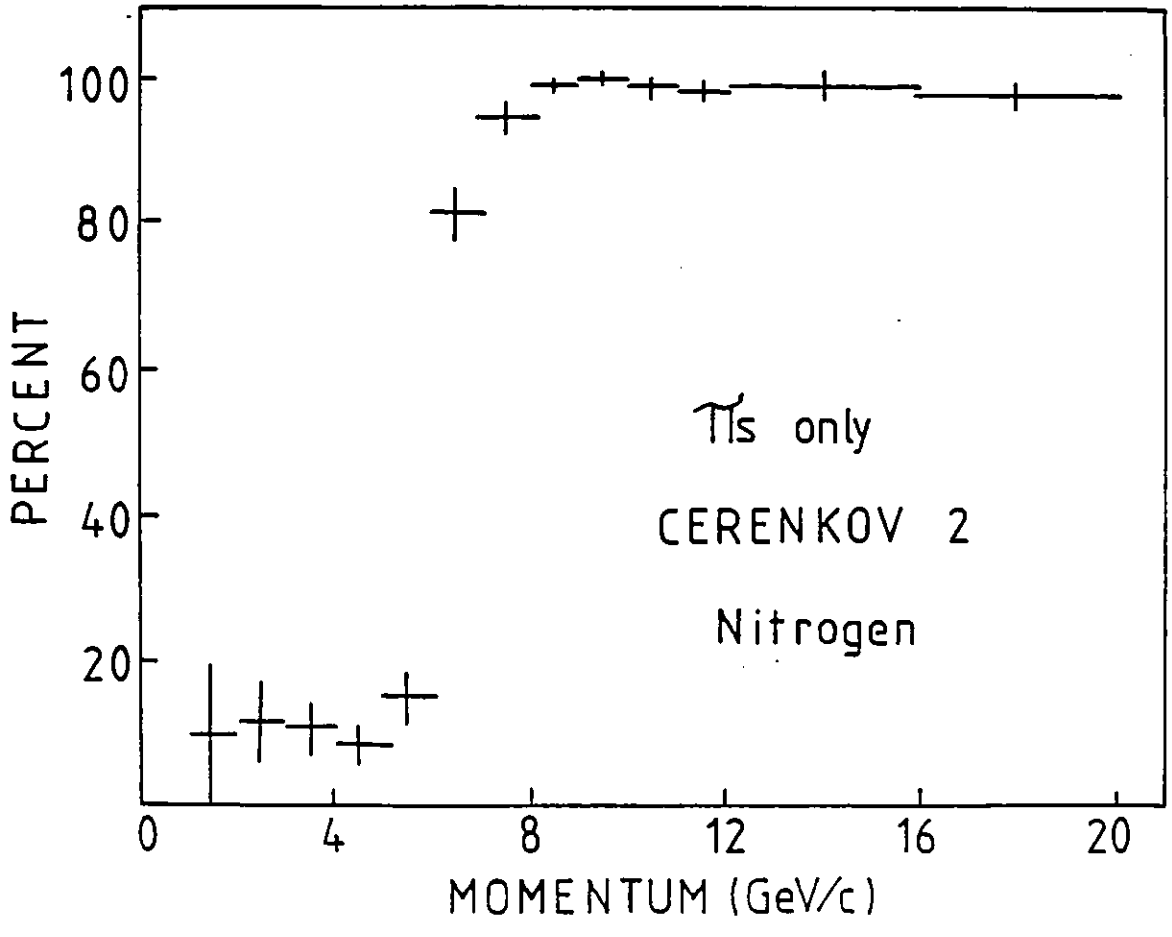

Figure 6.2.2 EFFICIENCY OF CERENKOV IDENTIFICATION OF PIONS AS A FUNCTION OF MOMENTUM (FROM REFERENCE 1)

(originally identified by fit) are correctly typed and more than 75% of kaons can be correctly flagged (considering only tracks passing through active regions of the counter which have been hybridised). The lower fraction of kaons identified is lower because about ten percent of tracks apparently below threshold go through cells in which light is produced. The probability of two tracks from the same primary interaction going through the same cell is less than 0.5%. The overall result is that while a clean but small sample of kaons (excepting some protons and antiprotons) can be obtained a clean sample of pions cannot be (though arguably the far greater number of pions makes the contaminant insignificant).

Given the variety of imperfect methods that must be used in order to minimise the presence of unwanted particles in a distribution it is worthwhile considering if their use is beneficial. Since they affect regions of the distribution variably the effect may be to obscure the physics under an accumulation of systematic errors rather than elucidate it.

A Q-frame based analysis of photoproduction (see section 5.5) requires that distributions be studied over their entire kinematic range, though modifications of the shape of the distributions central region are particularly important. Examining the differential cross section for evidence of point-like behaviour (section 4.4) however or in order to test the predictions of Chang and Hwa (section 5.4) focuses attention on the high X_F (beam fragmentation) region. Finally asymmetries in the behaviour of positive and negative particle distributions (section 4.5) are expected to be most significant at the high energy tail end.

Studying asymmetries involves taking ratios. If an identification process removes equal fractions of positive and negative particles respectively then there is no gain involved in its use. However, since

the initial system (photon, proton) carries both net charge and net baryon number so will the final system. This means that it is much more likely that a positive particle is a proton than it is that a negative particle is an antiproton. As the chance of misidentifying a proton as a pion is much less than that of misidentifying a kaon as a pion (above X_F values of around 0.5 background light would be required in both Cerenkovs not just the second), using information from the Cerenkovs makes a positive negative comparison more meaningful. Unless the systematic biases introduced affect the positive and negative distributions differently they can be ignored since their influence on the result is negated by the division of one distribution into the other. Although the biases may not be identical (partially due to associated production of lambdas which causes an excess of positive kaons over negative kaons) I shall assume they are small enough to discount.

The effect on the shape of a distribution at its tails depends both on the true shape of the distribution and on the acceptance of the Cerenkov system. If an attempt is made to type the particles the contributions to each region of the distribution must be weighted by the probability that a track can satisfy the criteria imposed by the identification process if it has an appropriate four momentum. Figure 6.2.3 compares the fraction of the data positively identified as pions to the estimated Cerenkov acceptance at two different P_t values. Figure 7.3.4 shows the calculated acceptance for the Cerenkovs as a function of X_F, integrated over P_t, for pion tracks which hybridise and traverse active regions of both Cerenkovs.

It is in searching for the Q-frame that compensation for the effects of attempting to restrict the distributions to pions is most difficult to achieve successfully. Whilst the procedure involved in using the Cerenkovs is well defined and well suited to a calculation of its effects, that used in identifying low energy particles by their

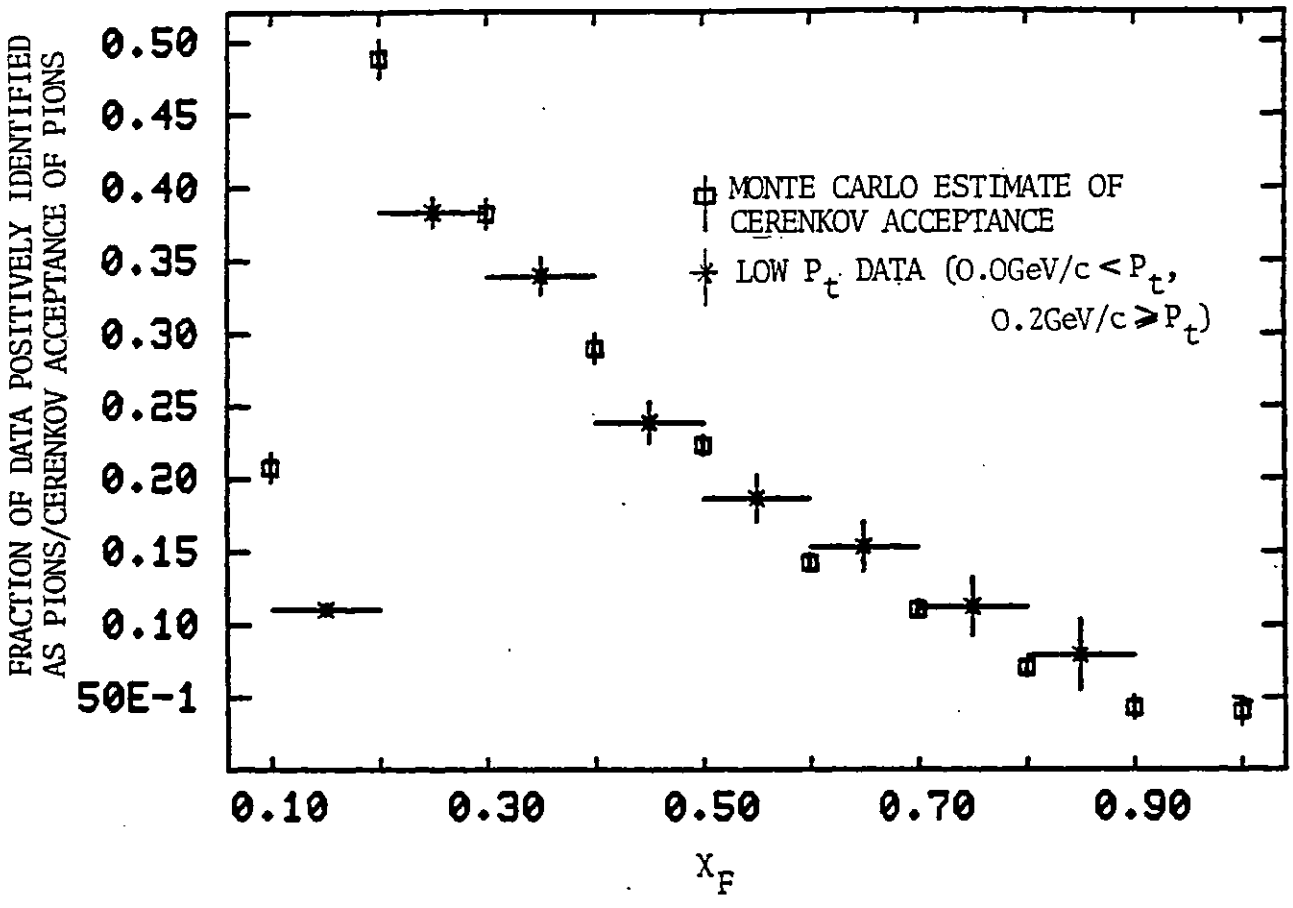

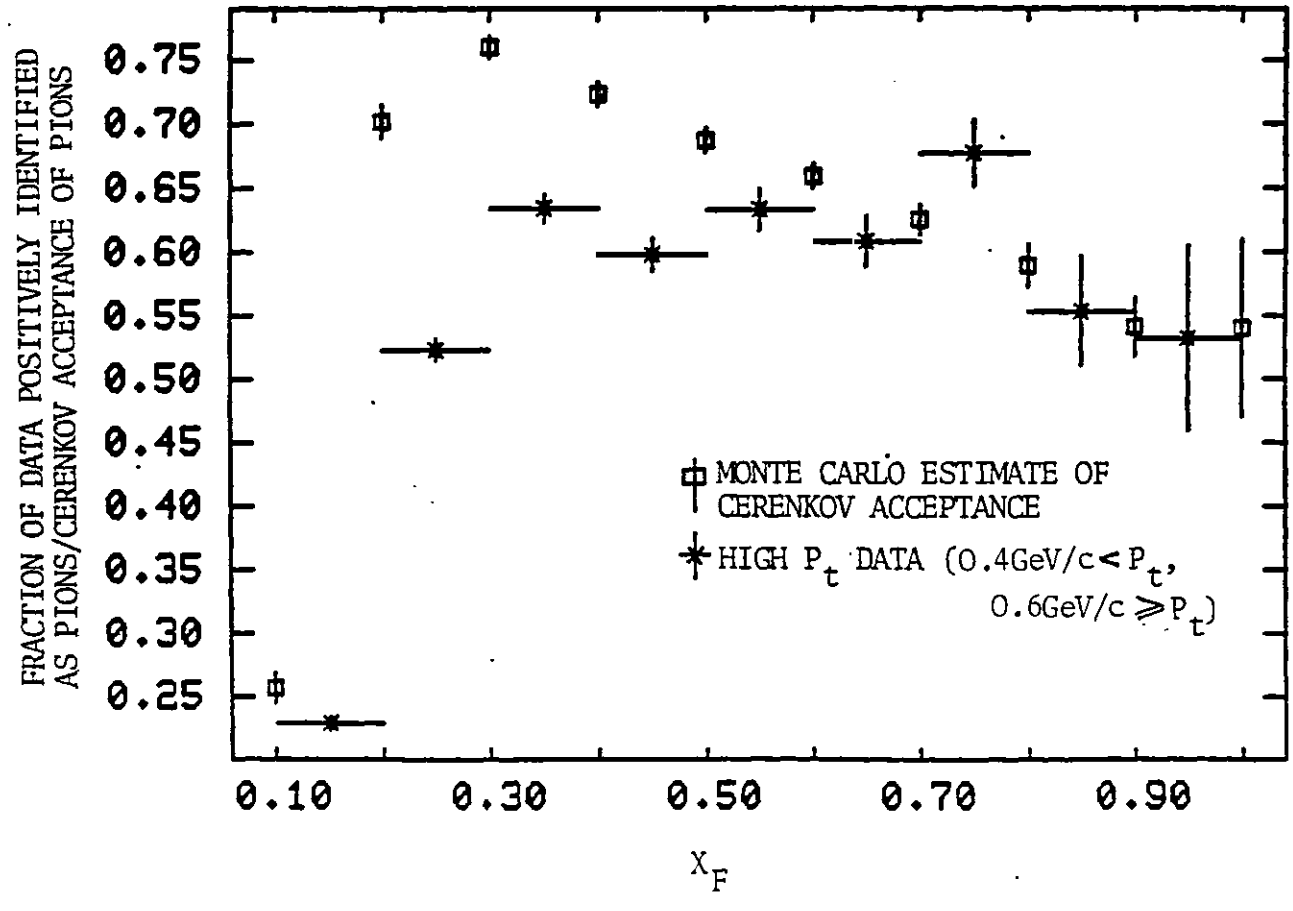

Figure 6.2.3 COMPARISON BETWEEN ESTIMATED CERENKOV ACCEPTANCE AND FRACTION OF ALL TRACKS POSITIVELY IDENTIFIED AS PIONS

ionisation trail is not. The decision involved is more subjective and the accuracy of such a decision varies from roll to roll because of changes in the optical quality of the pictures (and in the attention each picture receives from the scanner). The central region where the majority of tracks are and which is of primary interest is poorly covered by identification techniques. However, distributions comprised predominantly of mesons can be obtained by restricting the analysis to negative particles only. If the symmetry frame is to be universal it must be expected to be the same for pion or kaon production.

Unfortunately a distribution of mesons which is symmetric in a particular frame of reference will only look symmetric when the relevant laboratory quantities are transformed to that frame if the energy of the particles is known accurately. This implies that the mass of each particle must be specified. Distributions involving contributions from more than one type of particle are distorted if (for example) all the particles are assumed to be pions. The discrepancy between the true and the calculated value is greater for low momentum tracks since the effect of mass on the total energy of the track is proportionately larger in this case than for high momentum tracks.

It can be shown that both the X_F and the rapidity (y) values calculated for a track of a given momentum are greater (shifted away from the target fragmentation zone) for lighter particles. Figure 6.2.4 shows the difference between the calculated and the true X_F value, for a kaon of varying P_L and zero P_t, as a function of the calculated X_F value if the particle is assumed to be a pion. The ratio is shown as a function of the pion X_F value. The effects of the shift are shown in Figure 6.2.5 which shows the ratio of the number of tracks in a given X_F bin if all particles are assumed to be pions compared to the true number of tracks contributing if the particles are

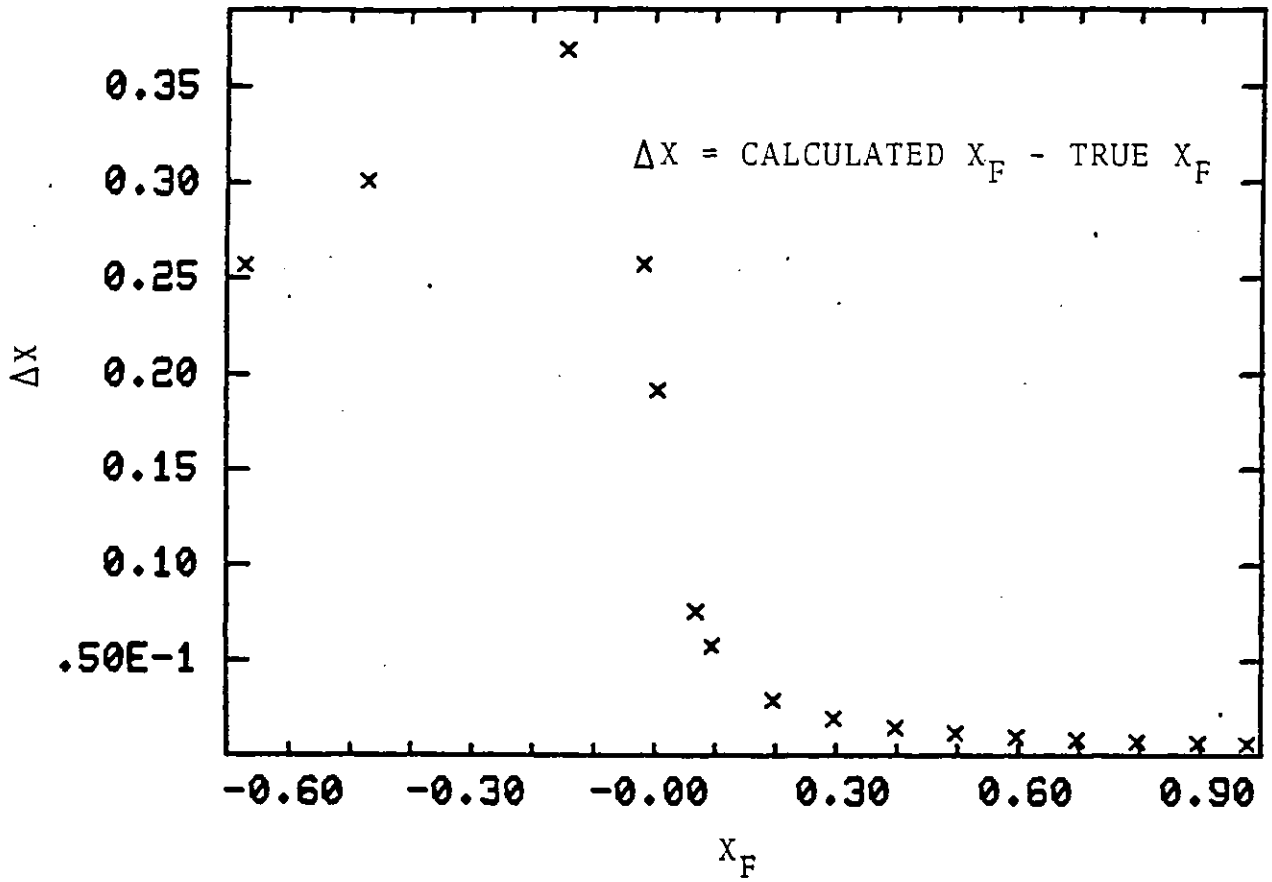

Figure 6.2.4 SHIFT IN CALCULATED VALUE OF X_F FOR KAONS MISIDENTIFIED AS PIONS

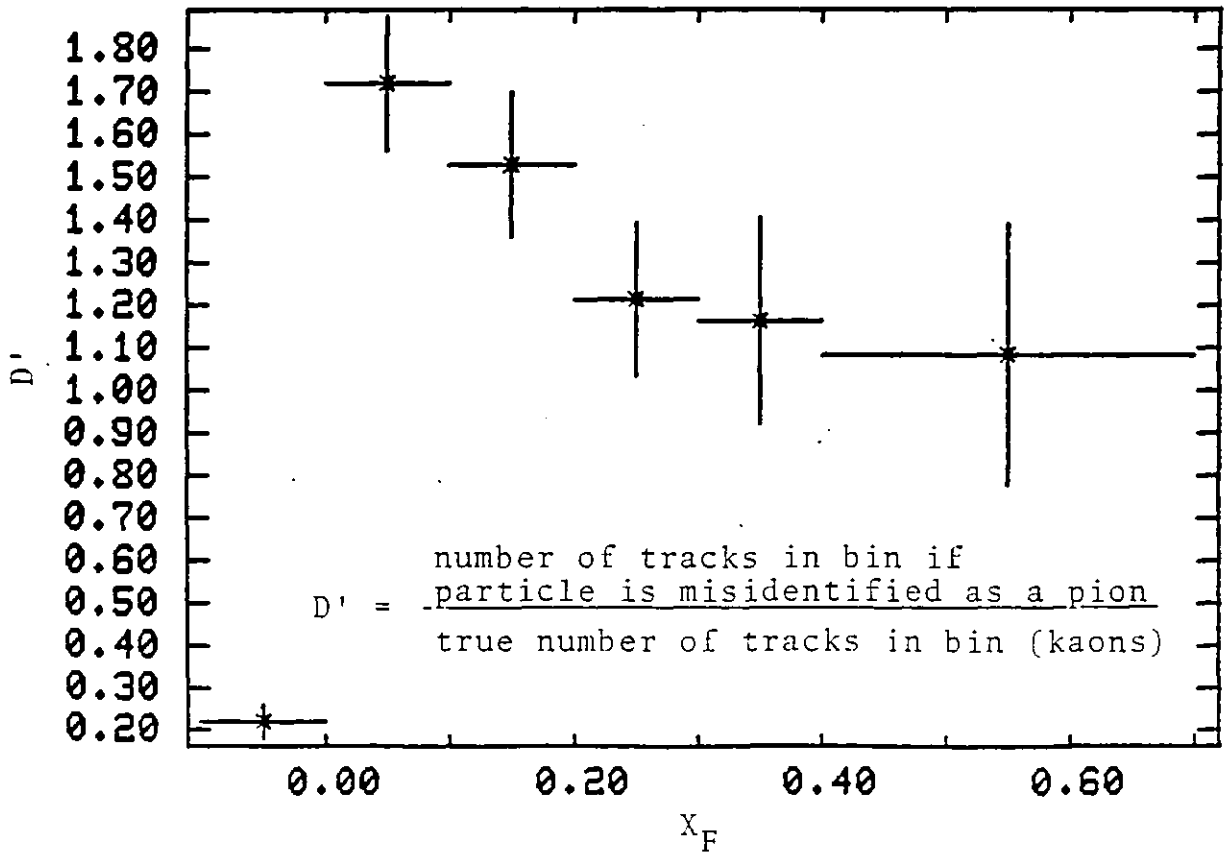

Figure 6.2.5 EFFECT OF PARTICLE MISIDENTIFICATION ON CALCULATED VALUE OF X

correctly identified (the original distribution was comprised of neutral kaons only). Nearly all the tracks have been shifted out of the target fragmentation zone into the central region.

To correct the shape of a pion distribution over its entire range not only knowledge of the probability of correctly typing a pion is needed but also data on the probability of kaons contributing to regions where no identification is possible. The latter requires that the shape of the kaon distribution is determined. Rather than remove some kaons from some regions I decided to remove none and to estimate their effect by Monte Carlo studies.

The program discussed in the previous section was developed so that as well as a given pion distribution being generated a kaon background was generated in the same frame(both distributions being symmetric about the same central value). The fraction of the total particles that were kaons was variable as was the slope of the kaon distribution compared to that of the pions. The slope was allowed to differ because even if all the mesons were formed from quarks and antiquarks with a photon source there might still be effects caused by the differences in the hidden masses of up, down and strange quarks.

Figure 6.2.6 shows the influence of a ten percent kaon contaminant on a particle distribution symmetric in the centre of mass frame. Both the pion and kaon distributions are assumed to fall off exponentially with longitudinal momentum in the forward and backward direction, each having the same slope. The quantity plotted against the absolute value of the longitudinal momentum of the particles in that frame is the apparent ratio of particles travelling in the forward direction to those going backwards. For comparison figure 6.2.7 shows what the same plot would look like if there were no kaon contaminant.

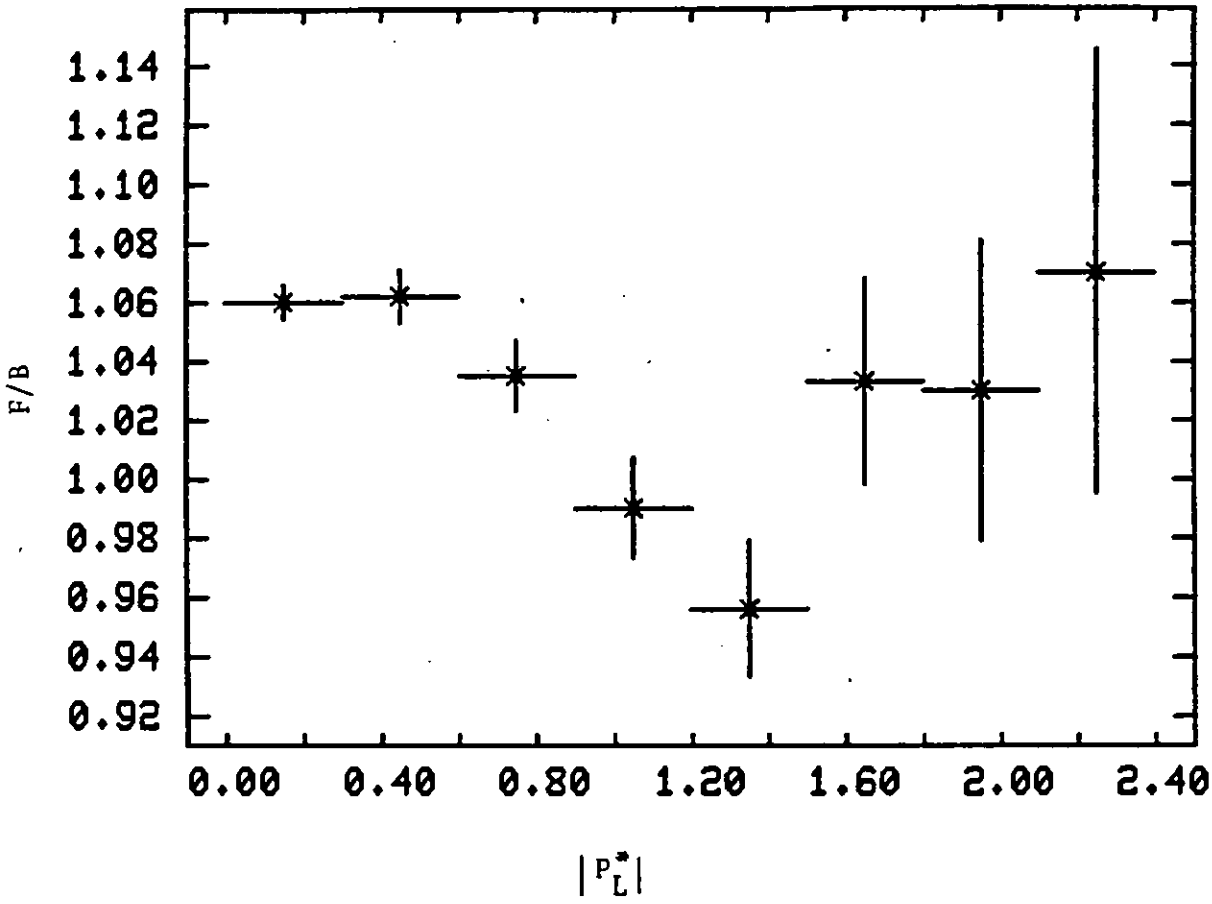

Figure 6.2.6 EFFECT OF BEAM SPREAD AND MISIDENTIFICATION OF A 10% KAON BACKGROUND ON A DISTRIBUTION SYMMETRIC IN THE CENTRE OF MASS FRAME

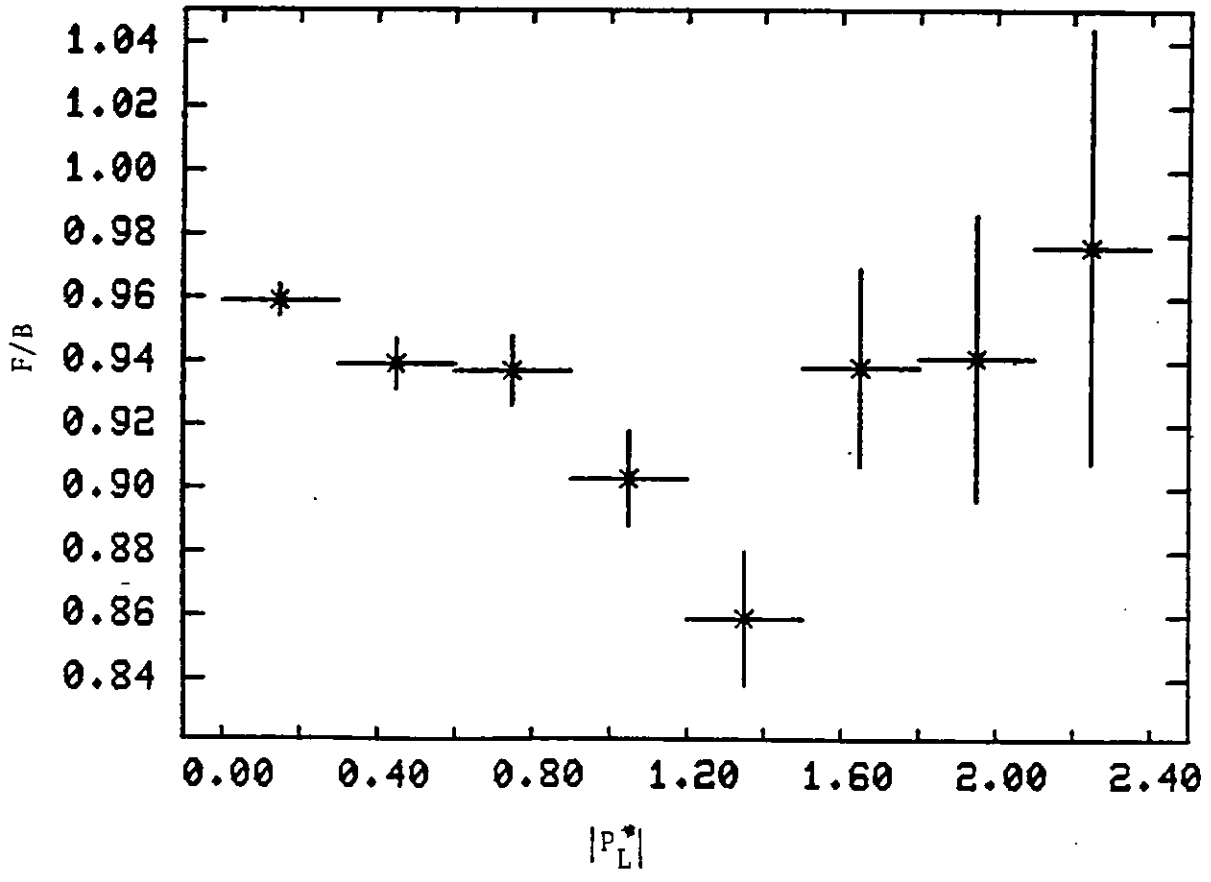

Figure 6.2.7 EFFECT OF BEAM SPREAD ONLY ON A DISTRIBUTION SYMMETRIC IN THE CENTRE OF MASS FRAME

If the distribution contained only pions it would appear that there was an excess of tracks in the backward direction. The presence of kaons compensates for the effects of beam spread and causes an apparent lack of tracks in the backward direction. This lack would affect a Q-frame analysis so as to make the Q value obtained favour fewer interacting components in the photon than would otherwise be the case.

6.3 The Effects of Trigger Acceptance

Trigger acceptance has already been discussed in some detail in section 3.9 when attention was focussed on the fraction of the total cross section triggering. To be confident that the true shape of a distribution has been obtained it is necessary to be sure that there is not a preferential loss from some regions because the trigger is particularly biased against certain exclusive channels. The most serious situation that can occur, if data from a triggered experiment is used in a study of inclusive physics, is if tracks of a particular momentum which rules out their initiating a flash tube trigger are never produced in association with triggering tracks.

In principle all three perpendicular components of a track's momentum vector are important. In practice for most of the distribution commonly investigated, it is the longitudinal momentum which is of most significance. The PWC trigger is biased against events which only produce tracks which are potential triggers (sufficient momentum to leave the bubble chamber via its exit window and penetrate into the downstream chambers) at small angles in the electromagnetic plane relative to the beam axis. The absence of other triggering tracks suggests that the majority of the momentum of the system is carried by tracks entering the dead

region. However, the number of such tracks and how they share the momentum between them is not necessarily known. The momentum carried by individual tracks may not always be high.

Figure 6.3.1. shows what proportion of the three prong data taken by the PWC trigger remains as a function of the X_F of the tracks as the dead region cuts imposed in the PWC algorithm are widened to ±15,±20 and ± 30 wire numbers. The difference in acceptance across the X_F range becomes more significant as the dead region is increased. Figure 6.3.2 repeats 6.3.1 but this time only events with seven or more tracks are studied. Although in this case the statistics are poorer there is a clear reduction in the effect of increasing the dead region. The variation in acceptance above X_F values of about 0.3 is less than ten percent.

Figures 6.3.3 and 6.3.4 show the variation in track acceptance as a function of rapidity for three prongs and high prongs. The variation seen is produced by a dead region of $\pm$ 40 wire numbers. The acceptance does not vary except at very high rapidities for the high track data. The variation of the three prong acceptance is much greater reflecting once more the influence of pions from diffractive rhos.

The addition of lead glass triggers increases the number of lower energy tracks. However, this is probably not because it is more biased than the PWC trigger against high momentum tracks, but is because of the neutral track triggers. I shall assume in the next chapter that the effect of the trigger can be ignored.

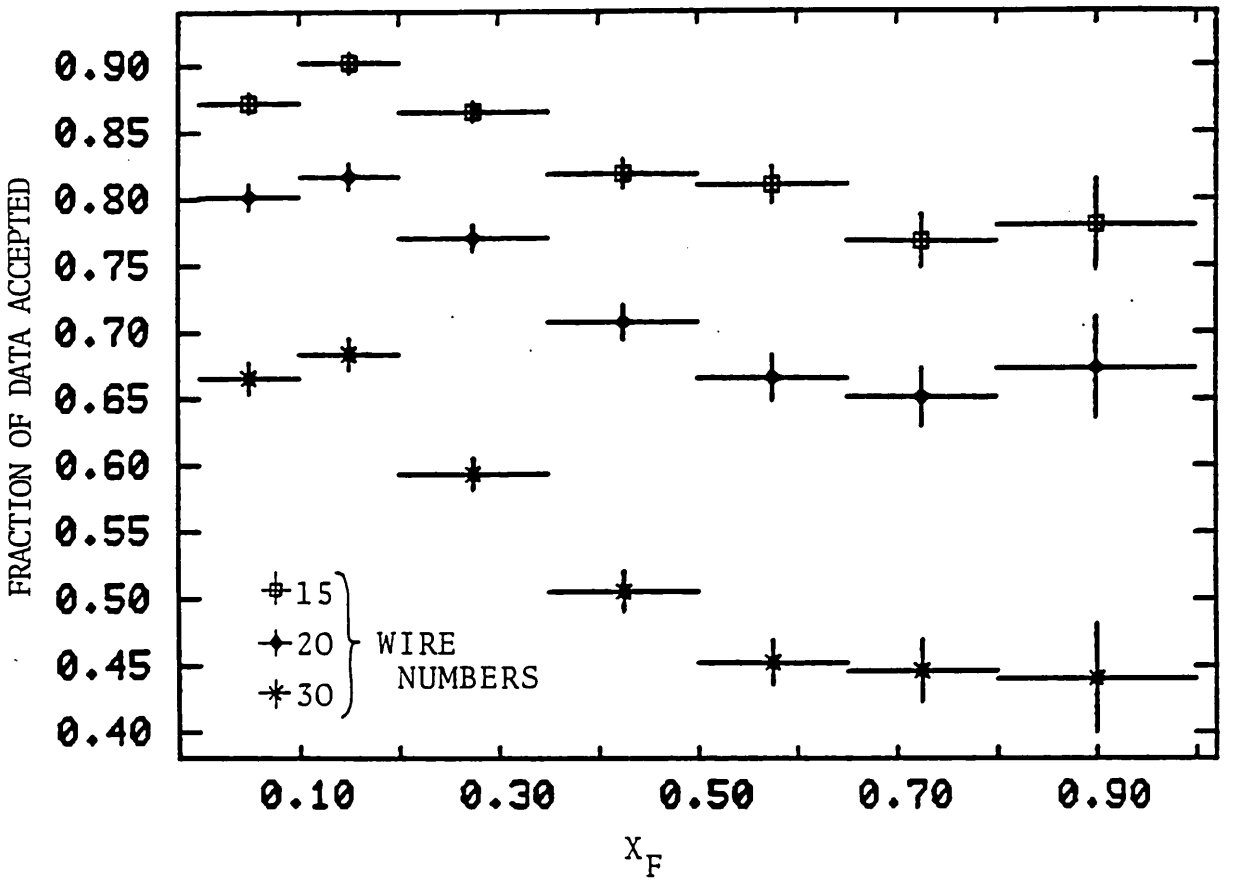

Figure 6.3.1 FRACTION OF THREE PRONG DATA REMAINING AS THE PWC TRIGGER DEAD REGION IS INCREASED (AS A FUNCTION OF X_F)

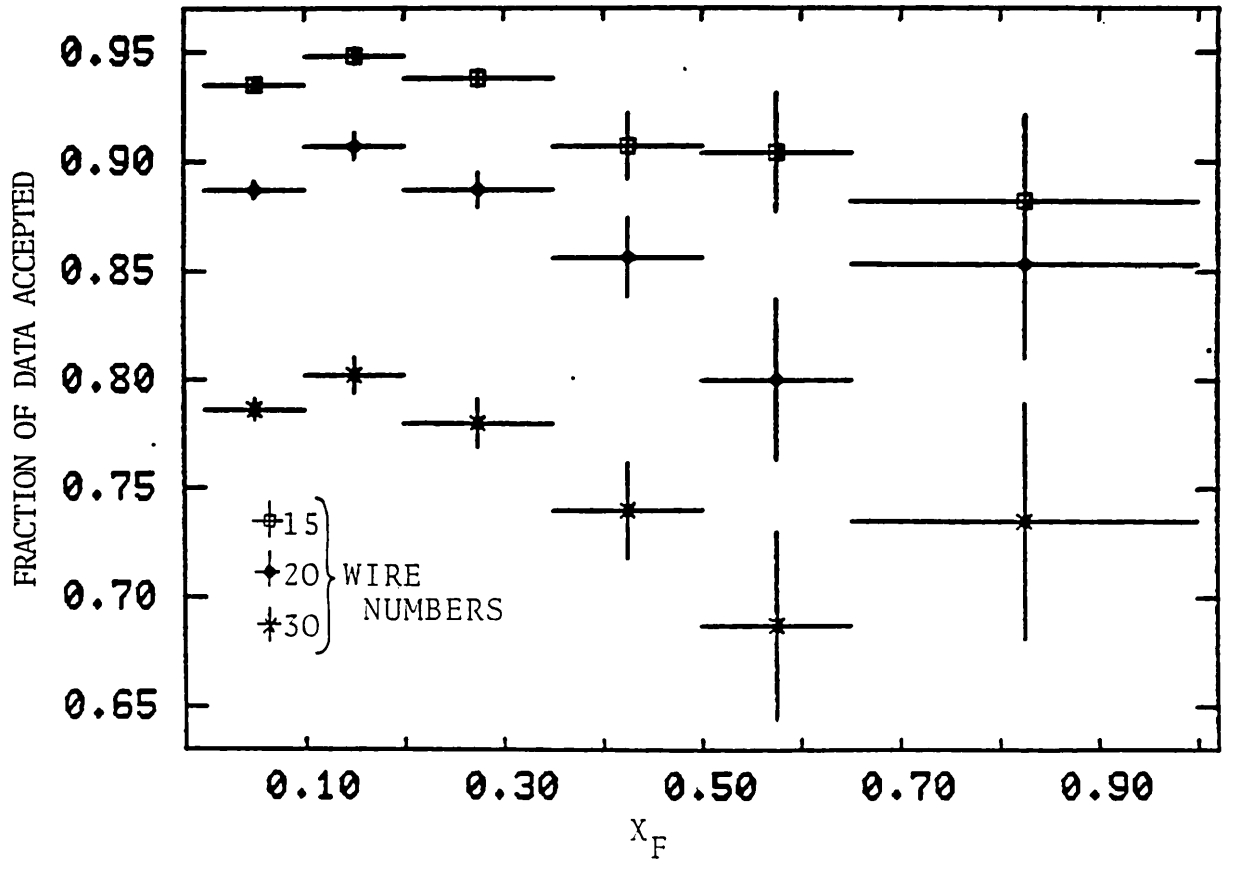

Figure 6.3.2 FRACTION OF HIGH PRONG DATA REMAINING AS THE PWC TRIGGER DEAD REGION IS INCREASED (AS A FUNCTION OF X_F)

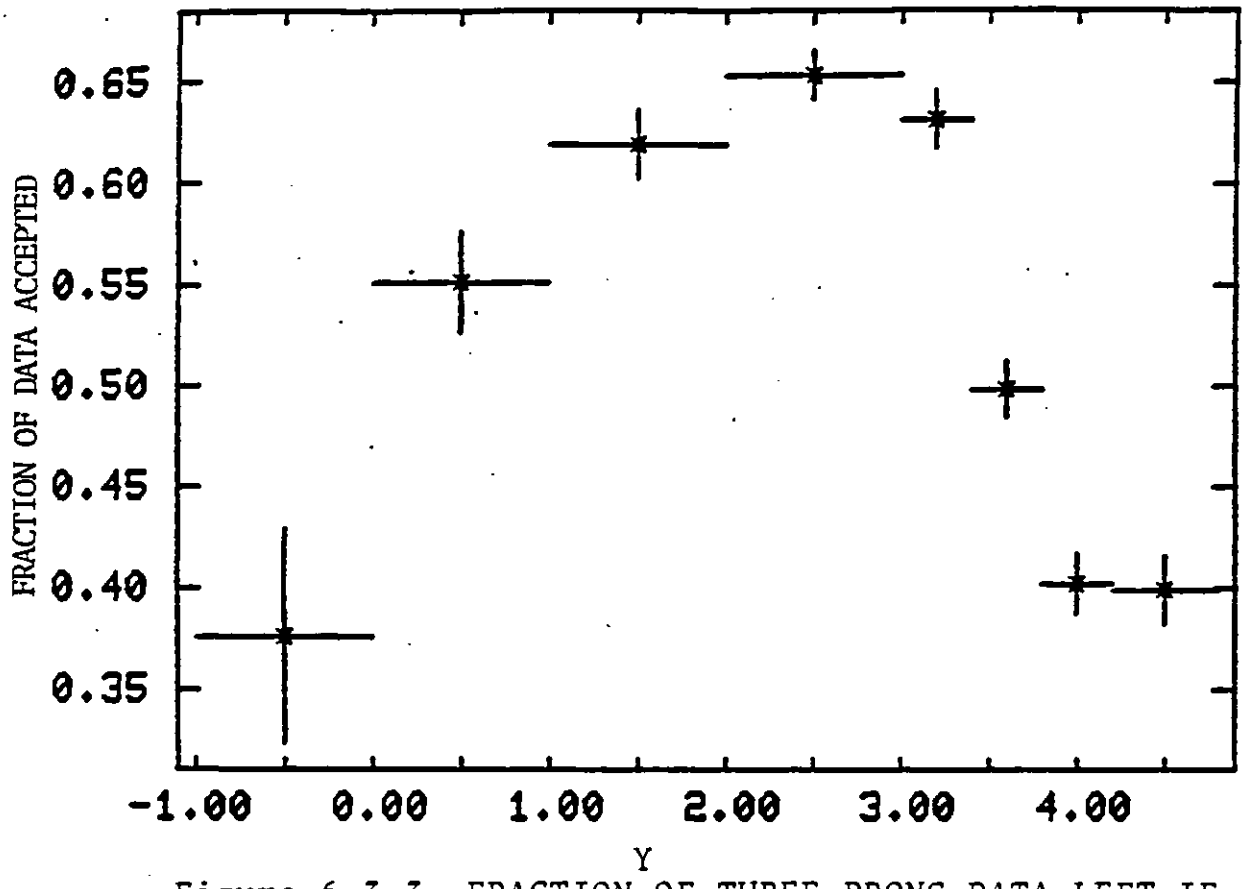

Figure 6.3.3 FRACTION OF THREE PRONG DATA LEFT IF PWC TRIGGER DEAD REGION IS INCREASED TO 40 WIRE NUMBERS(AS A FUNCTION OF Y)

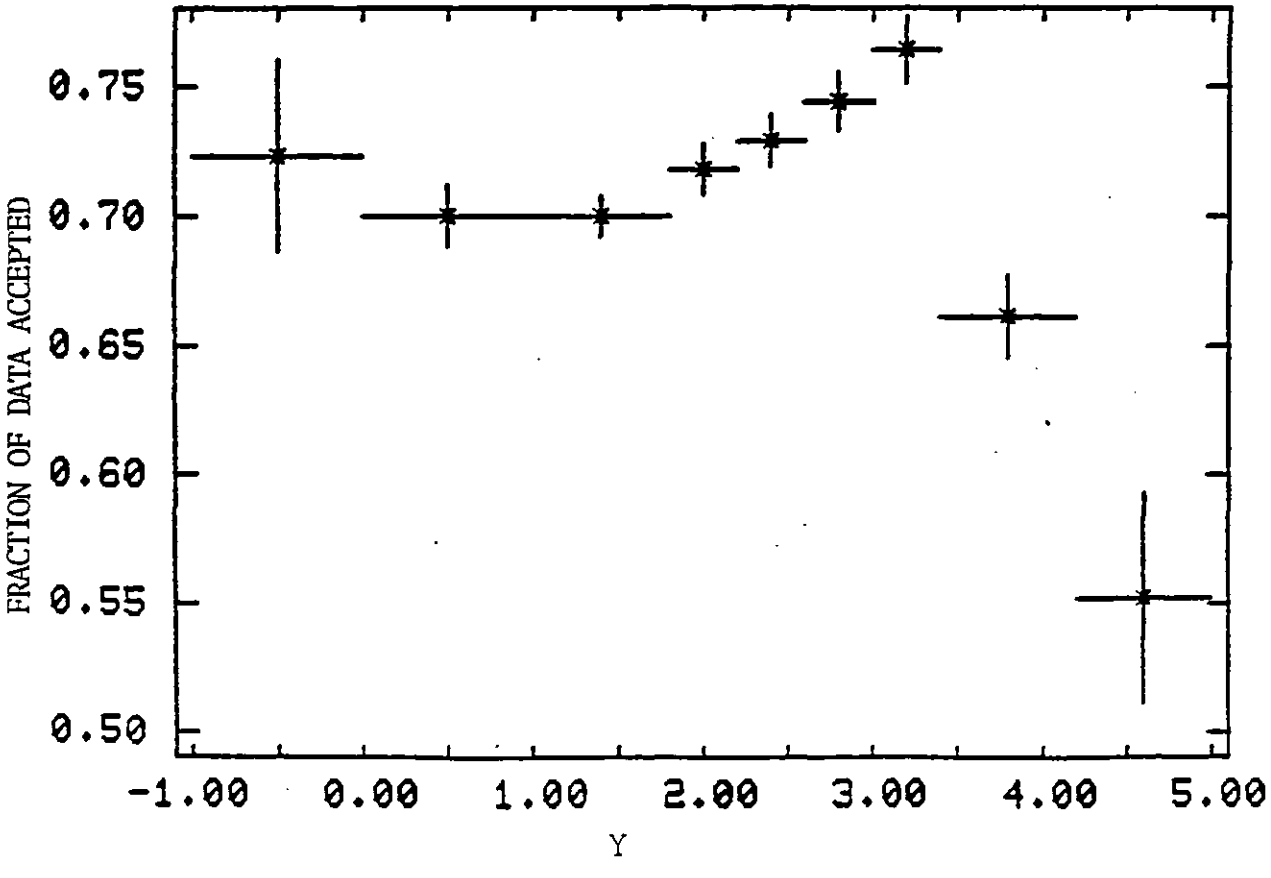

Figure 6.3.4 FRACTION OF HIGH PRONG DATA LEFT IF PWC TRIGGER DEAD REGION IS INCREASED TO 40 WIRE NUMBERS(AS A FUNCTION OF Y)

Chapter 6 - References

[1] A.V. Bevan et al; IC/HENP/82/1, submitted to NIM

CHAPTER 7

RESULTS

7.1 Results of a Search for the Photoproduction Symmetry Frame

Figures 7.1.1 to 7.1.3 show the longitudinal momentum distributions of negative particles only (all particles are assumed to be pions), in the centre of mass (Q = 1), VMD (Q = 1.5), and point-like (Q = 3.0) frames of reference. The distributions are all scaled by the same factor of $2/\sqrt{s}$ for convenience although only in the centre of mass frame does this yield an X_F distribution. The Q value denoting a frame of reference is smaller than that characterising the symmetry frame if the forward slope is gentler than the backward slope, and is larger if the backward slope is less steep than the forward (beam direction). Although the backward slope can be fitted by a single exponential the forward distribution is not well described by such a fit. However, the VMD frame does not approximate to a symmetry frame even for centrally produced particles since the asymmetry between the number of forward and backward travelling tracks is too large to be the result of beam spread effects and a kaon contaminant (of less than 25%). It would appear on this evidence that the photon does not always interact as a vector meson.

An alternative method to expressing the momentum distribution in several frames in order to find a frame in which the forward and backward slopes are similar is to find the centre of symmetry of the particles' rapidity distribution.

$$y = \frac{1}{2} \ln \left[\frac{E + P_L}{E - P_L} \right] \qquad 7.1.1$$

Since y is an additive variable E and P_L can be measured in any frame of reference. The Q value characterising the symmetry frame can then be found in terms of the Lorentz boost (β) needed to translate the distribution from that frame to the Q-frame (where it is symmetric about y = 0). Assuming E and P_L are measured in the laboratory frame;

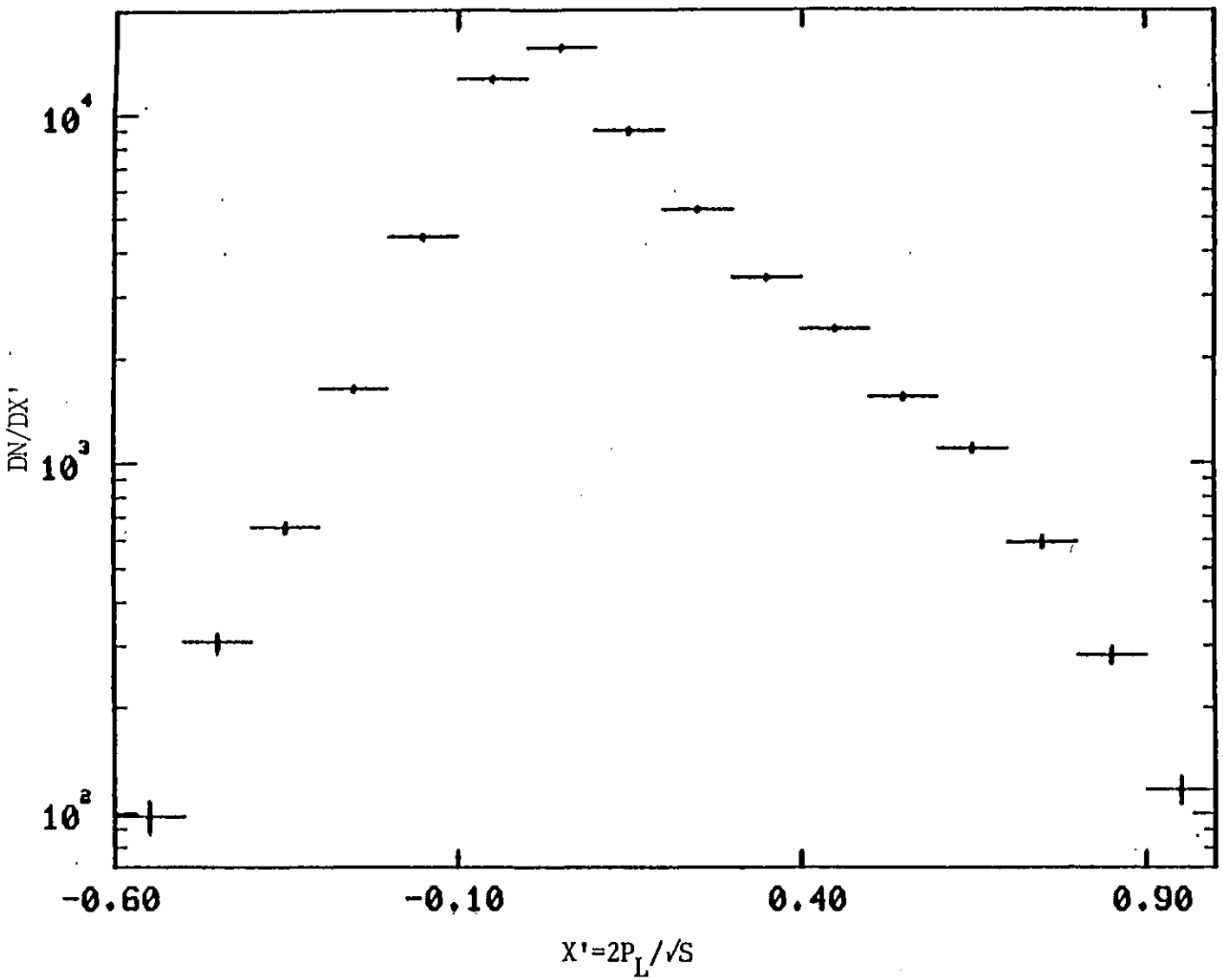

Figure 7.1.1 DISTRIBUTION OF LONGITUDINAL MOMENTA OF TRACKS AS MEASURED IN CENTRE OF MASS FRAME (Q = 1.0)

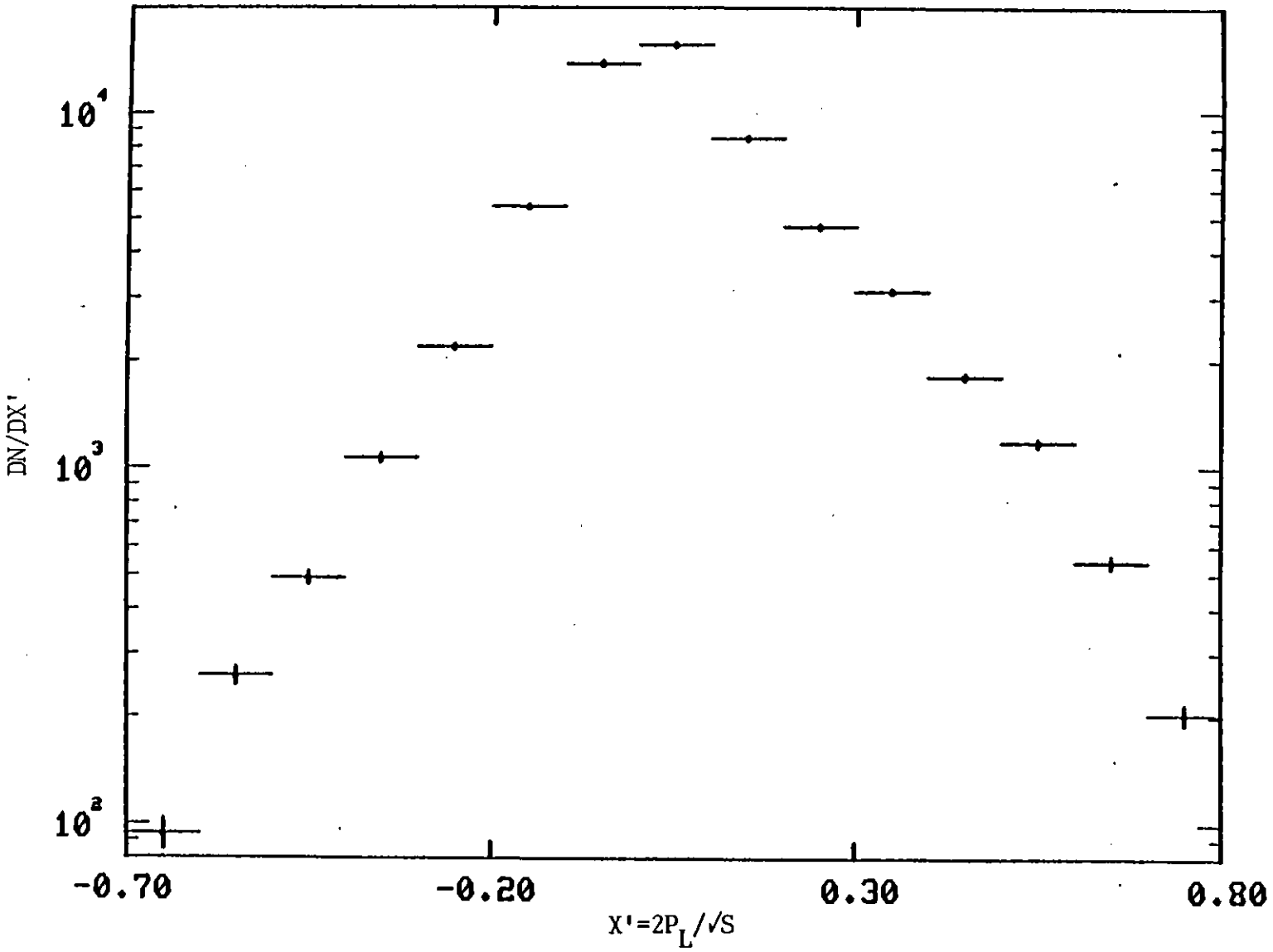

Figure 7.1.2 DISTRIBUTION OF LONGITUDINAL MOMENTUM OF TRACKS IN THE VMD FRAME (Q = 1.5)

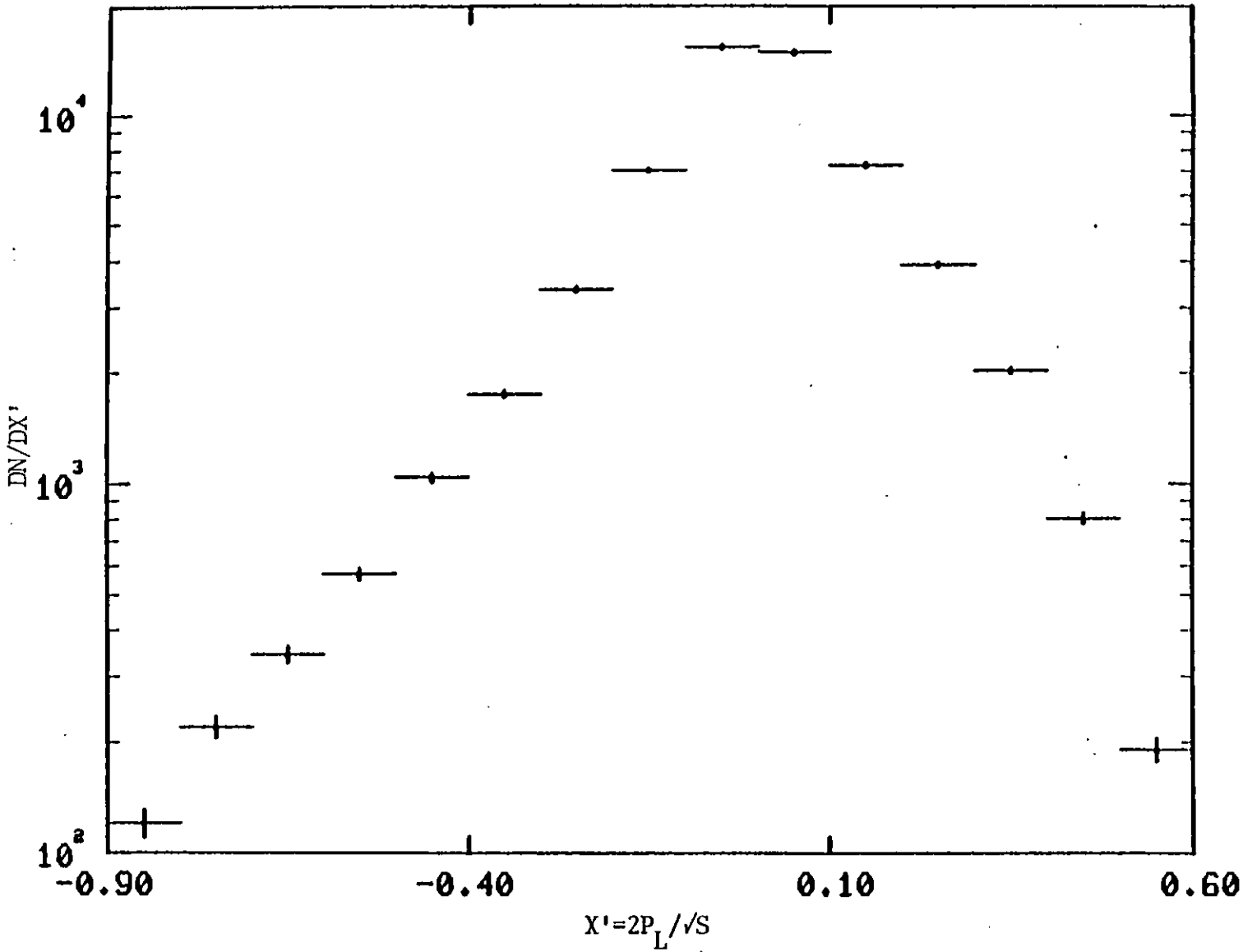

Figure 7.1.3 DISTRIBUTION OF LONGITUDINAL MOMENTUM OF TRACKS IN THE POINT-LIKE FRAME (Q = 3.0)

$$\beta = \frac{e^{2y_s} - 1}{e^{2y_s} + 1} \qquad 7.1.2$$

where, y_s is the centre of symmetry of the distribution in the laboratory frame.

Then,

$$Q = \frac{\beta m_p}{E_\gamma(1-\beta)} \qquad 7.1.3$$

where, m_p is the mass of the proton

and E_γ is the photon energy in the laboratory.

(The intermediate steps in the calculation and a proof that y is additive are given in appendix B).

A difficulty involved in using this method is that small changes in y_s result in significant differences between the corresponding Q values. Figure 7.1.4 shows the depencence of the Q value on y_s (assuming a nominal beam energy of 19.6 GeV). It is, therefore, necessary to locate the centre of the distribution as accurately as possible. The mean of the distribution is biased by beam spread effects and the kaon contaminant (all particles are assumed to be pions), its peak is only an approximate indication of the location of its true centre.

Figure 7.1.5 shows the y distribution for all negatively charged particles. The mean value of y for this distribution is about 2.4. Let

$$F/B = \frac{\text{Number of tracks at distance } \Delta y \text{ from } y_s \text{ (travelling forwards in rapidity space)}}{\text{Number of tracks at distance } -\Delta y \text{ from } y_s} \qquad 7.1.4$$

Figures 7.1.6 to 7.1.8 show the dependence of F/B on Δy, assuming y_s values of 2.3, 2.4 and 2.5 respectively. The choice of 2.4 for the value of y_s minimises the apparent forward/backward asymmetry.

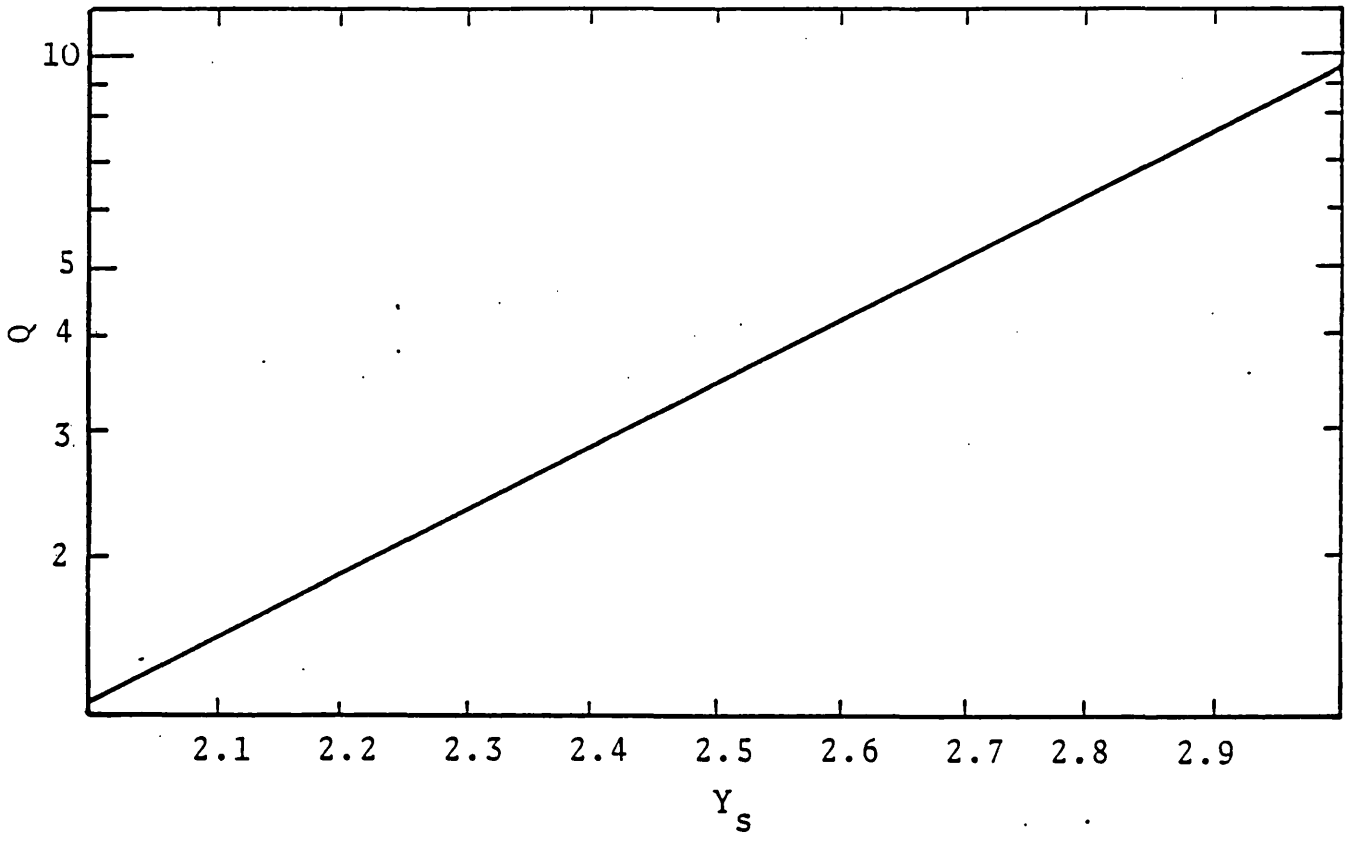

Figure 7.1.4 DEPENDENCE OF Q ON Y_s

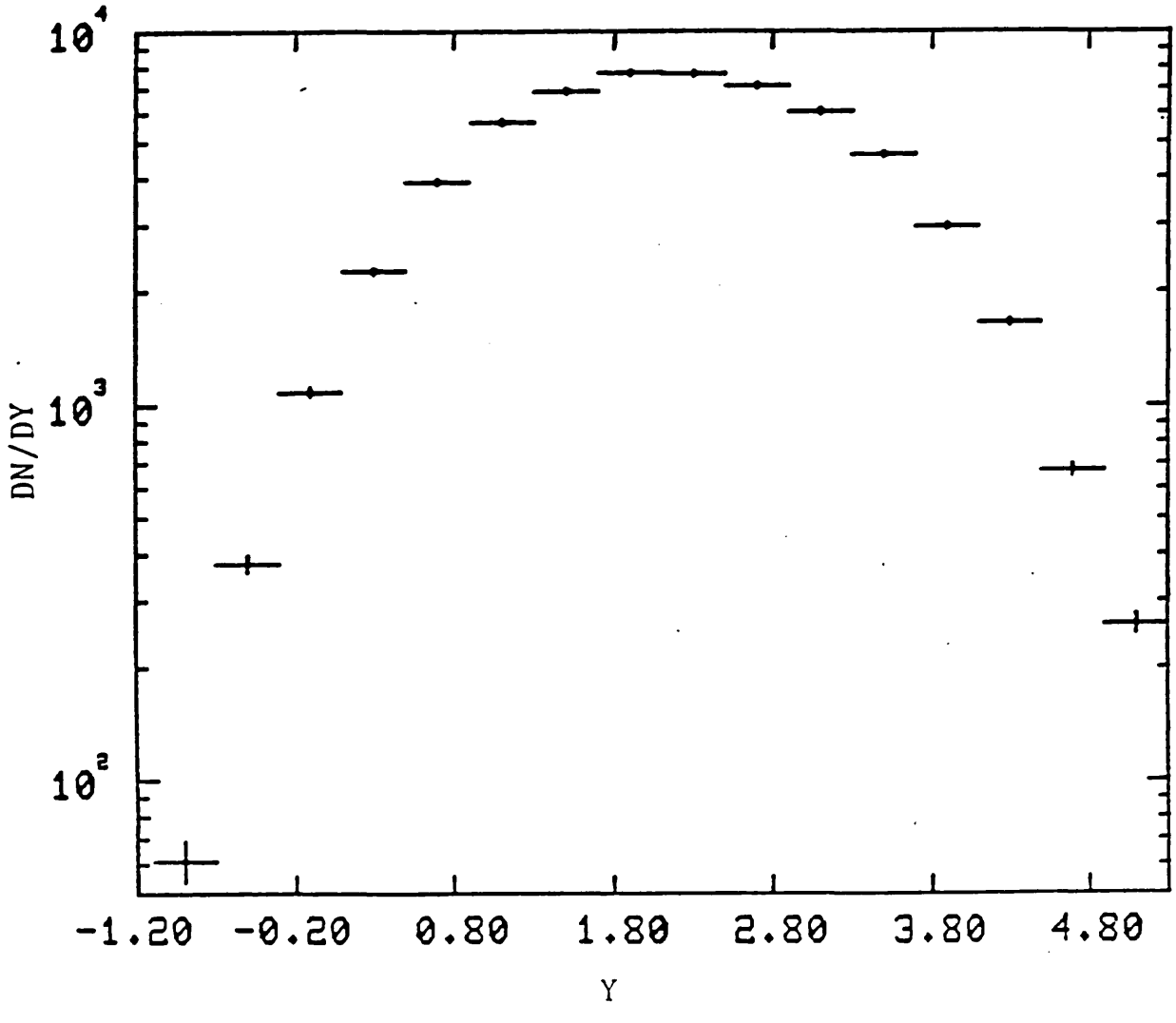

Figure 7.1.5 RAPIDITY DISTRIBUTION (MEASURED IN LABORATORY FRAME) FOR ALL NEGATIVE TRACKS

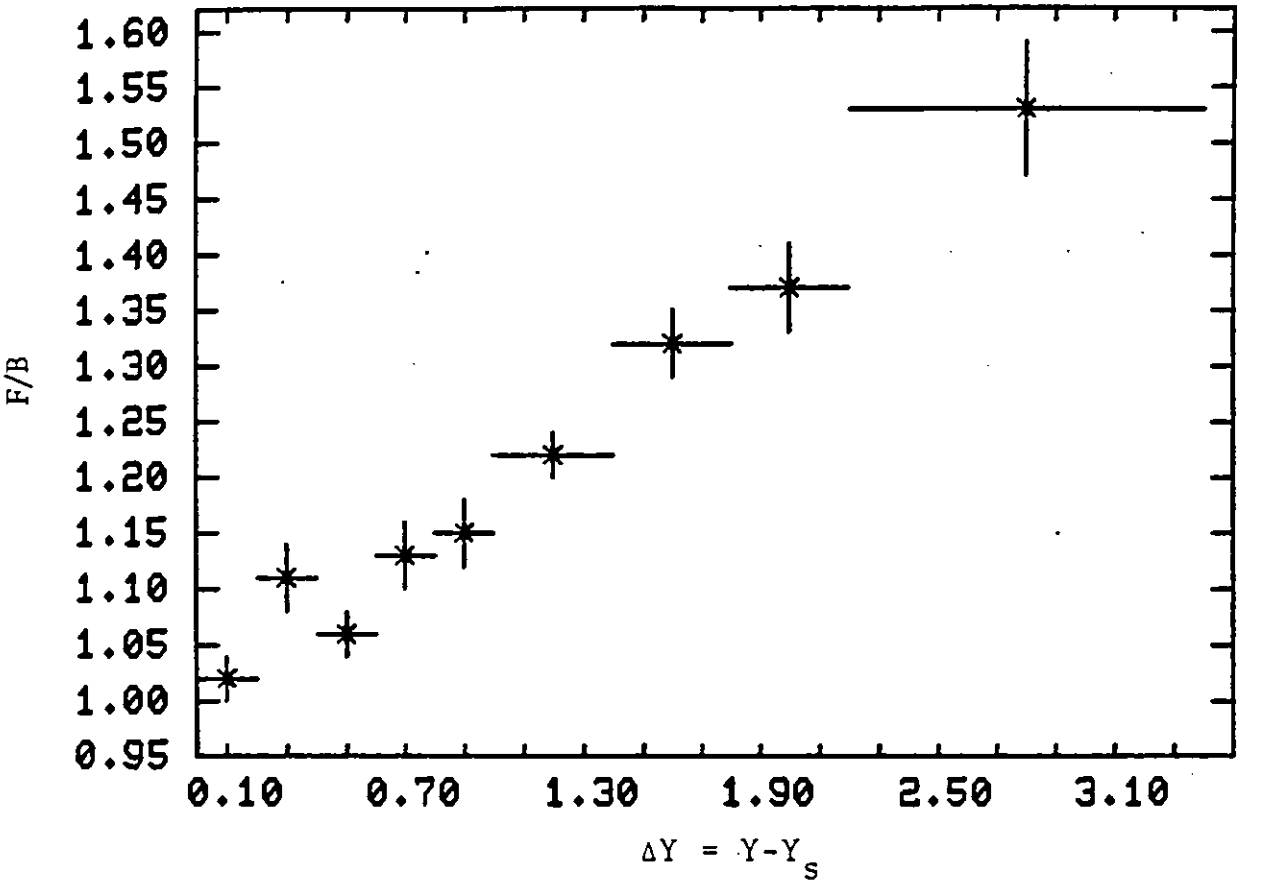

Figure 7.1.6 FORWARD BACKWARD ASYMMETRY IN RAPIDITY SPACE:Y_s=2.3

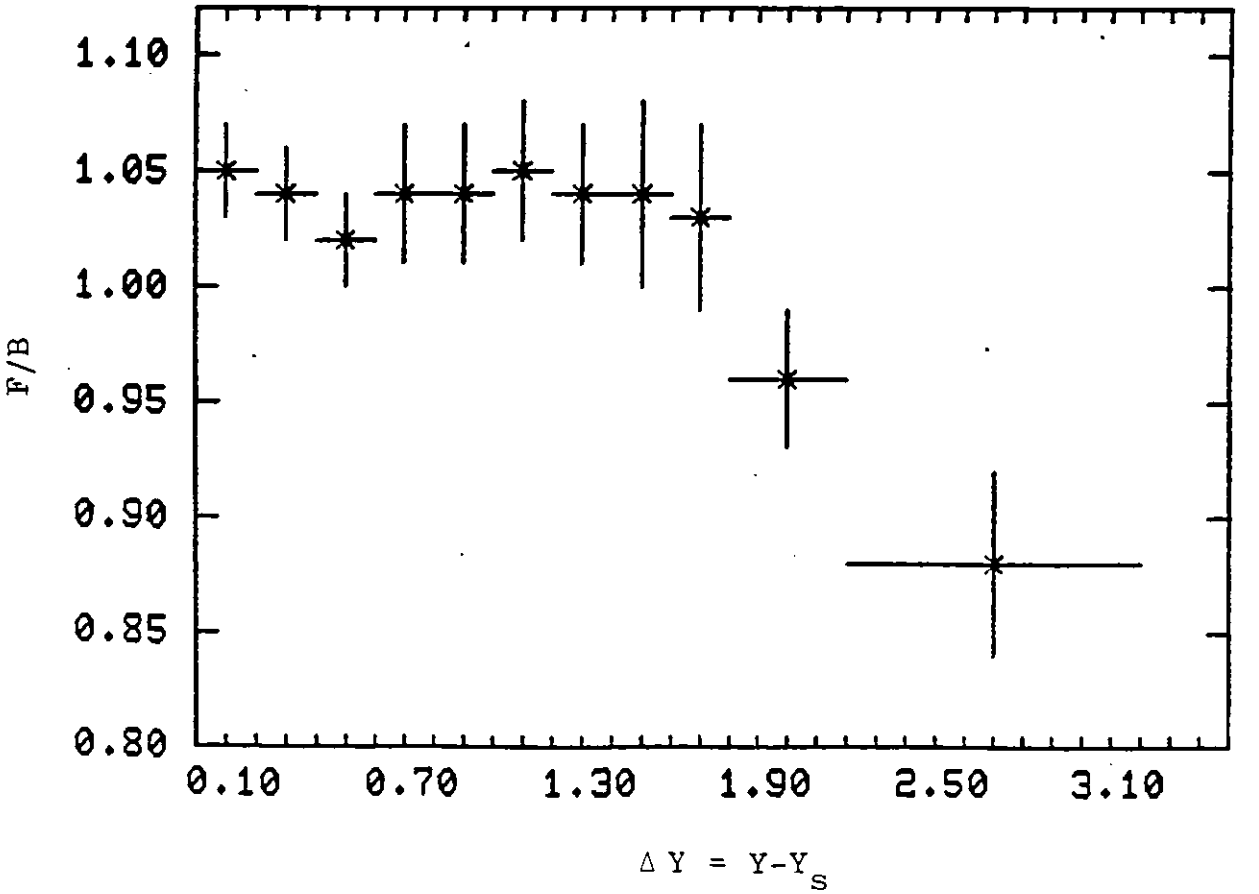

Figure 7.1.7 FORWARD BACKWARD ASYMMETRY IN RAPIDITY SPACE:Y_s=2.4

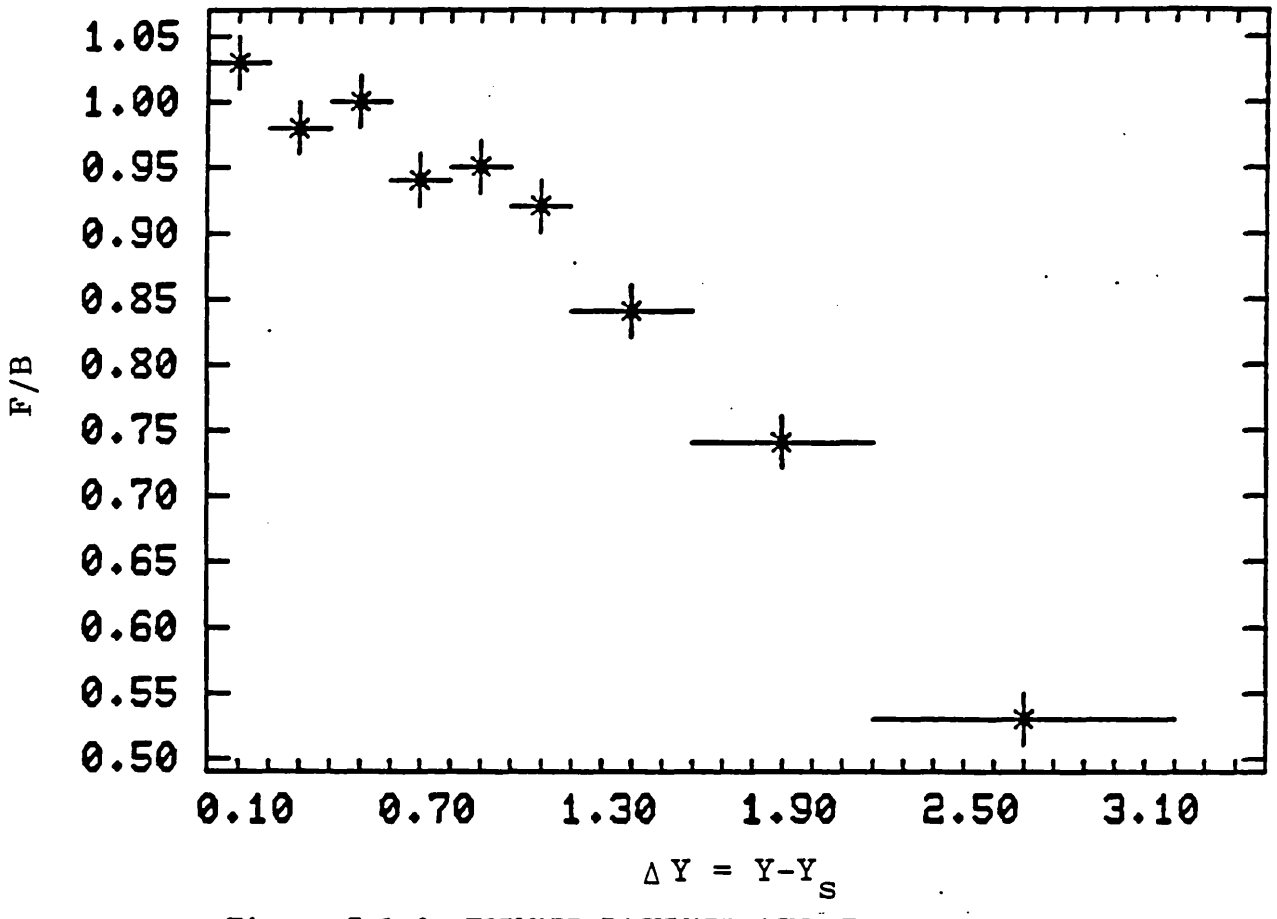

Figure 7.1.8 FORWARD BACKWARD ASYMMETRY IN RAPIDITY SPACE: Y_s=2.5

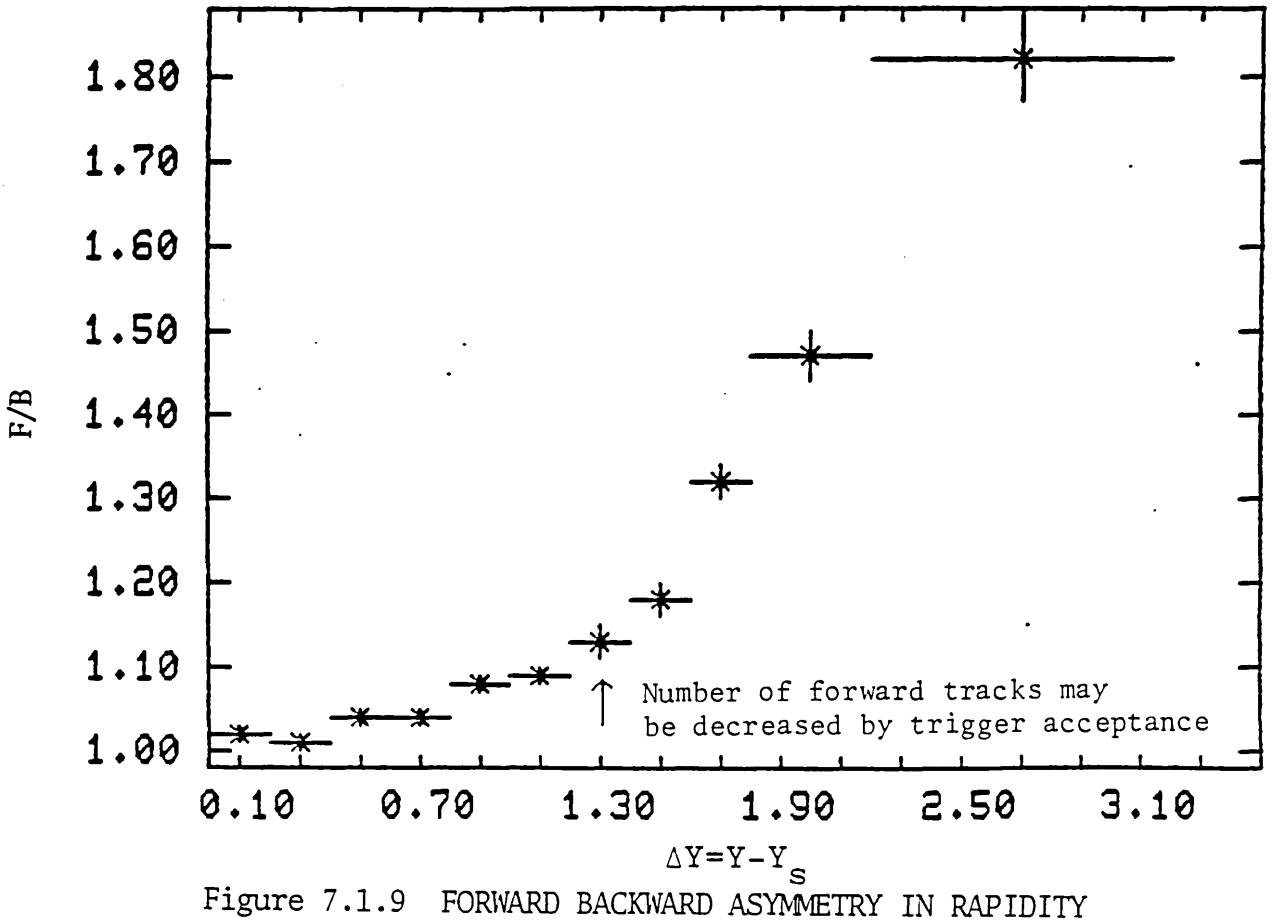

Figure 7.1.9 FORWARD BACKWARD ASYMMETRY IN RAPIDITY SPACE, MONTE CARLO RESULTS FOR Y_s=2.4 AS CENTRE OF SYMMETRY

Figure 7.1.9 shows how much asymmetry would be expected as a result of biases if the distribution were symmetric in the Q-frame related to a y_s value of 2.4 (Q equals 2.9). The original distribution was generated with a shape similar to that found for the rapidity distribution, which was, however, assumed to be symmetric and a ten percent kaon background was included (having the same shape). The results shown in Figure 7.1.9 do not depend strongly on the shape assumed. However, if the kaon distribution is less spread than the pion, the excess of forward tracks is increased at low values of Δy and decreased at high values of Δy. The results are also not very dependent on the Q frame assumed (for Q values in the range 2.4 to 3.5). The Monte Carlo was not modified to allow for a possible loss of high energy tracks due to limited trigger acceptance but the rapidity difference at which such effects may become important is marked.

The results show that the Q value specifying the symmetry frame lies within the limits 2.4 to 2.9. Since this result cannot be interpreted as meaning that the photon contains a fractional number of partons two hypotheses remain. The first, that the proton does not contain three valence quarks will not be discussed further. The second, that the result represents an admixture of data distributed symmetrically in the VMD frame and data produced by a point-like photon interacting, is consistent with the ideas discussed in chapters four and five. It suggests that a suitable selection of data might enable each component to be isolated (or at least enhanced) and studied separately. One way to divide up the data is to assign tracks to groups on the basis of the topology of the event in which they were produced.

Figure 7.1.10 shows the longitudinal momentum distribution in the VMD frame for tracks from events in which at least seven charged particles are produced (not including those formed as a result of neutral strange particles decaying). Figure 7.1.11 shows the asymmetry between the forward and backward travelling tracks in rapidity space for y_c equals

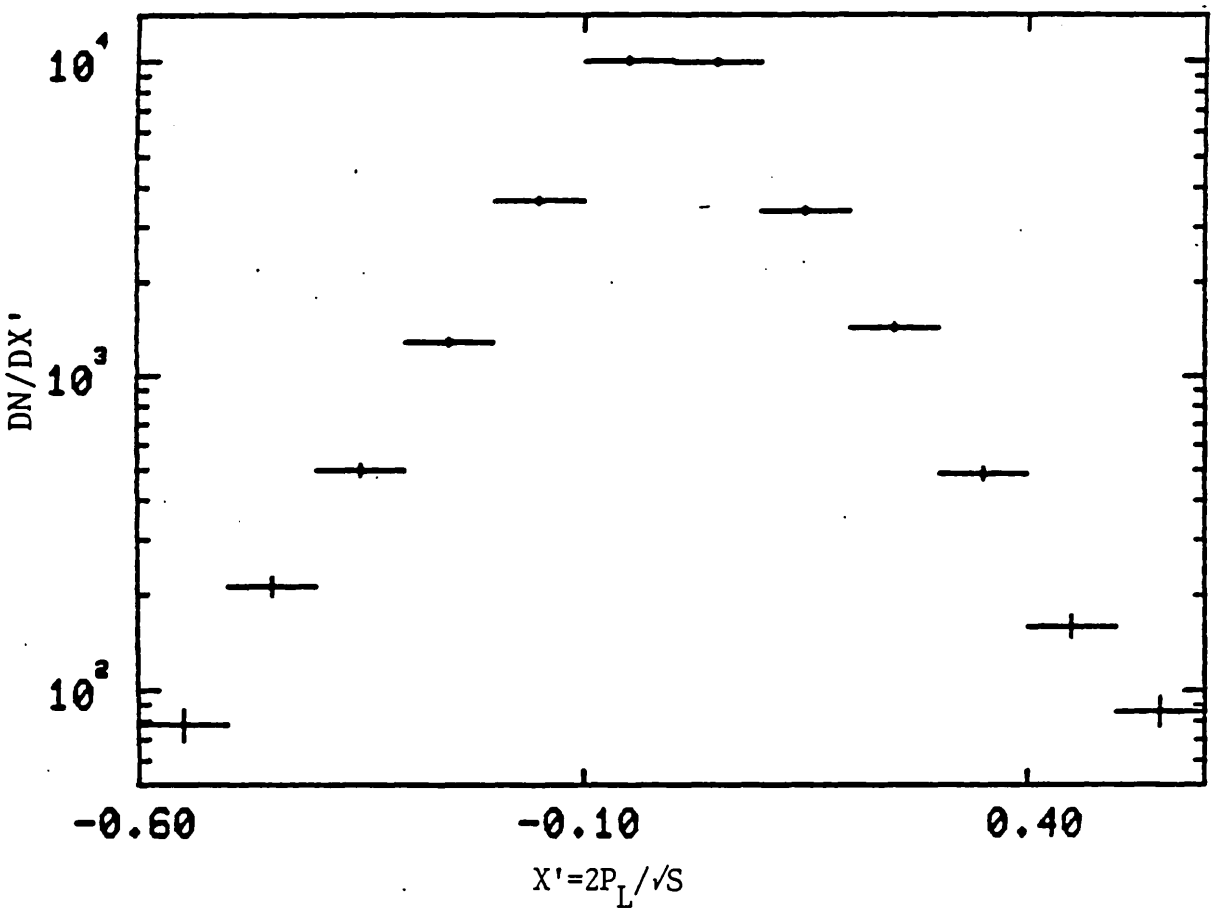

Figure 7.1.10 X' DISTRIBUTION FOR NEGATIVE TRACKS FROM HIGH PRONG EVENTS (Q = 1.5)

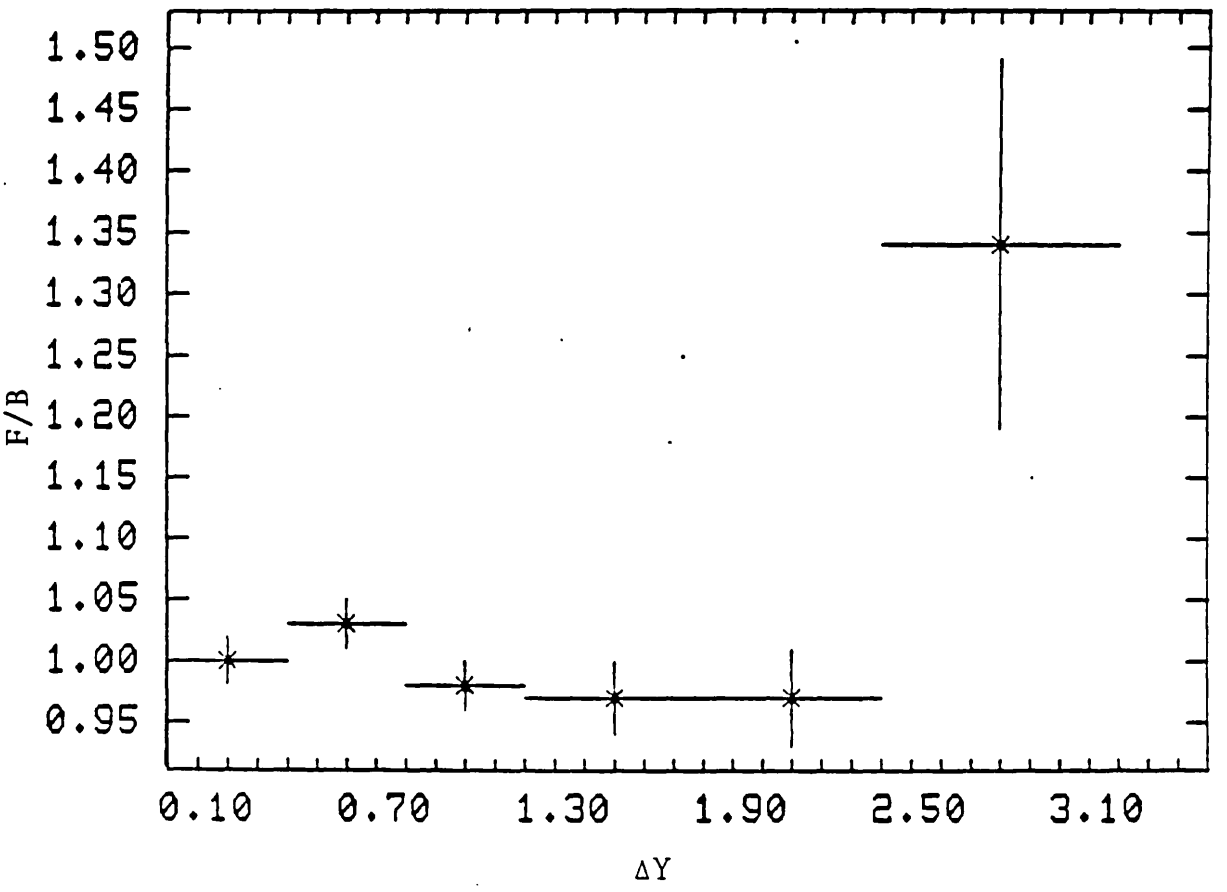

Figure 7.1.11 FORWARD/BACKWARD ASYMMETRY IN RAPIDITY SPACE FOR HIGH PRONGS,ASSUMING Q=1.5

2.08 (the assumption being made that the distribution is symmetric in the VMD frame). The asymmetry is very small, although there is a noticeable excess of fast forward tracks over very backwards tracks (which could indicate that the kaon distribution is flatter than that for the pion). This possibly indicates that the Q-value of the symmetry frame is below 1.5 (though in this case the Monte Carlo results are not conclusively higher than those obtained for the real distribution), however Q values of below 1.3 would be inconsistent with the data.

This result implies that the photon contains two interacting constituents. It might be argued that the point-like photon interacts as a quark-antiquark system. However in this case either the quark or the antiquark will tend to carry the majority of the photon momentum (compare the quark/antiquark division of the photon energy with the division of the photon energy between an electron and a positron in pair production) and so only one constituent dominates the interaction. When the photon interacts as or via a vector meson state the quark and anti-quark are more likely to share its momentum equally (otherwise the state will not be bound). The high charged multiplicity events can be interpreted therefore as being produced by the photon interacting hadronically.

The data symmetric in the point-like frame must, if it exists, be associated with low charged multiplicity events; therefore the study was restricted to three prong interactions. Figure 7.1.12 displays two sets of data, the first gives the y distribution of negative pions from rho decays (identified by fit), the second is the y distribution of negative particles from the remaining three prong events. Neither distribution is even approximately symmetric, the distribution for tracks from the rho decay being particularly distorted and suggesting a possible way to interpret both plots.

The two distributions may each be divided into two separate

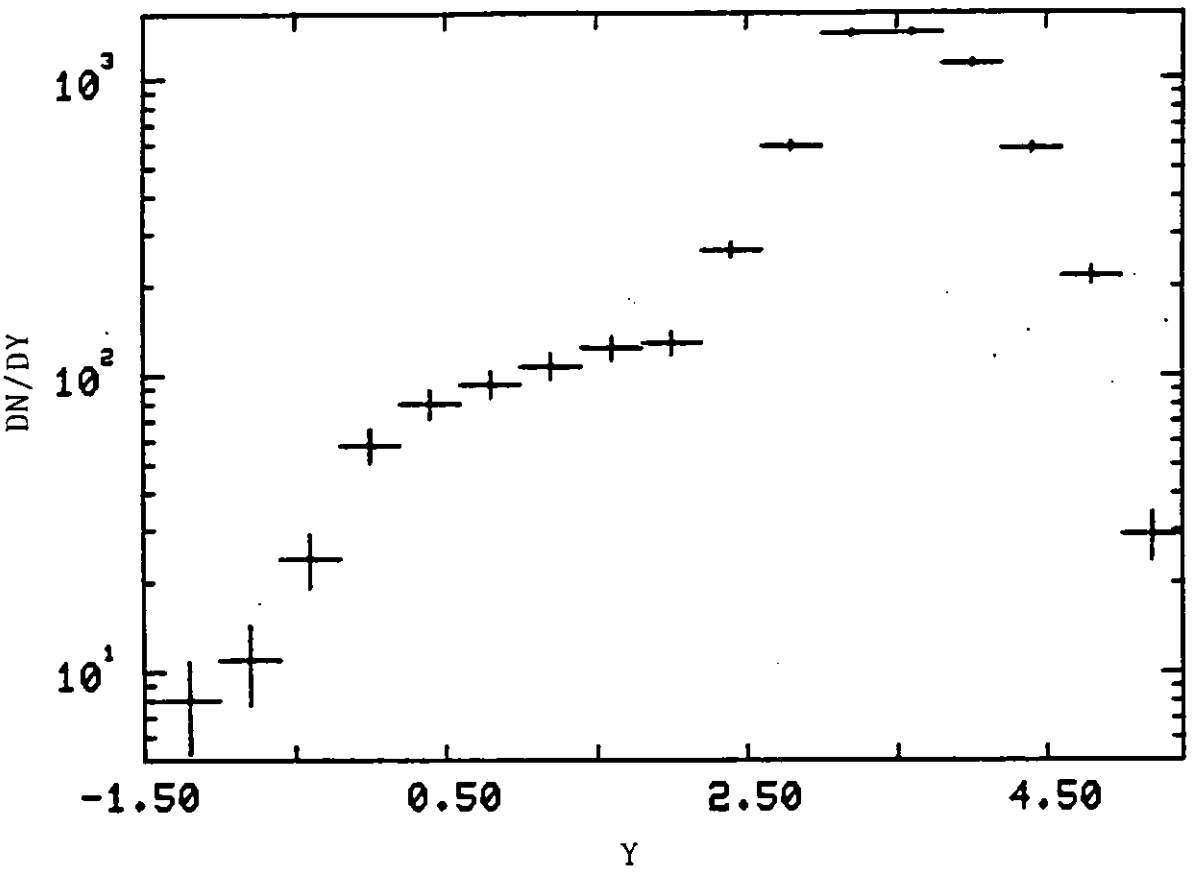

Figure 7.1.12a RAPIDITY DISTRIBUTION FOR NEGATIVE PIONS FROM RHO DECAYS

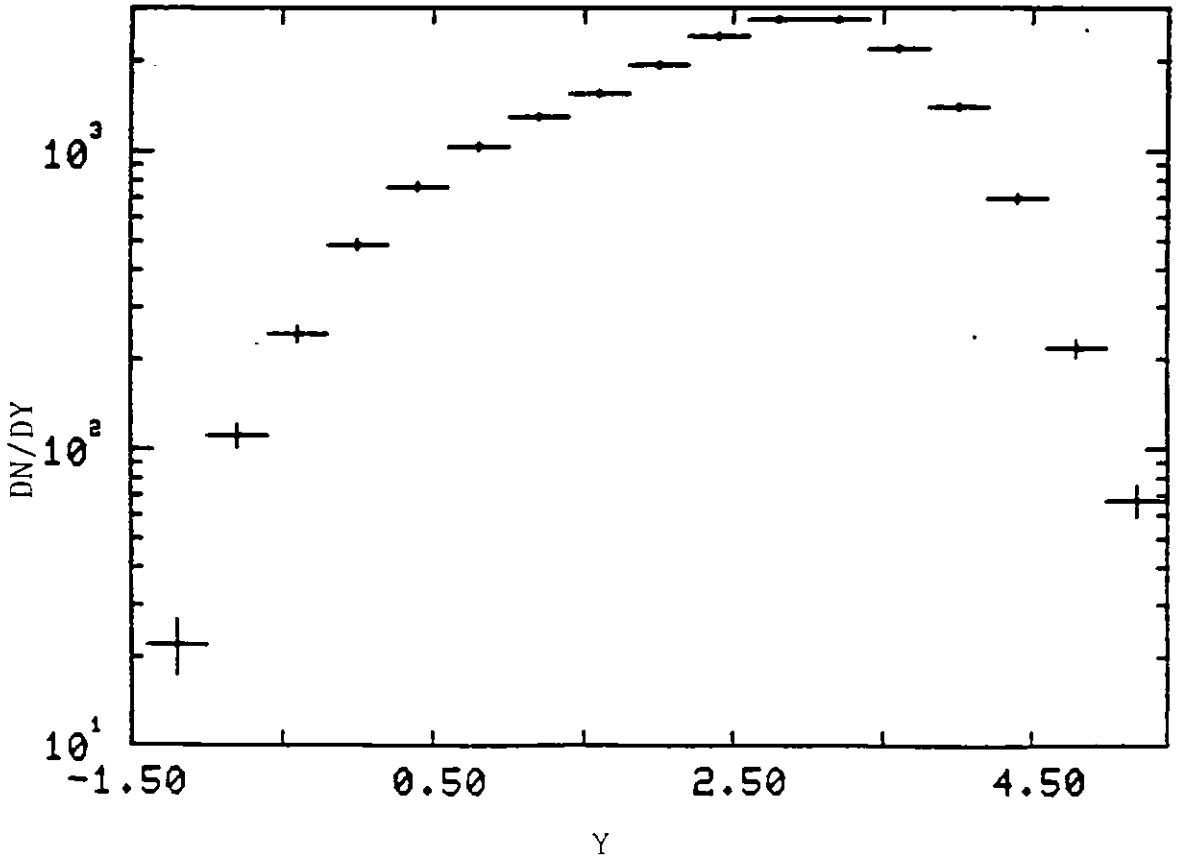

Figure 7.1.12b RAPIDITY DISTRIBUTION FOR NEGATIVE TRACKS FROM THREE PRONG EVENTS

contributions. The first is symmetric about y_s values of about 3.5 to 3.8 (corresponding to Q-values for the associated frames of reference of between 30 to 50). This component dominates the rho distribution and is associated with diffractive interactions of the photon to which a Q-frame analysis is inapplicable. It is also responsible for the levelling off of the forward slope at moderate longitudinal momentum values as seen (most clearly in Figure 7.1.1) in the distributions discussed at the start of this section. The second contribution is symmetric about much lower values of y_s.

The exact division into two distributions is however difficult to do accurately since both the original distributions have been distorted. If the approximation is made that these biases may be ignored, it is possible to extract distributions symmetric about y_s equals 3.5 and y_s equals 2.08 assuming that there is a contribution symmetric about y_s equals 2.08. However, this method also allows the extraction of distributions symmetric about y_s equals 3.5 and y_s equals 2.42 assuming this time that the point-like photon is dominant. Figure 7.1.13 compares the forward/backward asymmetries in the two cases if the diffractive contribution is assumed perfectly symmetric. There is no justification for preferring one solution over the other.

It may be argued that a decision between the two alternatives would be possible if all the systematic errors were fully understood. Whilst this may be possible in the future when results on the kaon distributions become available I think that the difficulty is inherent in the lack of separation in rapidity space between the two alternative centres of symmetry. It should be noted for future reference that the removal of rho fits does not remove entirely the presence of resonance decay effects from the three prong distributions.

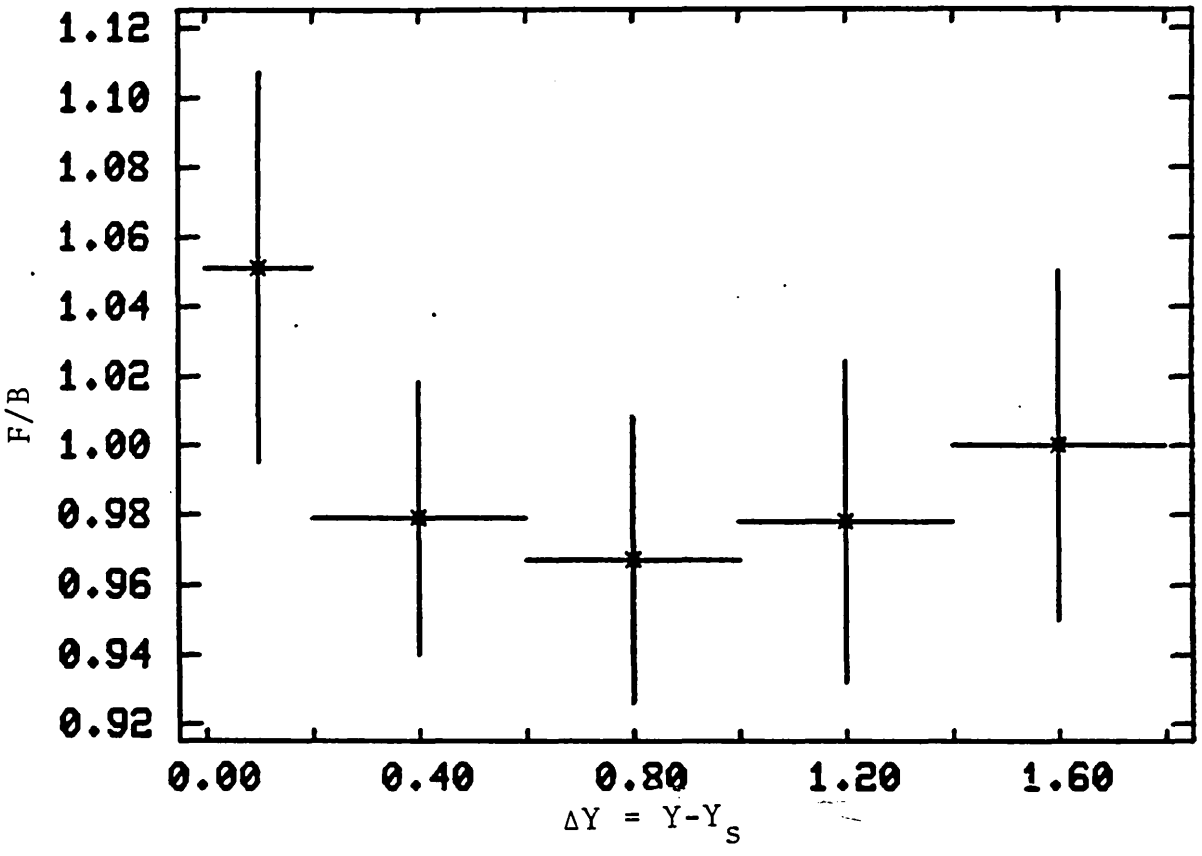

Figure 7.1.13a FORWARD/BACKWARD ASYMMETRY IN RAPIDITY SPACE IF ASSUME PART OF THREE PRONG DISTRIBUTION IS SYMMETRIC IN VMD FRAME (Q = 1.5)

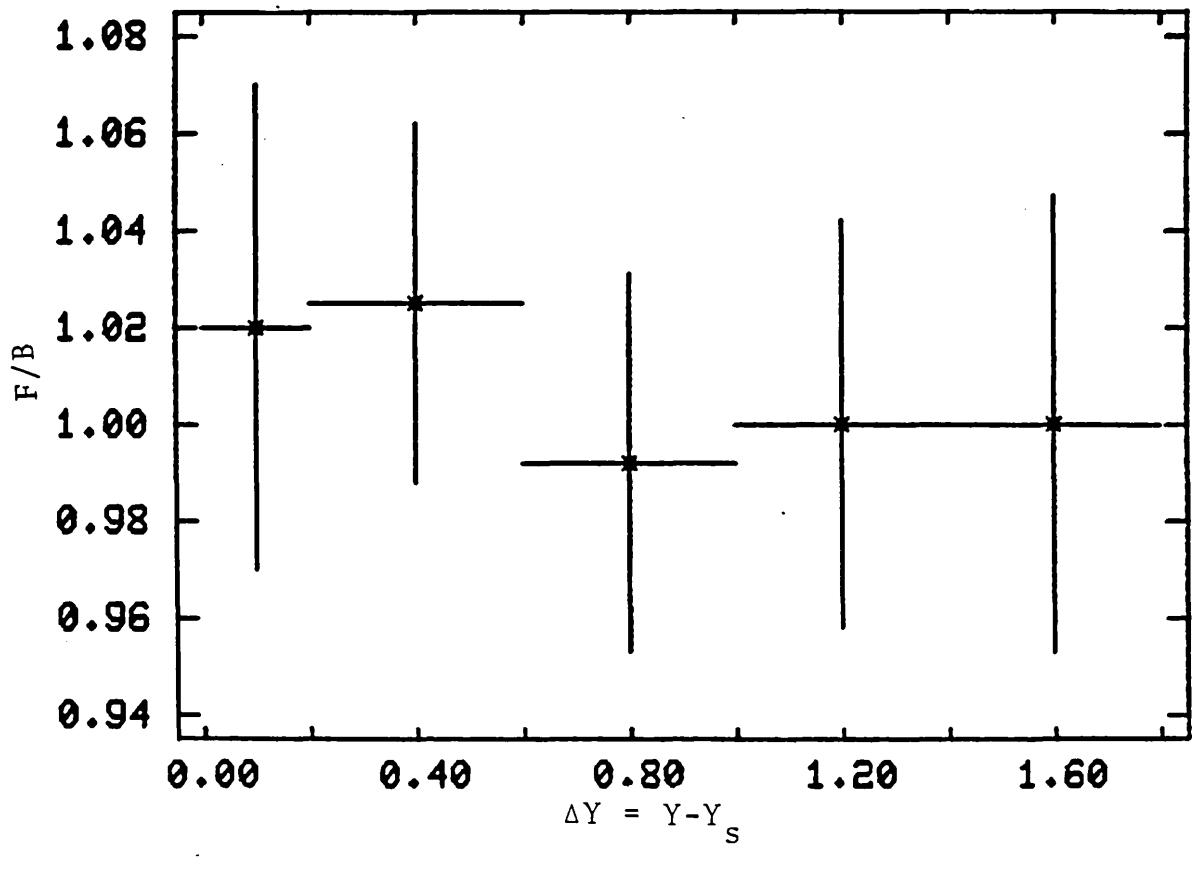

Figure 7.1.13b FORWARD/BACKWARD ASYMMETRY IN RAPIDITY SPACE IF ASSUME PART OF THREE PRONG DISTRIBUTION IS SYMMETRIC IN POINT-LIKE FRAME (Q = 3.0)

To summarise the results of this section;

i) The results from the analysis of longitudinal momentum distributions and from the rapidity frame analysis do not conflict so the concept of a symmetry frame may be considered meaningful.

ii) The system of symmetry cannot be uniquely identified with either the VMD or the point-like frame.

iii) The system of symmetry is dependent on the charged particle multiplicity of the events and for high prongs is consistent with expectations if the photon interacts as a vector meson.

iv) The analysis of the low charged multiplicity events is confused by the presence of tracks from resonance decays.

7.2 Asymmetries in the Beam Fragmentation Region

The quantity $\Delta^{\pi}(p)$ discussed in section 4.5 is defined by equation 4.5.4 in terms of the difference between the negative and the positive pion invariant cross sections so as to limit theoretical uncertainties. To minimise experimental biases the ratio, R, of the cross sections is a more suitable object for study;

$$R = \frac{\frac{dN}{dX_F}(\gamma p \to \pi^+ X)}{\frac{dN}{dX_F}(\gamma p \to \pi^- X)}$$

$$= \frac{\frac{dN}{dX_F} + (\frac{dN}{dX_F})^+}{\frac{dN}{dX_F} + (\frac{dN}{dX_F})^-} \qquad 7.2.1$$

where, $\frac{dN}{dX_F}$; represents terms which contribute equally to both the positive and negative cross sections

and $(\frac{dN}{dX_F})^+$, $(\frac{dN}{dX_F})^-$ represent the charge dependent contributions.

The advantage in using $\Delta^{\pi}(p)$ is that the masking effect of the vector meson mediated photon interactions is removed, however the effects of poor statistics at high X_F and a rapidly changing acceptance which may lead to large corrections can distort the result. The advantage of using R is that systematic biases are compensated for although the asymmetry may be masked by the effects of the $\frac{dN}{dX_F}$ term included in equation 7.2.1. The variation of R from unity is therefore evidence of an effect whilst a null result is not a disproof.

Figure 7.2.1 shows the dependence of R on X_F for tracks which are identified as pions on the basis of information from the Cerenkovs. The data are split into low P_t (less than 0.4 GeV/c) and high P_t (greater than or equal to 0.4 GeV/c) components. The contributions to the data associated with high prong(more than six tracks at the primary vertex) and three prong events are shown separately in Figures 7.2.2 and 7.2.3 respectively. In order to make the variation clearer the three data sets were each divided into four and R calculated for each kinematic region, Table 7.2.1 summarises the results. There is an implicit cut on X_F in order that the pions can be distinguished from other particles on the basis of the Cerenkov information.

Since the photon is neutral, when it fragments the products of the process carry no net charge. The behaviour of the positive and the negative fragments must correlate therefore; accumulation of positive pions at high X_F and P_t requires an increase above average in the number of negative pions at lower X_F and P_t values. The overall ratios in Table 7.2.1 are prevented from being unity partly because much of the X_F range is not covered, and partly because of the inclusion of misidentified protons and proton fragments. The effect of the target fragments should die out rapidly away from the central region and will alter the three prong results more significantly than the high prong (the ratio of

X_F \ P_t	<0.6 GeV/c	>0.6 GeV/c	ALL
<0.5	1.05 ± .02	1.05 ± .04	1.05 ± .02
≥0.5	1.04 ± .02	1.25 ± .09	1.08 ± .04
ALL	1.05 ± .02	1.10 ± .04	1.06 ± .02

NO TOPOLOGY SELECTION

X_F \ P_t	<0.6 GeV/c	>0.6 GeV/c	ALL
<0.5	1.08 ± .03	1.24 ± .08	1.10 ± .03
≥0.5	1.11 ± .05	1.45 ± .12	1.19 ± .05
ALL	1.09 ± .02	1.31 ± .06	1.12 ± .02

THREE PRONGS

X_F \ P_t	<0.6 GeV/c	>0.6 GeV/c	ALL
<0.5	0.95 ± .03	0.88 ± .06	0.94 ± .03
≥0.5	0.85 ± .12	1.56 ± .32	1.03 ± .12
ALL	0.94 ± .03	0.93 ± .06	0.94 ± .02

HIGH PRONGS

Table 7.2.1 DEPENDENCE OF R ON KINEMATIC REGION

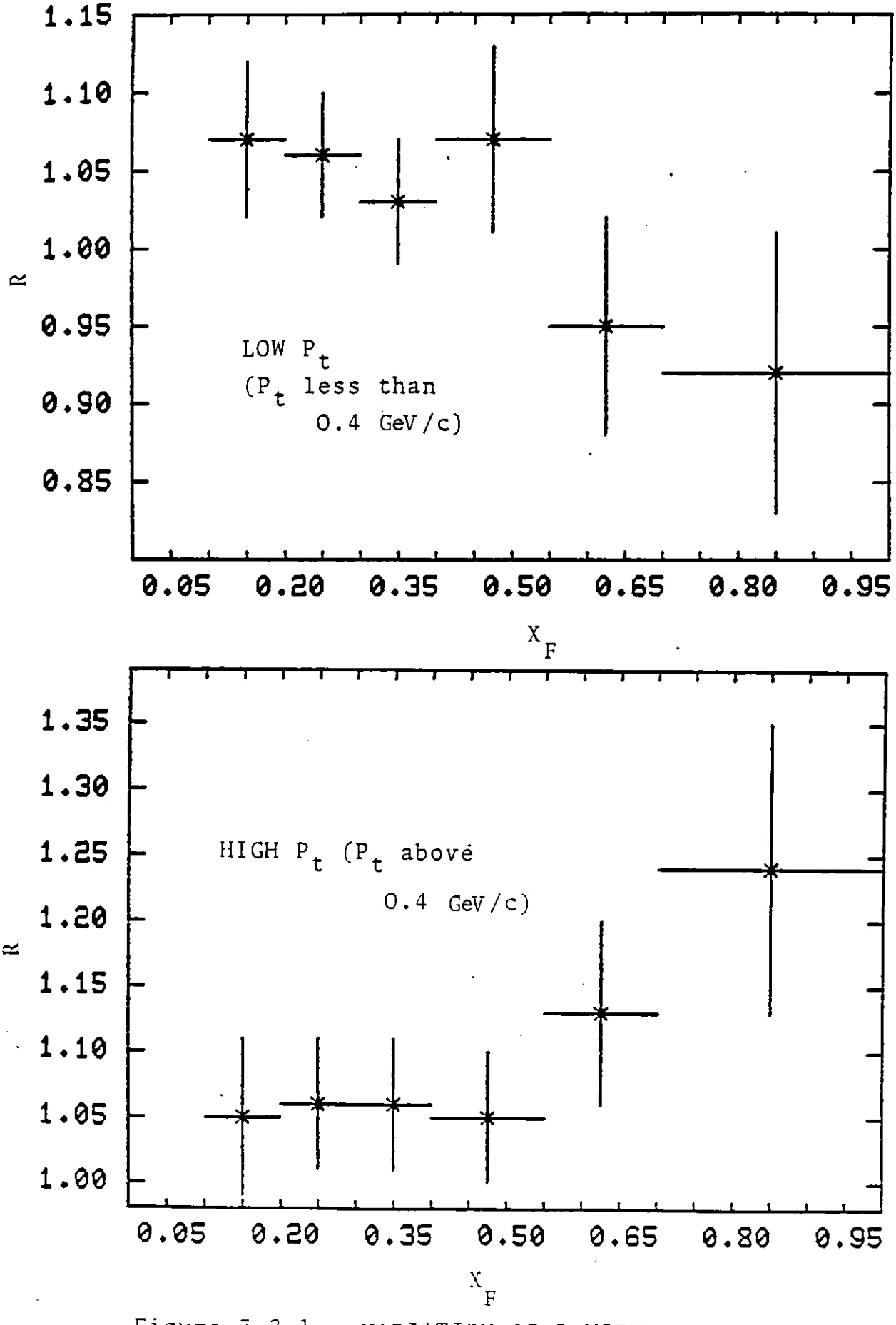

Figure 7.2.1 VARIATION OF R WITH X_F FOR PIONS

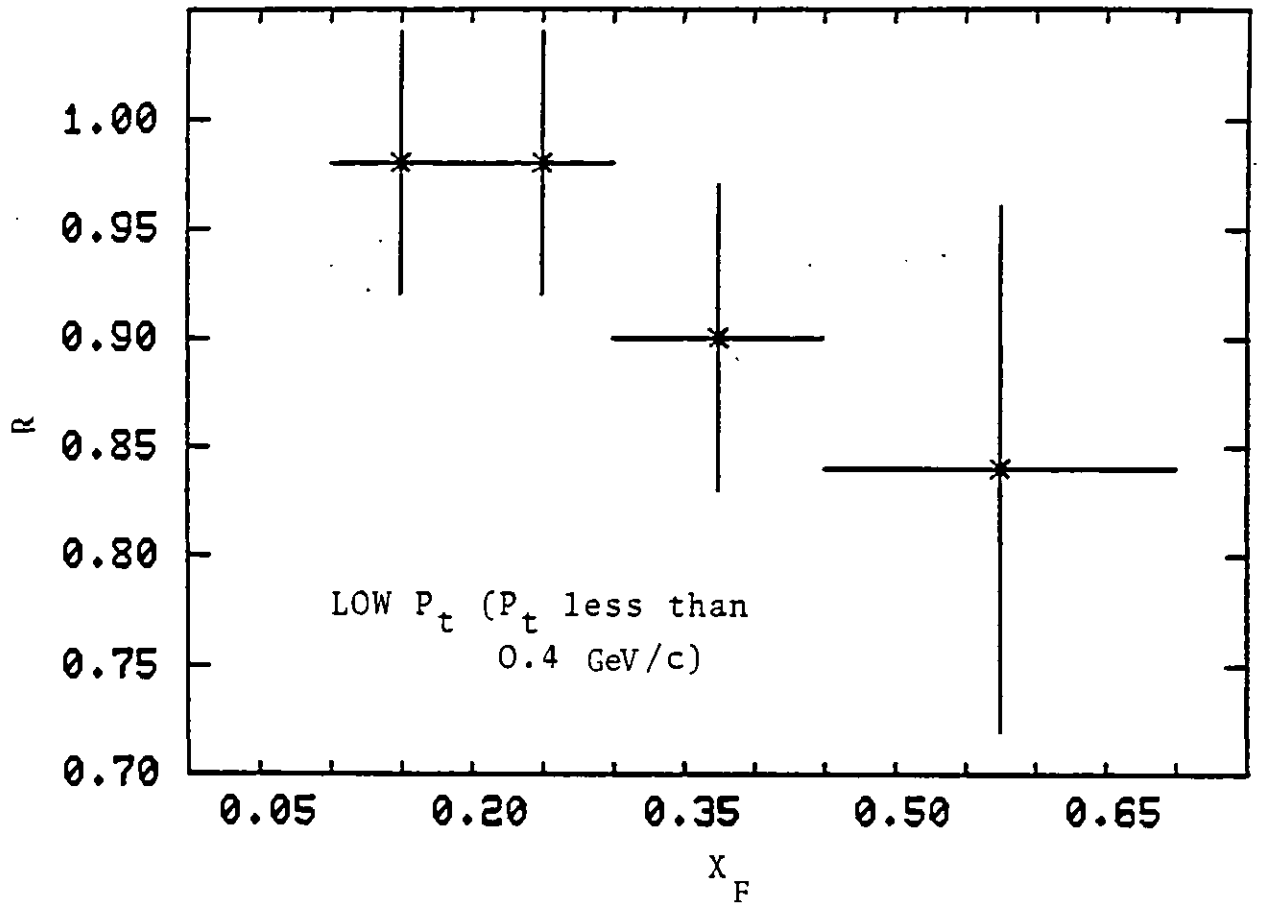

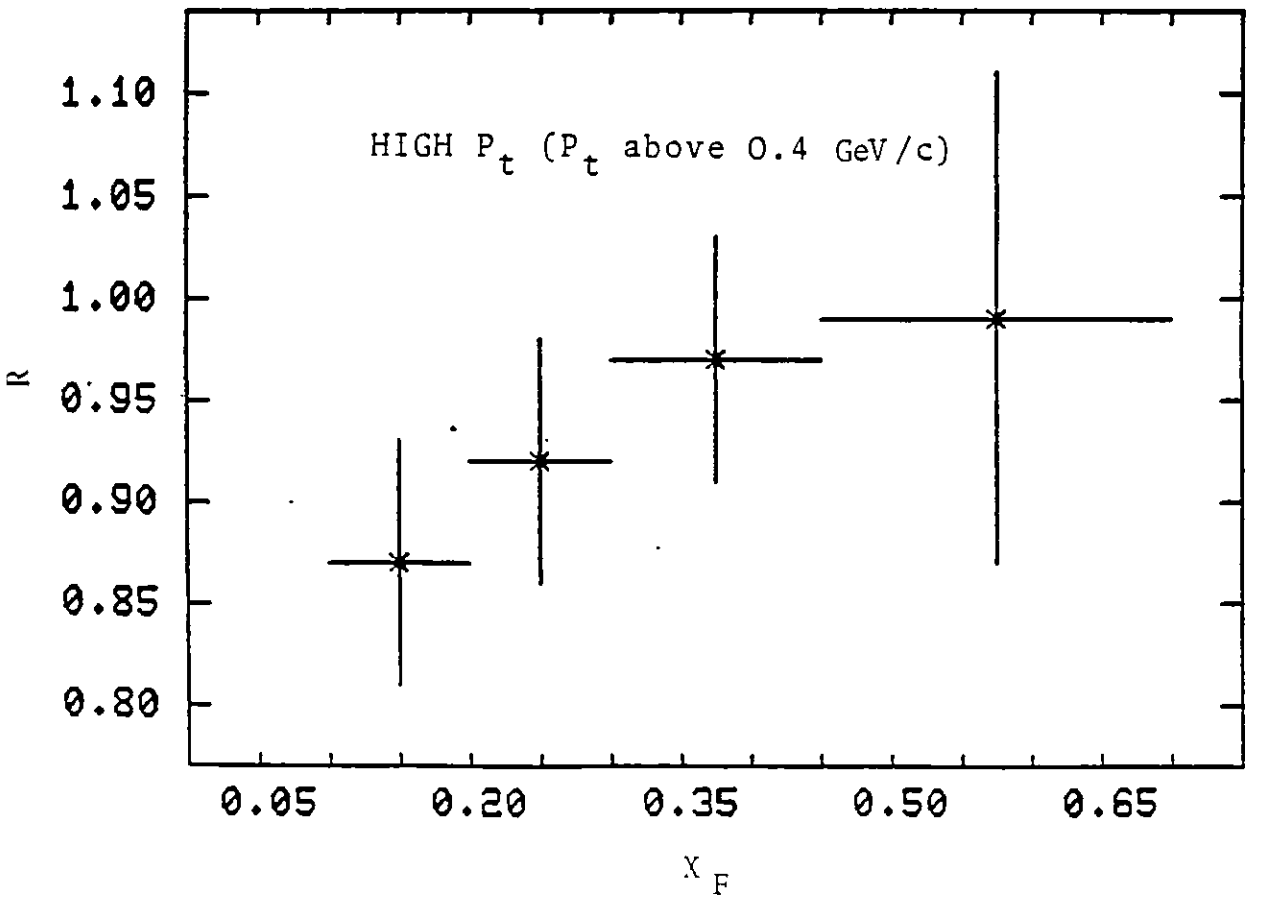

Figure 7.2.2 VARIATION OF R WITH X_F FOR PIONS FROM HIGH PRONG EVENTS

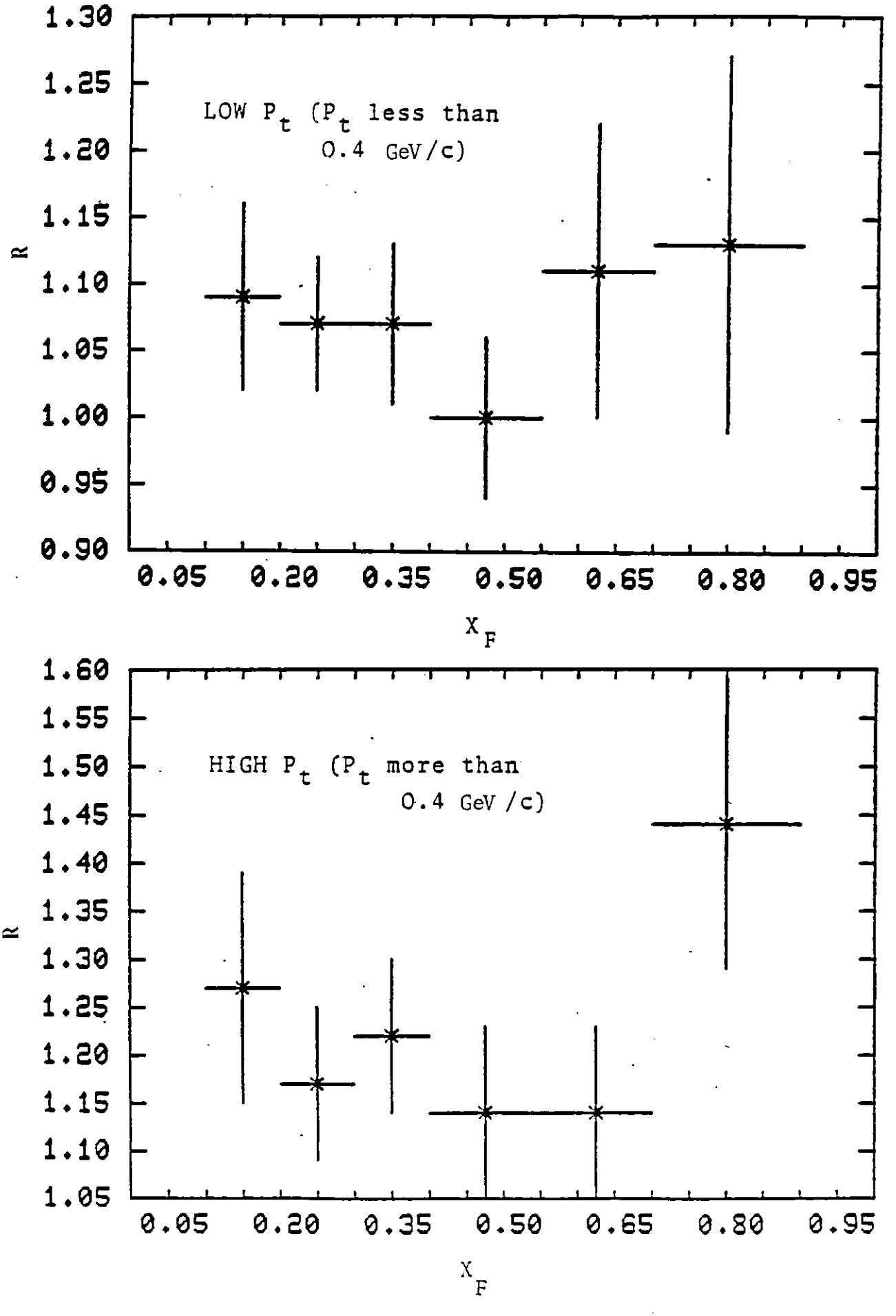

Figure 7.2.3 VARIATION OF R WITH X_F FOR PIONS FROM THREE PRONG EVENTS

positive particles to negative is larger). This explains the initial tendency for R to decrease which is seen in Figure 7.2.3.

The overall trend is for R to be a maximum at high X_F and P_t. This result is increased in importance by the fact it is seen in the three prong data most strongly and yet the asymmetry is not attributable to the diffractive component in the data. The presence of the asymmetry suggests that the photon fragmentation leads preferentially to fast u or anti-d quarks. A quark-photon Compton effect is predicted to favour u-quark coupling over d-quark coupling, however the asymmetry is much smaller than the factor of four yielded by the ratio of charges squared.

The high prong data in contrast to the three prong data shows an overall lack of positive pions in the forward region. The average ratio of positive to negative pions is $0.94 \pm .02$. This may be a consequence of the fact that there is an asymmetry in the valence quark distributions, a u quark is more likely to be found at high values of negative X_F than a d-valence quark and so fast proton fragments will tend to be positive [1]. If more than one charged meson is formed this implies an excess of negative mesons in the central region. If this mechanism is accepted as causing an increase in positive particles in the proton fragmentation zone then it is difficult to imply that the quark distributions in the proton also directly result in a positive excess in the photon fragmentation region.

7.3 The Slope of Pion Distributions in the Beam Fragmentation Region

The existence of a point-like component within the overall photon wave function is predicted to flatten the slope of the pion differential cross section at high X_F values. The prediction is based on the higher probability of finding a quark (or antiquark) at high X_F if the quark

(antiquark) distributions are structureless rather than like those of a vector meson. It does not depend on the flavour of the produced quarks. Both the negative and the positive charged pion distributions are therefore expected to show the effect and the presence of an asymmetry between the two sets of data (see section 7.2) does not make it invalid to combine them. It is usual in fact to amalgamate the data when comparing the theory with experiment and I shall do so to improve the statistical accuracy of the result.

Figures 7.3.1 to 7.3.3 show the behaviour of $\frac{dN}{dX_F}$ as a function of $(1 - X_F)$ for all the data, high prongs (more than six tracks) and three prongs (rho removed) respectively. The distributions are not corrected for the effects of Cerenkov acceptance and beam spread biases. The high prong distribution is steepest as would be expected since the energy available on average for each track is reduced. The three prong distribution is flattest and is the most likely on this basis to contain evidence of a point-like contribution.

Figure 7.3.4 shows the Cerenkov acceptance for each X_F bin as a function of $(1 - X_F)$. The acceptance is integrated over P_t, the assumed P_t distribution being that found for all (three prong) forward tracks before selection by particle type. The P_t distribution was assumed to be independent of X_F and particle type. As can be seen the correction factors needed to compensate for the Cerenkov acceptance are large. Figure 7.3.5 shows the fraction of tracks found in a particular X_F bin compared to the number generated in that bin, given the beam spectrum and assuming that the distribution behaves as $(1 - X_F)^{1.0}$. The corrections needed as a result of beam spread are smaller and do not depend strongly on the exact slope. Both sets of correction factors act so as to preferentially increase the number of tracks at high X_F and to decrease the slope of the $\frac{dN}{dX_F}$ distribution at high X_F, low$(1 - X_F)$.

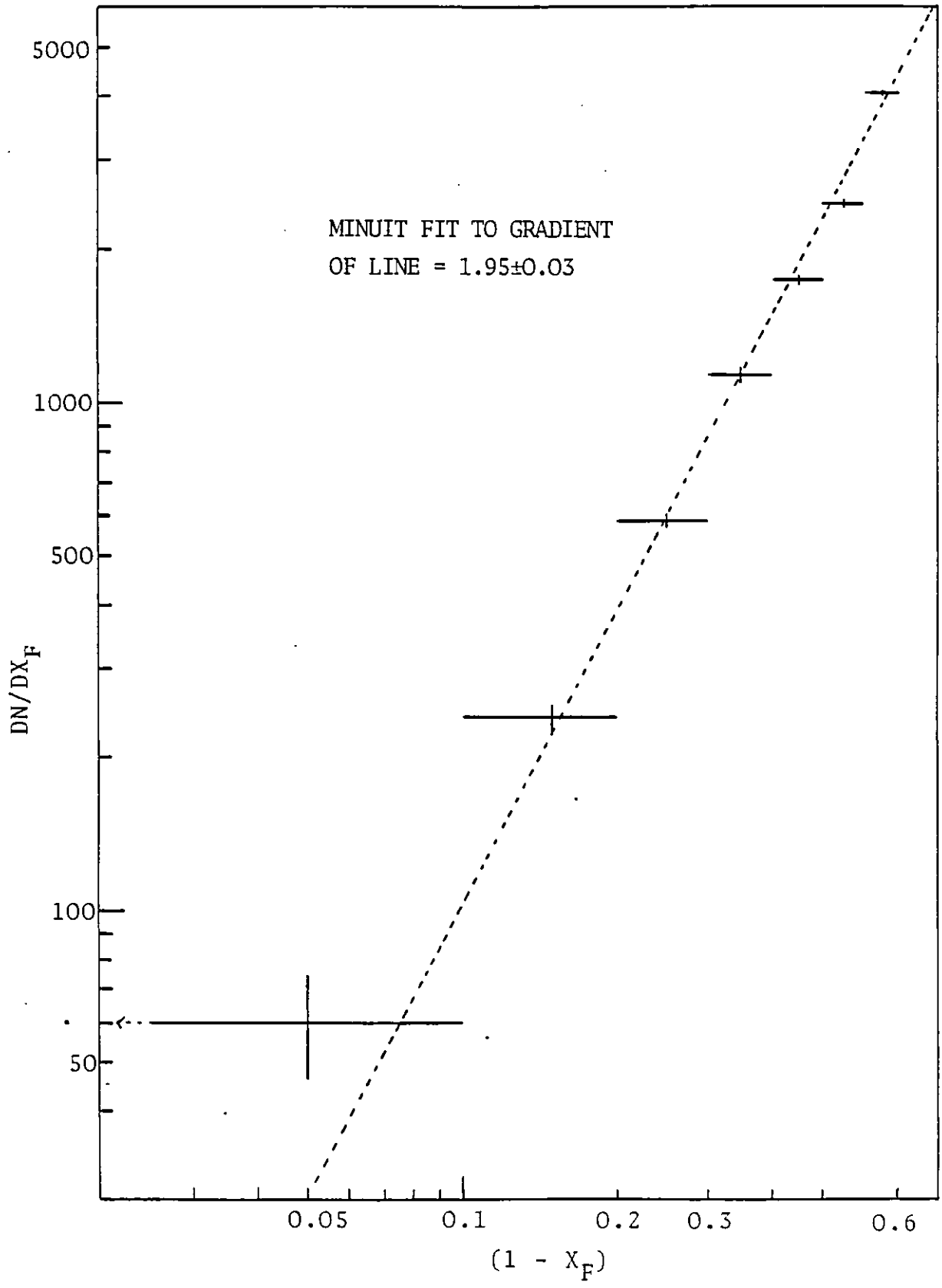

Figure 7.3.1 POWER LAW BEHAVIOUR OF DN/DX_F FOR PIONS (NO EVENT SELECTION)

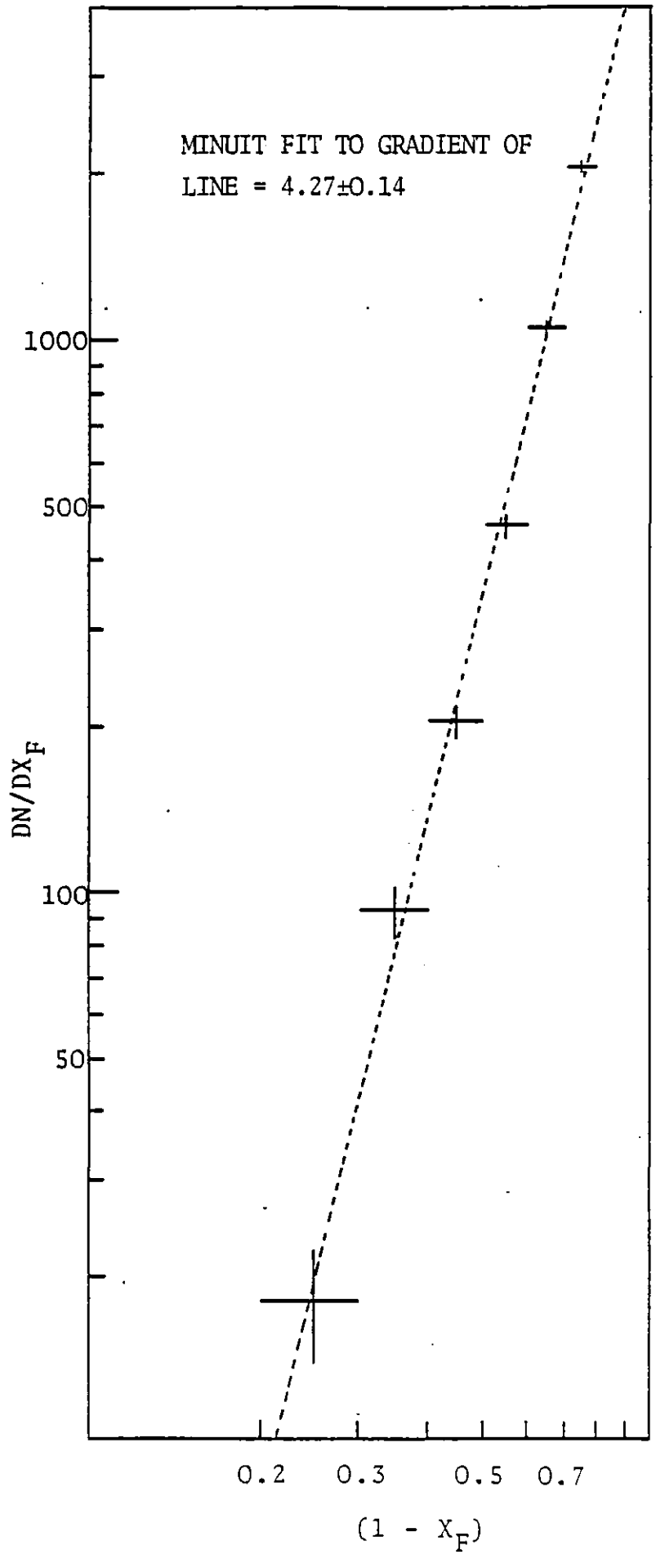

Figure 7.3.2 POWER LAW BEHAVIOUR OF DN/DX_F FOR HIGH PRONGS ONLY

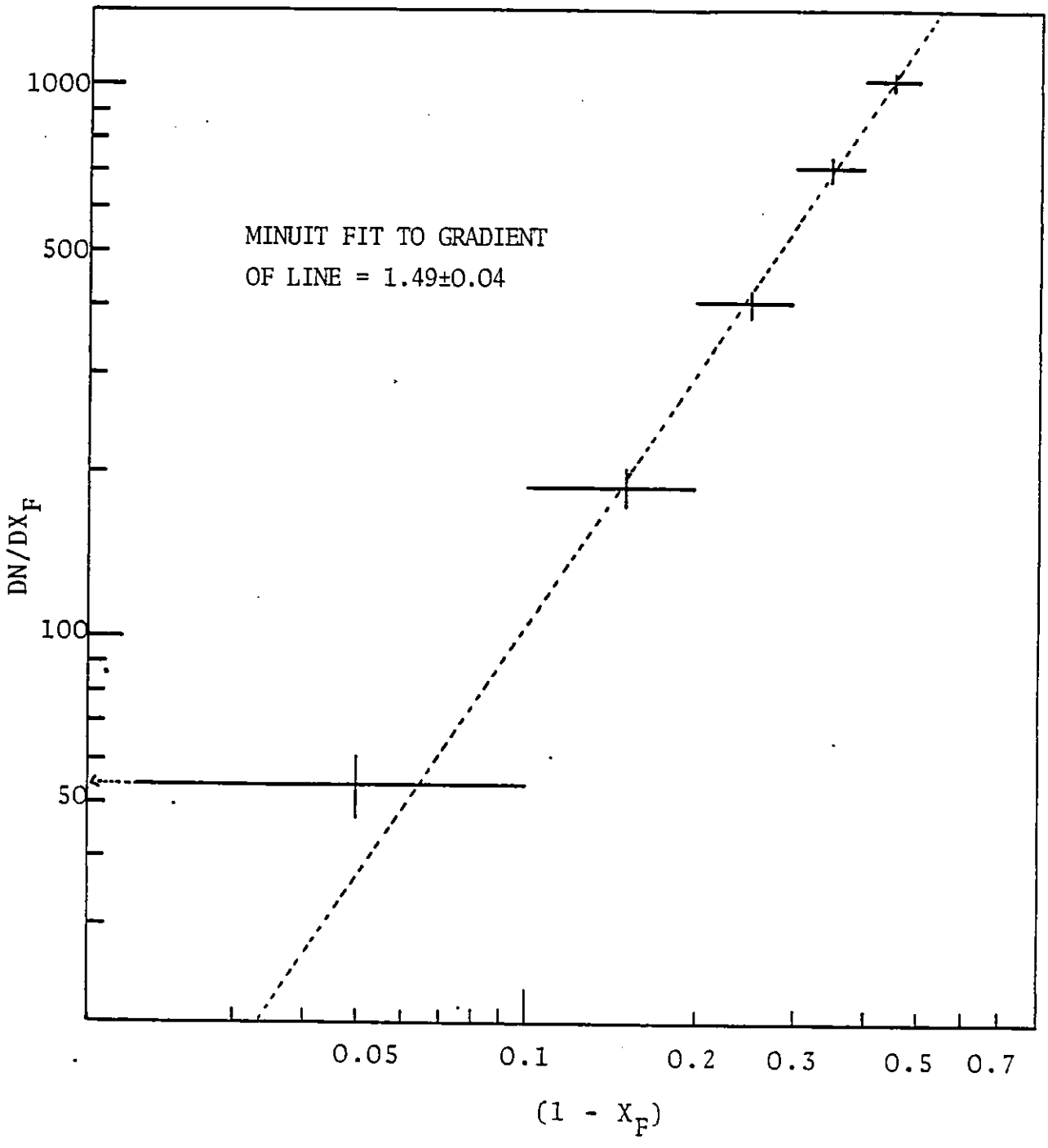

Figure 7.3.3 POWER LAW BEHAVIOR OF DN/DX_F FOR THREE PRONG EVENTS ONLY

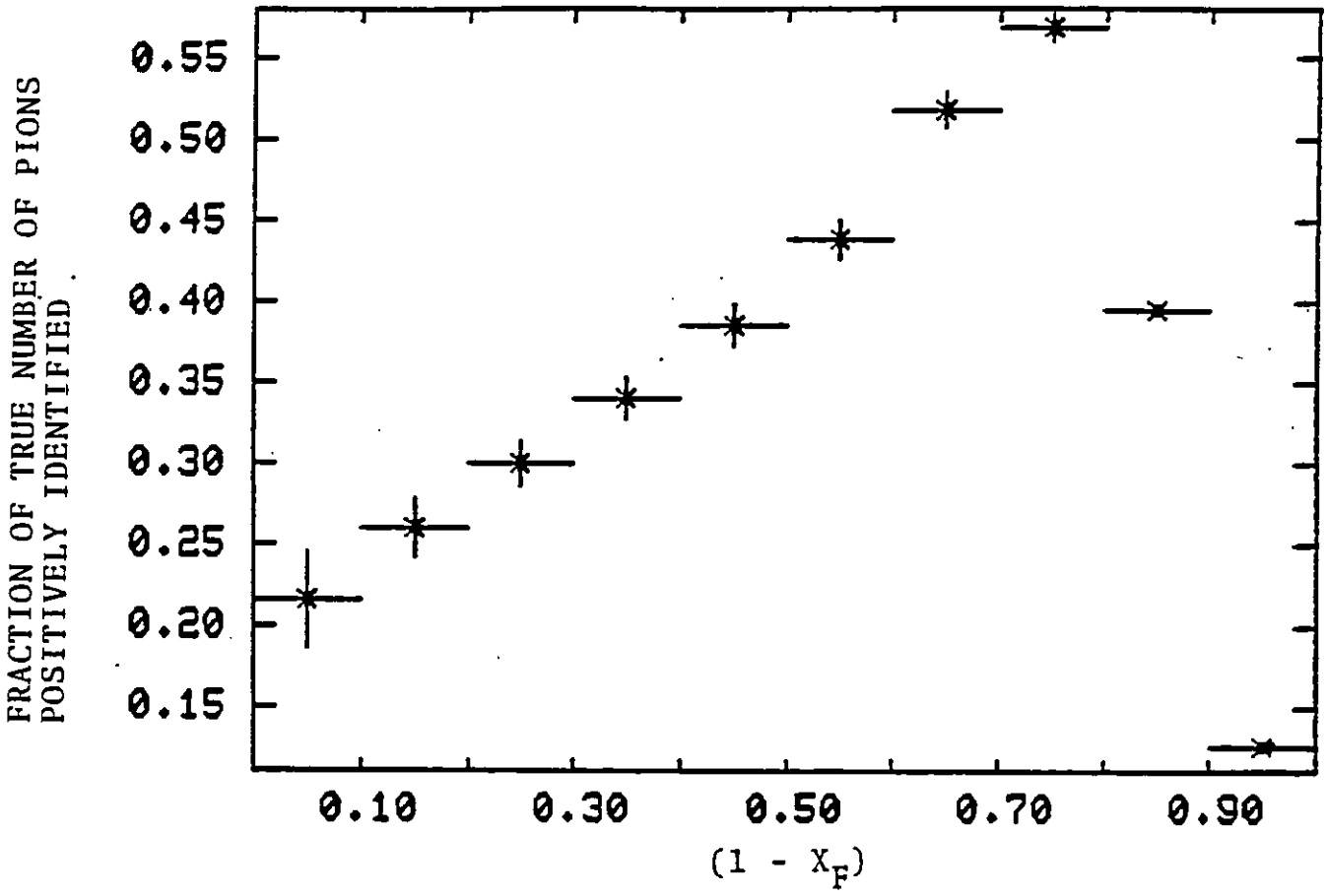

Figure 7.3.4 CERENKOV ACCEPTANCE, INTEGRATED OVER P_t

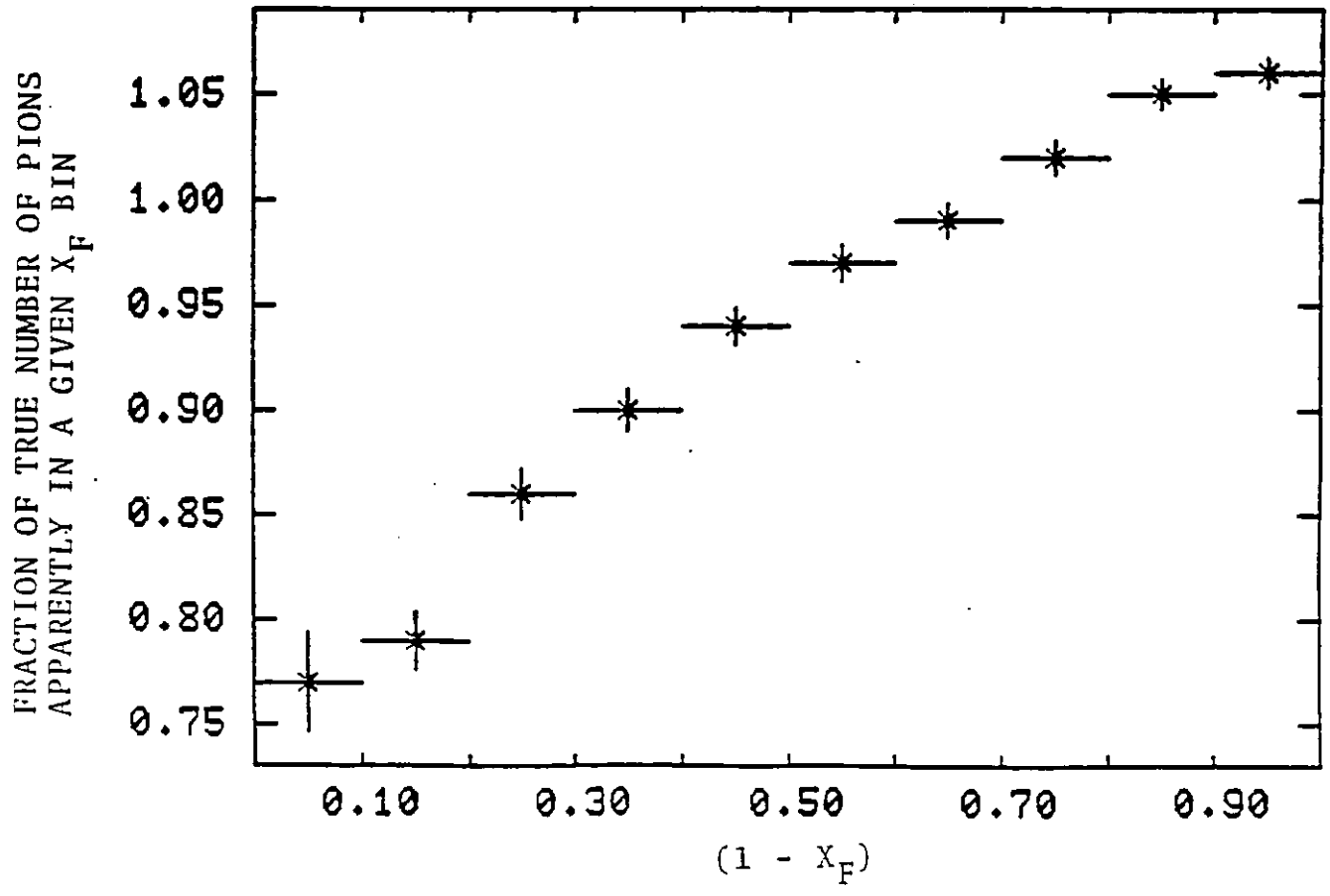

Figure 7.3.5 BEAM SPREAD CORRECTION FACTORS

Figure 7.3.6 shows the effect of folding in the correction factors into the three prong distribution. The result is that a best line fit to the data gives a slope of $1.0 \pm .01$. As a consistency check it was confirmed that generating a $(1 - X_F)^{1.0}$ distribution and folding in the effects of the acceptance of the Cerenkovs into the beam spread Monte Carlo resulted in a distribution with the slope of the unweighted three prong distribution. Figure 7.3.7 shows the contribution to Figure 7.3.6 from positive pions only; although the best line fit to this fraction of the data yields a slope of $0.96 \pm .03$ it is not strong evidence for a dominant point-like contribution.

It can be argued that the slope obtained is steepened by the presence of tracks from diffractive interactions, which the Q-frame analysis showed to still be a signficant contribution to the three prong data even after the subtraction of rho fits. However, the slope obtained for tracks identified by kinematic fit as pions from rho decays and as pions by the Cerenkovs is consistent with that obtained for the remaining three prong data. The value of 1.0 does not therefore result from an averaging of a very much steeper dependence and a point-like contribution. Trigger acceptance may increase the slope at high X_F but the events lost will tend to be diffractive (since these tracks on average have a lower P_t)and so the loss should decrease preferentially the diffractive background. Also the variation over the X_F bins of interest is not large. The conclusion is that the point-like contribution, if present, is masked.

Figure 7.3.8 compares the invariant cross section integrated over P_t for pions produced in three prong interactions(rho subtracted, corrected for acceptance and beam spread biases) with the predictions given in Chang and Hwa's[2] paper for both the Recombination model and the quark fragmentation model. The agreement with the Recombination model predictions is good and much better than the agreement with the

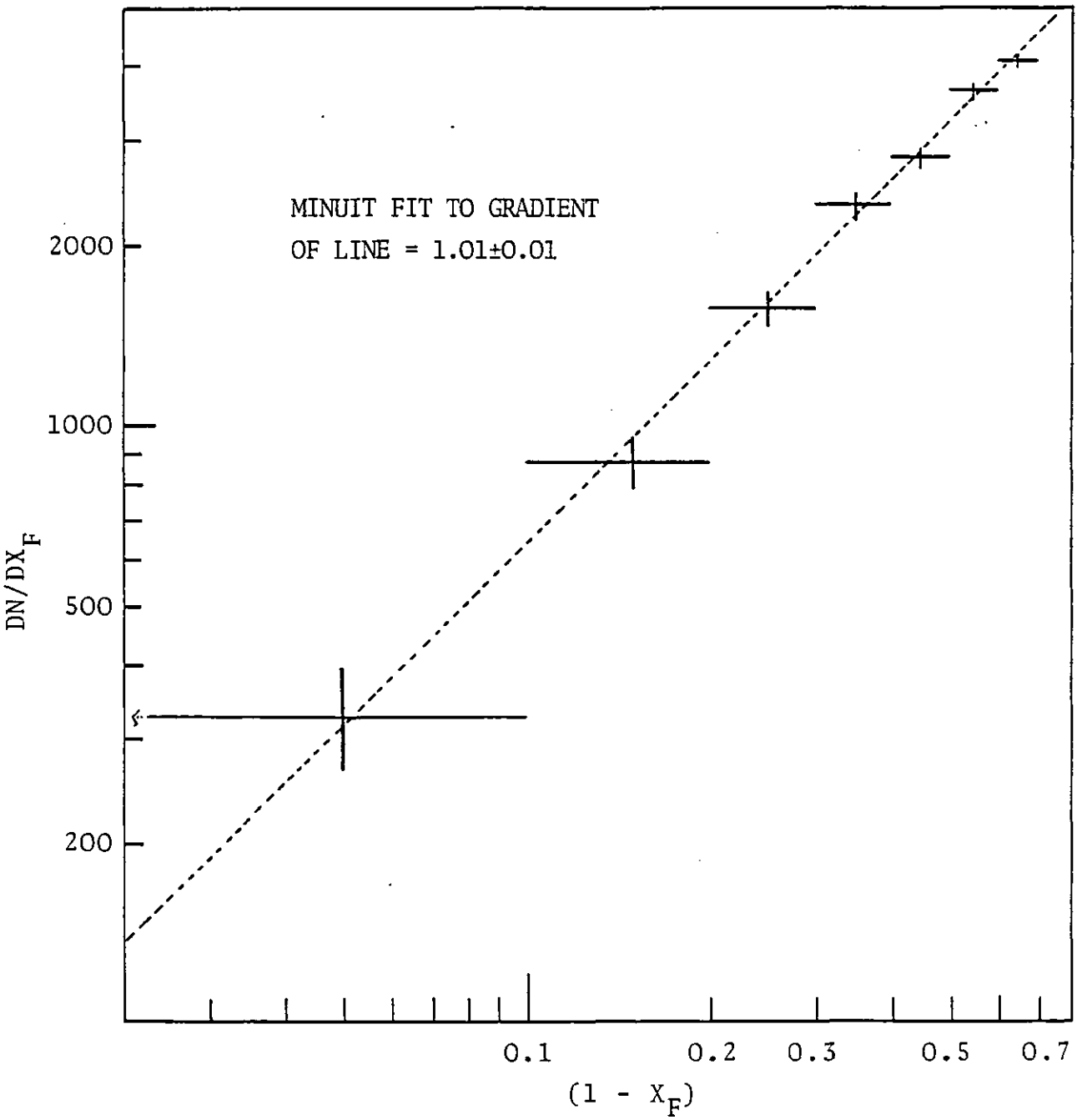

Figure 7.3.6 POWER LAW BEHAVIOUR OF DN/DX_F, FOR THREE PRONG EVENTS, CORRECTED FOR ACCEPTANCE AND BEAM SPREAD BIASES

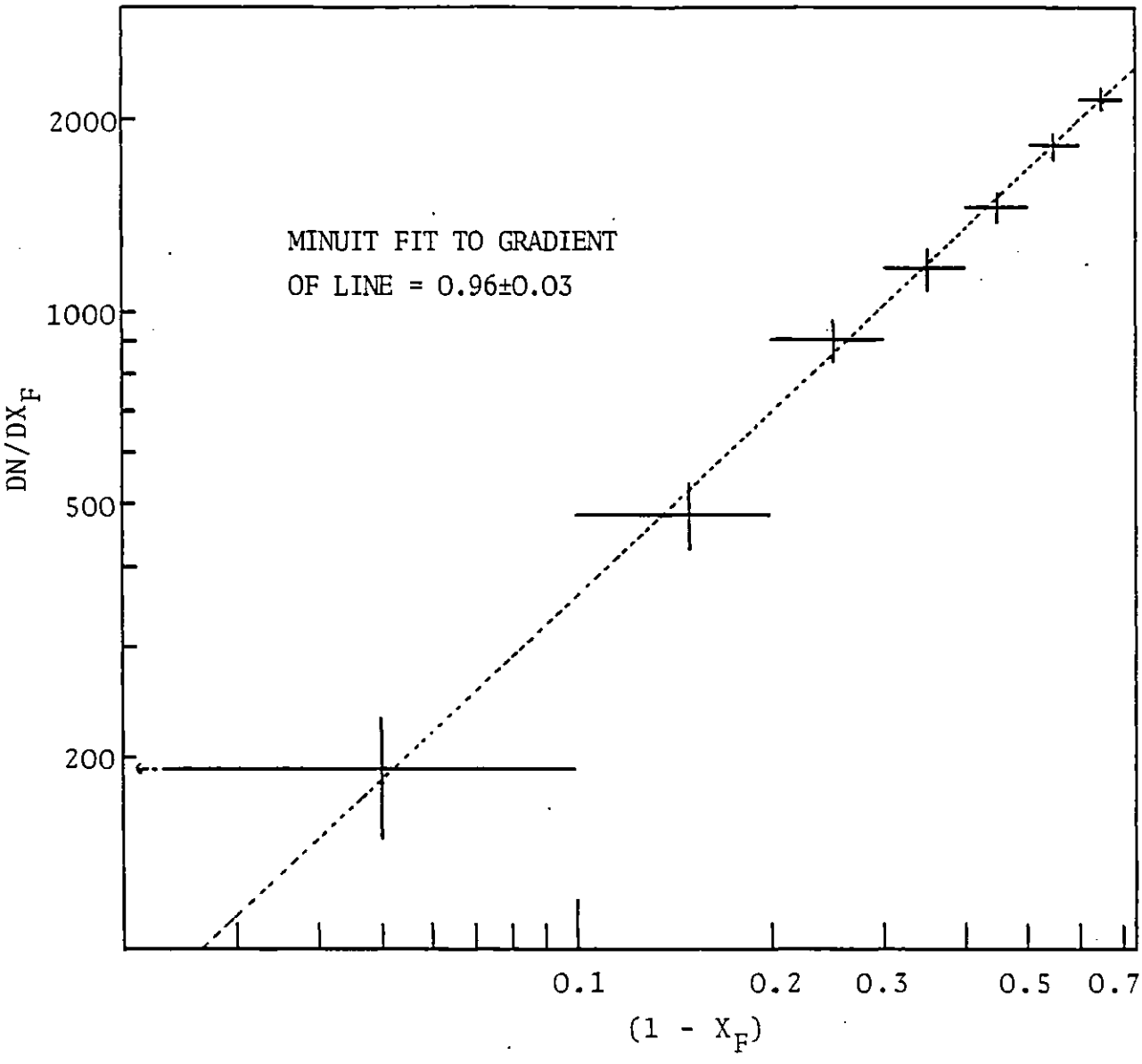

Figure 7.3.7 POWER LAW BEHAVIOUR OF DN/DX_F, FOR POSITIVE PIONS FROM THREE PRONG EVENTS ONLY, CORRECTED FOR ACCEPTANCE AND BEAM SPREAD BIASES

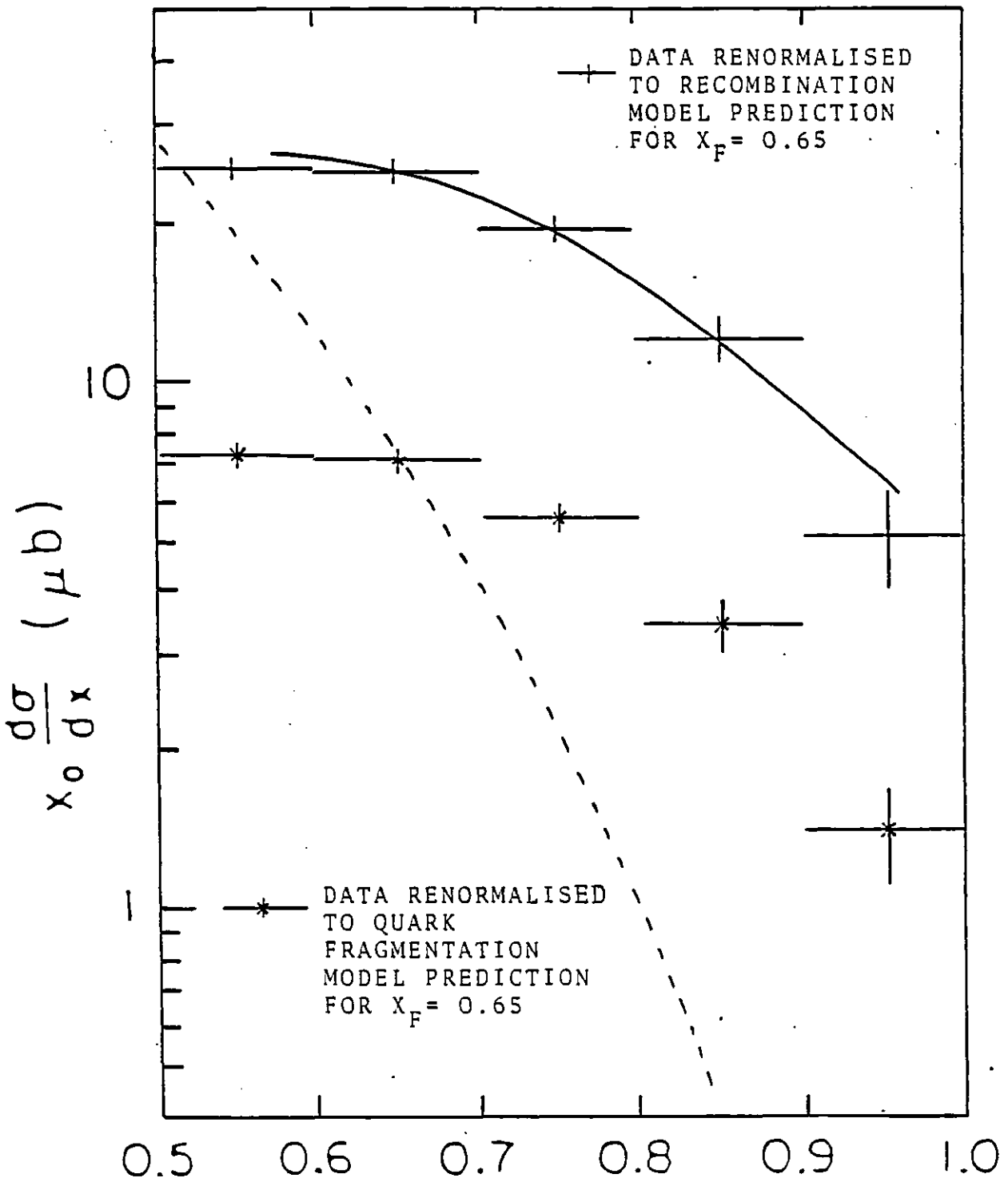

Figure 7.3.8 COMPARISONS BETWEEN DATA AND PREDICTIONS

SOLID LINE GIVES RECOMBINATION MODEL PREDICTION
DASHED LINE GIVES QUARK FRAGMENTATION MODEL PREDICTION

fragmentation model. However this agreement is with data that yields a pion distribution predicted for a vector meson like photon not a point-like photon.

Summary

The agreement between the data and the theoretical predictions of the pion cross section which are Recombination Model based is good and the fragmentation model alternative is not favoured. However, the predictions are based on the assumption that the two quark structure function is calculable and the two quark structure function is only calculable (at present) for the point-like component of the photon's wave function. The point-like component must therefore be considered to dominate the hadronic component in the beam fragmentation region. This dominance would lead to other predictable consequences;

i) The symmetry frame for photon interactions would have a Q value greater than 1.5

ii) The charge dependence of the photon coupling would result in an excess of positive pions at high X_F and P_t.

iii) The slope of the pion distribution as a function of $(1 - X_F)$ should be less than one.

Whilst a Q-frame analysis of the data as a whole implies the existence of both point-like and hadronic contributions to the photon wave function; attempting to isolate the point-like component throws doubt on this conclusion. The high prong data is consistent with being produced in the VMD frame. Although the presence of a point-like contribution cannot be ruled out from the three prong data its existence is not required.

Charge asymmetry effects are present, and as predicted it is positive pions which dominate at high X_F and P_t. However, the effect is not as large as would be expected if the point-like photon interacted predominantly via the QCD Compton effect producing up quarks at high X_F more frequently than down quarks.

The slope of the pion distributions at high X_F is consistent with the result expected if the distribution of quarks within the photon is similar to the distribution within a vector meson.

The failure to find clear indications of a point-like photon may well be because the data was not taken at sufficiently high enough energies and is not concentrated at the high X_F and P_t extremes. However this does not invalidate the conclusion that for this data the effects associated with the point-like component of the photon do not dominate over those associated with the hadronic component. This implies that the agreement between the data and the predictions of the Recombination model is accidental since the prediction is based on a false assumption (at this energy).

The fact that the agreement is so good between the theory and distributions associated with the photon acting as a vector meson imply that the theory must ultimately yield similar results for the behaviour of both components of the photon. If not then the data currently quoted in support of the theory (18 GeV photon bremsstrahlung beam data [3]) and the data of this experiment may later be used to disprove it.

Chapter 7 - References

[1] For a discussion of u-quark dominance see: R.P.Feynman; Photon Hadron Interactions, Chapter 31 (published in 1972 by W.A.Benjamin)

[2] V.Chang and R.C.Hwa; Phys. Rev. Lett. 44, 439 (1980)

[3] A.M.Boyarski et al.; Phys. Rev. D14, 1733 (1976)

APPENDIX A

BEAM KINEMATICS

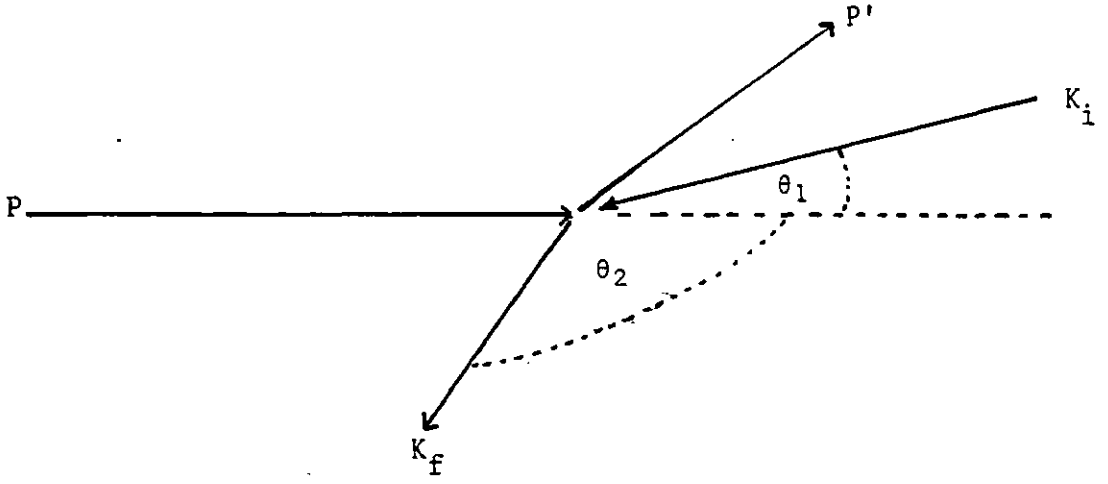

Let P = (E, $\underline{p}$) be the four-momentum of the incident electron mass m_e.

P'= (E',$\underline{p}'$)be the four-momentum of the scattered electron

K_i= (k_i, $\underline{k}_i$) be the four-momentum of the incident photon

K_f= (k_f, $\underline{k}_f$) be the four-momentum of the scattered photon

and S be the invariant mass squared of the system.

Then;

$$P + K_i = P' + K_f$$

$$P' = (P + K_i) - K_f$$

$$(P')^2 = (P + K_i)^2 + K_f^2 - 2K_f(P + K_i)$$

Therefore

$$M_e^2 = S - 2K_f(P + K_i)$$

$$= S - 2k_fE - 2k_fk_i + 2\underline{k}_f.\underline{p} + 2\underline{k}_f.\underline{k}_i$$

Hence

$$k_f = \frac{(S - M_e^2)}{2[(E - |p| \cos\theta_2) + k_i(1 + \cos(\theta_1 + \theta_2))]} \qquad A.1$$

For k_f to be a maximum it is required that

i) S be at a maximum, i.e. $\theta_1 = 0.0$

and

ii) The denominator of A.1 be at a minimum, i.e. $\theta_2 = 0.0$

Therefore

$$k_{f_{max}} = \frac{(S - M_e^2)}{2((E - |p|) + 2k_i)} \qquad A.2$$

However

$$S = M_e^2 + 2k_iE - 2\underline{k}_i \cdot \underline{p}$$

and

$$E^2 >> M_e^2$$

Therefore in this case

$$S = M_e^2 + 4k_i E \qquad A.3$$

Substituting for S in equation A.2 yields

$$k_{f_{max}} = E\left(1 - \frac{(E - |p|)}{2k_i + (E - |p|)}\right) \qquad A.4$$

$$= E(1 - a)$$

where a is the recoil parameter

but

$$(E-|p|) = E\left(1 - \left(1 - \frac{M_e^2}{E^2}\right)^{1/2}\right)$$

$$\simeq \frac{M_e^2}{2E}$$

substituting for $(E - |p|)$ into A.4 yields

$$K_{f_{max}} = E\left(\frac{2k_i}{2k_i + M_e^2/2E}\right)$$

$$= \left(\frac{4E^2k_i}{M_e^2}\right)\left(\frac{M_e^2}{4Ek_i}\right)\left(\frac{2k_i}{2k_i + M_e^2/2E}\right)$$

$$= \frac{4E^2k_i}{M_e^2}\left(\frac{(E - |p|)}{(E - |p|) + 2k_i}\right)$$

$$= \left(\frac{4E^2k_i}{M_e^2}\right) a$$

$$= \frac{4E^2k_i}{S} \qquad A.5$$

APPENDIX B

DERIVATION OF KINEMATIC RESULTS ASSUMED IN THE TEXT

1. The Systematic Shift in the Value of X_F which Results from Using A Nominal Beam Energy.

Let (k, $\underline{k}$) be the four-momentum of the interacting photon in the laboratory frame

(E, $\underline{p}$) be the four-momentum of the track of interest in the laboratory frame.

S be the invariant mass squared of the initial system (photon, proton)

M_p be the mass of the proton

the superscript * denotes quantities as measured in the centre of mass frame and the subscripts L, t, and n denote longitudinal components, true, and nominal values respectively.

Then, β, the Lorentz boost between the laboratory and centre of mass frames is given by

$$\beta = \frac{k}{k + m_p} \qquad \text{B.1}$$

and

$$\gamma = (1 - \beta^2)^{-\frac{1}{2}}$$

$$= \frac{k + m_p}{\sqrt{S}} \qquad \text{B.2}$$

Then

$$P_L^* = - \beta\gamma E + \gamma P_L$$

$$= \frac{kE}{\sqrt{S}} + \left\{\frac{k + m_p}{\sqrt{S}}\right\} P_L$$

Therefore

$$X_F = \frac{2}{S}\{k(P_L - E) + M_p P_L\} \qquad B.3$$

Let

$$\Delta X_F = X_t - X_n$$

$$= \frac{2}{S_t}\{k_t(P_L - E) + M_p P_L\} - \frac{2}{S_n}\{k_n(P_L - E) + M_p P_L\}$$

$$= \frac{2}{S_t S_n}\{k_t S_n(P_L - E) - k_n S_t(P_L - E) + (S_n - S_t)M_p P_L\}$$

$$= \frac{2}{S_t S_n}\{(k_t - k_n)(M_p{}^2(P_L - E) - 2M_p{}^2 P_L)\}$$

$$= \frac{2M_p{}^2}{S_t S_n}\{k_n - k_t)(E + P_L)\} \qquad B.4$$

Let $\Delta k = k_t - k_n$

Then substituting into B.4

$$\Delta X_F = -\Delta k \left(\frac{2M_p{}^2(E + P_L)}{S_n}\right)\left(\frac{1}{2(k_n + \Delta k)M_p + M_p{}^2}\right) \qquad B.5$$

Therefore ΔX_F is not a linear function of Δk

B.5 implies that understinating the energy of the interacting photon (Δk positive) leads to an overestimate of the X_F of the track (ΔX_F negative). For a given Δk, ΔX_F increases in magnitude with the momentum of the track.

2. Additivity of Rapidity Variable, y

Let the superscript Q refer to quantities in the Q frame and β now be the boost between the laboratory and the Q frame and other symbols be as defined in section 1 of this appendix

$$y = \frac{1}{2} \ln\left(\frac{E + P_L}{E - P_L}\right) \qquad \text{B.6}$$

and by definition

$$y^Q = \frac{1}{2} \ln\left(\frac{E^Q + P_L{}^Q}{E^Q - E_L{}^Q}\right) \qquad \text{B.7}$$

$$= \frac{1}{2} \ln\left(\frac{\gamma E - \beta\gamma P_L + \gamma P_L - \beta\gamma E}{\gamma E - \beta\gamma P_L - \gamma P_L + \beta\gamma E}\right)$$

$$= \frac{1}{2} \ln\left(\frac{\gamma - \beta\gamma}{\gamma + \beta\gamma}\right) + \frac{1}{2} \ln\left(\frac{E + P_L}{E - P_L}\right)$$

$$= \frac{1}{2} \ln\left(\frac{1 - \beta}{1 + \beta}\right) + y \qquad \text{B.8}$$

Therefore rapidity is an additive variable.

3. Relationship between Centre of Symmetry of Rapidity Distribution and Q Value Denoting the Symmetry Frame.

Using notation of earlier sections the symmetry frame is defined by

$$y_S^R = 0.0 \qquad \text{B.9}$$

where the subscript S denotes the centre of symmetry of the distribution.

Hence, using B.8 we have:

$$0.0 = \frac{1}{2} \ln\left(\frac{1 - \beta}{1 + \beta}\right) + y_S \qquad \text{B.10}$$

Therefore

$$y_S = \frac{1}{2} \ln\left(\frac{1 + \beta}{1 - \beta}\right)$$

and hence

$$\beta = \frac{e^{2y_S} - 1}{e^{2y_S} + 1} \qquad \text{B.11}$$

Let $(E_p, \underline{p}_p)$ be the four-momentum of the target proton in the laboratory frame.

Then;

$$\underline{p}^R = -\beta\gamma E_p + \gamma \underline{p}_p$$

$$= -\beta\gamma M_p$$

$$= -Q \underline{k}^R \qquad \text{by definition of Q-frame} \qquad \text{B.12}$$

$$\underline{k}^R = -\beta\gamma k + \gamma \underline{k}$$

$$= \gamma(1 - \beta)\underline{k} \qquad \text{B.13}$$

Using B.12 to substitute for $\underline{k}^R$ in B.13

$$|\underline{p}^R| = \gamma Q(1 - \beta)k \qquad \text{B.14}$$

Therefore

$$\beta\gamma M_p = \gamma Q(1 - \beta)k \qquad \text{B.15}$$

and hence

$$\beta = \frac{Qk}{M_p + Qk} \qquad \text{B.16}$$

and

$$Q = \frac{\beta M_p}{(1 - \beta)k} \qquad \text{B.17}$$

Using B.11 to substitute for β

$$Q = \frac{M_p}{2k}\left(e^{2y_S} - 1\right) \qquad \text{B.18}$$

Appendix C

SLAC-PUB-2726
April 1981
(I)

ON-LINE EXPERIENCE WITH THE 168/E*

J. T. Carroll, J. E. Brau, T. Maruyama and D. B. Parker
Stanford Linear Accelerator Center, Stanford, California 94305

J. S. Chima, D. R. Price and P. Rankin
Imperial College, London, England

R. W. Hatley
Rutherford Laboratory, Chilton, Didcot, England

ABSTRACT

Current 20 GeV/c photoproduction experiments at the SLAC Hybrid Facility require a decision to take a picture within 150-300 μs after the beam pulse. A charged track trigger is provided by a 168/E processor which finds tracks in a downstream PWC system. To meet trigger time requirements the 168/E SNOOP module CAMAC interface is augmented by a CAMAC Auxiliary Controller and dedicated I/O cards in the 168/E chassis. Between beam pulses a floating point Fortran program executing on a 168/E monitors data acquisition. Experience with software development and application are reviewed.

1. INTRODUCTION

The current SLAC Hybrid Facility (SHF) experiment studies photoproduction at 20 GeV/c using a backscattered laser beam.[1] Electronic detectors downstream of the 40" bubble chamber include eleven proportional wire chambers, two multi-cell atmospheric Čerenkov counters and a large neutral detector using lead glass blocks. To make this experiment practical as regards the quantity of film involved, data from these external detectors is used on-line to determine if a picture should be taken and enhance the ratio of pictures with hadronic production. Previous SHF experiments used assembly language algorithms executing on the host computer for picture selection. For this experiment a system of 168/E processors[2] was developed to provide more efficient and flexible support for on-line picture algorithms.

The main components of the SHF 168/E system are shown in Fig. 1. The host computer is a Data General NOVA 4/X running under RDOS with 256K bytes of memory and 20M bytes of disk space. The NC023C controllers in each CAMAC crate are daisy chained together on the NOVA I/O bus. The 168/E processors perform as slaves to the host computer which controls them via a SNOOP module CAMAC interface.[3] A 50 wire flat cable connects an interface card in each 168/E crate to SNOOP modules in the CAMAC crates. Processors #0 and #1 can be accessed by SNOOP modules in either crate 25_8 or 26_8 while 168/E CPU #2 is only connected to CAMAC crate 27_8. Using CAMAC programmed I/O to a SNOOP module, a program on the host computer can download a 168/E program, set the program counter, start/stop the processor, read results in 168/E memory, etc. SNOOP module CAMAC functions are described in Ref. 3.

The SNOOP also provides a direct transfer from CAMAC to 168/E data memory by eavesdropping on input from other CAMAC modules in the same crate. For example, a transfer from BADC[4] to 168/E #0 requires the following sequence of operations:

i) set interface address register(s) on target 168/E(s);

ii) set interface device select register for target processor(s);

* Work supported in part by the Department of Energy, contract DE-AC03-76SF00515 and by the U. K. Science Research Council.

(Contributed to the Topical Conference on Application of Microprocessors to High Energy Physics Experiments, Geneva, Switzerland, May 4-6, 1981.)

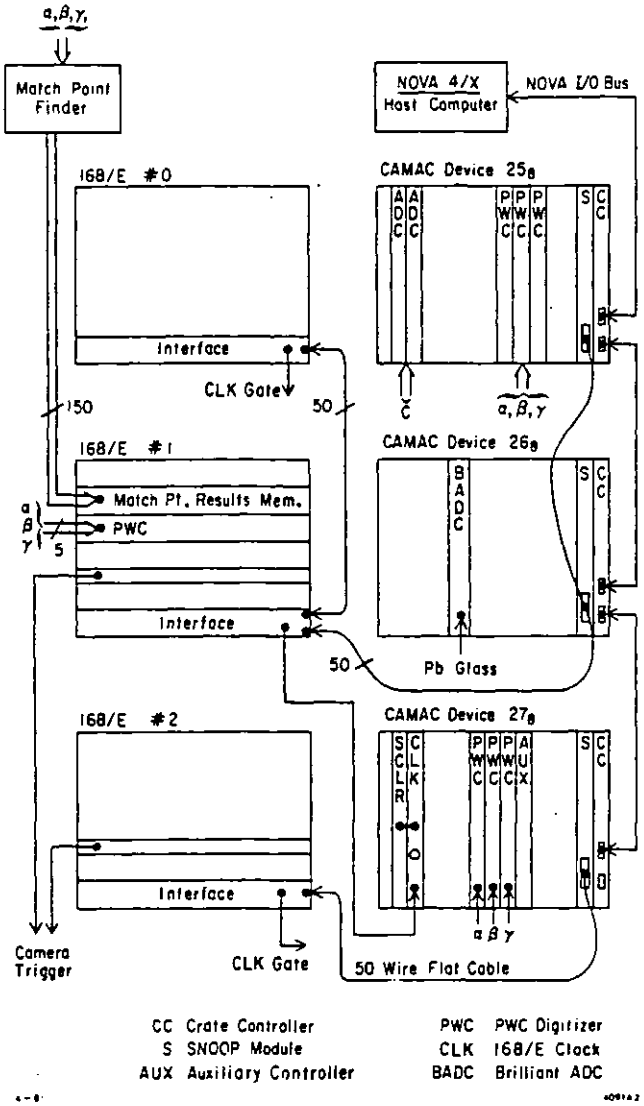

Fig. 1. Organization of the 168/E and CAMAC system at the SLAC Hybrid Facility.

iii) enable Listen Mode on SNOOP in crate 26_8;

iv) read BADC in single instruction or DMA mode;

v) disable Listen Mode, clear device select register and proceed with data transfer complete.

"Listen Mode" eliminates the overhead of first transferring data to the NOVA and then writing it back to 168/E memory. For SHF real-time applications the 168/E programs are stable (no overlays) and fast data transfer is only required for trigger algorithms. With CAMAC the hardware components of the interface are independent of the type of host computer and as evident in Fig. 1, there is considerable flexibility in the arrangement of processors and CAMAC crates.

Several key data acquisition modules in the 168/E - CAMAC system are shown in Fig. 1 and the current hardware configuration on each processor is listed in Table I. We assume the reader is familiar with the basic concepts and capabilities of the 168/E processor.

Following descriptions will focus on SHF on-line applications and supplemental hardware developed to meet the severe time constraint of the camera trigger.

TABLE I. 168/E Configuration

CPU #	Function/Contents
0	Full Algorithm and Fortran Monitor Program Interface to CAMAC Crates 25_8 and 26_8 Integer and Floating Point CPU Three Memory Boards (48K Bytes Data Memory)
1	Hardware and Algorithm Development Interface to CAMAC crates 25_8 and 26_8 Integer CPU One Memory Board (16K Bytes Data Memory) Eight Channel PWC Digitizer Card Match Point Results Memory Camera Trigger Card
2	Fast PWC Algorithm Interface to CAMAC Crate 27_8 Integer CPU One Memory Board (16K Bytes Data Memory) Camera Trigger Card

2. ON-LINE SOFTWARE SUPPORT

Programs for execution on the 168/E are written in IBM Fortran and/or assembly language and normally debugged and tested off-line on an IBM 370/168. Compiler and assembler object modules are processed by a 168/E Translator which produces microcode for the processor. Card image program and data memory files produced by the Translator are transferred to the NOVA 4/X and saved on disk using a 9600 bpi WYLBUR link. A Fortran callable subroutine (DPDOWN), written in NOVA assembly language, reads these disk files and loads 168/E program and data memory. After loading memory, DPDOWN reads 168/E memory, compares each halfword with the corresponding datum from disk and sets an error flag if any discrepancy is detected — any difference is a fatal error. This readback and compare is a vital step in loading 168/E memory. Errors can be produced by WYLBUR — NOVA transfer errors (each line includes a checksum), corrupt NOVA disk files, SNOOP I/O errors and 168/E memory failures. However, as discussed below, most errors result from legitimate contention for the CAMAC bus. Large blocks of constants, e.g., algorithm look-up tables, are maintained on NOVA disk files independent of Translator output and loaded into COMMON blocks in 168/E data memory using a separate utility (DPXFER).

The key program in development of this system has been the 168/E Editor (DPEDIT). With this interactive program executing on the NOVA 4/X, users can examine and control 168/E processors from the main NOVA console. DPEDIT can display and modify 168/E memory with a word size of half, full or double and a base of decimal, octal or hex. The ability to examine processor memory in fullword format is particularly convenient since the NOVA

has a 16 bit word size and the SNOOP transfers data in halfwords. DPEDIT can also write/read the 168/E program counter, start/stop processor execution, etc. With the exception of "Listen Mode", DPEDIT exercises all SNOOP interface functions required for data acquisition. Interface problems have usually been isolated using DPEDIT together with an oscilloscope on the interface flat cable or 168/E backplane. However, some problems have required placing 168/E interface, CPU and memory cards on an open test bus rather than the closed 168/E crate to allow easy access for test probes.

Listen Mode data transfers are tested using a memory module in the CAMAC crate. The SNOOP module Listen Mode in Crate 26_8 (see Fig. 1) can be tested as follows:

i) write a pattern into BADC memory;
ii) set interface device select register for CPU #0, #1 or both;
iii) enable Listen Mode and read BADC;
iv) disable Listen Mode and read 168/E data memory to compare with original pattern.

This type of test was important for system development but during the last nine months no errors have been observed.

To test the 168/E processor itself we have developed the Integer, Floating Point and Memory diagnostics listed in Table II. These diagnostic programs are written in assembly language and test all IBM 370 instructions supported by the 168/E. The programs have a common structure with definition of each test specified by a few registers. If a diagnostic program executing on the 168/E detects an error, it follows a standard procedure which includes dumping all registers to data memory for user examination. Checking for successful execution of these diagnostics is essential whenever the processor configuration or hardware are modified, but during scheduled data acquisition we usually rely on infrequent off-line

TABLE II. 168/E Diagnostics

Name	Instructions Tested
INTTEST1	Branch, Integer Load and Store
INTTEST2	Integer Arithmetic and Logical
INTTEST3	Logical Shift
INTTEST4	Arithmetic Shift
FLTTEST1	Non-Arithmetic Floating Point
FLTTEST2	Floating Point Arithmetic - Simple tests
FLTTEST3	Floating Point Shift Matrix
FLTTEST4 *	R*4 Floating Point Arithmetic
FLTTEST5 *	R*6 Floating Point Multiply/Divide
FLTTEST6 *	R*6 Floating Point Add/Subtract
MEMTEST *	Test any Window in Data Memory

* ⟹ Not executable on IBM 370/168.

checks to confirm normal processor operation. Perhaps the most serious flaw in the entire diagnostic procedure is the 168/E processor's inability to test its own program memory in the normal crate configuration. However, we have only experienced one program memory failure in the last two years.

3. NOVA FOREGROUND/BACKGROUND OPERATION

For SHF data acquisition the NOVA 4/X is run in a Foreground/Background mode. The Foreground program is written entirely in Data General-RDOS assembly language and performs all time critical functions while a run is in progress. Table III lists the sequence of 168/E related events which occur after the operating system responds to a CAMAC pre-beam interrupt and transfers control to the Foreground. Background tasks written mostly in Fortran perform functions which are not time critical and usually interactive, e.g., select a 168/E diagnostic. Background programs communicate with the Foreground via RDOS system calls which read/write to a communications array in the Foreground. The F/B communication array contains a set of control words for each 168/E processor, e.g., on/off flag, initial value for program counter, data memory address for algorithm results, etc. These control words allow 168/E hardware or algorithm development and real-time tests while a run is in progress. About 2.5 ms after each beam pulse the Foreground reads a forty word summary of algorithm results from each active processor and saves this summary in the communication array where it can be examined by the user.

TABLE III. Foreground 168/E Control

Time (μs)	Activity
- 2025	Pre-beam interrupt ⟹ RDOS suspends Background task and executes Foreground
- 1550*	Start match point processor and execute algorithm on 168/E CPU #1
- 1425*	Initialize algorithm on 168/E CPU #2 and Auxiliary Controller
0	Beam Pulse (100 ns)
+ 15	Z_α digitizer finishes in Crate 27_8 and sets trigger level to start Auxiliary Controller
+ 20	Z_β digitizer finished ⟹ trigger Auxiliary Controller
+ 33	Z_γ digitizer finished ⟹ trigger Auxiliary Controller
54	Auxiliary Controller starts algorithm on CPU #2
120-300	High Resolution camera trigger
620	DMA readout of Crate 25_8 complete ⟹ start algorithm on 168/E CPU #0
2500	Read results from all 168/E algorithms
3000	Main camera trigger
9500	DMA readout of BADC complete with data transferred to CPU #0
17000	Start monitor program on CPU #0
38000	Foreground suspends itself and RDOS restores Background execution
97975	Next Pre-beam interrupt

* These activities may be delayed by ~500 μs depending on the status of the background program at the time of the interrupt.

The Background start-run task reads 168/E control words and program/data filenames from a card image disk file and loads processor memory. Another task provides menus of diagnostic programs and algorithms with each menu read from a card image file. By editing

these card image files, 168/E programs can usually be tested and added to production run procedures without modification to NOVA Foreground or Background programs. Since Background SNOOP I/O can always be interrupted by the Foreground, data transfer errors are inevitable. This happens infrequently for the size of programs used in this experiment and when a 168/E program load error is detected the procedure is simply restarted.

Algorithm execution time is measured in micro-seconds using a 168/E CAMAC clock module (see crate 27_8 in Fig. 1). Each interface board provides a TTL level which is true (high) when the processor is running. This level opens or closes a gate for clock pulses to a CAMAC scaler. On each beam pulse the Foreground reads the corresponding scaler sub-address for each active processor and saves this execution time in the F/B communication array. This clock module also has three LED's to indicate when each processor is running. Observation of the frequency and intensity of these LED's provides a convenient check for abnormal processor behavior.

4. TRIGGER ALGORITHM

The standard SHF charged track trigger uses PWC's in the nonbend plane (Z) to search for straight-line trajectories originating from the bubble chamber fiducial volume. When a good trajectory is found, the corresponding coordinates in the bend plane (Y) of the BC field can be used to calculate the momentum. Experiment BC72/73 uses High Resolution Optics (HRO) to measure charm particle decay lengths and requires a decision to take a HRO picture within 150-300 μs after the beam pulse — the main 40" BC camera still has a flash delay of 3 ms. Digitization and NOVA readout of the three primary PWC stations (α,β,γ with Z,Y,U at each station) requires a minimum of 150 μs and space point calculation on the 168/E takes a few hundred micro-seconds for normal multiplicities. So these procedures are too slow for the HRO trigger which was proposed after the 168/E system and SNOOP interface had been developed.

To meet the HRO time constraint the current algorithm uses only Z-planes and an Auxiliary Controller provides a fast data transfer to the 168/E. The Auxiliary Controller executes CAMAC functions sequentially from its control memory with a cycle time of 1 μs. It has a 1024 word control memory and a corresponding 1024 word data memory which contains input/output data for each control memory read/write. Control word format and the logical relationship of 168/E, controller and digitizer modules are shown in Fig. 2. CAMAC functions for NOVA I/O to the controller itself are listed in Table IV.

At the start of each run the Auxiliary Controller is loaded with the sequence of functions required to read Z_α, Z_β, Z_γ (8 hits and multiplicity for each plane) and start 168/E CPU #2. Before each beam pulse the Foreground arms the Auxiliary Controller and then avoids I/O to crate 27_8 until the HRO trigger sequence is complete. The first control word to read each PWC plane has the corresponding trigger bit(s) set so the controller waits for the digitizer module to finish and set a TTL trigger level (True = Low). Since the SNOOP module is in Listen Mode, data read by the Auxiliary Controller is transferred to CPU #2. When the Controller has finished reading Z_γ, it disables Listen Mode and starts the processor using SNOOP module CAMAC functions (see Ref. 3). As shown in Table III, this entire sequence is completed in 54 μs. The NOVA 4/X would require ~15 μs just to disable Listen Mode and start the 168/E while the Auxiliary Controller executes this sequence in 3 μs.

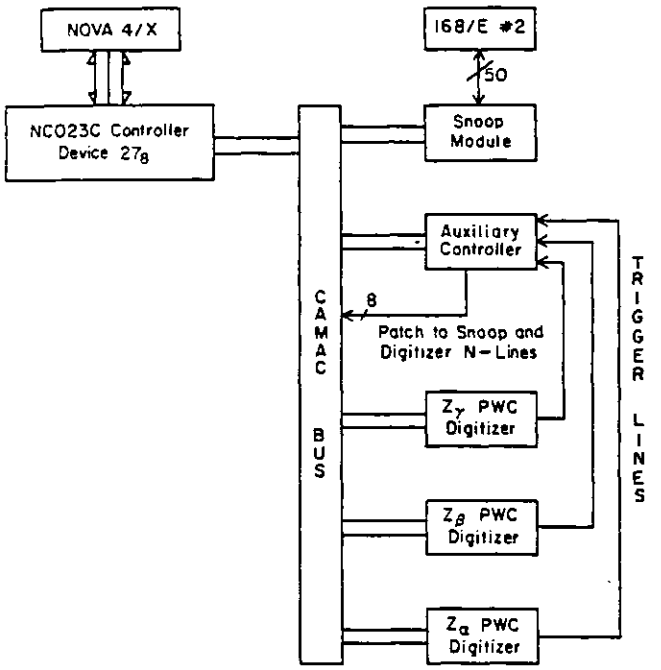

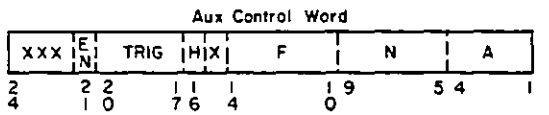

Bits 1-14 = CAMAC Sub-Address, Station # and Function

Bit 16 = HALT Flag (=1 to halt execution)

Bits 17-20 = Trigger Address

Bit 21 = Trigger Enable (=1 to enable)

Fig. 2. Relationship of CAMAC Auxiliary Controller, PWC and SNOOP modules and control word format.

TABLE IV. Auxiliary Controller Functions

F	A	Description
0	0	Read Data Memory at S1 and Increment Address Register at S2
0	1	Read Control Memory and Increment Address
0	2	Read Address Register
1	0	Read Data Memory
1	1	Read Control Memory
8	0	Test Done Flag (LAM if Enabled)
16	0	Write Data Memory and Increment Address
16	1	Write Control Memory and Increment Address
17	0	Write Data Memory
17	1	Write Control Memory
17	2	Write Address Register
24	0	Disable LAM
25	0	STOP Execution and Clear LAM
26	0	Enable LAM
27	0	Start Control Memory Execution

A flowchart of the algorithm on CPU #2 and profile of the bubble chamber and Z-planes are shown in Fig. 3. The algorithm is written in IBM assembly language and uses look-up tables rather than a calculation of allowed regions for maximum speed. A single 168/E memory board is quite sufficient for this program. PWC data and algorithm results are saved in a COMMON Block located at a fixed address by the 168/E Translator. Consequently algorithm modifications seldom require changes in on-line constants which provide 168/E data addresses for the NOVA Foreground.

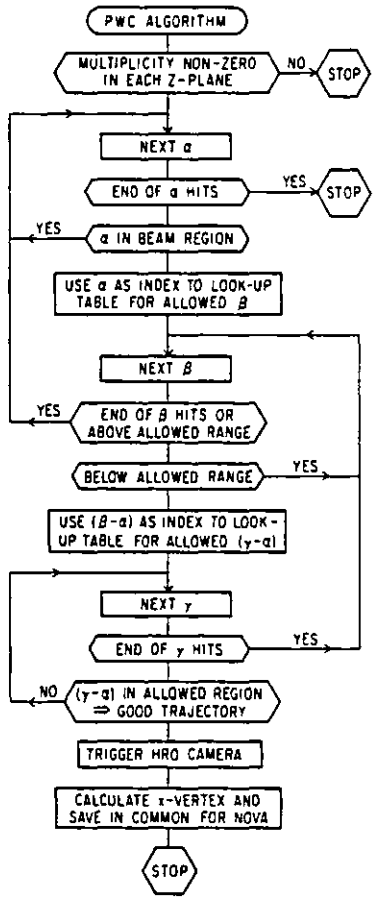

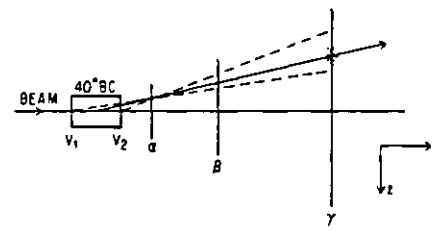

--- LOOK-UP TABLE BOUNDARY FOR β

ALLOWED REGION IN γ (SET BY MULTIPLE SCATTERING WHICH IS ±8 mm AT γ AND ±4 mm AT β)

$V_1 = -38$ cm, $V_2 = +38$ cm } BC VERTEX LIMITS

PWC	x (cm)	MAX WIRE*	BEAM REGION*	⟨HITS⟩†
α	80	240	± 9	1.7
β	121	312	±15	1.8
γ	203	600	±27	1.3

*ONE WIRE # = 1mm (xz PROFILE IS NOT DRAWN TO SCALE)

†AVERAGE MULTIPLICITIES FOR BEAM FLUX OF 20 PHOTONS/PULSE

Fig. 3. Flowchart and BC/PWC XZ-profile for algorithm to find straight-line trajectories.

When a good trajectory is found the algorithm generates the HRO trigger by writing to a camera trigger card in the 168/E crate. This is a simple card with a few gate circuits to define two high data memory addresses. An access to these addresses sets or clears an external TTL level which provides the camera trigger. The algorithm can access this pseudo-memory card in 300 ns while the NOVA 4/X would need ~17 μs to poll the processor and set a CAMAC register when a trigger is detected.

CPU #2 algorithm execution time is shown in Fig. 4 — this distribution does not include Auxiliary Controller data transfer time. This algorithm usually executes in less than 140 μs and the fraction of triggers arriving too late for the HRO camera is insignificant. The PWC algorithm triggers on ~66% of σ_t (γp) and 42% of pictures taken with this algorithm have hadronic production in the bubble chamber. (A logical OR of the PWC algorithm and a

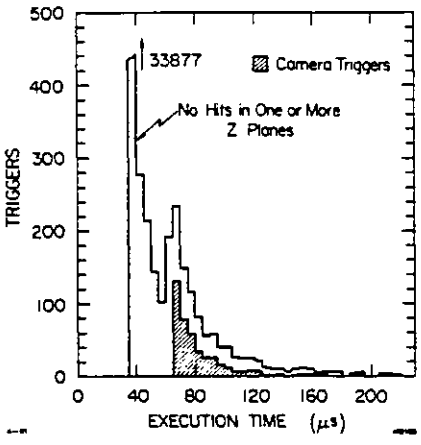

Fig. 4. PWC algorithm execution time on the 168/E.

dynode sum of energy deposited in the lead glass detector provides a trigger on ~90% of σ_t.) On the 168/E the algorithm runs ~2.4 times slower than on the IBM 370/168. Performance checks made by running the same algorithm and data off-line show no on-line processor errors since the start of production operation in July, 1980.

5. 168/E MONITOR PROGRAM

A Fortran program executing on 168/E CPU #0 monitors SHF data acquisition. Although NOVA Foreground and Background provide many monitor facilities, they each have limitations which are overcome with a dedicated processor. One is normally reluctant to modify the Foreground since it is vital for data acquisition and performance checks added to the Foreground decrease time available for Background execution. A Background program can only sample beam pulses and must be designed to be interrupted and replaced by another task while a run is in progress. The 168/E can monitor every beam pulse and the noninteractive Fortran program is easy to modify. Development/debugging are done on an IBM 370/168 and the same program can be used for both on-line and off-line applications without modification.

Currently the 168/E monitors data for three detectors — PWC, Čerenkov counters and Lead Glass. Statistics collected for each detector are listed in Table V. A subroutine which finds all charged tracks in the PWC system is used to calculate PWC efficiencies and Čerenkov counter performance. Monitor program execution time is 30-40 ms for normal PWC multiplicities so there is ample time available to support new routines and check other detectors (current pulse rate is 10 Hz).

TABLE V. Monitor Program Summary Data

A. PWC
   1. Illegal wire data, e.g., zero or negative wire #'s, wire # disorder, etc.
   2. Chamber multiplicities.
   3. Chamber efficiencies.
   4. Momentum and BC vertex distribution for PWC tracks.

B. Čerenkov
   1. Cell # and multiplicity.
   2. Average pulse height and pedestal for each cell.
   3. Momentum distribution for PWC tracks with signals above theshold in $\check{C}_1$ and $\check{C}_2$.

C. Lead Glass Columns
   1. Pulse height distribution in active converter and absorber.
   2. Pedestals for lead glass blocks, reference counters and hodoscopes.
   3. Average LED pulse heights for lead glass blocks and reference counters.

The program on CPU #0 and related Foreground control logic include support for a trigger algorithm. The 168/E MAIN program calls an assembly language algorithm and the monitor in the following sequence:

i) Foreground starts MAIN which calls the algorithm;
ii) algorithm finishes and executes a HALT instruction to stop the processor;
iii) Foreground reads algorithm results;
iv) lead glass data (not required by the algorithm) is transferred to CPU #0;
v) Foreground restarts the 168/E at instruction following HALT and algorithm returns to MAIN which calls monitor.

As indicated in Table III, the monitor program is executed after all trigger related Foreground functions and CAMAC data transfers are complete. All monitor input/output data and control variables are saved in COMMON blocks. The Foreground sets a single control flag which directs the monitor to initialize itself, collect data or produce a summary. At the end of each run a Backgroumd program reads this summary, saves it on disk and prints the results.

6. 168/E DIGITIZER CARD

Although the Auxiliary Controller provides satisfactory support for the algorithm using three Z-planes, data transfer time would become excessive for a trigger using all nine primary chambers. There is also a fourth station (δ) with Y- and Z-planes downstream of γ. Data transfer overhead is eliminated completely by placing the PWC digitizer in the 168/E crate where results are available as read only data memory.

The 168/E digitizer[5] with logic for one channel is shown in Fig. 5 — each card has eight identical channels. Before a digitizing sequence can begin a "Clear" pulse, usually generated externally but optionally from the 168/E, resets the Wire Address and Word Counters. Signals from PWC wires set corresponding bits in a shift register which, when shifted by "Clock" pulses, are presented as "Data" signals to the digitizer together with "Clock" pulses. The "Clock" signal increments a Wire Address Counter which contains the wire #. If a "Data" pulse also arrives indicating a wire has been hit, the contents of the Wire Address Counter are loaded into memory for that channel. "Clear", "Clock" and "Data" signals are input through BNC connectors added to the front panel of the 168/E crate.

The loading sequence increments a Word Count register which also acts as an address register for channel memory. Each channel can hold sixteen 12-bit wire numbers in sequential locations and input which exceeds this limit is lost. The eight channels operate in parallel and the digitization sequence ends when the Wire Address Counter reaches its (selectable) terminal count and sets the "Ready" flag. The 168/E algorithm is started before the beam pulse so it can interrogate the "Ready" flag and proceed as soon as data is available.

To read the digitizer, Data Address signals from the 168/E bus are multiplexed onto channel memory address inputs as shown in Fig. 5. Channel memory data are read through a block of 128 (8×16) addresses followed by address space for eight word counts. The base address is selectable by switch settings — it is currently memory card #3 with address

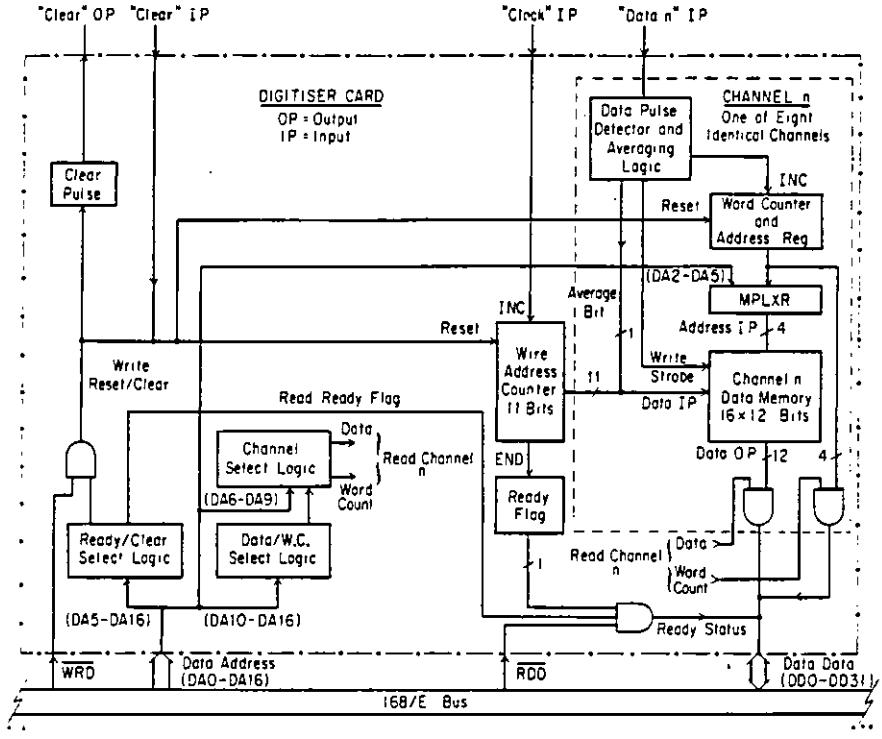

Fig. 5. Block diagram of 168/E PWC digitizer card.

$DC00_{16}$ for channel wire numbers and $DE00_{16}$ for multiplicities. Wire numbers are read onto Data Data lines 0-11 and multiplicities normally go to 168/E Data Data lines 0-3. In addition to this normal access mode, a switch option allows word counts to be included with wire numbers on Data Data lines 12-15. "Ready" flag and "Clear" pulse share a common address ($FC00_{16}$) which can also be selected by switches. A read to this address returns the "Ready" flag on Data Data line 15 (1 = ready). A write to this address generates "Clear" and reset pulses.

Development of the Digitizer card was completed recently, and it is currently operational on 168/E CPU #1. The production algorithm from CPU #2 has been modified to read the digitizer and is normally executed on every beam pulse. CPU #1 algorithm results are read by NOVA Foreground and saved on SHF data tapes for off-line analysis.

7. MATCH POINT RESULTS MEMORY

The Z,Y,U planes at each of the three PWC stations (α,β,γ) form a 3-4-5 right triangle and "Space" or "Match Points" are defined by the relation:

$$|3Z + 4Y - 5U - \text{constant}| \leq \text{tolerance} \quad .$$

A hardware match point-finder (one for each PWC station) has been developed to make match point results available within the time constraint of the HRO trigger.[6] After finding a straight-line trajectory in the Z-planes, the 168/E algorithm could use match point results to check for one or more confirmation hits in the Y-planes and calculate momentum.

The interface between the point-finder and 168/E is a Results Memory card in the 168/E crate. The interface was designed to meet the following requirements:

i) compatibility with existing 168/E systems;

ii) results from each point-finder should be accessible as soon as it has finished;

iii) the 168/E program should be able to check match point-finder status;

iv) the 168/E should be able to initialize each result's memory location.

We considered the option of a multi-port memory permitting DMA transfers from several external sources. This would require logic to arbitrate contention between two or more ports including the 168/E CPU itself. This option fails requirement i) since 168/E data memory control logic would have to be modified to allow a temporary delay in execution of a memory access.

A block diagram of Results Memory designed to meet the above requirements is shown in Fig. 6. Three separate memory units are write-only from each point-finder and read-only from the 168/E. Match points for a PWC station are transferred to the corresponding memory unit over a 50-wire flat cable (one cable from each point-finder). Each memory unit has two blocks, P and R, and each block has sixteen halfwords, permitting a maximum of sixteen matched (P,R) coordinate pairs per station. If coordinate pairs are transferred they would be loaded into sequential locations in memory with 3*Z in P and 4*Y in the R block. The α point-finder currently transfers 4*Y to a location in P with address set by the corresponding Z hit.

The memory chip used, 74S289, has the advantage for this application of separate data-in and data-out lines. However, to avoid the possibility of putting spurious signals on the 168/E data bus when the point-finder writes to memory, the output lines are buffered by 25LS240 bus drivers. These 3-state outputs are only enabled when a 168/E access is

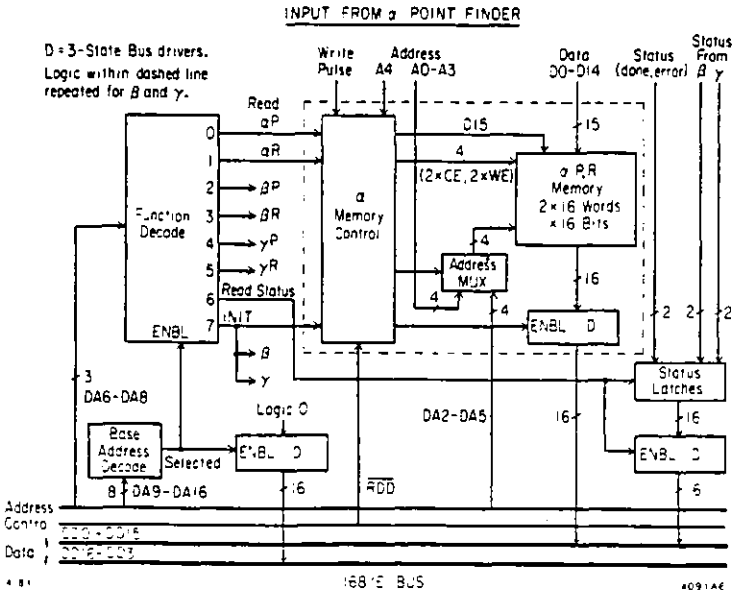

Fig. 6. Block diagram of 168/E Results Memory card.

decoded. To make this pseudo-memory compatible with 168/E logic the memory access time plus propagation delay of the bus drivers must be less than or equal to that of normal 168/E memory which is ~55 ns. The 168/E PWC digitizer uses the same type of memory and bus drivers.

Results memory is currently memory card #2 on CPU #1 with a base address of $9C00_{16}$. Memory-to-Register load instructions are used for both control and data input with eight functions decoded from data address lines 6-8 as shown in Fig. 6. Memory unit addresses are multiplexed with the address from each point-finder normally selected. For read functions 0-5 the multiplexor is switched to select P,R memory locations from 168/E data address lines 2-5. Data from a selected memory unit is placed on the least significant half of the 168/E data memory bus (DD0-DD15) and the upper halfword is logic zero.

To avoid possible interference with point-finder input, a 168/E program should not attempt to read α,β or γ memory units until the corresponding data transfer is complete. The status word with ERROR and DONE bits for each point-finder can be read at any time (function = 6):

		γ	γ	β	β	α	α
Not Used		D	E	D	E	D	E
31			4		2		0

Results Memory Status Word

ERROR bits are set to one and DONE bits to zero when the point-finders are initialized. Each point-finder clears its ERROR bit when the first match point is transferred and sets the DONE bit when processing is finished.

The seventh function, initialization, sets a logic one in bit 15 of the addressed word (DA2-DA5) in all six memory blocks. The algorithm on CPU #1 is started before the beam pulse and initializes all memory blocks by reading the sixteen words with data address bits 6-8 set to one for function seven. The algorithm polls the status word to determine when match point data is available and could use bit 15 in each results memory location as a flag for valid data. The α match point-finder is operational and Results Memory has been read by a 168/E algorithm, saved on NOVA run tapes and verified off-line.

8. SUMMARY

The 168/E processor has been versatile and stable in the SHF on-line operating environment. Program development and hardware tests can be done with minimal dedicated time on the NOVA host computer. Most algorithm development and testing is done off-line on an IBM 370 and most Results Memory tests were made during production runs. The PWC Digitizer and Results Memory cards provide fast 168/E data input, however, they also require algorithms which cannot be completely tested off-line. Diagnostic procedures for these cards would be more robust if their design allowed the 168/E to write any valid pattern to Results Memory and execute production algorithms using this test data. Results Memory is a convenient approach to special 168/E I/O since design only requires familiarity with the processor bus and timing.

ACKNOWLEDGEMENTS

We thank D. Bernstein and L. Paffrath for design and development of the SNOOP module interface and Auxiliary Controller. Consultation with P. F. Kunz has been most helpful in development of this system and V. Bevan provided software development for the point-finder.

REFERENCES

1. K. C. Moffeit et al., SLAC Proposal BC72 (1979); G. Kalmus et al., SLAC Proposal BC73 (1979).

2. P. F. Kunz et al., "The LASS Hardware Processor," Proc. of the 11th Annual Microprogramming Workshop, SIGMICRO Newsletter 9, 25 (1978).

3. D. Bernstein et al., "SNOOP Module CAMAC Interface to the 168/E Microprocessor," Proc. of the 1979 Nuclear Science Symposium, IEEE Trans. on Nucl. Sci. NS-27, 587 (1980).

4. M. Breidenbach et al., "Semi-Autonomous Controller for Data Acquisition the Brilliant ADC," Proc. of the 1977 Nuclear Science Symposium, IEEE Trans. on Nucl. Sci. NS-25, 706 (1978).

5. This digitizer was adapted from a design by D. Freytag, "A Compact Time Digitizer in CAMAC Format," Nucl. Instrum. Methods 138, 685 (1976).

6. BC72/73 Collaboration Letters from Dave Price, Imperial College (1979-1980).

SLAC-PUB-2870
RL 82-005
TUHEL 82-01
January 1982
(T/E)

fetimes of Charmed Particles Produced in a 20 GeV γp Experiment*

SLAC Hybrid Facility Photon Collaboration

K. Abe[13], T.C. Bacon[5], J. Ballam[11], L. Berny[12], A.V. Bevan[5], H.H. Bingham[15], J.E. Brau[11], D. Brick[2], W.M. Bugg[17], J. Butler[11], W. Cameron[5], J.T. Carroll[11], C.V. Cautis[11], J.S. Chima[5], H.O. Cohn[9], D.C. Colley[1], G.T. Condo[17], S. Dado[12], R. Diamond[4], P.J. Dornan[5], R. Erickson[11], T. Fieguth[11], R.C. Field[11], L. Fortney[3], B. Franek[10], N. Fujiwara[8], R. Gearhart[11], J. Goldberg[12], G.P. Gopal[10], A.T. Goshaw[3], E.S. Hafen[7], V. Hagopian[4], G. Hall[5], E.R. Hancock[10], T. Handler[17], H.J. Hargis[17], E.L. Hart[17], P. Haridas[7], K. Hasegawa[13], T. Hayashino[13], D.Q. Huang[7†], R.I. Hulsizer[7], S. Isaacson[12], M. Jobes[1], G.E. Kalmus[10], D.P. Kelsey[10], J. Kent[15], T. Kitagaki[13], P. Lang[11†], J. Lannutti[4], A. Levy[16], P.W. Lucas[3], W.A. Mann[14], T. Maruyama[14], M. MacDermott[10], R. Merenyi[14], R. Milburn[14], C. Milstene[16], K.C. Moffeit[11], J.J. Murray[11], S. Naguchi[8], A. Napier[14], F. Ochiai[6], S. O'Neale, A.P.T. Palounek[3], I.A. Pless[7], M. Rabin[11], P. Rankin[5], W.J. Robertson[3], A.H. Rogers[17], E. Ronat[18], H. Rudnicka[2], T. Sato[6], J. Schneps[14], J. Shank[15], A.M. Shapiro[2], C. Sinclair[11], R. Sugahara[6], A. Suzuki[6], K. Takahashi[6], K. Tamai[13], S. Tanaka[13], S. Tether[7], H.B. Wald[14], W.D. Walker[3], M. Widgoff[2], C.G. Wilkins[1], S. Wolbers[15], C.A. Woods[5], Y. Wu[7], A. Yamaguchi[13], R.K. Yamamoto[7], S. Yamashita[8], G. Yekutieli[18], Y. Yoshimura[6], G.P. Yost[15], H. Yuta[13].

Submitted to Physical Review Letters

Work supported in part by the Department of Energy, contract DE-AC03-SF00515, Japan-US Co-operative Research Project on High Energy Physics under the Japanese Ministry of Education, Science and Culture and the US Department of Energy, UK Science and Engineering Research Council, US-Israel B.S.F., US National Science Foundation and Israel Academy of Sciences Commission for Basic Research.

1. Birmingham University, Birmingham, England
2. Brown University, Providence, Rhode Island, USA
3. Duke University, Durham, North Carolina, USA
4. Florida State University, Tallahassee, Florida, USA
5. Imperial College, London, England
6. KEK, Oho-machi, Tsukuba-gun, Ibaraki, Japan
7. Massachusetts Institute of Technology, Cambridge, Massachusetts, USA
8. Nara Womens University, Nara, Japan
9. ORNL, Oak Ridge, Tennessee, USA
10. Rutherford Appleton Laboratory, Didcot, England
11. Stanford Linear Accelerator Center, Stanford University, Stanford, California, USA
12. Technion-Israel Institute of Technology, Haifa, Israel
13. Tohoku University, Sendai, Japan
14. Tufts University, Medford, Massachusetts, USA
15. University of California, Berkeley, California, USA
16. University of Tel Aviv, Tel Aviv, Israel
17. University of Tennessee, Knoxville, Tennessee, USA
18. Weizmann Institute, Rehovot, Israel

† On leave of absence from the Institute of High Energy Physics, Beijing, China

Eleven neutral and nine charged decays of charmed particles have been observed in a sample of 205000 hadronic interactions in a 1.2 million picture exposure of the SLAC hybrid facility to a 20 GeV/c backward scattered laser beam. The charged and neutral lifetimes were determined to be $8.2 \pm \frac{4.5}{2.5} \times 10^{-13}$ sec and $6.7 \pm \frac{3.5}{2.0} \times 10^{-13}$ sec, respectively, with a ratio of $1.2 \pm \frac{0.9}{0.5}$.
PACS numbers 14.40.Pe, 13.25. + m.

The lifetimes of charged and neutral charmed particles have been the subject of recent experimental and theoretical interest[1,2]. In this letter, we present new measurements of these lifetimes.

The experiment was performed at the SLAC Hybrid Facility with a backward scattered laser beam incident on the 1 m hydrogen bubble chamber operated at 10 Hz. The beam was 3 mm in diameter, peaked at 20 GeV with a FWHM of 2 GeV, and usually contained 25 photons per pulse. Following the bubble chamber were four sets of multiwire proportional chambers (MWPC's), two atmospheric pressure Cerenkov counters, and a lead-glass wall[3]. All the downstream detectors were deadened in the region containing the e^+e^- pairs from beam conversions.

In order to detect charm decays near the interaction vertex, a fourth camera having a resolution of 55 microns over a depth of ±6 mm, was used. The bubble chamber was operated at an elevated temperature and the flash lamps were triggered 200 microseconds after the beam passage. This resulted in 70 bubbles/cm of 55 micron diameter.

The cameras were triggered on either of two conditions. The first condition was the passage through three MWPC stations of any charged particle originating

in the fiducial volume of the bubble chamber. The required calculation was performed within the 200 μsec time limit by a 168/E processor[4]. The second trigger condition was based on the energy deposited in the lead-glass wall[3]. With this combination, we triggered on 90 percent of the total hadronic cross section with a yield of 1 event per 6 photographs. Monte Carlo studies indicate that approximately 80 percent of the charm cross section is included by the trigger.

The results presented here are based on 1.2×10^6 pictures containing approximately 205000 hadronic interactions. All hadronic events were closely examined for the decays of short-lived particles within 1 cm of the interaction vertex. In order for an event to be considered a charm candidate, either the decay point had to be visible or the backward projection of one of the tracks in the event had to miss the production vertex (the impact distance) by at least one track width. Only decays having two or more charged tracks were considered. Decays consistent with strange particle hypotheses were eliminated. Twenty-nine events remained with one or two visible charm particle decays. Three cuts were imposed on these events:

C1. An impact distance greater than 110 μm (2 track widths) was required for at least one track in each event to ensure high efficiency for finding charged and neutral decays (see d^{max} in Figure 1).

C2. A minimum impact distance cut of 40 μm was imposed on a second track from the same decay vertex to eliminate 1-prong decays, which happen to be superimposed on other tracks (see d_2 in Figure 1).

C3. A minimum decay length cut of 500 μm was imposed to allow a clean separation of the charged and neutral decays.

After imposing these cuts, 21 events remained; 14 had a single visible decay and 7 had two, where the second decay needed only to have one track with an impact distance greater than 40 μm.

A total of 23 decays satisfied all three conditions. These included 11 neutral (7 two-prongs and 4 four-prongs), 4 positive (all three-prongs, but one with an additional Dalitz pair), 5 negative (all three-prongs), and 3 charged/neutral ambiguous decays. Three of the neutral and 5 of the charged decays are compatible with Cabibbo-allowed D decays with no missing neutral particles; the rest are compatible if a missing π^o, $(\bar{K})^o$, or ν is assumed. In most cases, not all charged tracks are identified. Thus, for most $D^{\pm}$ candidates, the $F^{\pm}$ hypothesis cannot be excluded, and for two candidates, Λ_c^+ is also possible. Despite the lack of complete neutral particle detection, it has often been possible, because of the relatively low beam energy, to obtain good limits on the momentum used for the flight time determination.

For each of the 23 accepted decays, an effective length (L_{eff}) was calculated. This is defined as the actual distance (L) travelled by the particle, minus the length from the production vertex to the first point along its path where its decay would have satisfied all three acceptance conditions (C1, C2, C3). Note that this first detection point is uncorrelated with the decay distance. Thus, L_{eff} is the path length over which a charmed particle would have been accepted as such, and it provides an unbiased means for calculating the lifetime. When the momentum, P, of each of N charmed particles of mass M is known, then the mean lifetime is given by:

$$\tau = \frac{1}{N} \sum_{i=1}^{N} \left(\frac{L_{eff}}{P} \frac{M}{c} \right)_i .$$

This method (Method I) allows us to use only 5 charged and 3 neutral decays.

In order to use all the events, several other methods for estimating the lifetimes were also employed. One of these (Method II) used upper (P_{max}) and lower (P_{min}) limits on the momentum P determined on an event by event basis to calculate an average lifetime $\bar{T}_{eff}$:

$$\langle \bar{T}_{eff} \rangle = \frac{K}{N} \sum_{i=1}^{N} \frac{L_{eff.M}}{P'.c}$$

where P' is an estimate of the real momentum.

$$\frac{1}{P'} = \frac{1}{2} \left(\frac{1}{P_{max}} + \frac{1}{P_{min}} \right)$$

Monte Carlo studies suggest that $\langle \bar{T}_{eff} \rangle$ is good estimator of the lifetime with the value of K in the range 0.85 to 1.0.

Other methods involved generating Monte Carlo events with the same cuts as applied to the data. The lifetime dependences of the means of various distributions were calculated. The means of the corresponding experimental distributions were then used to determine the lifetimes. The distributions chosen were the maximum projected impact distance d^{max} (Method III), the projected total length L (Method IV), and the projected effective length L_{eff} (Method V). The lifetime as determined from different charm production models differs by less than 20 percent.

Figure 2 gives the experimental distributions of L, L_{eff}, d^{max} and $\bar{T}_{eff}$. In comparing the charged and neutral decays, note the similarities in the distributions and their mean values. The momentum distributions were also similar. The distributions of the ambiguous decays are compatible with both the charged and neutral distributions.

Table I gives the values of the lifetimes obtained by each of the methods described above. It can be seen from this table that all methods give consistent results. We have combined the parameters of Methods II, III, IV and V in a maximum likelihood determination of the lifetime, where these parameters (T_{eff}, d^{max}, L, L_{eff}) are compared on an event by event basis to the Monte Carlo. From this we obtain:

$$\tau^{\pm} = (8.2 \pm \begin{matrix} 4.5 \\ 2.5 \end{matrix}) \times 10^{-13} \text{ sec},$$

$$\tau^{o} = (6.7 \pm \begin{matrix} 3.5 \\ 2.0 \end{matrix}) \times 10^{-13} \text{ sec, and}$$

$$\tau^{\pm}/\tau^{o} = 1.2 \pm \begin{matrix} 0.9 \\ 0.5 \end{matrix}$$

The errors are dominated by statistics but include also systematic effects. The results are insensitive to reasonable changes in the values of the cuts C1, C2, C3. The curves on Figure 2 represent the distributions expected for these lifetimes. One neutral four-prong decay is worthy of mention because it has the invariant mass of a $\bar{D}^{o}$ without missing neutral particles and has an effective proper flight time of 21.8×10^{-13} sec.

In conclusion, we have examined the decays of 11 neutral and 9 charged charmed particles photoproduced in a high-resolution bubble chamber. Backgrounds from all sources are small compared to 1 event. The charged lifetime obtained is compatible with previous measurements of $D^{\pm}$ lifetimes; however, the neutral lifetime is significantly longer than has been found in previous experiments[1], and leads to a charged to neutral lifetime ratio consistent with unity.

ACKNOWLEDGEMENTS

We wish to thank the SLAC bubble chamber crew for their dedication in achieving high quality under difficult conditions. We are especially indebted to the film scanners for their efforts in finding the events.

This work was supported by:

Japan-US Co-operative Research Project on High Energy Physics under the Japanese Ministry of Education, Science and Culture and the US Department of Energy

UK Science and Engineering Research Council

US Department of Energy

US-Israel B.S.F.

US National Science Foundation

Israel Academy of Sciences Commission for Basic Research

References

1. N. Ushida et al, Phys. Rev. Lett., 45, 1049 (1980) and Phys. Rev. Lett. 45, 1053 (1980).

   D. Allasia et al, Nucl. Phys. 176, 13 (1980).

   A. Fiorino et al, Lett. Al Nuovo Cim. 30, 166 (1981).

   M.I. Adamovich et al, Phys. Lett. 99B, 271 (1981) and Phys. Lett. 89B, 427 (1980).

   W. Bacino et al, Phys. Rev. Lett. 45, 329 (1980).

   R. Schindler et al, Phys. Rev. D24, 78 (1981).

   G. Trilling, Physics Reports 75, 57 (1981).

2. N. Cabibbo and L. Maiani, Phys. Lett. 79B (1978) 109.

   N. Cabibbo, G. Corbo and L. Maiani, Nucl. Phys. B155, 93 (1979).

   B. Guberina et al, Phys. Lett. 89B, 111 (1979).

   W. Bernreuther, O. Nachtmann and B. Stech, Z Physik C, Particles and Fields 4, 257 (1980).

   H. Fritzch and P. Minkowski, Phys. Lett. 90B, 455 (1980).

   M. Bander, B. Silverman and A. Soni, Phys. Rev. Lett. 44, 7 (1980).

3. J.E. Brau et al, SLAC-PUB-2773, July 1981 (submitted to Nucl. Inst. and Methods).

4. J.T. Carroll et al, SLAC-PUB-2726, April, 1981 (unpublished).

TABLE I. Lifetimes of charged and neutral charmed particles and their ratios, as determined by various methods explained in the test.

Method		Charged lifetime (10^{-13}s)	Neutral lifetime (10^{-13}s)	Charged / Neutral
I.	$\langle L_{eff} \rangle$ constrained decays	$8.2 \pm {}^{6.5}_{2.5}$ (5 decays)	$9.4 \pm {}^{12.0}_{4.0}$ (3 decays)	0.9
II.	$\langle T_{eff} \rangle$	7.6	6.4	1.1
III.	$\langle d^{max} \rangle$	9.6	7.4	1.3
IV.	$\langle L \rangle$	8.4	6.8	1.3
V.	$\langle L_{eff} \rangle$	8.1	6.7	1.2

Figure Captions

Figure 1 An event showing the decay of a positive charmed particle into 3 charged tracks after 0.86 mm and the decay of a neutral charmed particle after 1.8 mm. Both decays contain missing neutrals and cannot come from strange particles. The quantities d^{max} and d_2, the largest and second largest impact distances for the 3-prong decay are indicated.

Figure 2 Distributions of L, L_{eff}, d^{max} and $\bar{T}_{eff}$. The curves are from Monte Carlo calculations using the charged and neutral lifetimes given in the text normalised to the number of decays.

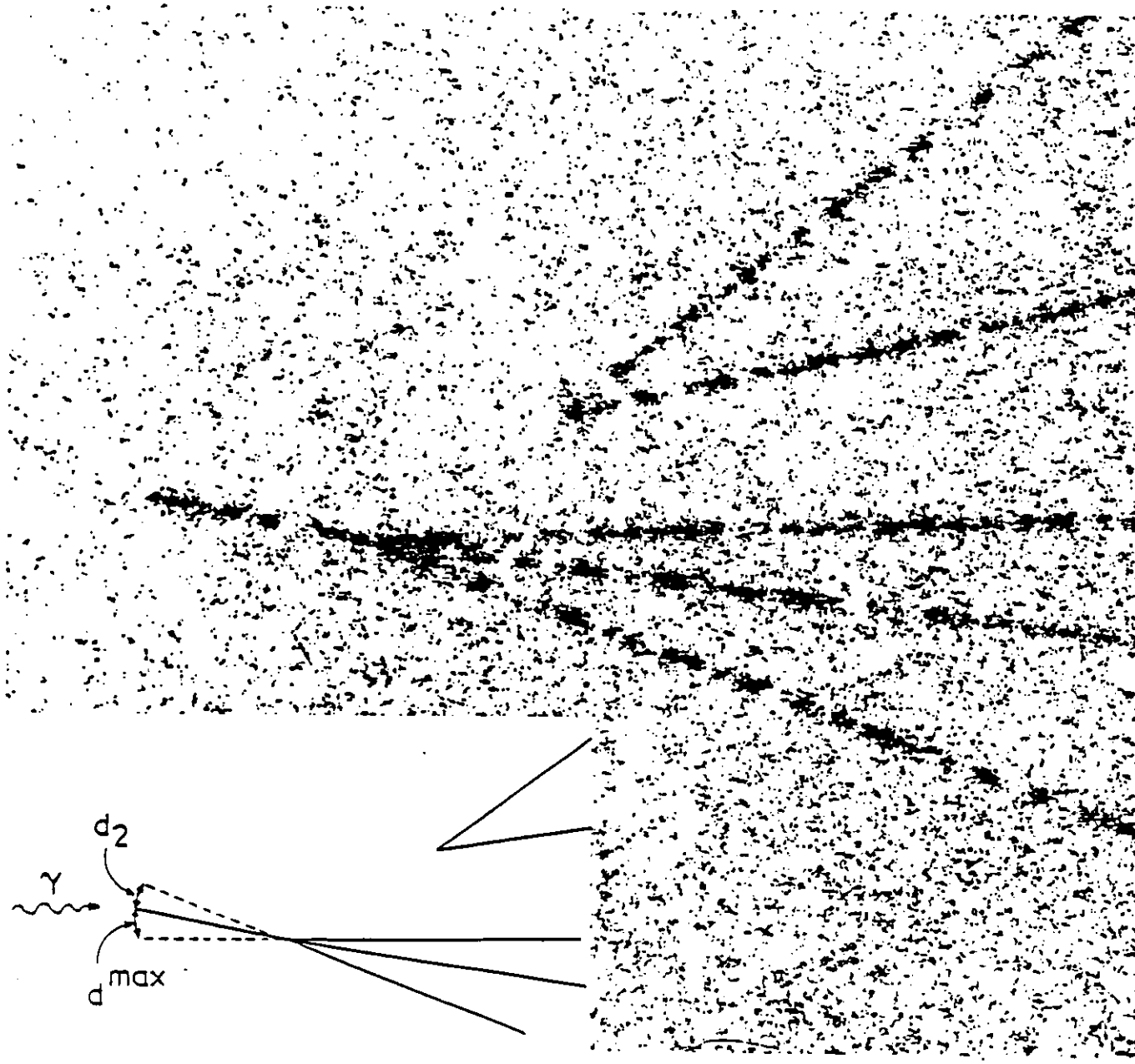

Fig. 1

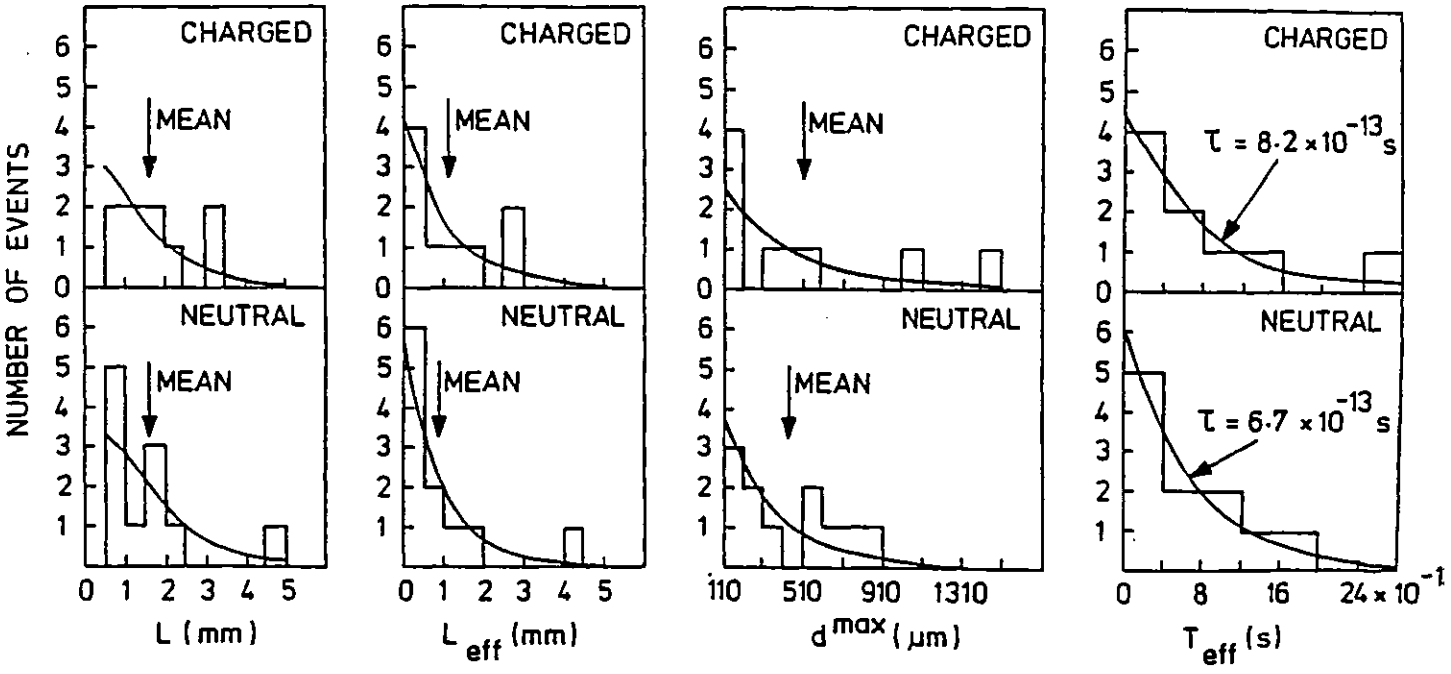
NUMBER OF EVENTS
CHARGED
MEAN
NEUTRAL
MEAN
L (mm)
CHARGED
MEAN
NEUTRAL
MEAN
L eff (mm)
CHARGED
MEAN
NEUTRAL
MEAN
d max (μm)
CHARGED
τ = 8·2 x 10^-13 s
NEUTRAL
τ = 6·7 x 10^-13 s
T eff (s)

Fig. 2

ACKNOWLEDGEMENTS

I would like to thank all the members of the HENP group at Imperial College especially the scanners, computing staff and physicists directly involved in the experiment.

In particular especial thanks are due to Dr. T.C. Bacon my supervisor for his guidance, Dr. P.J. Dornan who was directly responsible for my work on the PWC trigger, and to Professor I. Butterworth who gave me the opportunity of working with the HENP group.

I would also like to thank all the physicists who form the SLAC Photon Collaboration and who made participation in the experiment such a pleasure.

The role played by the SLAC bubble chamber crew and beam operators is gratefully acknowledged.

The SERC provided financial support for a period of three years.

The excellent typing of this thesis by Janie Coghill is greatly appreciated.

Finally, in acknowledgement of the fact that this work would not have been possible without the support of my parents, this thesis is dedicated to May and Sidney Rankin.